ISSN 1590-8844
Vol. 26 No. 02
2025

International Journal of Mechanics and Control

Editor: Andrea Manuello Bertetto

Scopus Indexed Journal

Reference Journal of IFToMM Italy
International Federation for the Promotion
of Mechanism and Machine Science

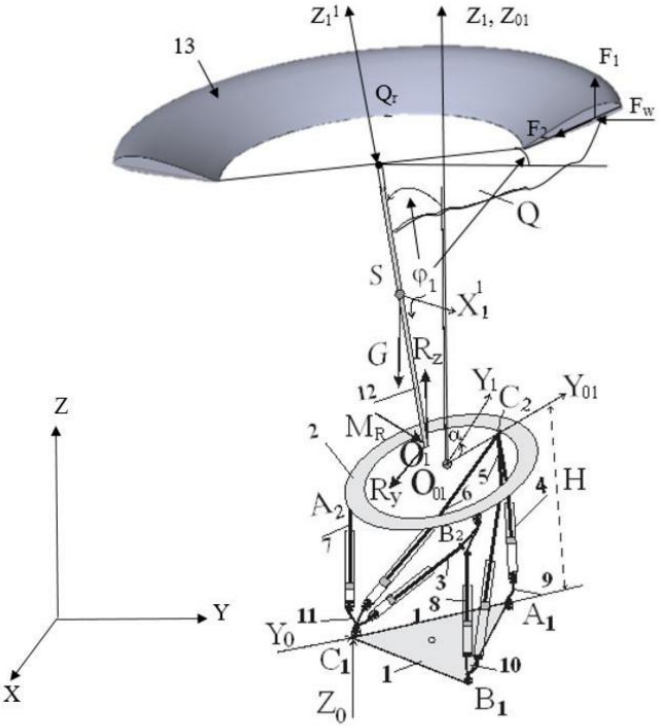

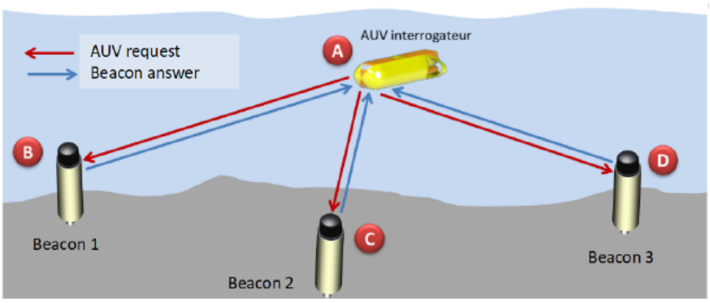

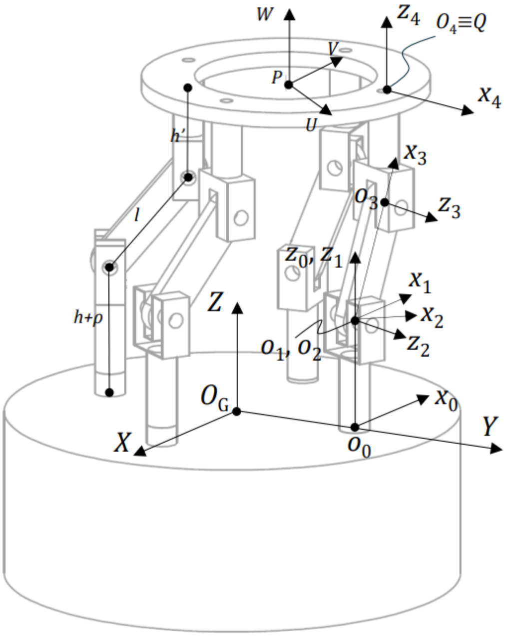

Published by ASTRA M B S.R.L.
Via Febo, 22 – 10133 – Torino (Italy)

International Journal of Mechanics and Control

Associate Editors

Published by ASTRA M B S.R.L. – Torino – Italy E.C.

Honorary editors
Guido Belforte
Kazuo Yamafuji

Editor: **Andrea Manuello Bertetto**

General Secretariat:
Matteo D. L. Dalla Vedova
Simone Venturini
Alessandro Aimasso

Mario Acevedo
Universidad Panamericana
Mexico City – Mexico

Giovanni Boschetti
University of Padova
Vicenza – Italy

Luca Bruzzone
Università degli Studi di Genova
Genova – Italy

Giuseppe Carbone
Università della Calabria
Rende – Italy

Marco Ceccarelli
Università degli Studi di Roma Tor Vergata
Roma – Italy

Alberto Concu
AC Technologies S.r.l.s., Italy

Matteo Davide Lorenzo Dalla Vedova
Politecnico di Torino
Torino – Italy

Amalia Ercoli Finzi
Politecnico di Milano
Milano – Italy

Francesca Di Puccio
University of Pisa
Pisa – Italy

Carlo Ferraresi
Politecnico di Torino
Torino – Italy

Alexey Fomin
Mechanical Engineering Research Institute of the Russian Academy of Sciences (IMASH RAN)
Moscow – Russia

Walter Franco
Politecnico di Torino
Torino – Italy

Rafael Lopez Garcia
University of Jaen
Jaen – Spain

Viktor Glazunov
Mechanical Engineering Research Institute of the Russian Academy of Sciences (IMASH RAN)
Moscow – Russia

Rogério Sales Gonçalves
Federal University of Uberlândia
Uberlândia – Brazil.

Kenji Hashimoto
Waseda University
Tokyo – Japan

Giovanni Jacazio
Politecnico di Torino
Torino – Italy

Juan Carlos Jauregui Correa
Universidad Autonoma de Queretaro
Queretaro – Mexico

Med Amine Laribi
University of Poitiers
Poitiers – France.

Paolo Maggiore
Politecnico di Torino
Torino – Italy

Amedeo Manuello Bertetto
Politecnico di Torino
Torino – Italy

Mingfeng Wang
Brunel University
London – United Kingdom

Massimiliano Pau
University of Cagliari
Cagliari – Italy

Paolo Emilio Lino Maria Pennacchi
Politecnico di Milano
Milano – Italy

Giuseppe Quaglia
Politecnico di Torino
Torino – Italy

Roberto Ricciu
Università di Cagliari
Cagliari – Italy

Aleksandar Rodic
Institute Mihajlo Pupin
Belgrade – Serbia

Shuangji Yao
Yanshan University
Qinhuangdao – China

Patrizia Trovalusci
Sapienza - University of Rome
Roma – Italy

Mauro Velardocchia
Politecnico di Torino
Torino – Italy

Simone Venturini
Politecnico di Torino
Torino – Italy

Renato Vidoni
Free University of Bolzano
Bolzano – Italy

Ion Visa
Transilvania University of Brasov
Brasov – Romania

Yu-Hsun Chen
National Taiwan University of Science and Technology
Taipei City – Taiwan

Jaroslav Zapomel
VSB - Technical University of Ostrava
Ostrava - Czech Republic

Leon Zlajpah
Jozef Stefan Institute
Ljubljana – Slovenia

Official Torino Italy Court Registration
n. 5390, 5th May 2000
Deposito presso il Tribunale di Torino
n. 5390 del 5 maggio 2000
Direttore responsabile:
Andrea Manuello Bertetto

International Journal of Mechanics and Control

The Journal is addressed to scientists and engineers who work in the fields of mechanics (mechanics, machines, systems, control, structures). It is edited in Turin (Northern Italy) by ASTRA M B S.R.L., with an international board of editors. It will have not advertising. Turin has a great and long tradition in mechanics and automation of mechanical systems. The journal would will to satisfy the needs of young research workers of having their work published on a qualified paper in a short time, and of the public need to read the results of researches as fast as possible.
Interested parties will be University Departments, Private or Public Research Centres, Innovative Industries.

Aims and scope

The *International Journal of Mechanics and Control* publishes as rapidly as possible manuscripts of high standards. It aims at providing a fast means of exchange of ideas among workers in Mechanics, at offering an effective method of bringing new results quickly to the public and at establishing an informal vehicle for the discussion of ideas that may still in the formative stages.

Language: English

International Journal of Mechanics and Control will publish both scientific and applied contributions. The scope of the journal includes theoretical and computational methods, their applications and experimental procedures used to validate the theoretical foundations. The research reported in the journal will address the issues of new formulations, solution, algorithms, computational efficiency, analytical and computational kinematics synthesis, system dynamics, structures, flexibility effects, control, optimisation, real-time simulation, reliability and durability. Fields such as vehicle dynamics, aerospace technology, robotics and mechatronics, machine dynamics, crashworthiness, biomechanics, computer graphics, or system identification are also covered by the journal.

Please address contributions to

Prof. Andrea Manuello Bertetto
PhD Eng. Matteo D. L. Dalla Vedova

Dept. of Mechanical and Aerospace Engineering
Politecnico di Torino
C.so Duca degli Abruzzi, 24
10129 - Torino - Italy

www.jomac.it
e_mail: jomac@polito.it

Subscription information

Subscription order must be sent to
the publisher:

ASTRA M B S.R.L.
Via Febo, 22
10133 - Torino - Italy

e_mail: astra.mb.srl@gmail.com
mob.: +39 347 490 2080

International Journal of Mechanics and Control

Scientific Board

Published by ASTRA M B S.R.L.– Torino – Italy

Official Torino Italy Court Registration
n. 5390, 5th May 2000

Deposito presso il Tribunale di Torino
n. 5390 del 5 maggio 2000

Editor in Chief

Direttore responsabile:
Andrea Manuello Bertetto

ISSN 1590-8844
International Journal of Mechanics and Control, Vol. 26, No. 2, 2025
https://doi.org/10.69076/jomac.2025.0019

DEVELOPMENT OF ENHANCED MATLAB-BASED THERMODYNAMIC CYCLE SOFTWARE: COMPREHENSIVE ANALYSIS OF GAS CYCLES WITH POLYNOMIAL SPECIFIC HEAT DEPENDENCE

Ardit Gjeta Artan Hoxha Majlinda Alcani Altin Dorri

Energy Department, Mechanical Engineering Faculty, Polytechnic University of Tirana, Albania

ABSTRACT

In the present study, an innovative Matlab-based software package has been developed to facilitate the configuration of engine thermodynamic parameters, with a particular focus on internal combustion engine cycles. The software includes a user-friendly graphical interface designed to support lecturers in improving teaching applications related to engine parameter changes, providing an efficient tool for visual presentations. Furthermore, students can use the program code to solve examples and compare manual results in their projects. In contrast to the previous article, this paper presents an extension of the software package, covering a wider range of thermodynamic cycles, including the Atkinson cycle and the Brayton cycle of the gas turbine. A distinctive aspect of this research lies in the comprehensive treatment of the polynomial dependence of specific heat in all thermodynamic cycles. In particular, the engineering model used in this study adopts simplifications, treating air as an ideal gas, considering the piston-cylinder assembly as a closed system, and assuming adiabatic compression and expansion processes. Internal reversibility characterizes all processes, while kinetic and potential energy effects are negligible. The software application demonstrates the influence and comparison of thermodynamic parameters in thermodynamic cycles, such as internal combustion engines (ICE) and gas turbine cycles, displaying key metrics such as engine work output, cycle thermal efficiency, Carnot efficiency, etc. The study culminates in graphical presentations of cycle diagrams, providing a comprehensive comparison with the results presented in the previous article.

Keywords: Internal Combustion Engines (ICE), Atkinson, Gas Turbine, Brayton, Matlab GUI

1 INTRODUCTION

Thermodynamic cycles are the foundation of energy conversion systems, powering everything from internal combustion engines to gas turbines and power plants [1]. Understanding and analyzing these cycles is crucial for engineers, scientists, and students in the field of energy systems.

However, common methods of calculating thermodynamic properties that are based on property tables are time-consuming and prone to calculation errors [2]. To facilitate the user, the Gas Power Cycle Program offers an advanced and interactive Graphical User Interface (GUI), enabling users to analyze and graphically visualize various thermodynamic cycles as easily as possible [3]. The graphical user interface (GUI) of the MATLAB applications was created using MATLAB App Designer [4]. The Gas Power Systems program is designed to provide users with a comprehensive tool for the study of various thermodynamic cycles [8], [9], including the spark ignition engine, Otto cycle, the compression ignition engine, Diesel cycle [5], the dual combustion engine, Sabathe cycle[6], the variable compression ratio engine, Atkinson cycle [7] and the gas turbine engine, Brayton cycle [7].

Contact author: Ardit Gjeta [1]
[1] Energy Department, Mechanical Engineering Faculty, Polytechnic University of Tirana, Albania
E-mail: agjeta@fim.edu.al

Matlab GUI allows users to enter several key parameters such as pressure, temperature, compression ratio, and heat capacity ratios, the software instantly calculates essential thermodynamic values [3]. It generates detailed pressure-volume (P−v) and temperature-entropy (T−s) diagrams, offering clear visual insights into the processes within each cycle. Building on the work presented in the previous study [3], which focused on simulating the ideal Otto, Diesel and Sabathe air cycles using a Matlab graphical user interface.

This study aims to extend the range of thermodynamic cycles, such as the Brayton and Atkinson cycles, and to achieve more accurate cycle design.

Although the Matlab graphical user interface (GUI) in the earlier work was a useful tool for examining engine characteristics and the impact of thermodynamic parameters under simplified assumptions [3], a more thorough investigation necessitates the investigation of less idealized conditions. Consequently, this study will go beyond the simplification of the constant specific heat assumed in the original model [3] and examine the impact of non-constant specific heat [10], [11].

The distinguishing feature of this study is the implementation of a polynomial dependence of the specific heat of air [10]. The software can simulate thermodynamic behavior across a broad temperature range thanks to this advanced model. The NASA Seven-Term Polynomial Equation [10] is used to calculate specific heat, enthalpy, and entropy, yielding extremely precise results for every cycle.

2 MATLAB GRAPHICAL USER INTERFACE

One of the most important applications of MATLAB is in thermodynamics and energy systems analysis, where it can model, simulate, and visualize various thermodynamic cycles. The advanced MATLAB-based software developed in this study facilitates the work of users in the analysis and visualization of various thermodynamic cycles, through a Graphical User Interface.

The graphical user interface (GUI) allows users to set initial thermodynamic parameters, making it easy to configure different thermodynamic conditions for analysis. Users can specify the mass of the working gas, set the initial pressure and temperature, determine the compression ratio, and adjust the specific heat ratios of the gas, either as a constant or using polynomial dependencies. This flexibility makes it suitable for studying a wide range of thermodynamic conditions, increasing its value as an educational and analytical tool.

After the users have set the desired parameters, the software calculates key thermodynamic parameters, including cycle work output, thermal cycle efficiency, Carnot efficiency, heat transfer in each process, and many other parameters.

By selecting the desired cycle, the results are immediately displayed in table form. In addition, the program creates graphical representations in pressure-volume ($P - v$) and temperature-entropy ($T - s$) diagrams for each cycle. These diagrams provide clear visual insights into thermodynamic processes, helping users understand how parameters affect cycle performance.

3 METHODOLOGY

The NASA seven-term polynomial is a widely used mathematical model for representing the thermodynamic properties of gases that depend on temperature [10]. This model is widely used in computational simulations, such as those involving combustion and thermodynamic cycle analysis [11]. A commonly used polynomial expression [7], for the specific heat at constant pressure is shown below:

$$\frac{c_p}{R} = \alpha + \beta \cdot T + \gamma \cdot T^2 + \delta \cdot T^3 + \varepsilon \cdot T^4 \quad (1)$$

The coefficients α, β, γ, δ and ε are function of temperature, usually divided into two ranges, the temperature range 300 K ÷ 1000 K and the temperature range 1000 K ÷ 6000 K [11]. However, for general reference, one set of coefficients for this polynomial expression might be for the specific heat of air within the temperature range of $300 \div 1000\ K$ [7]:

$$\begin{aligned} &a = 3.653;\ \beta = -1.337 \cdot 10^{-3} \\ &\gamma = 3.294 \cdot 10^{-6};\ \delta = -1.913 \cdot 10^{-9}; \\ &\varepsilon = 0.2763 \cdot 10^{-12} \end{aligned} \quad (2)$$

And for the temperature range of $1000 \div 6000$ K, the coefficients are [11]:

$$\begin{aligned} &a = 3{:}\,08793;\ \beta = 12{:}\,4597 \cdot 10^{-4}; \\ &\gamma = -0{:}\,42372 \cdot 10^{-6};\ \delta = 67{:}\,4775 \cdot 10^{-12} \\ &\varepsilon = -3{:}\,97077 \cdot 10^{-15} \end{aligned} \quad (3)$$

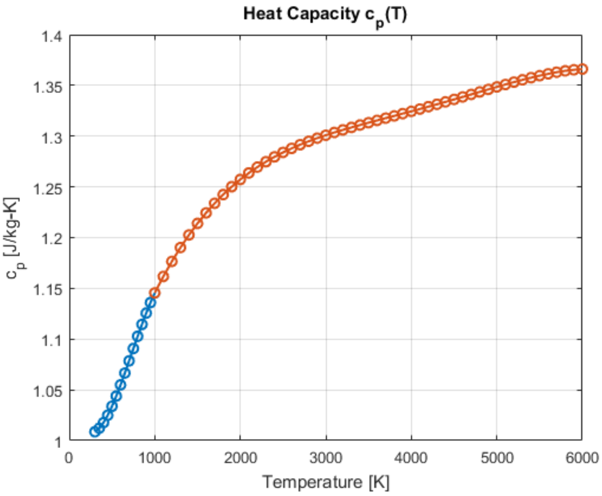

Figure 1 Specific heat temperature dependence.

For a thermodynamic process i-j, we perform a derivative and obtain the heat capacity from T_i to T_j, and multiplying by R (where R is the ideal gas constant) gives the enthalpy change, as following expression [7]:

$$h_2 - h_1 = R \int_{T_i}^{T_j} (\alpha + \beta \cdot T + \gamma \cdot T^2 + \delta \cdot T^3 + \varepsilon \cdot T^4) \cdot dT \quad (4)$$

$$\begin{aligned} h_2 - h_1 \\ = R \cdot \begin{bmatrix} \alpha \cdot (T_j - T_i) + \dfrac{\beta}{2} \cdot ({T_j}^2 - {T_i}^2) + \dfrac{\gamma}{3} \cdot ({T_j}^3 - {T_i}^3) \\ + \dfrac{\delta}{4} \cdot ({T_j}^4 - {T_i}^4) + \dfrac{\varepsilon}{5} \cdot ({T_j}^5 - {T_i}^5) \end{bmatrix} \end{aligned} \quad (5)$$

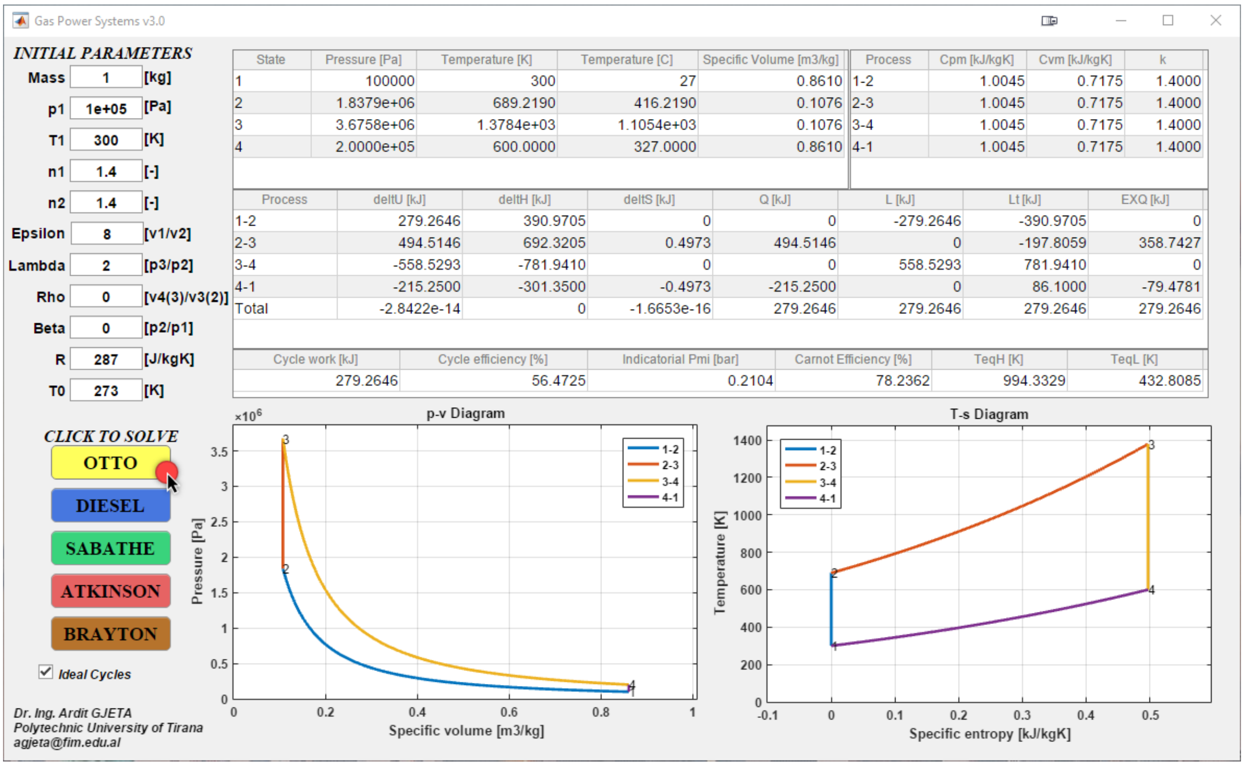

INITIAL PARAMETERS

Mass 1 [kg]
p1 1e+05 [Pa]
T1 300 [K]
n1 1.4 [-]
n2 1.4 [-]
Epsilon 8 [v1/v2]
Lambda 2 [p3/p2]
Rho 0 [v4(3)/v3(2)]
Beta 0 [p2/p1]
R 287 [J/kgK]
T0 273 [K]

State	Pressure [Pa]	Temperature [K]	Temperature [C]	Specific Volume [m3/kg]
1	100000	300	27	0.8610
2	1.8379e+06	689.2190	416.2190	0.1076
3	3.6758e+06	1.3784e+03	1.1054e+03	0.1076
4	2.0000e+05	600.0000	327.0000	0.8610

Process	Cpm [kJ/kgK]	Cvm [kJ/kgK]	k
1-2	1.0045	0.7175	1.4000
2-3	1.0045	0.7175	1.4000
3-4	1.0045	0.7175	1.4000
4-1	1.0045	0.7175	1.4000

Process	deltU [kJ]	deltH [kJ]	deltS [kJ]	Q [kJ]	L [kJ]	Lt [kJ]	EXQ [kJ]
1-2	279.2646	390.9705	0	0	-279.2646	-390.9705	0
2-3	494.5146	692.3205	0.4973	494.5146	0	-197.8059	358.7427
3-4	-558.5293	-781.9410	0	0	558.5293	781.9410	0
4-1	-215.2500	-301.3500	-0.4973	-215.2500	0	86.1000	-79.4781
Total	-2.8422e-14	0	-1.6653e-16	279.2646	279.2646	279.2646	279.2646

Cycle work [kJ]	Cycle efficiency [%]	Indicatorial Pmi [bar]	Carnot Efficiency [%]	TeqH [K]	TeqL [K]
279.2646	56.4725	0.2104	78.2362	994.3329	432.8085

☑ Ideal Cycles

Dr. Ing. Ardit GJETA
Polytechnic University of Tirana
agjeta@fim.edu.al

Figure 2 Results, analysis, and visualization of the Otto cycle (constant specific heat).

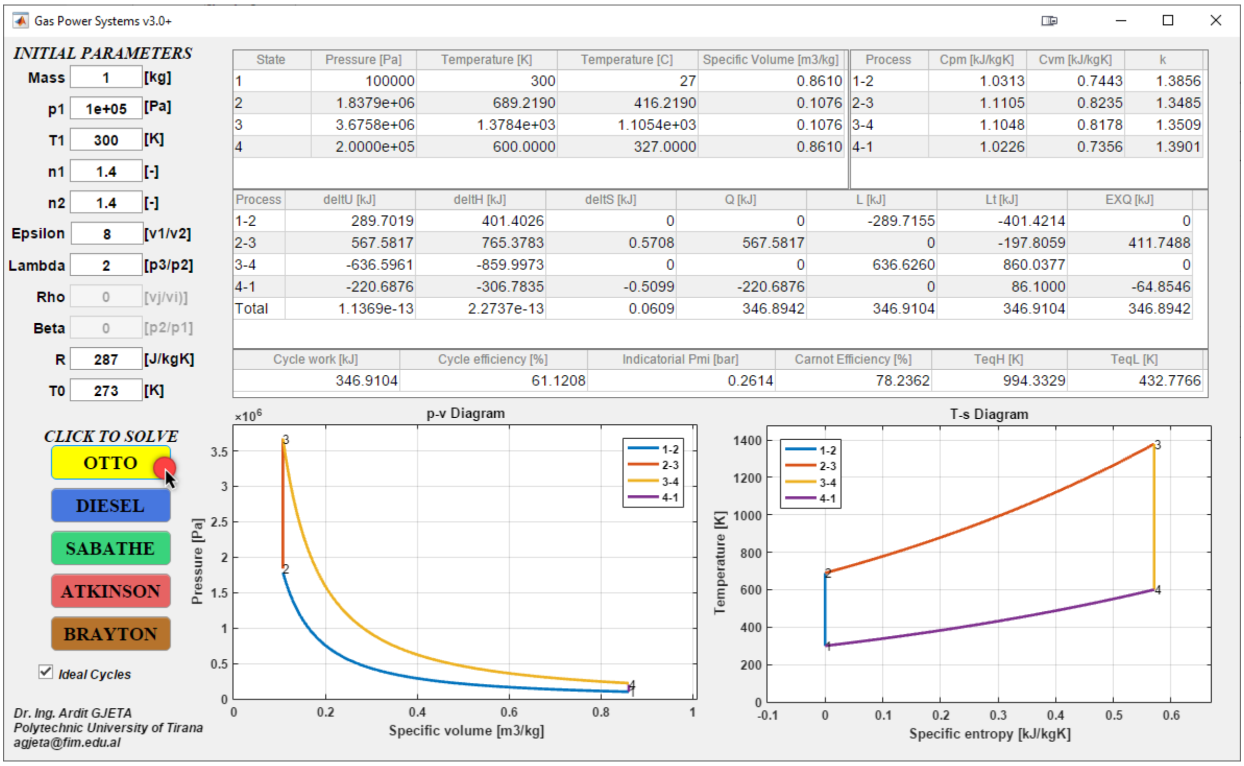

INITIAL PARAMETERS

Mass 1 [kg]
p1 1e+05 [Pa]
T1 300 [K]
n1 1.4 [-]
n2 1.4 [-]
Epsilon 8 [v1/v2]
Lambda 2 [p3/p2]
Rho 0 [vj/vi)]
Beta 0 [p2/p1]
R 287 [J/kgK]
T0 273 [K]

State	Pressure [Pa]	Temperature [K]	Temperature [C]	Specific Volume [m3/kg]
1	100000	300	27	0.8610
2	1.8379e+06	689.2190	416.2190	0.1076
3	3.6758e+06	1.3784e+03	1.1054e+03	0.1076
4	2.0000e+05	600.0000	327.0000	0.8610

Process	Cpm [kJ/kgK]	Cvm [kJ/kgK]	k
1-2	1.0313	0.7443	1.3856
2-3	1.1105	0.8235	1.3485
3-4	1.1048	0.8178	1.3509
4-1	1.0226	0.7356	1.3901

Process	deltU [kJ]	deltH [kJ]	deltS [kJ]	Q [kJ]	L [kJ]	Lt [kJ]	EXQ [kJ]
1-2	289.7019	401.4026	0	0	-289.7155	-401.4214	0
2-3	567.5817	765.3783	0.5708	567.5817	0	-197.8059	411.7488
3-4	-636.5961	-859.9973	0	0	636.6260	860.0377	0
4-1	-220.6876	-306.7835	-0.5099	-220.6876	0	86.1000	-64.8546
Total	1.1369e-13	2.2737e-13	0.0609	346.8942	346.9104	346.9104	346.8942

Cycle work [kJ]	Cycle efficiency [%]	Indicatorial Pmi [bar]	Carnot Efficiency [%]	TeqH [K]	TeqL [K]
346.9104	61.1208	0.2614	78.2362	994.3329	432.7766

☑ Ideal Cycles

Dr. Ing. Ardit GJETA
Polytechnic University of Tirana
agjeta@fim.edu.al

Figure 3 Results, analysis, and visualization of the Otto cycle (polynomial dependence of specific heat).

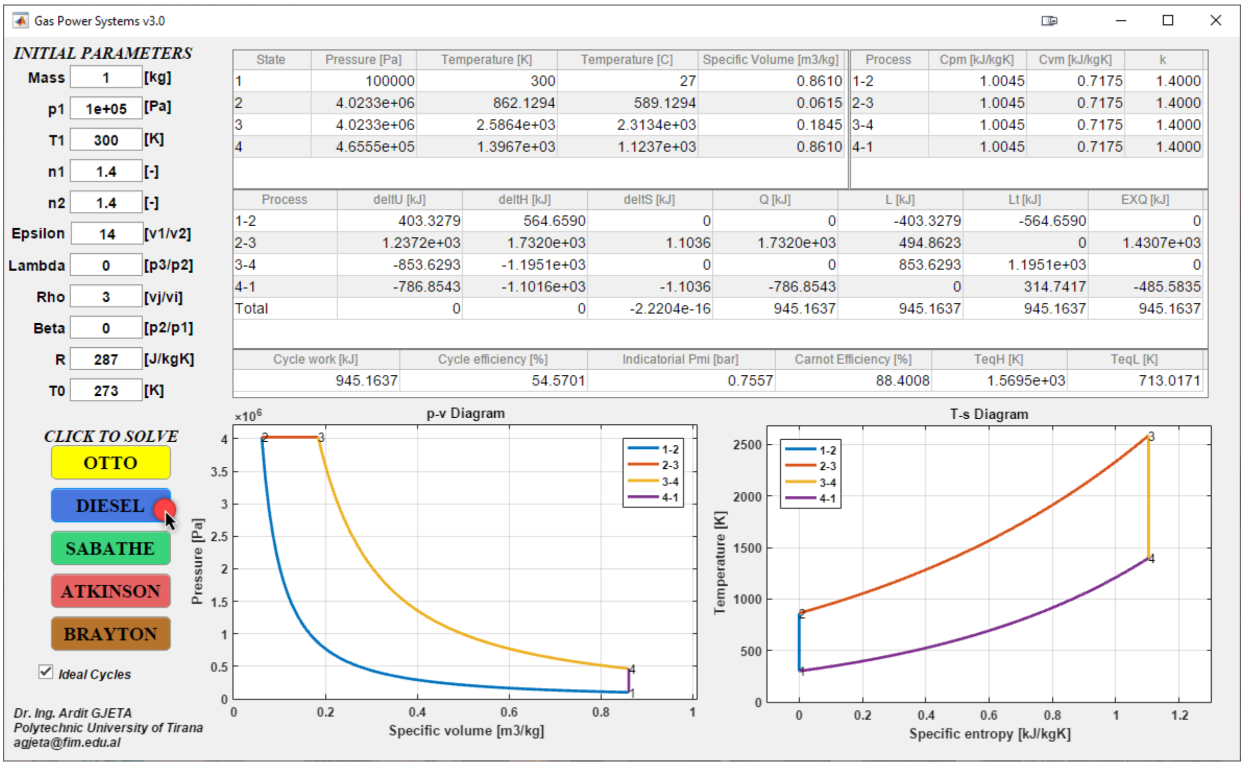

Gas Power Systems v3.0

INITIAL PARAMETERS

Mass 1 [kg]
p1 1e+05 [Pa]
T1 300 [K]
n1 1.4 [-]
n2 1.4 [-]
Epsilon 14 [v1/v2]
Lambda 0 [p3/p2]
Rho 3 [vj/vi]
Beta 0 [p2/p1]
R 287 [J/kgK]
T0 273 [K]

State	Pressure [Pa]	Temperature [K]	Temperature [C]	Specific Volume [m3/kg]
1	100000	300	27	0.8610
2	4.0233e+06	862.1294	589.1294	0.0615
3	4.0233e+06	2.5864e+03	2.3134e+03	0.1845
4	4.6555e+05	1.3967e+03	1.1237e+03	0.8610

Process	Cpm [kJ/kgK]	Cvm [kJ/kgK]	k
1-2	1.0045	0.7175	1.4000
2-3	1.0045	0.7175	1.4000
3-4	1.0045	0.7175	1.4000
4-1	1.0045	0.7175	1.4000

Process	deltU [kJ]	deltH [kJ]	deltS [kJ]	Q [kJ]	L [kJ]	Lt [kJ]	EXQ [kJ]
1-2	403.3279	564.6590	0	0	-403.3279	-564.6590	0
2-3	1.2372e+03	1.7320e+03	1.1036	1.7320e+03	494.8623	0	1.4307e+03
3-4	-853.6293	-1.1951e+03	0	0	853.6293	1.1951e+03	0
4-1	-786.8543	-1.1016e+03	-1.1036	-786.8543	0	314.7417	-485.5835
Total	0	0	-2.2204e-16	945.1637	945.1637	945.1637	945.1637

Cycle work [kJ]	Cycle efficiency [%]	Indicatorial Pmi [bar]	Carnot Efficiency [%]	TeqH [K]	TeqL [K]
945.1637	54.5701	0.7557	88.4008	1.5695e+03	713.0171

☑ Ideal Cycles

Dr. Ing. Ardit GJETA
Polytechnic University of Tirana
agjeta@fim.edu.al

Figure 4 Results, analysis, and visualization of the Diesel cycle (constant specific heat).

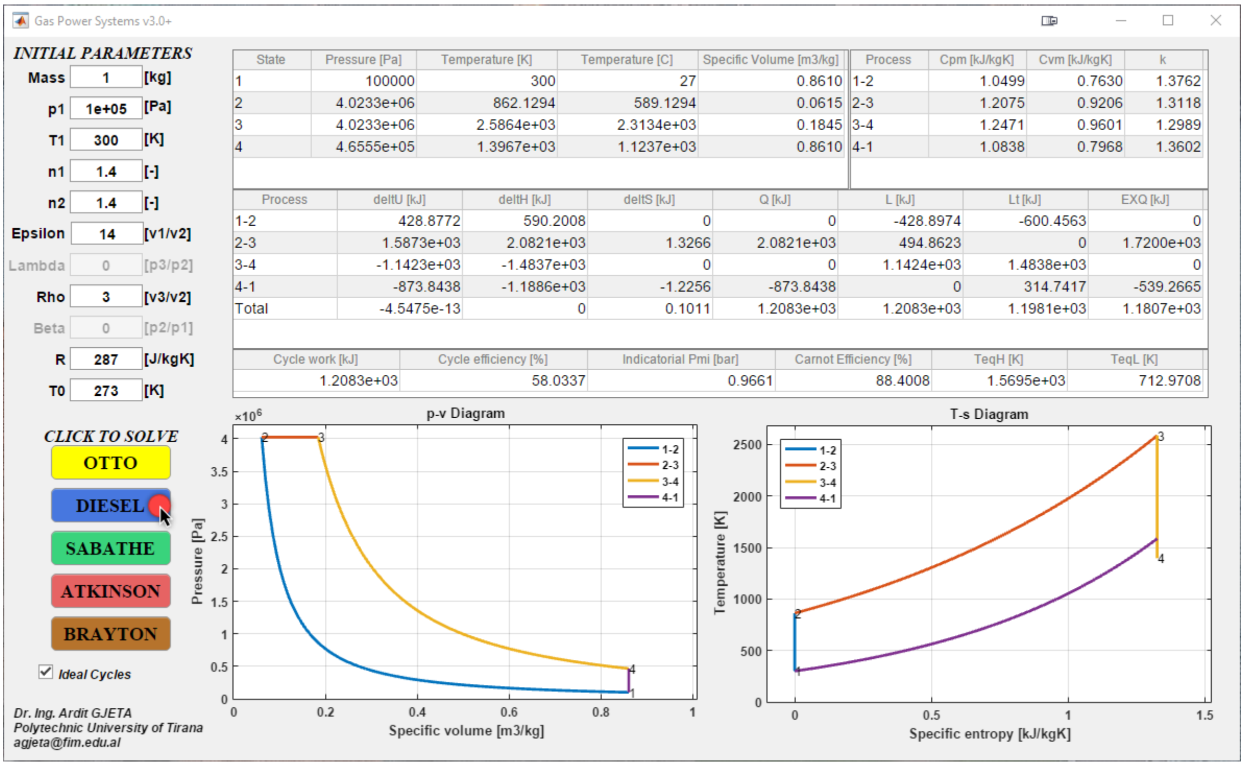

Gas Power Systems v3.0+

INITIAL PARAMETERS

Mass 1 [kg]
p1 1e+05 [Pa]
T1 300 [K]
n1 1.4 [-]
n2 1.4 [-]
Epsilon 14 [v1/v2]
Lambda 0 [p3/p2]
Rho 3 [v3/v2]
Beta 0 [p2/p1]
R 287 [J/kgK]
T0 273 [K]

State	Pressure [Pa]	Temperature [K]	Temperature [C]	Specific Volume [m3/kg]
1	100000	300	27	0.8610
2	4.0233e+06	862.1294	589.1294	0.0615
3	4.0233e+06	2.5864e+03	2.3134e+03	0.1845
4	4.6555e+05	1.3967e+03	1.1237e+03	0.8610

Process	Cpm [kJ/kgK]	Cvm [kJ/kgK]	k
1-2	1.0499	0.7630	1.3762
2-3	1.2075	0.9206	1.3118
3-4	1.2471	0.9601	1.2989
4-1	1.0838	0.7968	1.3602

Process	deltU [kJ]	deltH [kJ]	deltS [kJ]	Q [kJ]	L [kJ]	Lt [kJ]	EXQ [kJ]
1-2	428.8772	590.2008	0	0	-428.8974	-600.4563	0
2-3	1.5873e+03	2.0821e+03	1.3266	2.0821e+03	494.8623	0	1.7200e+03
3-4	-1.1423e+03	-1.4837e+03	0	0	1.1424e+03	1.4838e+03	0
4-1	-873.8438	-1.1886e+03	-1.2256	-873.8438	0	314.7417	-539.2665
Total	-4.5475e-13	0	0.1011	1.2083e+03	1.2083e+03	1.1981e+03	1.1807e+03

Cycle work [kJ]	Cycle efficiency [%]	Indicatorial Pmi [bar]	Carnot Efficiency [%]	TeqH [K]	TeqL [K]
1.2083e+03	58.0337	0.9661	88.4008	1.5695e+03	712.9708

☑ Ideal Cycles

Dr. Ing. Ardit GJETA
Polytechnic University of Tirana
agjeta@fim.edu.al

Figure 5 Results, analysis, and visualization of the Diesel cycle (polynomial dependence of specific heat).

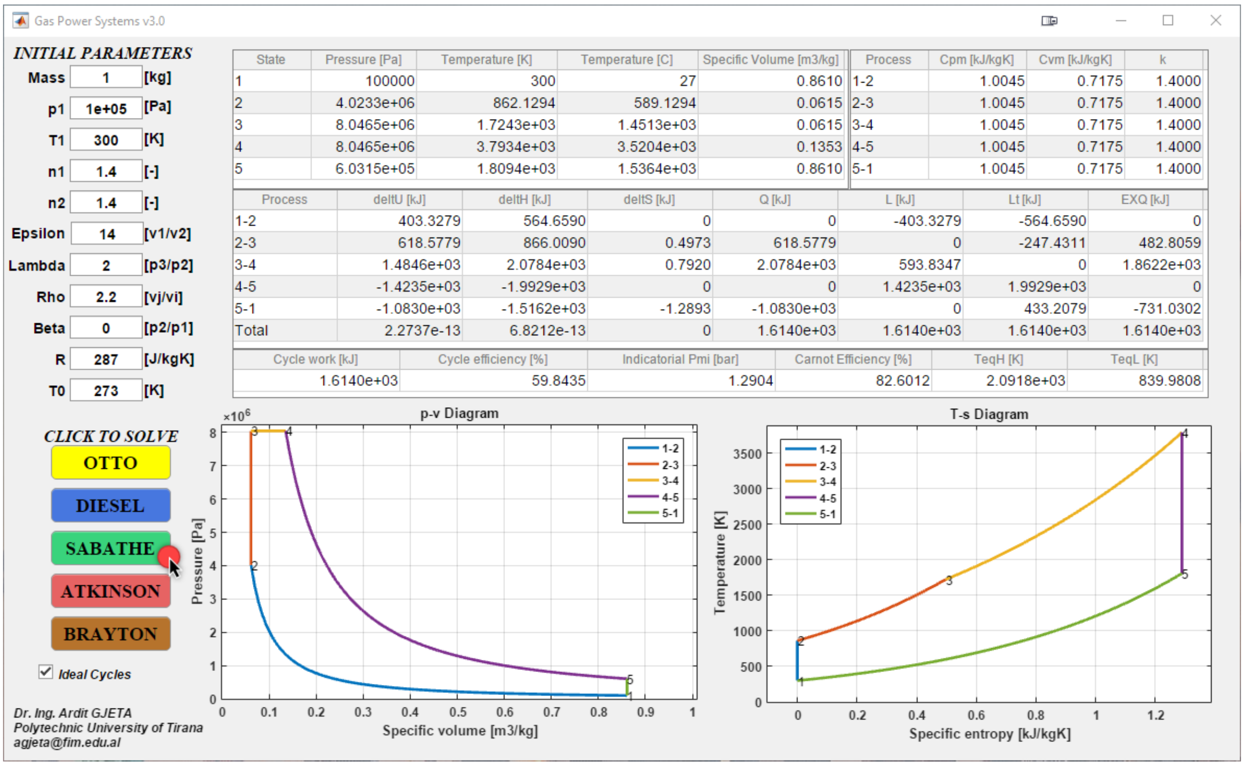

INITIAL PARAMETERS
Mass 1 [kg]
p1 1e+05 [Pa]
T1 300 [K]
n1 1.4 [-]
n2 1.4 [-]
Epsilon 14 [v1/v2]
Lambda 2 [p3/p2]
Rho 2.2 [vj/vi]
Beta 0 [p2/p1]
R 287 [J/kgK]
T0 273 [K]

State	Pressure [Pa]	Temperature [K]	Temperature [C]	Specific Volume [m3/kg]
1	100000	300	27	0.8610
2	4.0233e+06	862.1294	589.1294	0.0615
3	8.0465e+06	1.7243e+03	1.4513e+03	0.0615
4	8.0465e+06	3.7934e+03	3.5204e+03	0.1353
5	6.0315e+05	1.8094e+03	1.5364e+03	0.8610

Process	Cpm [kJ/kgK]	Cvm [kJ/kgK]	k
1-2	1.0045	0.7175	1.4000
2-3	1.0045	0.7175	1.4000
3-4	1.0045	0.7175	1.4000
4-5	1.0045	0.7175	1.4000
5-1	1.0045	0.7175	1.4000

Process	deltU [kJ]	deltH [kJ]	deltS [kJ]	Q [kJ]	L [kJ]	Lt [kJ]	EXQ [kJ]
1-2	403.3279	564.6590	0	0	-403.3279	-564.6590	0
2-3	618.5779	866.0090	0.4973	618.5779	0	-247.4311	482.8059
3-4	1.4846e+03	2.0784e+03	0.7920	2.0784e+03	593.8347	0	1.8622e+03
4-5	-1.4235e+03	-1.9929e+03	0	0	1.4235e+03	1.9929e+03	0
5-1	-1.0830e+03	-1.5162e+03	-1.2893	-1.0830e+03	0	433.2079	-731.0302
Total	2.2737e-13	6.8212e-13	0	1.6140e+03	1.6140e+03	1.6140e+03	1.6140e+03

Cycle work [kJ]	Cycle efficiency [%]	Indicatorial Pmi [bar]	Carnot Efficiency [%]	TeqH [K]	TeqL [K]
1.6140e+03	59.8435	1.2904	82.6012	2.0918e+03	839.9808

☑ *Ideal Cycles*

Dr. Ing. Ardit GJETA
Polytechnic University of Tirana
agjeta@fim.edu.al

Figure 6 Results, analysis, and visualization of the Sabathe cycle (constant specific heat).

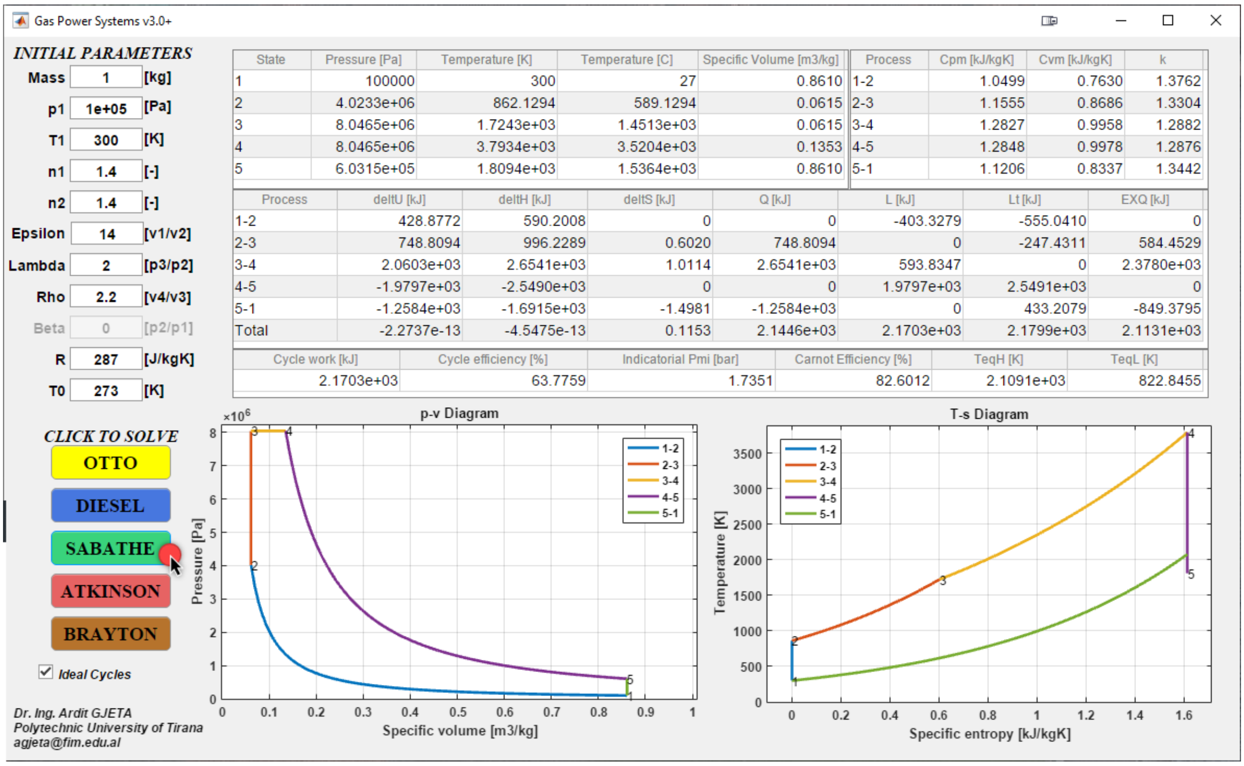

INITIAL PARAMETERS
Mass 1 [kg]
p1 1e+05 [Pa]
T1 300 [K]
n1 1.4 [-]
n2 1.4 [-]
Epsilon 14 [v1/v2]
Lambda 2 [p3/p2]
Rho 2.2 [v4/v3]
Beta 0 [p2/p1]
R 287 [J/kgK]
T0 273 [K]

State	Pressure [Pa]	Temperature [K]	Temperature [C]	Specific Volume [m3/kg]
1	100000	300	27	0.8610
2	4.0233e+06	862.1294	589.1294	0.0615
3	8.0465e+06	1.7243e+03	1.4513e+03	0.0615
4	8.0465e+06	3.7934e+03	3.5204e+03	0.1353
5	6.0315e+05	1.8094e+03	1.5364e+03	0.8610

Process	Cpm [kJ/kgK]	Cvm [kJ/kgK]	k
1-2	1.0499	0.7630	1.3762
2-3	1.1555	0.8686	1.3304
3-4	1.2827	0.9958	1.2882
4-5	1.2848	0.9978	1.2876
5-1	1.1206	0.8337	1.3442

Process	deltU [kJ]	deltH [kJ]	deltS [kJ]	Q [kJ]	L [kJ]	Lt [kJ]	EXQ [kJ]
1-2	428.8772	590.2008	0	0	-403.3279	-555.0410	0
2-3	748.8094	996.2289	0.6020	748.8094	0	-247.4311	584.4529
3-4	2.0603e+03	2.6541e+03	1.0114	2.6541e+03	593.8347	0	2.3780e+03
4-5	-1.9797e+03	-2.5490e+03	0	0	1.9797e+03	2.5491e+03	0
5-1	-1.2584e+03	-1.6915e+03	-1.4981	-1.2584e+03	0	433.2079	-849.3795
Total	-2.2737e-13	-4.5475e-13	0.1153	2.1446e+03	2.1703e+03	2.1799e+03	2.1131e+03

Cycle work [kJ]	Cycle efficiency [%]	Indicatorial Pmi [bar]	Carnot Efficiency [%]	TeqH [K]	TeqL [K]
2.1703e+03	63.7759	1.7351	82.6012	2.1091e+03	822.8455

☑ *Ideal Cycles*

Dr. Ing. Ardit GJETA
Polytechnic University of Tirana
agjeta@fim.edu.al

Figure 7 Results, analysis, and visualization of the Sabathe cycle (polynomial dependence of specific heat).

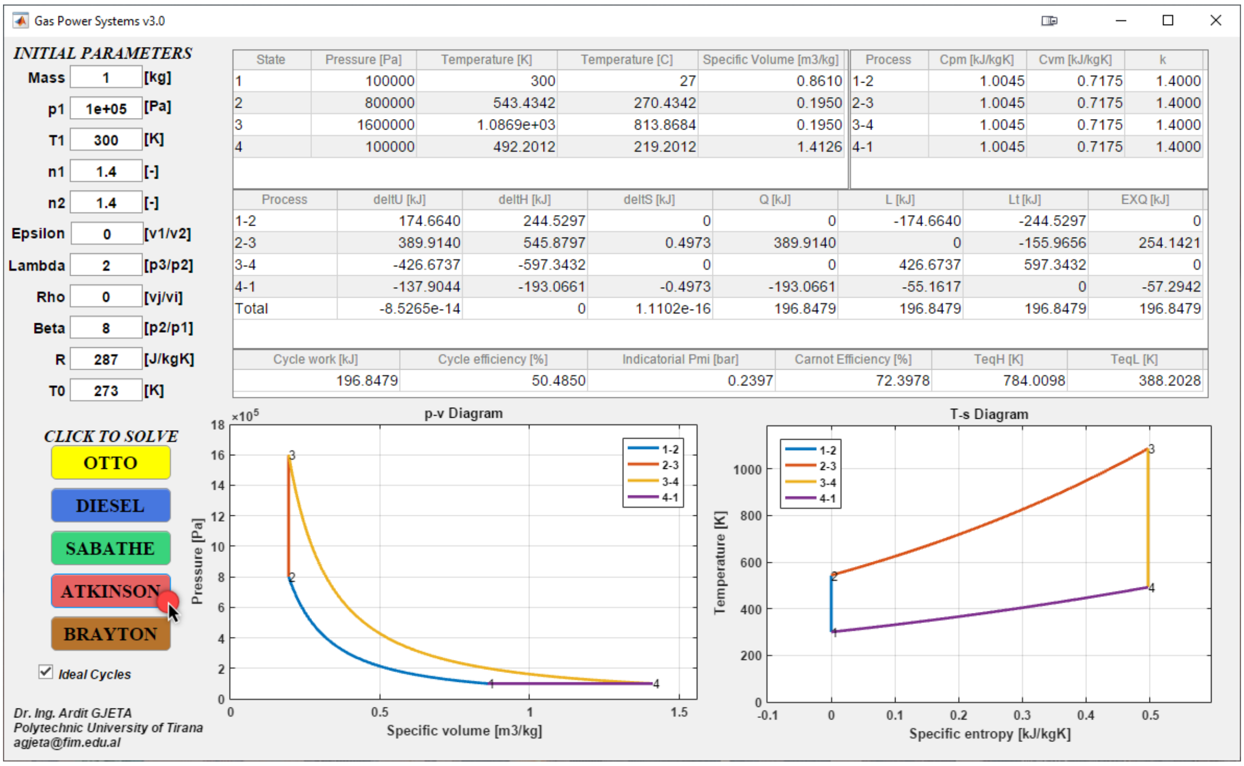

Gas Power Systems v3.0

INITIAL PARAMETERS

Mass 1 [kg]
p1 1e+05 [Pa]
T1 300 [K]
n1 1.4 [-]
n2 1.4 [-]
Epsilon 0 [v1/v2]
Lambda 2 [p3/p2]
Rho 0 [vj/vi]
Beta 8 [p2/p1]
R 287 [J/kgK]
T0 273 [K]

State	Pressure [Pa]	Temperature [K]	Temperature [C]	Specific Volume [m3/kg]
1	100000	300	27	0.8610
2	800000	543.4342	270.4342	0.1950
3	1600000	1.0869e+03	813.8684	0.1950
4	100000	492.2012	219.2012	1.4126

Process	Cpm [kJ/kgK]	Cvm [kJ/kgK]	k
1-2	1.0045	0.7175	1.4000
2-3	1.0045	0.7175	1.4000
3-4	1.0045	0.7175	1.4000
4-1	1.0045	0.7175	1.4000

Process	deltU [kJ]	deltH [kJ]	deltS [kJ]	Q [kJ]	L [kJ]	Lt [kJ]	EXQ [kJ]
1-2	174.6640	244.5297	0	0	-174.6640	-244.5297	0
2-3	389.9140	545.8797	0.4973	389.9140	0	-155.9656	254.1421
3-4	-426.6737	-597.3432	0	0	426.6737	597.3432	0
4-1	-137.9044	-193.0661	-0.4973	-193.0661	-55.1617	0	-57.2942
Total	-8.5265e-14	0	1.1102e-16	196.8479	196.8479	196.8479	196.8479

Cycle work [kJ]	Cycle efficiency [%]	Indicatorial Pmi [bar]	Carnot Efficiency [%]	TeqH [K]	TeqL [K]
196.8479	50.4850	0.2397	72.3978	784.0098	388.2028

☑ Ideal Cycles

Dr. Ing. Ardit GJETA
Polytechnic University of Tirana
agjeta@fim.edu.al

Figure 8 Results, analysis, and visualization of the Atkinson cycle (constant specific heat).

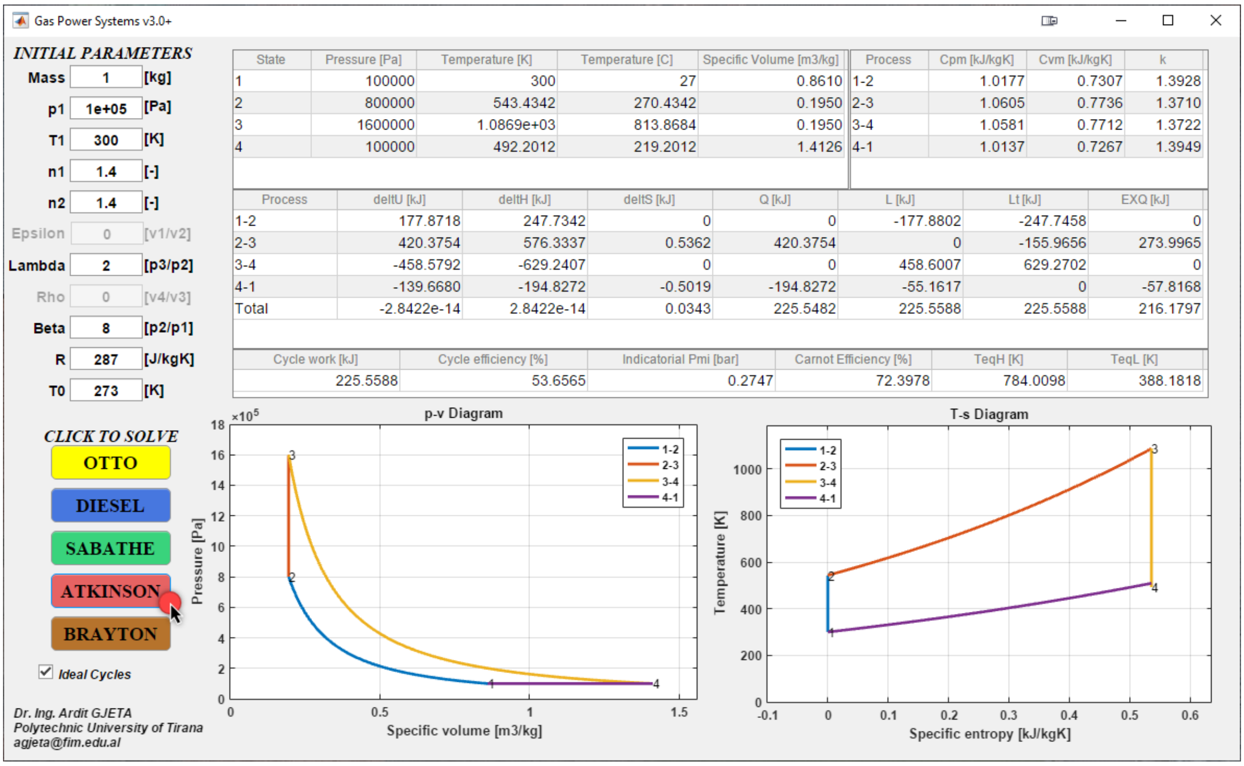

Gas Power Systems v3.0+

INITIAL PARAMETERS

Mass 1 [kg]
p1 1e+05 [Pa]
T1 300 [K]
n1 1.4 [-]
n2 1.4 [-]
Epsilon 0 [v1/v2]
Lambda 2 [p3/p2]
Rho 0 [v4/v3]
Beta 8 [p2/p1]
R 287 [J/kgK]
T0 273 [K]

State	Pressure [Pa]	Temperature [K]	Temperature [C]	Specific Volume [m3/kg]
1	100000	300	27	0.8610
2	800000	543.4342	270.4342	0.1950
3	1600000	1.0869e+03	813.8684	0.1950
4	100000	492.2012	219.2012	1.4126

Process	Cpm [kJ/kgK]	Cvm [kJ/kgK]	k
1-2	1.0177	0.7307	1.3928
2-3	1.0605	0.7736	1.3710
3-4	1.0581	0.7712	1.3722
4-1	1.0137	0.7267	1.3949

Process	deltU [kJ]	deltH [kJ]	deltS [kJ]	Q [kJ]	L [kJ]	Lt [kJ]	EXQ [kJ]
1-2	177.8718	247.7342	0	0	-177.8802	-247.7458	0
2-3	420.3754	576.3337	0.5362	420.3754	0	-155.9656	273.9965
3-4	-458.5792	-629.2407	0	0	458.6007	629.2702	0
4-1	-139.6680	-194.8272	-0.5019	-194.8272	-55.1617	0	-57.8168
Total	-2.8422e-14	2.8422e-14	0.0343	225.5482	225.5588	225.5588	216.1797

Cycle work [kJ]	Cycle efficiency [%]	Indicatorial Pmi [bar]	Carnot Efficiency [%]	TeqH [K]	TeqL [K]
225.5588	53.6565	0.2747	72.3978	784.0098	388.1818

☑ Ideal Cycles

Dr. Ing. Ardit GJETA
Polytechnic University of Tirana
agjeta@fim.edu.al

Figure 9 Results, analysis, and visualization of the Atkinson cycle (polynomial dependence of specific heat).

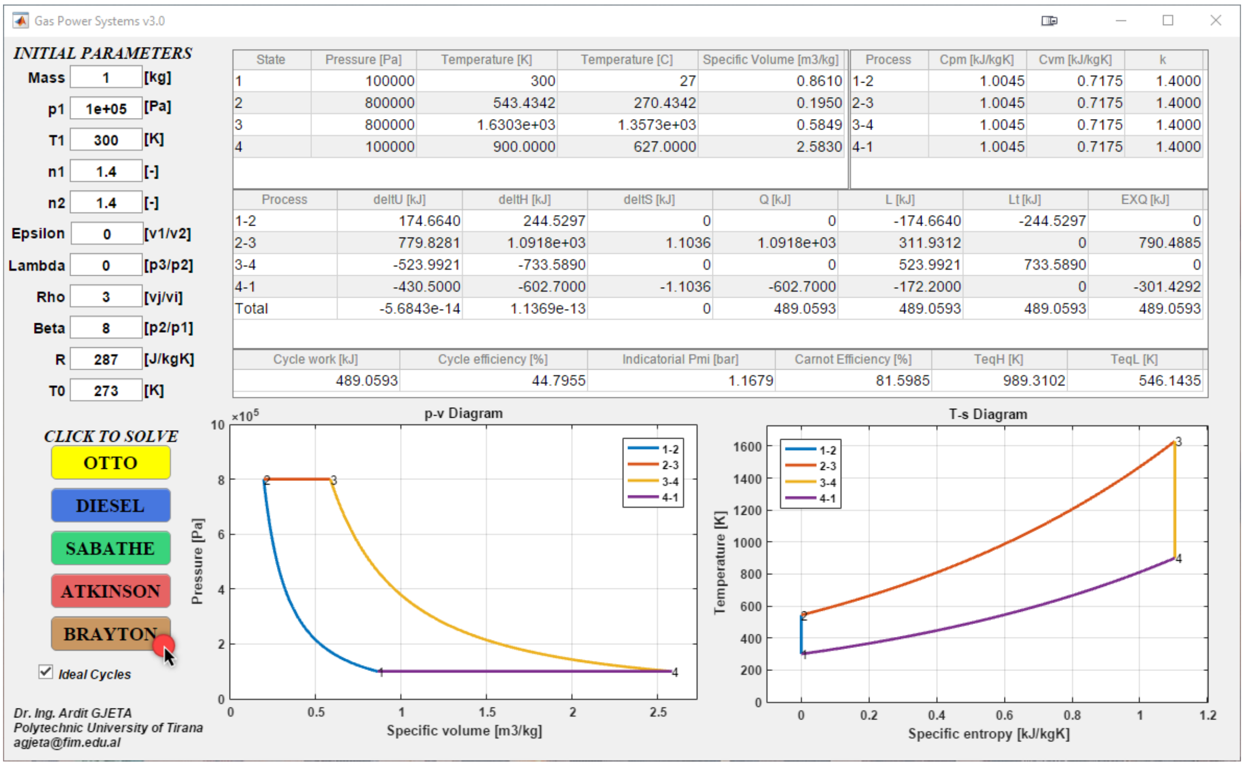
Gas Power Systems v3.0

INITIAL PARAMETERS

Mass 1 [kg]
p1 1e+05 [Pa]
T1 300 [K]
n1 1.4 [-]
n2 1.4 [-]
Epsilon 0 [v1/v2]
Lambda 0 [p3/p2]
Rho 3 [vj/vi]
Beta 8 [p2/p1]
R 287 [J/kgK]
T0 273 [K]

State	Pressure [Pa]	Temperature [K]	Temperature [C]	Specific Volume [m3/kg]
1	100000	300	27	0.8610
2	800000	543.4342	270.4342	0.1950
3	800000	1.6303e+03	1.3573e+03	0.5849
4	100000	900.0000	627.0000	2.5830

Process	Cpm [kJ/kgK]	Cvm [kJ/kgK]	k
1-2	1.0045	0.7175	1.4000
2-3	1.0045	0.7175	1.4000
3-4	1.0045	0.7175	1.4000
4-1	1.0045	0.7175	1.4000

Process	deltU [kJ]	deltH [kJ]	deltS [kJ]	Q [kJ]	L [kJ]	Lt [kJ]	EXQ [kJ]
1-2	174.6640	244.5297	0	0	-174.6640	-244.5297	0
2-3	779.8281	1.0918e+03	1.1036	1.0918e+03	311.9312	0	790.4885
3-4	-523.9921	-733.5890	0	0	523.9921	733.5890	0
4-1	-430.5000	-602.7000	-1.1036	-602.7000	-172.2000	0	-301.4292
Total	-5.6843e-14	1.1369e-13	0	489.0593	489.0593	489.0593	489.0593

Cycle work [kJ]	Cycle efficiency [%]	Indicatorial Pmi [bar]	Carnot Efficiency [%]	TeqH [K]	TeqL [K]
489.0593	44.7955	1.1679	81.5985	989.3102	546.1435

Dr. Ing. Ardit GJETA
Polytechnic University of Tirana
agjeta@fim.edu.al

Figure 10 Results, analysis, and visualization of the Brayton Gas Turbine Cycle (constant specific heat).

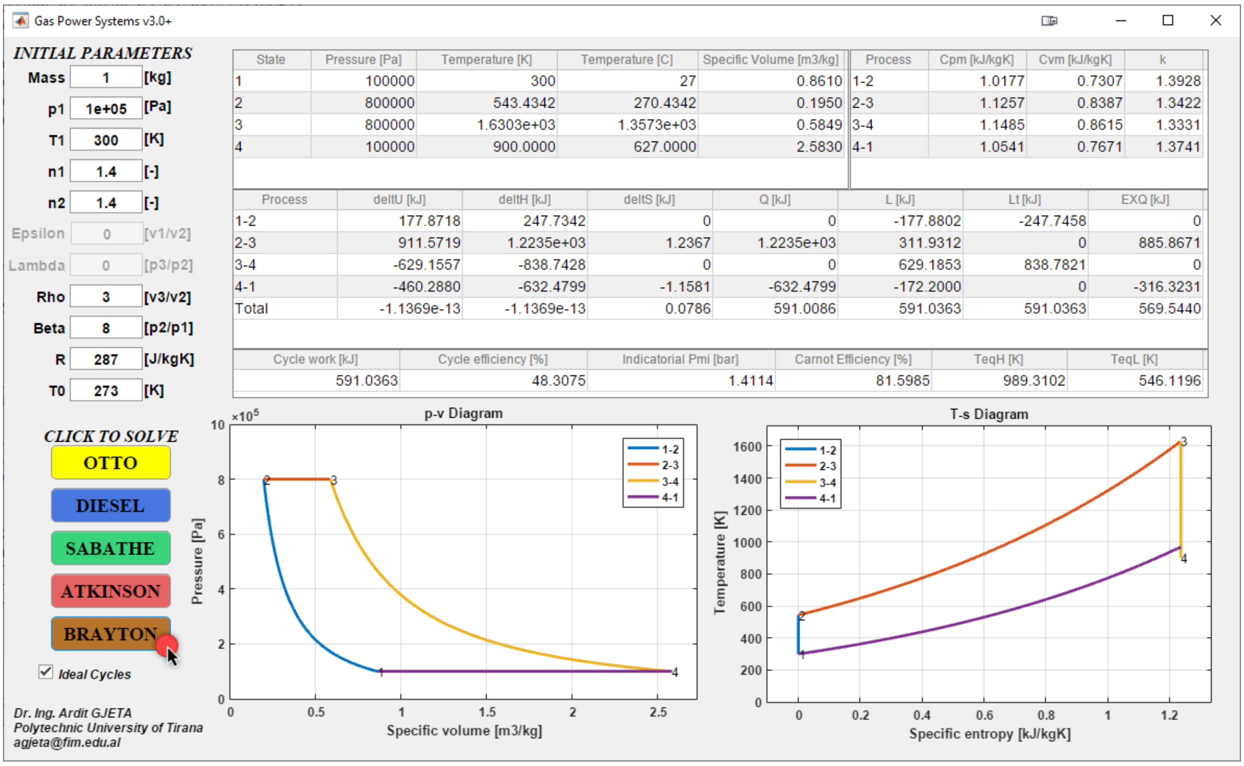
Gas Power Systems v3.0+

INITIAL PARAMETERS

Mass 1 [kg]
p1 1e+05 [Pa]
T1 300 [K]
n1 1.4 [-]
n2 1.4 [-]
Epsilon 0 [v1/v2]
Lambda 0 [p3/p2]
Rho 3 [v3/v2]
Beta 8 [p2/p1]
R 287 [J/kgK]
T0 273 [K]

State	Pressure [Pa]	Temperature [K]	Temperature [C]	Specific Volume [m3/kg]
1	100000	300	27	0.8610
2	800000	543.4342	270.4342	0.1950
3	800000	1.6303e+03	1.3573e+03	0.5849
4	100000	900.0000	627.0000	2.5830

Process	Cpm [kJ/kgK]	Cvm [kJ/kgK]	k
1-2	1.0177	0.7307	1.3928
2-3	1.1257	0.8387	1.3422
3-4	1.1485	0.8615	1.3331
4-1	1.0541	0.7671	1.3741

Process	deltU [kJ]	deltH [kJ]	deltS [kJ]	Q [kJ]	L [kJ]	Lt [kJ]	EXQ [kJ]
1-2	177.8718	247.7342	0	0	-177.8802	-247.7458	0
2-3	911.5719	1.2235e+03	1.2367	1.2235e+03	311.9312	0	885.8671
3-4	-629.1557	-838.7428	0	0	629.1853	838.7821	0
4-1	-460.2880	-632.4799	-1.1581	-632.4799	-172.2000	0	-316.3231
Total	-1.1369e-13	-1.1369e-13	0.0786	591.0086	591.0363	591.0363	569.5440

Cycle work [kJ]	Cycle efficiency [%]	Indicatorial Pmi [bar]	Carnot Efficiency [%]	TeqH [K]	TeqL [K]
591.0363	48.3075	1.4114	81.5985	989.3102	546.1196

Dr. Ing. Ardit GJETA
Polytechnic University of Tirana
agjeta@fim.edu.al

Figure 11 Results, analysis, and visualization of the Brayton Gas Turbine Cycle.

4 RESULTS

The Matlab GUI calculates and visualizes the thermodynamic states, process properties, and performance parameters of the selected cycle, and plots the corresponding ideal cycle diagrams ($P-v$ and $T-s$) based on the user-defined initial conditions.

In the table below, the variations of the specific heats are presented for the Otto cycle. The values were obtained for representative operating conditions with randomly selected initial parameters. The purpose of this comparison is to illustrate the influence of the temperature dependence of specific heats on the thermodynamic behavior of the cycle.

It is evident that both Cp and Cv do not remain constant but instead vary with temperature throughout the individual processes of the cycle. Consequently, the adiabatic index $k = Cp/Cv$ also changes slightly from one process to another.

Across the Otto cycle, the inclusion of temperature-dependent specific heats shows that both Cp and Cv increase compared to the constant-k assumption, with the largest relative changes occurring in the high-temperature processes (2–3 and 3–4), while at lower temperatures (1–2 and 4–1) the deviations remain small.

Table I - Specific heat for each cycle

Process	Cpm $[kJ/kg \cdot K]$	Cvm $[kJ/kg \cdot K]$	k
1–2	1.0313	0.7443	1.3856
2–3	1.1105	0.8235	1.3485
3–4	1.1048	0.8178	1.3509
4–1	1.0226	0.7356	1.3901

Table II - Specific heat variations (constant/polynomial)

Process	Cpm $[kJ/kg \cdot K]$	Cvm $[kJ/kg \cdot K]$	k
1–2	2.6%	3.6%	-1.0%
2–3	9.5%	12.9%	-3.8%
3–4	9.1%	12.3%	-3.6%
4–1	1.8%	2.5%	-0.7%

Such changes affect the predicted work output, heat transfer, and efficiency of the cycle. Incorporating variable specific heats therefore provides a more accurate description of engine performance compared to the classical idealized model.

5 CONCLUSIONS

The gas power system graphical interface presented in this study is a Matlab application that allows users to evaluate various gas power cycles, such as the Otto, Diesel, Sabathe, Atkinson, and Brayton cycles.

This graphical interface will assist users in the analysis and graphical visualization of various thermodynamic cycles through direct input of parameters and automatic calculation of thermodynamic cycle results.

The main goal of this MATLAB-based Gas Power Systems Graphical User Interface is to provide users, including students, engineers, and researchers with an intuitive and powerful tool for analyzing gas power cycles, as well as being a suitable tool for educational purposes, engine analysis, and thermodynamic studies

REFERENCES

[1] Çengel, Y. A., & Boles, M. A., *Thermodynamics: An Engineering Approach (8th ed.).* McGraw-Hill Education, 2015.

[2] Priya T. Goeser and Anderson Duong., *MATLAB Graphical User Interfaces (GUIs) for Problem Solving in Thermodynamics,* ASEE Southeastern Section Conference, 2019.

[3] Gjeta, A., Alcani, M., Dorri, A., *The Influence of Thermodynamic Parameters on Internal Combustion Engines and the Graphical Presentation of Cycles Diagrams Using Matlab.* Lecture Notes on Multidisciplinary Industrial Engineering. Springer, Cham. 2024.

[4] MATLAB, *Matlab app building documentation*, The Math- Works, Inc., Natick, MA, 2022.

[5] B. Akash., *Effect of heat transfer on the performance of an air-standard diesel cycle*, International Communications in Heat and Mass Transfer 28 (1) 87–95, 2001.

[6] Siddhartha Bhowmick, Bishal Singh, Md Mushahid Ansari, Manish Sharma., *Simulation of Dual Combustion Cycle in Internal Combustion Engines using MATLAB,* pp. 9308-9311.

[7] Michael J. Moran, Howard N. Shapiro., *Fundamentals of engineering thermodynamics 5th edition,* pp.119, 770, 2006.

[8] J. C. Domínguez, D. Lorenzo, J. García, C. Hopson, V. Rigual, M. V. Alonso, and M. Oliet., *MATLAB applications for teaching Applied Thermodynamics: Thermodynamic cycles*, Comput. Appl. Eng. Educ.; 31:900–915, 2023.

[9] Sorin Vlase, Marin Marin, Ahmed Elkhalfi, Praveen Ailawalia., *Mathematical model for dynamic analysis of internal combustion engines,* Journal of Computational Applied Mechanics, 2022.

[10] Rong Wang, Ugne Balciunaite, Juncai Chen, Cheng Yuan, Alec Owens, Jonathan Tennyson., *NASA Polynomial representation of molecular specific heats*, Journal of Quantitative Spectroscopy and Radiative Transfer, 2023.

[11] E. Abu-Nada, I. Al-Hinti, A. Al-Sarkhi, B. Akash., *Thermodynamic modeling of spark-ignition engine: Effect of temperature dependent specific heats,* International Communications in Heat and Mass Transfer 33 1264–1272, 2006.

ISSN 1590-8844
International Journal of Mechanics and Control, Vol. 26, No. 02, 2025
https://doi.org/10.69076/jomac.2025.0020

DYNAMIC MODEL OF A 3T1R PARALLEL KINEMATICS MACHINE

Maurizio Ruggiu* Pierluigi Rea* Erika Ottaviano**

* Dept. of Mechanical, Chemical and Materials Engineering, University of Cagliari, Piazza d'Armi – 09123 Cagliari, Italy

** Dept. of Civil and Mechanical Engineering, University of Cassino and Southern Latium, Via G. Di Biasio – 03043 Cassino, Italy

ABSTRACT

This paper presents the dynamic model of a parallel kinematic manipulator (PKM) able to generate the Schönflies motion of its moving platform. The motion consists of a spatial translation (3T) with a rotation about a fixed axis (1R). The PKM consists of a fixed base connected to a moving platform by four kinematic chains with four prismatic actuators at the base. The model was developed in the framework of the Lagrange formulation according to a multibody approach with an augmented formulation without the need of solving the kinematics in terms of the independent coordinates. The model has been used to solve both the inverse and forward problems. In the former the trajectory of the moving platform is treated as a servo-constraint reducing the PKM as a kinematically driven mechanism, in the latter the constraint equations at acceleration level are adjoined to the equations of motion leading to a differential-algebraic equations. Finally, the dynamic model was validated via a solid model simulation.

Keywords: Computational dynamics; Schönflies motion; parallel kinematic machine; Lagrange formulation.

1 INTRODUCTION

The focus of this work is on a special class of parallel manipulators able to produce the Schönflies motion of the moving platform. This motion is a subgroup of the Euclidean group $SE(3)$ which allows for three independent translations and a rotation about a fixed axis. Because of the nature of the motion the manipulator is indicated as 3T1R, too. Various designs have been proposed either with serial or parallel architectures. The former can boast a large workspace and a long reach, the latter high load-carrying capacity, speed, stiffness and lightweight architecture making them ideal for pick-and-place operations. The first Schönflies motion generator (SMG), with serial architecture, was the Selective-Compliance-Assembly-Robot-Arm (SCARA) [1]. On the other hand, most of the parallel manipulators proposed came from the idea reported in [2] then developed by the same research group in [3–5]. These ideas led to commercialized robots as Adept Quattro and the Veloce. There are, indeed, numerous works in literature on 3T1R robots inspired by the cited works [6–10]. Another very common SMG design comes from the Delta-based architectures [11]. For example, IRB 340 Flexpicker, manufactured by ABB Robotics, is a Delta-based robot provided by a telescopic Cardan shaft to actuate the rotational motion. Besides, there are some researchers who have proposed a two-limbs SMG design in order to reduce the complexity and the cost of the robot [12, 13]. Great attention was paid to design the SMG for enhancing the rotational capability of the end-effector. In Quattro and its developments, for example, there was the relative movement between two sub-platforms amplified by various transmission systems as rack-pignon, gears [14] ans screw mechanisms [3, 15]. Despite of the considerable work on the kinematics and design of the SMG, there is definitely less work dedicated to their dynamics. In general, Newton-Euler method [16–18], method based on the principle of virtual work [19] and the Lagrangian formulation [20–22] are invariably used to establish the relationship between actuated torques/forces and the motion of the robot. The Newton-Euler method needs the equations of motion for each body of the robot leading to a large number of equations

---

Contact author: Maurizio Ruggiu[1]
[1]Dept. of Mech., Chemical and Mat. Eng., UNICA, Piazza d'Armi – 09123 Cagliari, Italy.
E-mail: maurizio.ruggiu@unica.it

with poor computational efficiency. Method based on the principle of virtual work represents a more efficient technique for obtaining the equations of motion although it still requires the analysis of the forces/torques on each body of the robot. As it is well known, the Lagrangian formulation avoids to deal with bodies equilibrium as it introduces the calculation of the kinetic and potential energy of the manipulator. However, it is very demanding or even practically impossible to derive explicit equations of motion in terms of a set of independent coordinates because of the constrains imposed by the closed loops. Therefore, it can be convenient to write the equations of motion in terms of redundant coordinates adjoined to the constraint equations forming a system of differential-algebraic equations. In this paper, we build a dynamic model of a 4-PUU* manipulator belonging to a special class of Schönflies motion generators. Because of its geometry, a Lagrangian approach was used without introducing relevant simplifications and by means of redundant coordinates involving either the actuators or the moving platform kinematics. The paper extends the work presented in [23] where only the direct dynamics was solved. The motivation of this work is to present a general procedure to solve both the forward and inverse dynamic problems for this class of Schönflies motion generators.

The paper is organized as follows. Section 2 outlines the formulation used to solve the dynamic problems of the PK machines. Section 3 lists the steps for modeling the dynamic model of a PKM. Sections 2, 3 are general and therefore valid for any type of PKM. Section 4 introduces the geometry of the manipulator under study while section 5 shows the simulation results. Section 6 draws the conclusions of the work.

2 FORMULATION OF THE DYNAMIC PROBLEMS FOR PKM

Equations of motion of a PKM can be written in terms of n redundant coordinates $\mathbf{q}(t)$ subjected to m holonomic kinematic constraints $\mathbf{C}(\mathbf{q}(t)) = \mathbf{0}$ derived from its geometry:

$$\mathbf{M}(\mathbf{q})\ddot{\mathbf{q}} + \mathbf{V}(\mathbf{q}, \dot{\mathbf{q}}) + \mathbf{G}(\mathbf{q}) + \mathbf{C}_q^T \boldsymbol{\lambda} = \mathbf{f}. \tag{1}$$

In Eq. (1), $\mathbf{M} \in \mathbb{R}^{n \times n}$, is the generalized inertia matrix, $\mathbf{V} \in \mathbb{R}^n$, is the Coriolis/centrifugal forces vector, $\mathbf{G} \in \mathbb{R}^n$, is the vector of gravitational forces and $\mathbf{f} \in \mathbb{R}^n$, is the vector of forces applied to the system including the motors torques/forces. Term $-\mathbf{C}_q^T \boldsymbol{\lambda}$ represents the constraints forces with $\mathbf{C}_q \in \mathbb{R}^{n \times m}$ being the Jacobian matrix of the constraints with respect to the coordinates, $\mathbf{C}_q = \partial \mathbf{C}/\partial \mathbf{q}$, and $\boldsymbol{\lambda} \in \mathbb{R}^m$, is the vector of the Lagrangian multipliers. We define the inverse and forward dynamical problems as follows.

2.1 INVERSE DYNAMICS

Given the motion, at least 2-times continuously differentiable, of the moving platform, $\boldsymbol{\gamma}(t)$, expressed by the coordinates $\mathbf{p} \in \mathbf{q}$ with $\boldsymbol{\gamma}(t) = \mathbf{p}$ and the external forces applied to the moving platform, $\mathbf{f}_e \in \mathbf{f}$, let calculate the forces/torques exerted by the motors $\boldsymbol{\tau} \in \mathbf{f}$. The imposed motion is treated as a servo-constraint such that the PKM becomes a kinematically driven mechanism whose inverse dynamic problem can be solved straightforwardly.

- Position problem

  The vector of the constraint equations is augmented by the servo-constraint and takes dimension n:

  $$\mathbf{C}(\mathbf{q}(t), t) = [C_1(\mathbf{q}), \cdots, C_m(\mathbf{q}), \mathbf{p} - \boldsymbol{\gamma}(t)]^T, \tag{2}$$

  as well as the Jacobian matrix takes $n \times n$ dimension:

  $$\mathbf{C}_q = \begin{bmatrix} \frac{\partial C_1}{\partial q_1} & \cdots & \frac{\partial C_1}{\partial \mathbf{p}} \\ \vdots & \ddots & \vdots \\ \frac{\partial C_m}{\partial q_1} & \cdots & \frac{\partial C_m}{\partial \mathbf{p}} \\ \mathbf{0}_{(n-m) \times m} & & \mathbf{1}_{(n-m) \times (n-m)} \end{bmatrix}. \tag{3}$$

  Further, $\mathbf{C}_q$ is a nonsingular matrix as the constraint equations are linearly independent since the PKM is assumed not to be overconstrained. At each instant the constraint equations can be solved numerically. For example, the iterative Newton algorithm leads to the updated position vector:

  $$\mathbf{q}_{k+1} = \mathbf{q}_k - \mathbf{C}_{q_k}^{-1} \mathbf{C}(\mathbf{q}_k), \tag{4}$$

  with stopping condition: $\|\mathbf{C}_{q_k}^{-1} \mathbf{C}(\mathbf{q}_k)\| \leq \epsilon$.
  k is the iteration number and ϵ is the iteration threshold.

- Velocity problem

  A time derivative of the constraint vector allows to solve the problem at the velocity level:

  $$\dot{\mathbf{q}} = -\mathbf{C}_q^{-1} \mathbf{C}_t \tag{5}$$

  with

  $$\mathbf{C}_t = [\mathbf{0}_{1 \times m}, \dot{\boldsymbol{\gamma}}]^T. \tag{6}$$

- Acceleration problem

  A time derivative of the velocity equation $\mathbf{C}_q \dot{\mathbf{q}} + \mathbf{C}_t = \mathbf{0}$, provides the acceleration equation:

  $$(\mathbf{C}_q \dot{\mathbf{q}})_q \dot{\mathbf{q}} + \mathbf{C}_q \ddot{\mathbf{q}} + \mathbf{C}_{tt} = \mathbf{0}, \tag{7}$$

  with

  $$\mathbf{C}_{tt} = [\mathbf{0}_{1 \times m}, \ddot{\boldsymbol{\gamma}}]^T, \tag{8}$$

  such that

  $$\ddot{\mathbf{q}} = -\mathbf{C}_q^{-1} (\mathbf{C}_{tt} + (\mathbf{C}_q \dot{\mathbf{q}})_q \dot{\mathbf{q}}). \tag{9}$$

---

[*] P stands for prismatic joint, U for universal joint.

Eqs. (4), (5) and (9) solve the PKM kinematics computing all the coordinates from the motion of the moving platform. This calculation can be regarded as a pre-computation of the inverse dynamics that can be solved managing eq. (1). In the inverse dynamics context, eq. (1) has n unknowns: m Lagrangian multipliers $\boldsymbol{\lambda}$ and $(n-m)$ actuators forces/torques $\boldsymbol{\tau}$. The unknowns are partially uncoupled, in fact it is convenient to select firstly the m equations that contain only the Lagrangian multipliers such that

$$\boldsymbol{\lambda} = \mathbf{C}_q^{\star -T}(\mathbf{f}_e - \mathbf{M}^\star \ddot{\mathbf{q}} - \mathbf{V}^\star - \mathbf{G}^\star). \tag{10}$$

Eqs. (10) is a set of linear equations whose solution is straightforward. Matrices $\mathbf{M}^\star$ and $\mathbf{C}_q^{\star T}$ are square with dimension $m \times m$, vectors $\mathbf{V}^\star$ and $\mathbf{G}^\star$ have m terms. Vector $\mathbf{f}_e$ contains m external forces, if any, that are known in the context of inverse dynamics. Once the Lagrangian multipliers are calculated the rest of equations, *i.e.* $(n-m)$, can be used to compute the actuators forces/torques such that

$$\boldsymbol{\tau} = \mathbf{M}^\dagger \ddot{\mathbf{q}} + \mathbf{V}^\dagger + \mathbf{G}^\dagger + \mathbf{C}_q^{\dagger T}\boldsymbol{\lambda}. \tag{11}$$

In eqs. (11), $\mathbf{M}^\dagger$ is $(n-m) \times n$, $\mathbf{C}_q^{\dagger T}$ is $(n-m) \times m$, vectors $\mathbf{V}^\dagger$ and $\mathbf{G}^\dagger$ have $(n-m)$ terms.

2.2 FORWARD DYNAMICS

Given the forces applied to the moving platform $\mathbf{f}_e \in \mathbf{f}$ and the forces/torques exerted by the motors $\boldsymbol{\tau} \in \mathbf{f}$, let calculate the motion of the moving platform $\mathbf{p} \in \mathbf{q}$. In the context of the forward dynamics the n equations of motion eq. (1) has $n+m$ unknowns, that is, $\boldsymbol{\lambda}$ and $\ddot{\mathbf{q}}$. To solve, we follow the augmented formulation in which the constraint equations at acceleration level are adjoined to eqs. (1) forming a set of differential-algebraic equations (DAE).

$$\begin{bmatrix} \mathbf{M} & \mathbf{C}_q^T \\ \mathbf{C}_q & \mathbf{0} \end{bmatrix} \begin{bmatrix} \ddot{\mathbf{q}} \\ \boldsymbol{\lambda} \end{bmatrix} = \begin{bmatrix} \mathbf{f} - \mathbf{V} - \mathbf{G} \\ -(\mathbf{C}_q \dot{\mathbf{q}})_q \dot{\mathbf{q}} \end{bmatrix}. \tag{12}$$

Eq. (12) can be solved directly as the leading matrix is non singular. Alternatively, $\boldsymbol{\lambda}$ can be eliminated by exploiting the orthogonality between the constraint forces and any admissible $\dot{\mathbf{q}}$ which belongs to the null space of $\mathbf{C}_q$ since that $\mathbf{C}_q\dot{\mathbf{q}} = \mathbf{0}$. Thus, the first matrix block of Eq. (12) is projected onto the transpose of the null space of $\mathbf{C}_q$ (orthogonal complement of $\mathbf{C}_q$), namely $\mathbf{B}^T$, obtaining the following system:

$$\begin{bmatrix} \mathbf{B}^T\mathbf{M} \\ \mathbf{C}_q \end{bmatrix} \ddot{\mathbf{q}} = \begin{bmatrix} \mathbf{B}^T(\mathbf{f} - \mathbf{V} - \mathbf{G}) \\ -(\mathbf{C}_q \dot{\mathbf{q}})_q \dot{\mathbf{q}} \end{bmatrix}. \tag{13}$$

Eqs. (13) is a set of n ordinary differential equations as $\mathbf{B}^T \in \mathbb{R}^{(n-m)\times n}$. Matrix $\mathbf{B}$ can be computed either via QR, eigen or singular value decompositions of $\mathbf{C}_q$. Any integration method can, then, be used to obtain $\dot{\mathbf{q}}(t)$ and $\mathbf{q}(t)$ via a standard fixed/variable step size explicit method starting from known initial configuration and velocity.

3 PKM MODEL PROCEDURE

In order to model a PKM composed by $i = 1, \cdots, n_l$ legs, a fixed base and a moving platform mp the following general procedure is outlined:

- Definition of the Denavit-Hartenberg (DH) homogeneous transformation matrices for leg $i^{th\cdot}$;
- Definition of the redundant coordinates;
- Definition of the kinematic constraints;
- Analytical calculation of the terms of eq. (1);
- Numerical implementation.

To model the kinematics of the legs is mandatory to define the coordinates of the PKM to which the moving platform coordinates will be added to. It will turn out a redundant number of coordinates constrained by the vector-loop equations connecting the base to the moving platform by means of the legs kinematic chains. Therefore, terms of eq. (1) can be obtained by a simple analytical computation of the kinetic $K = K_{mp} + \sum_1^{n_l} K_i$ and gravitational $U = U_{mp} + \sum_1^{n_l} U_i$ energy of PKM according to Lagrange formulation:

$$\mathcal{L} = K - U;$$

$$\frac{d}{dt}\left(\frac{\partial \mathcal{L}}{\partial \dot{\mathbf{q}}}\right) - \frac{\partial \mathcal{L}}{\partial \mathbf{q}} = \mathbf{M}(\mathbf{q})\ddot{\mathbf{q}} + \mathbf{V}(\mathbf{q}, \dot{\mathbf{q}}) + \mathbf{G}(\mathbf{q}). \tag{14}$$

As well as, the vector of the forces $\mathbf{f}$ is obtained directly from the virtual work with respect to the redundant coordinates without the need of introducing the Jacobian matrix, that maps the dependent coordinates into the independent ones.

4 PKM GEOMETRY

Figure 1 shows the PKM under study. The manipulator consists of a fixed base and a moving platform connected by four legs. Each leg is a serial kinematic chain with an actuated prismatic joint (P), a two couple of revolute joints (R) with their axes being perpendicular and coplanar, namely a couple of R joints forms a U joint. For each leg, the axis of the P joint is normal to the base and parallel to the first and last R joints of the leg. The second and third R joint axes are parallel, too. The motion of the moving platform is a spatial translation with a rotation about a fixed axis known as Schönflies motion. This 3T1R PKM was synthesized by X. Kong and C. Gosselin [24] whereas the complete kinematic analysis was solved by M. Ruggiu [25]. In order to model the PKM we define the reference systems on the $i^{th\cdot}$ leg according to the standard DH convention and the reference systems either on the base or on the moving platform, respectively, $\mathcal{G} : \{O_G XYZ\}$, $\mathcal{P} : \{PUVW\}$. Figure 2 shows the reference systems on the PKM, Table I shows the DH parameters for the leg[†].

It is worth noting that only three coordinates (joints variables) can represent the leg kinematics to be included

---

[†] For sake of clarity the index i for the leg is omitted in Figure 2.

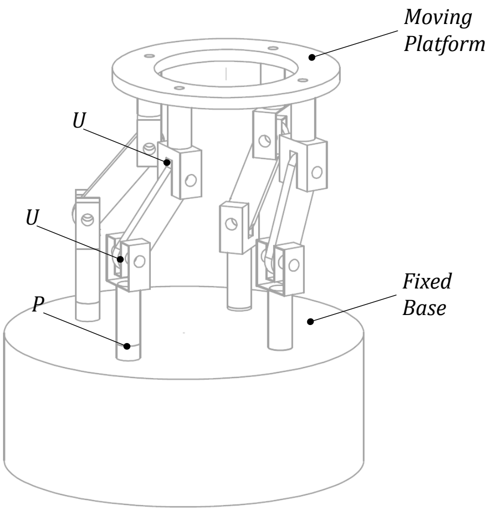

Figure 1 The Schönflies motion generator.

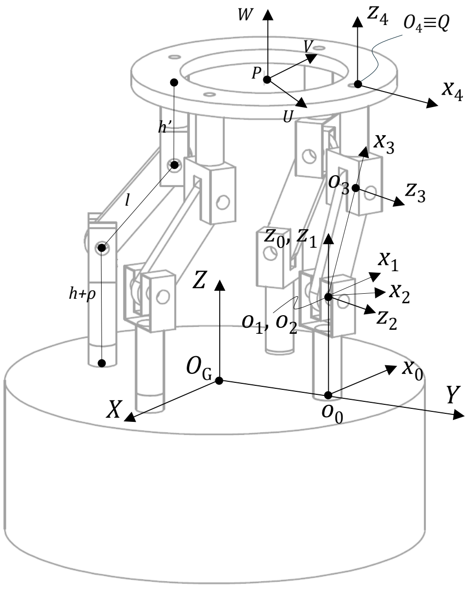

Figure 2 Reference systems for the PKM.

Table I - DH-table, leg i

link/joint j	α_j	a_j	d_j	$\theta_{j,i}$
1	0	0	$\rho_i + h$	0
2	$\frac{\pi}{2}$	0	0	$\theta_{1,i}$
3	0	l	0	$\theta_{2,i}$
4	$-\frac{\pi}{2}$	0	h'	$-\theta_{2,i}$

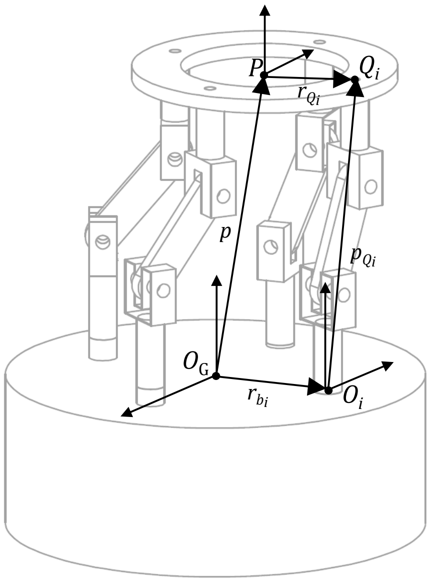

Figure 3 Vector kinematic chain loop.

into dynamic model to which the coordinates defining the pose of the moving platform are added. In total, we deal with 16 coordinates, $\mathbf{q} = \left[\{\rho_i, \theta_{1i}, \theta_{2i}\}_1^4, x, y, z, \phi\right]^T$. There are, however, the vector loop equations representing the kinematic constraints of the PKM where the coordinates are related. Thus, summing up, there are only four independent coordinates, as expected.

4.1 KINEMATIC CONSTRAINTS

As it is said, the constraint equations $\mathbf{C}(\mathbf{q}) = \mathbf{0}$ are the loop equations from point O_G to P following each kinematic chain of the leg (Figure 3):

$$ {}^G\mathbf{r}_{b_i} + {}^{0_i}\mathbf{R}_G^{T}\,{}^{0_i}\mathbf{p}_{Q_i} - {}^G\mathbf{p} - {}^G\mathbf{Q}_P\,{}^P\mathbf{r}_{Q_i} = \mathbf{0} \qquad (15) $$

where ${}^{0_i}\mathbf{p}_{Q_i}$ is expressed in the base reference system of the leg i and it contains the leg joint variables, ${}^G\mathbf{p}$ provides the position of the moving platform centre of mass, x, y, z, ${}^G\mathbf{Q}_P$ is the matrix that represents the orientation of the moving platform. The moving platform can only rotate by ϕ about z_G such that ${}^G\mathbf{Q}_P \equiv {}^G\mathbf{R}_z(\phi)$. Vectors in eq. (15) are expressed in the PKM base reference system, matrices ${}^{0_i}\mathbf{R}_G^T$ and vectors ${}^G\mathbf{r}_{b_i}$, ${}^P\mathbf{r}_{Q_i}$ are constants whose values depend of which leg is considered. Thus, there are $m = 12$ constraint equations to obtain $f = n - m = 4$ degrees of freedom for the PKM, as expected. The (12×16) Jacobian constraint matrix $\mathbf{C}_q$ can, thus, be easily computed.

5 SIMULATION RESULTS

The correctness and the the reliability of the model proposed was verified by two different tests.

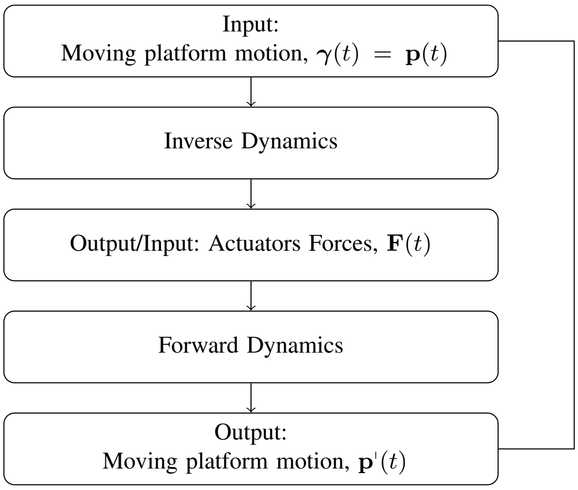

Figure 4 Auto-Test routine.

Table II - PKM geometrical parameters

$h\ (mm)$	$l\ (mm)$	$h'\ (mm)$	$r_b\ (mm)$	$r_Q\ (mm)$
66.34	80	75	92.73	75

5.1 AUTO-TEST

The correctness of the model was tested by an *auto-test* routine shown in Figure 4.

Either the inverse or the forward codes will be auto-proved whenever $\mathbf{p}(t) \equiv \mathbf{p}'(t)$. The simulation consists of a $2s$ long prescribed motion of the moving platform described by a sixth-order polynomial for each of the coordinates. The motion is free from both kinematic and constraint singularities such that the actuators forces are bounded and the constraint Jacobian is invertible. All geometric parameters and mass properties of the PKM used for the simulation are given in Tables II and III, respectively.

Link 1 only translates, all the bodies are considered homogeneous. Figure 5 shows the driven forces obtained from the inverse dynamics and then used to solve the forward dynamics. The integration method used was the fourth order Runge-Kutta with step size of 0.001s. Figure 6 shows the prescribed motion and the motion computed by the forward dynamics code. They practically coincide each to the other.

The validation was carried out through the forward dynamics computation. The simulation consists of a 1.5s motion with motors 2 and 3 not activated and the gravity effect omitted. The prescribed motors laws are given in Figure 8.

Table III - PKM mass parameters

	mass (g)	inertia $(kgmm^2)$
link 1	93.31	–
link 3	63.71	$\mathrm{diag}(3.83, 49.86, 52.64)$
moving platform	454.74	$\mathrm{diag}(0, 0, 2874.21)$

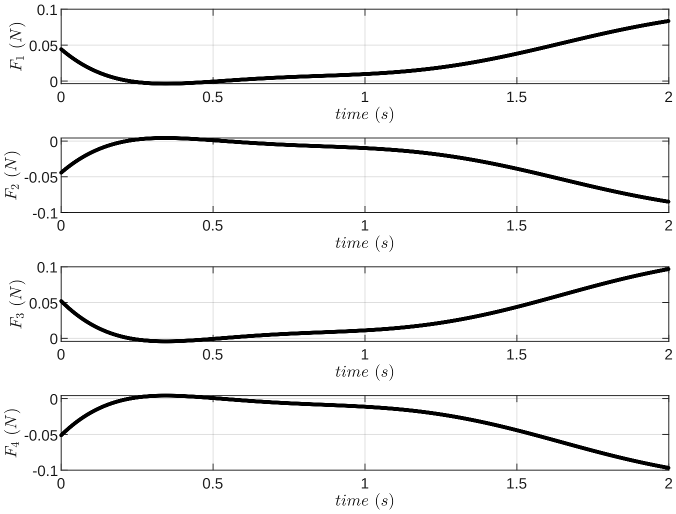

Figure 5 Actuators Forces of the *Auto-Test* simulation.

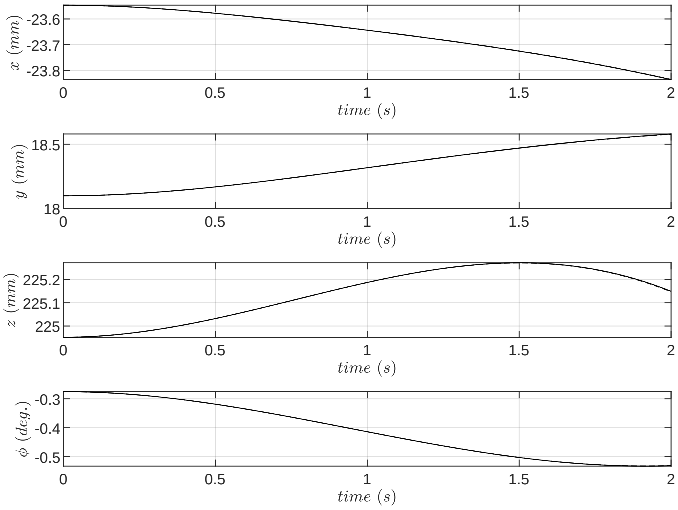

Figure 6 *Auto-Test* results -: computed, –: prescribed.

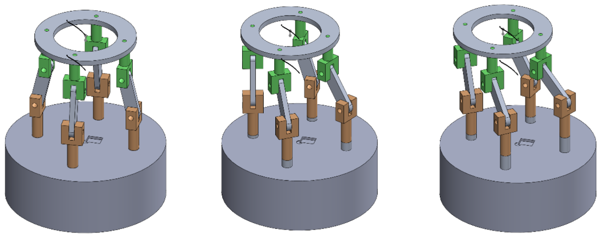

Figure 7 PKM solid model motion frames.

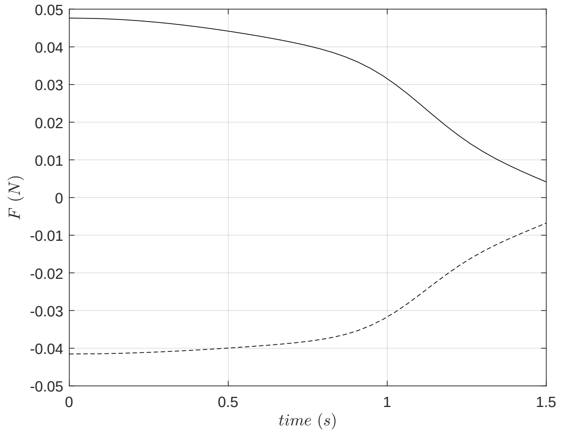

Figure 8 Motor forces of the comparison test: F_1(—), F_4(- -).

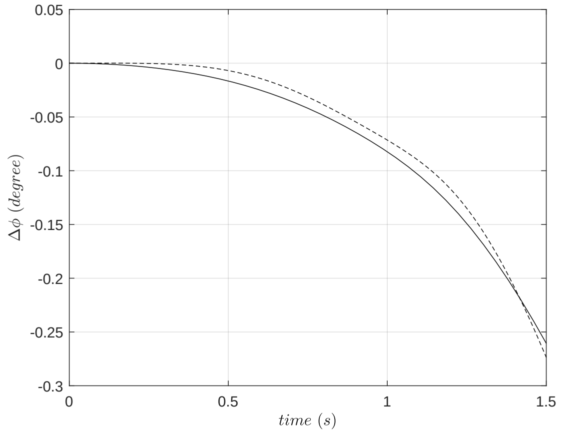

Figure 9 Comparison test. Angular Displacement: Solid Model(—), Math Model(- -).

Figures 9 and 10 show the angular displacement of the moving platform and the linear displacements of its reference point P obtained either by the porposed model and by the solid model simulation.

5.2 COMPARISON TEST

The dynamic model was validated by comparing the results of a simulation with those obtained by a solid model built by a commercial software (Figure 7). Eventually, Figure 11 shows the comparison between the elongation $\Delta\rho_1$ of the prismatic joint calculated by the two models. From the plots it can be concluded that the models are in good agreement. Despite of the fairly results for the reference point displacement of the moving platform and for the actuators displacements, a discrepancy was found in the moving platform rotation. A possible explanation can be

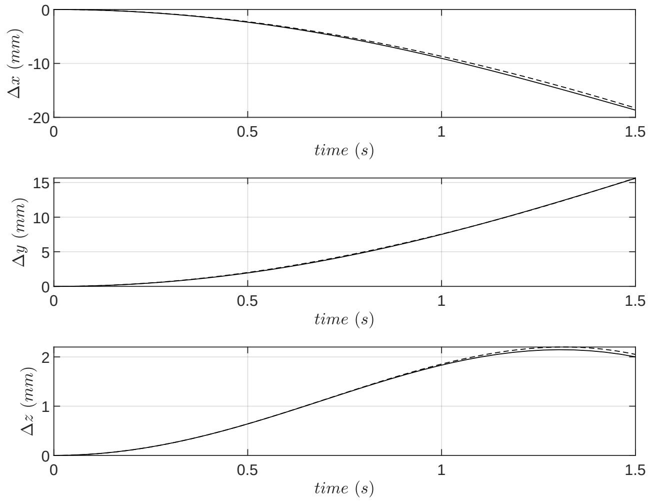

Figure 10 Comparison test. Linear Displacements: Solid Model(—), Math Model(- -).

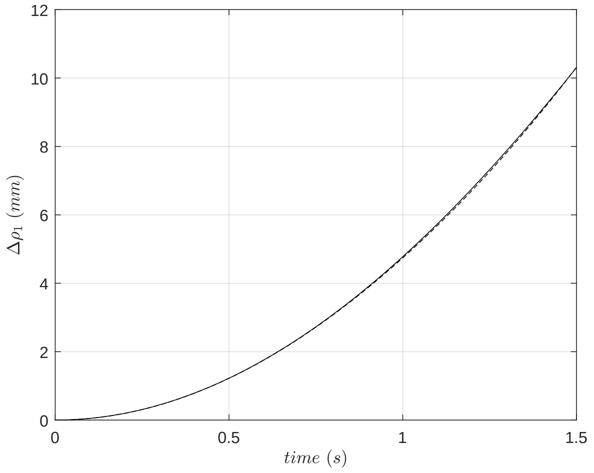

Figure 11 Comparison test. Motor elongation $\Delta\rho_1$: Solid Model(—), Math Model(- -).

found in the fact that the U joints are immaterial in the mathematical model and their contribution in the rotational inertia may become important for such small value attained by the moving platform rotation.

6 CONCLUSION

A model of the dynamics of a Schönflies motion generator was developed. The model was based on the Lagrange formulation with redundant coordinates comprising either the kinematics of the legs or the moving platform. Both the forward and the inverse dynamic problems were dealt with. The reliability and correctness of the model was tested via the *auto-test*. The forward and inverse computations were, indeed, implemented with reversed input/oputput providing the same results. Furthermore, a validation of the model was carried out by comparing the results from the model with those obtained by a solid model built by a commercial software. The comparison shows a good agreement between the models proving that the model developed is reliable. Moreover, the model is simple and the computational cost is low. The approach used, borrowed from the computational multibody community, can be used for other parallel architectures with small modifications.

REFERENCES

[1] Makino, H. and Furuya, N. Selective compliance assembly robot arm. In: *Proc. 1st Intern. Conf. on Assembly Automation (ICAA)*, pp. 77–86, Brighton, 1980.

[2] Pierrot, F. and Company, O. H4: a new family of 4-dof parallel robots. In: *Proc. of the IEEE/ASME Intern. Conf. on Advaned Intelligent Mechatronics*, pp. 508–513, Atlanta, 1999.

[3] Krut, S., Company, O., Benoit, M., Ota, H., and Pierrot, F. I4: A new parallel mechanism for scara motions. In: *Proc. of the IEEE Intern. Conf. on Robotics and Automation (ICRA03)*, Taipei, 2003.

[4] Nabat, V., Company, O., Krut, S., Rodriguez, M., and Pierrot, F. Par4: Very high speed parallel robot for pick-and-place. In: *Proc. of the IEEE Intern. Conf. on Intelligent Robots and Systems (IROS05)*, Edmonton, 2005.

[5] Krut, S., Company, O., Nabat, V., and Pierrot, F. Heli4: A parallel robot for scara motions with a very compact traveling plate and a symmetrical design. In: *Proc. of the IEEE Intern. Conf. on Intelligent Robots and Systems (IROS06)*, pp. 1656–1661, Beijing, 2006.

[6] Liu, S., T. Huang, T., J., M., Zhao, X., Wang, P., and Chetwynd, D.G. Optimal design of a 4-dof scara type parallel robot using dynamic performance indices and angular constraints. *ASME J. Mech. Robot.*, Vol. 4, No. 3, 2012.

[7] Xie, F. and Liu, S. Design and development of a high-speed and high-rotation robot with four identical arms and a single platform. *ASME J. Mech. Robot.*, Vol. 7, No. 4, 2015.

[8] Wu, G., Bai, S., and Hjørnet, P. Architecture optimization of a parallel Schönflies-motion robot for pick-and-place applications in a predefined workspace. *Mech. Mach. Theory*, Vol. 106, pp. 148–165, 2016.

[9] Wu, G. Kinematic analysis and optimal design of a wall-mounted four-limb parallel Schönflies motion robot. *J. Intell. Robot. Syst.*, Vol. 85, No. 3, pp. 663–677, 2017.

[10] Callegari, M., Carbonari, L., Palmieri, G., and Palpacelli, M.C. Functional design of a manipulator for the automation of laboratory precision tasks. *International Journal of Mechanics and Control*, Vol. 21, No. 2, pp. 29–37, 2020.

[11] Pierrot, F., Reynaud, C., and Fournier, A. Delta: a simple and efficient parallel robot. *Robotica*, Vol. 8, No. 2, pp. 105–109, 1990.

[12] Angeles, J., Caro, S., Khan, W., and Morozov, A. Kinetostatic design of an innovative Schönflies motion generator. *Proc. Ins. Mech. Eng. Part C: J. Mech. Eng. Sci.*, Vol. 220, No. 7, pp. 935–943, 2006.

[13] Lee, P.C. and Lee, J.J. Singularity and workspace analysis of three isoconstrained parallel manipulators with Schönflies motion. *Front. Mech. Eng.*, Vol. 7, No. 2, pp. 163–187, 2012.

[14] Wu, G., Lin, Z., Zhao, W., Zhang, S., Shen, H., and Caro, S. A four-limb parallel Schönflies motion generator with full-circle end-effector rotation. *Mech. and Machine Theory*, Vol. 146, 2020.

[15] Corbel, D., Gouttefarde, M., Company, O., and Pierrot, F. Actuation redundancy as a way to improve the acceleration capabilities of 3t and 3t1r pick-and-place parallel manipulators. *ASME J. Mech. Robot.*, Vol. 2, No. 4, 2010.

[16] Dasgupta, B. and Mruthyunjaya, T. Closed-form dynamic equations of the general stewart platform through the newton–euler approach. *Mech. Mach. Theory*, Vol. 33, No. 7, pp. 993–1012, 2016.

[17] Gosselin, C. Parallel computational algorithms for the kinematics and dynamics of planar and spatial parallel manipulators. *ASME J. Dyn. Syst. Meas. Control*, Vol. 118, No. 1, pp. 22–28, 1996.

[18] Sholanov, K.S., Abzhaparov, K.A., Zhumasheva, Z.T., and Ceccarelli, M. A new parallel manipulator hydraulically actuated. *International Journal of Mechanics and Control*, Vol. 17, No. 1, pp. 49–57, 2016.

[19] Tsai, L. Solving the inverse dynamics of a stewart–gough manipulator by the principle of virtual work. *ASME J. Mech. Des.*, Vol. 122, No. 1, pp. 3–9, 2000.

[20] Lebret, G., Liu, K., and Lewis, F.L. Dynamic analysis and control of a stewart platform manipulator. *J. Robot. Syst.*, Vol. 10, No. 5, pp. 629–655, 1993.

[21] Abdellatif, H. and Heimann, B. Computational efficient inverse dynamics of 6-dof fully parallel manipulators by using the lagrangian formalism. *Mech. Mach. Theory*, Vol. 44, No. 1, pp. 192–207, 2009.

[22] Zhou, Z. and Gosselin, C. Simplified inverse dynamic models of parallel robots based on a lagrangian approach. *Meccanica*, Vol. 59, pp. 657–680, 2024.

[23] Ruggiu, M., Rea, M., and Ottaviano, E. Forward dynamics of a 3t1r parallel manipulator. In: *LNNS, Vol 1129, 4th International Conference on Reliable Systems Engineering, (ICORSE2024)*, Bucharest, 2024.

[24] Kong, X. and Gosselin, C. *Type Synthesis of Parallel Mechanisms*. Springer, Berlin Heidelberg, 2007.

[25] Ruggiu, M. Mobility and kinematic analysis of a special class of 3t1r parallel manipulator. *International Journal of Mechanics and Control*, Vol. 18, No. 02, pp. 123–127, 2017.

ISSN 1590-8844
International Journal of Mechanics and Control, Vol. 26, No. 02, 2025
https://doi.org/10.69076/jomac.2025.0021

STRUCTURAL CHARACTERIZATION OF A SHAPE MEMORY ALLOY (CU-AL-NI) MANUFACTURED BY FUSION

Mokhtar Benarioua* Cherif Saib*** Salah Amroune**** Sarkaut Ahmed Ameen*****
Barhm Mohamad****** Said Zergane*** Necib Kamel*******

*Mechanical Department, Faculty of Technology, Batna 2 University, Batna Algeria.
**Mechanical Structures and Materials Laboratory (MSML), Batna 2 University, Batna, Algeria
***Department of Mechanical Engineering, Faculty of Technology, Mohamed Boudiaf University of M'sila, Pôle universitaire route BBA, M'sila, Algeria
****Laboratory of Materials and Mechanics of Structures (LMMS), University of M'sila, Algeria
*****Automotive Technology Engineering Department, Erbil Technology College, Erbil Polytechnic University, 44001 Erbil, Iraq
******Department of Petroleum Technology, Koya Technical Institute, Erbil Polytechnic University, 44001 Erbil, Iraq
*******LMGMA,laboratoire de Métallurgie et Génie des Matériaux, Annaba, Algeria, Algeria

ABSTRACT

This study presents a comprehensive analysis of the crystalline structure of the Cu-Al-Ni shape memory alloy, emphasizing the influence of melting processes on its chemical composition. The investigation encompasses transformation temperatures, microhardness, and induced transformations, providing a detailed understanding of the alloy's behavior. The results highlight complex interactions between chemical composition and crystalline structures while demonstrating the significant impact of thermal variations on shape memory properties. These properties are crucial for the material's performance, particularly its ability to recover its original shape after deformation. The findings offer valuable insights for optimizing manufacturing processes and heat treatments to enhance the mechanical and functional characteristics of these alloys. Moreover, this research contributes to the development of advanced industrial applications, particularly in demanding sectors such as aerospace, automotive, and medical devices, where the reliability and precision of shape memory materials are essential.

Keywords: Ternary shape memory alloys, structural characterization, thermoelastic transformations, martensite, transformation temperatures

1 INTRODUCTION

Shape memory alloys (SMAs) are among the most prominent smart materials due to their remarkable ability to revert to their original shape after deformation. This unique characteristic makes them highly valuable for both research and industrial applications. SMAs are increasingly being employed across various sectors, including aviation, automotive, biomedical engineering, robotics, civil engineering, and electronics [1-8].

Their first significant application dates back to the 1970s when SMA-based hydraulic pipe connectors were integrated into F-14 fighter jets [9]. Since then, interest in these materials has steadily grown, fostering numerous innovations. Notably, SMAs have the potential to prevent catastrophic failures in critical industries such as petrochemicals and pharmaceuticals. As research progresses, these alloys continue to demonstrate their ability to address emerging technological and industrial

---

Contact author: Barhm Mohamad[5]
[5]Department of Petroleum Technology, Koya Technical Institute, Erbil Polytechnic University, 44001 Erbil, Iraq
E-mail: barhm.mohamad@epu.edu.iq

challenges, reinforcing their role as indispensable solutions for a wide range of complex applications.

Memory alloys can exist in two distinct phases: martensite and austenite. The martensitic phase has a stable crystal structure at low temperatures, whereas the austenitic phase remains stable at high temperatures [10]. Upon heating, the alloy transitions from martensite to austenite, beginning at the austenite start temperature (A_s) and completing the transformation at the austenite finish temperature (A_x). Once the temperature exceeds A_s, the SMA starts to contract and revert to its original shape. Conversely, during cooling, austenite transforms back into martensite, starting at the martensite start temperature (M_s) and concluding at the martensite finish temperature (M_x) [9]. A similar transformation occurs when the material is subjected to external stress.

The chemical composition of the materials used in manufacturing SMAs is crucial, as any deviation from the required composition can lead to a deterioration in their properties. Additionally, maintaining an appropriate range of martensitic transformation temperatures is equally important [9].

In recent decades, Cu-based shape memory alloys have gained prominence in various applications, including high-damping materials, sensors, and actuators [11]. Among them, Cu-Al-Ni alloys are particularly distinguished by their high thermal stability [11]. To contribute to the advancement of research in this field, this study focuses on characterizing a Cu-Al-Ni ternary alloy synthesized through a fusion process, with a martensitic transformation start temperature near ambient conditions. The studies by Moskvichev et al. [12], Said et al. [13], Zeghdane et al. [14], and Abolhasani et al. [15] provide complementary insights into the development and performance of Cu-based SMAs using different processing methods. Moskvichev et al. [12] employed electron beam additive manufacturing (EBAM) to fabricate Cu–Al–Mn alloys, emphasizing the role of heat input in controlling the structure, phase composition, mechanical properties, and tribological behavior. Their findings revealed that higher heat input promoted the formation of a $\beta1' + \alpha$ decomposed structure, while lower heat input suppressed decomposition and favored an ordered $\beta1$ structure, leading to variations in microhardness (2.0–2.75 GPa) and friction coefficient (0.1–0.175). In contrast, Said et al. [13] and Zeghdane et al. [14] focused on Cu–Al–Ni SMAs prepared by conventional fusion methods, where microscopy, X-ray diffraction, and dilatometry were applied to investigate microstructural evolution, martensite formation, and transformation temperatures under different heat treatments. These studies established fundamental knowledge on thermoelastic transformations in Cu–Al–Ni alloys, providing a baseline for understanding their phase stability. Moving towards advanced additive manufacturing strategies, Abolhasani et al. [15] introduced two distinct approaches. In one study, a dual-structure Cu–Al–Ni SMA was fabricated via powder bed fusion for 4D printing applications, where the coexistence of structures with different hardness and recovery temperatures enhanced the recovery strain through thermal gradients, residual stress mismatch, and the formation of secondary martensite plates. In another study, alumina (Al_2O_3) reinforcement layers were incorporated into Cu–Al–Ni SMAs to mitigate brittle fracture at triple junctions. The optimized design, with 0.3 wt% alumina and a thicker reinforcement layer, improved fracture strain and preserved the shape memory effect, while excessive reinforcement led to martensite stabilization and reduced performance. Collectively, these studies illustrate the progression from conventional fusion-based characterization of phase transformations to advanced additive manufacturing approaches that enable microstructural tailoring, improved recovery behavior, and enhanced mechanical reliability of Cu-based SMAs for potential applications in smart actuators, biomedical devices, and adaptive systems.

The originality of this study lies in its comprehensive approach to analyzing the effects of melting processes and heat treatments on the crystalline structure and functional properties of Cu-Al-Ni shape memory alloys. By investigating transformation temperatures, microhardness, and induced transformations, this research provides an in-depth understanding of the intricate relationships between chemical composition, crystalline structures, and shape memory behavior. Moreover, the integration of experimental findings with practical industrial applications, particularly in high-performance sectors such as aerospace, automotive, and medical devices, enhances the study’s practical significance. This work contributes to a deeper understanding of the fundamental mechanisms governing these alloys and offers valuable insights for optimizing manufacturing processes and heat treatments, addressing the increasing demand for innovations in smart materials.

2 MATERIALS AND METHODS

2.1 SAMPLES PREPARATION

The experimental investigations were conducted on specimens prepared from a single elaborated Cu–Al–Ni alloy batch, whose chemical composition was verified using spectrometry. All subsequent tests, including structural characterization, microhardness evaluation, and electrical resistance measurements, were performed on these specimens. This study focused on the manufacturing of a ternary shape memory alloy (Cu-Al-Ni) whose martensitic transformation start temperature lies within the limits of the ambient environment.

The calculation, according to the ratios of the mass contents of the alloy elements to the content of the base element (Cu), and the transformation start point M_s, gives the following composition in mass percentage:

$$Cu(\approx 82.5\%),\ Al(\approx 13.5\%),\ Ni(\approx 4\%),\ \text{for } Ms(\approx 91.5^{\circ}C) \quad (1)$$

The alloy manufacturing protocol (Figure 1) is inspired by a method developed in 2013 by Bouabdallah et al. [16].

Table I - Composition of the samples elaborated

Elements	Cu	Al	Ni	Fe	As	S	Cr	Sn	Sb	Mg	Mn	Ag
Mass%	82.7	13.	4.00	0.06	0.015	0.001	0.014	0.006	0.017	0.05	0.045	0.007

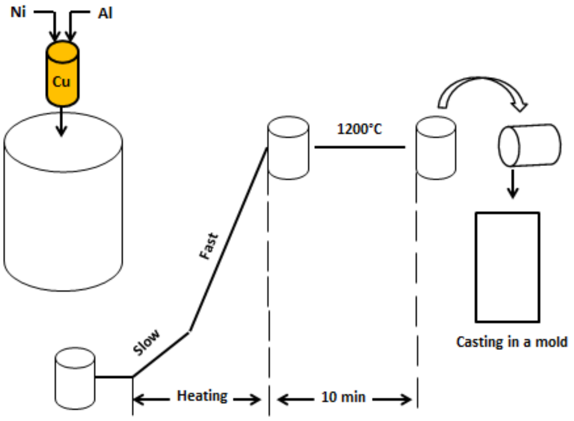

Figure 1 Schematic representation of the alloy manufacturing process.

After weighing each alloy element and determining their proportions, copper (Cu) serves as the base material and acts as a container for aluminum (Al) and nickel (Ni). The elements are shaped into wafers, arranged in an alumina crucible, and placed in a melting furnace under a controlled atmosphere. Once melted, the liquid alloy is poured into a steel mold and allowed to cool in ambient air. The composition of the samples (Table I) was determined using spectrometry

2.2 STRUCTURAL CHARACTERIZATION

To analyze the material's structure, a comprehensive structural characterization was performed. This process involved capturing micrographs using a Leitz Widefield optical microscope, known for its high precision and capability to produce detailed images of microscopic structures. These observations enabled a thorough examination of the material’s morphological features and the identification of any potential anomalies in the sample. The data obtained from these micrographs serve as a crucial foundation for understanding the structural and functional properties of the material under investigation.

2.3 MICRO HARDNESS MEASUREMENTS

The microhardness of the Cu–Al–Ni alloy was evaluated using the Vickers pyramidal indentation method. A controlled load of 100 grams was applied to the material surface to ensure uniform penetration depth and accurate assessment at the microscopic scale. The indentation was carried out with a Vickers indenter, a diamond-shaped pyramidal penetrator that leaves a small impression on the sample surface. The hardness value (Hv) was then calculated based on the size of the indentation diagonals. The tests were performed systematically across different regions of the sample to identify potential variations in local hardness. To maintain measurement accuracy and repeatability, the procedure was conducted under controlled conditions using Ordered Powder Lithography (OPL) equipment, which allows for precise positioning of the indenter and reliable recording of hardness values. This approach provided an average hardness value of about 368 Hv in the raw state, which increased to 416 Hv after heat treatment, confirming the material’s structural strengthening due to thermal processing.

2.4 HEAT TREATMENTS ADOPTED

To reveal the martensitic phase formed from the liquid β phase, the elaborated Cu–Al–Ni alloy underwent a controlled thermal treatment. The procedure involved heating the alloy to 850 °C for 10 minutes, followed by rapid quenching in water to suppress undesired phase decomposition and to stabilize the martensitic structure. Subsequently, a tempering process at 100 °C for one hour was performed to restore thermodynamic equilibrium and relieve internal stresses induced by the supersaturated state. This combined sequence of heating, quenching, and tempering effectively enhanced phase visibility and optimized the alloy’s functional stability.

The treatment process not only revealed the martensitic morphology but also modified the alloy’s microstructural and mechanical characteristics.

2.5 MEASUREMENT OF THE ELECTRICAL RESISTANCE VARIATION

The measurement of electrical resistance variation is conducted to determine the start and end temperatures of phase transformations in the material, as well as the associated heat exchange. In copper-based shape memory alloys, martensitic transformation is accompanied by an increase in electrical resistivity of approximately 25%, enabling the identification of key transformation temperatures through resistance tracking.

For this purpose, a four-wire measurement technique, forming a Thompson bridge, was selected due to its high precision in measuring low resistances. This method ensures reliable and repeatable results, even for subtle resistance variations. Additionally, temperature control during the experiment was achieved using a regulated thermal chamber, capable of heating and cooling the sample at an average rate of 2°C per minute, ensuring precise and controlled temperature measurements [6], [16-22].

3 RESULTS AND DISCUSSIONS

3.1 STRUCTURAL CHARACTERIZATION

In Figure 2, the surface of the sample is shown in its raw state after the melting process and subsequent electrochemical polishing for 10 minutes using a reagent mixture of H_3PO_4 and H_2O. This polishing process was conducted to refine the surface texture.

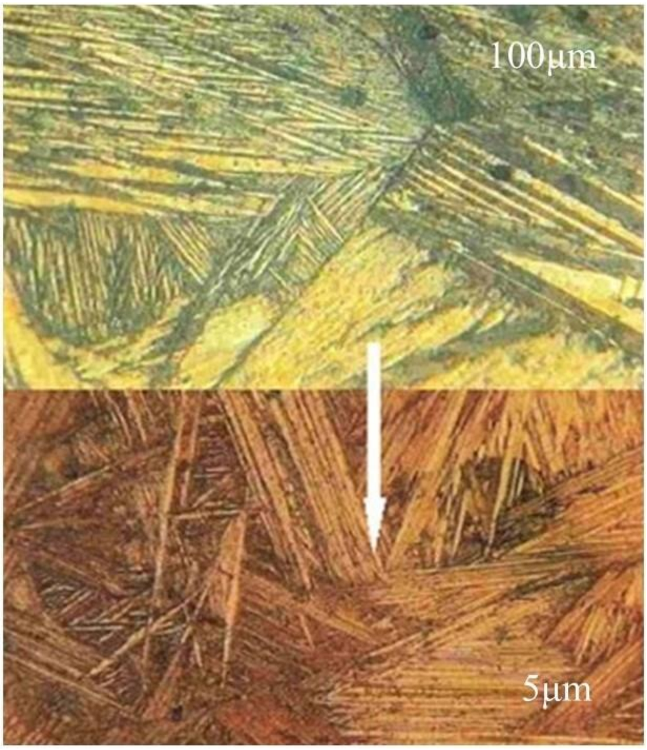

Figure 2 Raw structure of Cu-Al-Ni (Highlighting martensitic structure).

The measured average grain size of the sample after treatment is 0.7 mm. This measurement serves as a key indicator of the material's structural characteristics post-polishing, offering insights into the effects of the process on the sample's surface and its potential impact on the alloy's performance in subsequent applications.

3.2 MICRO HARDNESS MEASUREMENTS

Figure 3 presents the microhardness profile diagram for the Cu-Al-Ni alloy, illustrating the variation in microhardness across different regions of the material. The average hardness value is measured to be approximately 368 Hv, providing an indication of the alloy's resistance to localized deformation at the microscopic level.

Microhardness measurements are crucial for evaluating the mechanical properties of the alloy, as they help assess its durability and performance under stress. The obtained hardness value reflects the overall strength of the material in its current state, offering insights into its suitability for applications where hardness and wear resistance are critical. Additionally, the profile diagram aids in identifying any inhomogeneities or variations in hardness (Hv) within the material, which may influence its mechanical behavior under different operating conditions.

3.4 HEAT TREATMENTS ADOPTED

Figure 4 presents a micrograph of the sample surface after undergoing the designated heat treatment, specifically applied to reveal the martensitic phase. The treatment effectively highlighted the martensitic structure, demonstrating its success in phase transformation. However, it also influenced other material properties, particularly grain size and hardness.

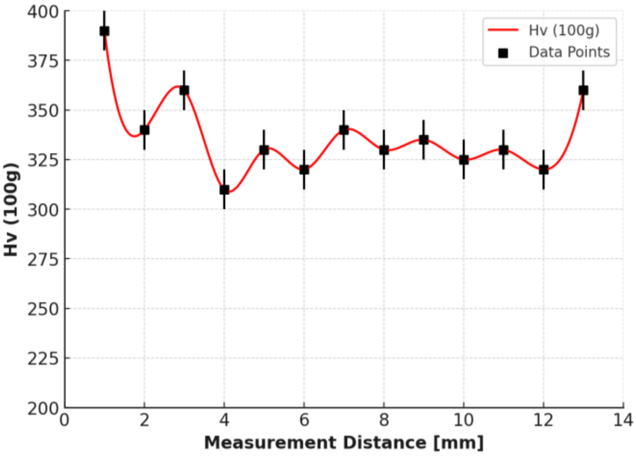

Figure 3 Micro hardness evolution of raw samples.

Table II - Characteristic transformation points

Parameter	Raw state	Heat treated
Particle size (mm)	0.7	0.83
Micro-hardness Hv (100g)	368	416

Such changes are inherent to thermal processing, as heat treatments often modify the microstructural characteristics of the material. As summarized in Table II of the article, the average grain size increased from 0.70 mm to 0.83 mm, while the microhardness improved from 368 Hv to 416 Hv, demonstrating the strengthening effect of the thermal cycle. These results confirm that appropriate heat treatment conditions are critical for achieving the desired balance between structural refinement and mechanical performance in Cu-based shape memory alloys. The adopted methodology aligns with findings from similar studies on Cu–Al–Ni SMAs, where heat treatment has been reported to significantly influence phase transformations, hardness, and grain growth. For instance, Said et al. [13] and Chentouf et al. [23] observed that water quenching after high-temperature treatment preserved the β-phase stability and promoted the formation of thermoelastic martensite, enhancing the functional properties of the alloy.

3.5 DETERMINATION OF TRANSFORMATION TEMPERATURES

The outcomes of this test have been converted into physical values in accordance with the AFNOR A51080 standard [16]. These results are visually represented in Figure 5, which provides a detailed illustration of the data obtained from the analysis. The diagram highlights key aspects of the material's transformation behavior, capturing specific points where significant changes occur during the testing process. From this diagram, the critical transformation points indicating major phase transitions or material responses have been systematically identified and recorded. These characteristic points are summarized in Table III, offering a clear and concise presentation of the results.

Table III - Average particle size and micro-hardness for raw and heat treated Cu-Al-Ni alloys

Characteristic point	Martensitic-start-temperature Ms	Martensitic-finish-temperature Mf	Austenite-start-temperature As	Austenite-finish-temperature Af
Value (°C)	49	39	71	80

Figure 4 Structure of the Cu-Al-Ni alloy after heat treatment.

This comprehensive approach ensures that the data remains standardized and accessible, facilitating accurate interpretation and comparison with similar studies or applications in related fields. The combination of graphical representation and tabulated values enhances the overall understanding of the material's transformation properties.

4 CONCLUSIONS

This study underscores the critical role of melting processes and heat treatments in shaping the crystalline structure of alloys, directly influencing their properties. Additionally, temperature variations significantly affect the shape recovery characteristics of materials, impacting their ability to revert to their original form. The analysis of resistance variations with temperature, as depicted in the figure, reveals distinct phase transformation points (Mf, Ms, As, Af), identifying the critical temperatures at which structural changes occur during heating and cooling cycles. The observed hysteresis between heating and cooling curves further highlights the influence of thermal cycling on material behavior. Moreover, the alloy composition plays a fundamental role in thermo-mechanical transformations, as different alloy mixtures exhibit distinct phase transition behaviors, ultimately affecting overall material performance. These findings emphasize the necessity of carefully controlling processing conditions and alloy composition to optimize shape memory properties and enhance mechanical performance.

ACKNOWLEDGEMENTS

This research is supported by PRFU Project-N° A11N01UN280120220001 organized by the Algerian Ministry of Higher Education and Scientific Research (MESRS). The authors would like to thank Mr. Belkacem Aouifi Assistant Ingenious University of M'sila, Faculty of Technology, Mr Laifa FAkerdien, Mr. Tarek Bidi and Mr.Hassan Mokrani company manager Alger precision.

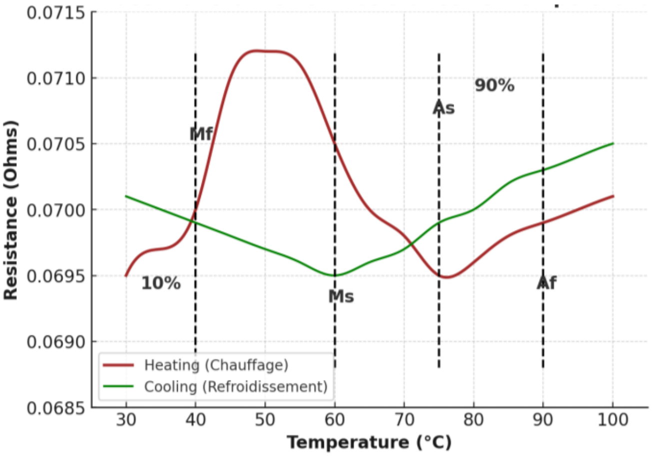

Figure 5 Results of the resistance variation measurements.

REFERENCES

[1] Balasubramanian, M., Ramesh, S., Kumar, K., Prakash, S., and Suresh, V. "Shape Memory Alloy Applications in Engineering." *Journal of Physics: Conference Series*, vol. 2054, no. 1, pp. 012078, 2021.

[2] Song, G., Ma, N., and Li, H. N. "Applications of Shape Memory Alloys in Civil Structures." *Engineering Structures*, vol. 28, no. 9, pp. 1266–1274, 2006.

[3] Rajput, G. S., Vora, J., Prajapati, P., and Chaudhari, R. "Areas of Recent Developments for Shape Memory Alloy: A Review." *Materials Today: Proceedings*, vol. 62, pp. 7194–7198, 2022.

[4] Bucht, A., Pagel, K., Eppler, C., and Kunze, H. "Industrial Applications of Shape Memory Alloys: Potentials and Limitations." Innovative Small Drives and Micro-Motor Systems; 9. *GMM/ETG Symposium*, Nuremberg, Germany, pp. 1–6, 2013.

[5] Khulief, Z. T. "Applications of Shape Memory Alloys." *Journal of University of Babylon for Engineering Sciences*, vol. 28, 2020.

[6] Costanza, G., and Tata, M. E. "Shape Memory Alloys for Aerospace: Recent Developments and New Applications-A Short Review." *Materials*, vol. 13, no. 8, p. 1856, 2020.

[7] Hartl, D. J., and Lagoudas, D. C. "Aerospace Applications of Shape Memory Alloys." Proceedings of the Institution of Mechanical Engineers, Part G: *Journal of Aerospace Engineering*, vol. 221, no. 4, pp. 535–52, 2007.

[8] Mohd Jani, J., Leary, M., Subic, A., and Gibson, M. A. "A Review of Shape Memory Alloy Research, Applications and Opportunities." *Materials & Design*, vol. 56, pp. 1078–113, 2014.

[9] Maalolan, B., and Santosh, S. "A Review on CuAlNi Shape Memory Alloys: Production Methods, Applications, and Current Trends." *Materials Today: Proceedings*, 2024.

[10] Benchekkour, A., Terfaya, N., Mohamad, B. A., Elmir, M., and Jálics, K. "Numerical Investigation of Thermal Influence on Debonding Behavior in Composite Structures through a Friction and Cohesive Coupled Model." *International Review of Applied Sciences and Engineering*, 2024.

[11] Makri, H., Saib, C., Amroune, S., Zergane, S., Mohamad, B., Benarioua, M., and Necib, K. "Elaboration and Characterization of Cu–Zn–Al Shape Memory Alloys." *Pollack Periodica*, 2024.

[12] Moskvichev, E., N. Shamarin, and A. Smolin. "Structure and Mechanical Properties of Cu–Al–Mn Alloys Fabricated by Electron Beam Additive Manufacturing." *Materials*, vol. 16, no. 1, p. 123, 2023.

[13] Said, Z., K. Necib, and A. Britah. "Structural Characterization of Cu–13.58% Al–3.94% Ni (wt. %) Shape Memory Alloy Elaborated by Fusion." *EPJ Web of Conferences*, vol. 6, p. 29001, 2010.

[14] Abolhasani, Daniyal, Sang Wook Han, Chester J. VanTyne, Namhyun Kang, and Young Hoon Moon. "Powder Bed Fusion of Two-Functional Cu–Al–Ni Shape Memory Alloys Utilized for 4D Printing." *Journal of Alloys and Compounds*, vol. 922, p. 166228, 2022.

[15] Abolhasani, Daniyal, H.-N. Kwon, Y.-H. Park, and Y.-H. Moon. "Enhancing the Mechanical Properties of Cu–Al–Ni Shape Memory Alloys Locally Reinforced by Alumina through the Powder Bed Fusion Process." *Materials*, vol. 16, no. 11, p. 3936, 2023.

[16] Bouabdallah, M., G. Baguenane-Benalia, A. Saadi, H. Cheniti, J.-C. Gachon, and E. Patoor. "Precipitation Sequence During Ageing in β_1 Phase of Cu–Al–Ni Shape Memory Alloy." *Journal of Thermal Analysis and Calorimetry*, vol. 112, no. 1, pp. 279-283, 2013.

[17] Farsi, C., Zergane, S., Amroune, S., Mohamad, B., Benyahia, A., and Latrache, M. "Evolution of the Electrical Potential for the Cathodic Protection of Pipelines According to the Variation of the Imposed Current." *Journal of Harbin Institute of Technology (New Series)*, 2023.

[18] Mobark, H. F. H., Al-Azzawi, A. H., Abid Ali, A. K., and Mohamad, B. "Comparative Tribological Analysis of Al-Fe-Si and Al-Fe-Cr Based Alloys." *Structural Integrity and Life*, vol. 24, no. 3, pp. 386–392, 2024.

[19] Fnides, M., Amroune, S., Mohamad, B., Fnides, B., and Toufik, B. "Optimization of Surface Roughness and MRR When Milling 25CrMo4-25 Steel Using Taguchi Design." *Academic Journal of Manufacturing Engineering*, vol. 22, no. 4, 2024.

[20] Aldriasawi, S. K., Ameen, N. H., Fadheel, K. I., Anead, A. M., Mhabes, H. E., and Mohamad, B. "An Experimental Artificial Neural Network Model: Investigating and Predicting Effects of Quenching Process on Residual Stresses of AISI 1035 Steel Alloy." *Journal of Harbin Institute of Technology (New Series)*, vol. 31, no. 5, pp. 78–92, 2024.

[21] Wahrhaftig, A. de M., Plevris, V., Mohamad, B. A., and Pereira, D. L. "Minimum Design Bending Moment for Systems of Equivalent Stiffness." *Structures*, vol. 57, p. 105224, 2023.

[22] Bodi, I., Piperi, E., Osmani, M., Doumalin, P., and Dupre, J. C. "3D Analysis of the Mechanical Behaviour for Material Properties by Using Terahertz Imaging." *International Journal of Mechanics and Control*, vol. 25, no. 01, 2024, pp. 89–96.

[23] Chentouf, S. M., M. Bouabdallah, H. Cheniti, and M. Keddam. “Stable Phase Formation in a 85.67 wt.% Cu-9.9 wt.% Al-4.43 wt.% Ni Shape Memory Alloy.” *European Symposium on Martensitic Transformations*, EDP Sciences, p. 05005, 2009.

ISSN 1590-8844
International Journal of Mechanics and Control, Vol. 26, No. 02, 2025
https://doi.org/10.69076/jomac.2025.0022

TRACKING ALGORITHM FOR UNDERWATER OBJECTS USING ACOUSTIC POSITIONING SYSTEM DATA WITH MOTION MODEL ADAPTATION

Andrey A. Kostoglotov[1] Anton S. Penkov[1] Li Shaokang[2]

[1] Rostov State Transport University, Rostov-on-Don, Russia
[2] Yantai Huitong Network Technology Co., LTD, Yantai, China

ABSTRACT

In this paper, an algorithm for tracking objects based on acoustic positioning data using an adaptive motion model is synthesized; its efficiency is analyzed using numerical simulation. The model of a moving object obtained using the decomposition principle is adapted based on the Kiefer-Wolfowitz stochastic approximation procedure to improve the accuracy of trajectory parameter estimation. This makes it possible to consider the dynamic characteristics of underwater objects based on the acoustic positioning system data. Simulation modeling is performed to confirm the efficiency of the algorithm using the example of tracking the trajectory of an underwater object using a long baseline system with acoustic beacons. The proposed algorithm allows increasing the accuracy of tracking the trajectory of an underwater object by an average of 5-20% depending on the maneuver type with computational costs equal to those of the traditional Kalman algorithm. The efficiency of the algorithm is confirmed for different values of observation noise and the period of receipt of measurement data.

Keywords: estimation, Kalman filter, acoustic location, underwater tracking, long baseline system, adaptation

LIST OF ABBREVIATIONS USED

GNSS	Global navigation satellite system
LBL	Long baseline
SBL	Short baseline
USBL	Ultra short baseline
INS	Inertial Navigation System
KF	Kalman filter

1 INTRODUCTION

Oceans cover almost 71% of the Earth's surface. [1,2]. Rich in natural resources such as organisms, minerals, oil and natural gas, the oceans have become a focus for countries around the world [3]. Marine scientific research, marine environmental monitoring, deep-sea resource development and other marine activities are becoming increasingly common [4].

The world's largest powers are creating their own national positioning and navigation systems [5,6], which are a systemic project that includes the integration of land, sea, air and sky, and can provide high-precision spatial and temporal information services. Positioning and navigation of air and land targets rely on the global navigation satellite system (GNSS), which is based on the use of electromagnetic waves. However, the attenuation of the electromagnetic wave under water is extremely fast. Therefore, the electromagnetic wave cannot propagate over long distances and cannot be directly used for positioning and navigation of underwater targets. For a safe underwater navigation, underwater vehicles require a fundamentally different system [7], capable of providing information such as the position, speed and orientation of an underwater object [8]. The attenuation of the acoustic signal under water is small, so it can propagate over long distances [4]. Therefore, underwater target positioning is done with systems, based on acoustic signals [9,10]. Currently, the most widely used acoustic navigation methods are long baseline (LBL), short baseline (SBL) and ultra short baseline (USBL) navigation [11,12]. Among them, the LBL system can provide the most accurate positioning information. It is based on acoustic measurement of the distance between the underwater vehicle and the underwater beacon [13].

Contact authors: Anton S. Penkov

Rostov State Transport University. Rostovskogo Strelkovogo Polka Narodnogo Opolcheniya Sq. 2, Rostov-on-Don, Russia, 344038
E-mail: pencha_@mail.ru

When an underwater vehicle receives an acoustic signal from an underwater beacon, the transmission time of the acoustic signal between them can be determined. Knowing the local sound velocity profile and the geometric position of each underwater beacon, the position of the underwater vehicle can be determined [14,15]. The ocean is a complex hydrodynamic environment where environmental noise [4] and variable sound speed [16] seriously affect the accuracy of the LBL system. Since LBL systems are aimed at positioning various classes of underwater objects, the information processing algorithms in their composition must have the ability to structurally and parametrically adapt to the dynamic characteristics and typical modes of motion of each individual class of tracked targets. The most common example is the adaptation of the standard Kalman filter with respect to unknown covariance matrices of state and observation noise [17,18]. It is assumed that the filter divergence is caused solely by incorrectly specified noise parameters, and not by other reasons related to the start of the maneuver. However, targets of many classes can perform arbitrary maneuvers of unknown intensity at random times. The resulting uncertainty of the motion model is one of the main processing problems associated with constructing a motion trajectory. Its solution involves the synthesis of a new class of motion models for maneuvering objects and corresponding algorithms, which are called "tracking algorithms" [19]. The aim of the work is to synthesize an adaptive tracking algorithm that considers the dynamic characteristics of an underwater object and, based on the results of measurements of the LBL system, provides an increase in the accuracy of trajectory tracking in comparison with the traditional algorithm. When forming the algorithm, methods of stochastic synthesis of trajectory processing known in the literature [20–22] and elements of a new approach of constructing a model of the maneuvering objects movement are used [23,24]. The article has the following structure. In the first section synthesis of the motion model using the decomposition principle is conducted. The second section presents a mathematical description of the trajectory tracking algorithm, where the main stages of trajectory processing are considered and methods for solving each stage of the problem are selected in accordance with its specifics. The third section presents mathematical modeling of the synthesized algorithm, using the example of processing data, obtained during the operation of the LBL hydroacoustic system. The final section presents the main conclusions of the work.

2 METHODOLOGICAL APPROACHES TO UNDERWATER NAVIGATION

Underwater navigation is a complex problem, the solution of which requires the use of specialized methods, adapted to the conditions of aquatic environment. The main methodological approaches can be divided into three categories: autonomous, corrected and external navigation systems [8]. Autonomous systems are based on inertial measurements and Doppler log data. Inertial navigation systems (INS) calculate the coordinates and orientation of an object by integrating the readings of accelerometers and gyroscopes. Although modern INS have high accuracy in the short term, their fundamental limitation is the unlimited accumulation of errors over time due to gyroscope drift and integration errors [25]. To compensate for these errors, Doppler logs are used to measure the speed relative to the bottom, which allows for a significant reduction in the accumulation of positioning errors [12]. Corrected navigation systems combine autonomous measurements with periodic correction from external sources. An important role here is played by hydroacoustic correction systems, such as hydroacoustic beacons and buoys [10]. These systems provide periodic coordinate updates using ultrasonic signals, which allows the accumulated INS error to be reset. Modern developments in this area include the use of underwater acoustic modules, deployed according to a specific geometry for optimization of coverage and positioning accuracy [26]. External navigation systems are based on infrastructure deployed in the water area. The most accurate solution in this class are long baseline (LBL) acoustic positioning systems, consisting of a network of bottom transponders with precisely known coordinates [14]. These systems provide high-precision positioning within their operating area, but require preliminary deployment and calibration of equipment. Less accurate, but easier to deploy are ultra-short baseline (USBL) systems, which measure the range and direction to an object relative to a single transceiver module [13]. A promising direction is the development of hybrid navigation systems that combine the advantages of different methodological approaches [27]. Such systems usually combine data from INS, Doppler logs, acoustic correction systems and geophysical navigation methods (comparison with bottom relief or magnetic field maps) [28]. Synthesis of algorithms for processing heterogeneous navigation information is a separate complex problem that requires the use of modern filtering and state estimation methods [29]. Each of the listed methodological approaches has its own areas of application and limitations, determined by the requirements for accuracy, autonomy, cost and deployment efficiency. The choice of a specific configuration for navigation system depends on it’s tasks, the characteristics of the underwater vehicle and the operating conditions [30]. Among the considered methods, acoustic long-baseline (LBL) positioning systems are of particular interest for high-precision tracking of underwater objects. These systems, based on a network of bottom transponders with precisely known coordinates, provide strapdown positioning with high accuracy, which significantly exceeds alternative approaches [13,14]. The key advantage of LBL systems for tracking maneuvering objects is their ability to provide stable positioning accuracy regardless of the orientation and depth of the object, as well as a relatively low sensitivity to hydrological conditions compared to other acoustic systems. However, the effective use of the LBL systems potential requires the development of promising algorithms for processing measurement information, that can adequately reflect the dynamic characteristics of maneuvering objects.

Particularly difficult is the processing of trajectory data of objects, performing arbitrary maneuvers of unknown intensity. Traditional state estimation algorithms based on uniform rectilinear motion models prove inadequate under conditions of intensive maneuvering [21]. This is due to fundamental uncertainty in the motion model, which requires the development of new approaches to the synthesis of adaptive tracking algorithms [18]. In this regard, the development of adaptive motion models that allow for the change in the dynamic characteristics of the tracked object during maneuvering is of considerable interest. One of the promising approaches to solving this problem is the use of the decomposition principle, which allows the complex motion of an object to be represented as a set of independent subsystems [31,32].

3 SYNTHESIS OF AN ADAPTIVE MODEL OF UNDERWATER OBJECT MOTION BASED ON THE DECOMPOSITION PRINCIPLE

Existing solutions to the problem of constructing a model, which are used in motion trajectory estimation systems, are based on the use of optimization methods, such as the Pontryagin maximum principle, which are highly complex due to the need to solve a high-dimensional two-point boundary value problem for conjugate variables.

Currently, in the theory of estimation, there is a tendency to develop optimal methods of synthesis that make maximum use of information about the physical properties of the object under study. Considering the physical characteristics of the system in the form of its invariants allows for significant progress in solving the problem of synthesizing effective tracking systems. The new synthesis method is based on the use of variational principles, which allows for representation of the object trajectory with a given kinetic energy as a solution to a boundary value problem [24]

$$\begin{cases} \dfrac{d}{dt}\left(\dfrac{\partial T}{\partial \dot{q}_s}\right)+\dfrac{\partial T}{\partial q_s}=\lambda^{-1}\left[\mu_s\left(q_s,\dot{q}_s\right)\dot{q}_s+\dfrac{\partial F}{\partial q_s}\right], & s=\overline{1,n}, \\ \left(A-T\right)+\lambda^{-1}F\Big|_{t_0}^{t_1}=0, & \end{cases} \tag{1}$$

where $\mu_s\left(q_s,\dot{q}_s\right)$ – a synthesizing function, obtained from the condition of the maximum of the generalized power function [23],

λ – Lagrange multiplier,

$T=T\left(\mathbf{q},\dot{\mathbf{q}}\right)$ – kinetic energy,

$A=\sum\limits_{s=1}^{n}\int\limits_{q_s(t_0)}^{q_s(t_1)}Q_s dq_s,\ s=\overline{1,n}$ – work of a priori unknown external forces Q_s,

$F=\left(\mathbf{z}-\hat{\mathbf{q}}\right)^T\mathbf{N}^{-1}\left(\mathbf{z}-\hat{\mathbf{q}}\right)$ – function, characterizing the accuracy of trajectory construction,

$\mathbf{z}(t)=\mathbf{q}(t)+\mathbf{v}(t)$ – observation vector,

$\mathbf{v}(t)\in R^n$ – interference vector in the observation channel,

$\mathbf{N}\in R^{n\times n}$ – diagonal matrix, characterizing the intensity of interference $\mathbf{v}(t)$ in the observation channel [33],

the ^ sign means estimates,

$\mathbf{q}(t)=\left[q_1(t),\,q_2(t),\ldots,q_n(t)\right]^T$ – vector of generalized coordinates, $\mathbf{q}\in R^n$.

The formal attribution of the entire energy of the object's motion to the work of generalized forces $Q_s\left(q,\dot{q}\right)$ for the case of principal coordinates allows the introduction of the simplest positively-defined quadratic form of generalized velocities, which is interpreted as the kinetic energy of the system

$$T=\frac{1}{2}\dot{\mathbf{q}}^T\mathbf{A}\dot{\mathbf{q}}, \tag{2}$$

where $\mathbf{A}(\mathbf{q})\in R^{n\times n}$ – symmetric diagonal matrix of quadratic form.

To find a solution to the boundary value problem (1), one of the possible approaches to solving problems of constructing motion models of controlled objects without using a linear approximation can be used – the decomposition principle [34]. The essence of this principle is to completely eliminate the dynamic mutual influence between the elements using an admissible vector of generalized forces, to bring the system to motion in the decomposition mode [31] in such a way that the system (1) moves in accordance with the control goal, providing a given value of the functional characterizing the accuracy of constructing the trajectory. This means that a nonlinear multi-connected dynamic system begins to move after a finite time interval due to the simplest system. This fact can be used when constructing a motion model of an underwater object [35]. The movement, when the work of the generalized control forces $A=0$, corresponds to the predicted movement and in the decomposition mode [32,36–37] the following is valid

$$T=\lambda^{-1}F,$$

or taking into account (2)

$$\dot{\mathbf{q}}^T\mathbf{A}\dot{\mathbf{q}}=\lambda^{-1}\left(\mathbf{z}-\mathbf{q}\right)^T\mathbf{N}^{-1}\left(\mathbf{z}-\mathbf{q}\right). \tag{3}$$

Consequently [34] the motion of the system is determined by a set of unrelated Lagrange differential equations and represents a combination of non-interacting subsystems [31]. Taking into account the relation (3), the following notations for spatial coordinates in 3-dimensional Euclidean space is introduced

$$x_1^{(j)}=q_s,\ x_2^{(j)}=\dot{q}_s,\ s=\overline{1,3},\ j\in\left[X,Y,Z\right],$$

then the motion model can be represented in vector form for each spatial coordinate [24]

$$\dot{\mathbf{x}}^{(j)}(t)=\mathbf{F}^{(j)}\mathbf{x}^{(j)}(t)+\mathbf{G}^{(j)}w^{(j)}(t),\ j\in\left[X,Y,Z\right], \tag{4}$$

$$\mathbf{F}^{(j)}=\begin{bmatrix}0 & 1\\ 0 & -\sqrt{\alpha^{(j)}}\end{bmatrix},\ \mathbf{G}^{(j)}=\begin{bmatrix}0\\ -\alpha^{(j)}\end{bmatrix}, \tag{5}$$

where $\mathbf{x}^{(j)}=\begin{bmatrix}x_1^{(j)}\\ x_2^{(j)}\end{bmatrix}$ – state vector,

$\mathbf{F}$ – state transition matrix,

$\mathbf{G}$ – disturbance vector,

$\alpha^{(j)}=\lambda^{-1}a_{ss}^{-1}N_{ss}^{-1},\ s=\overline{1,3},\ j\in[X,Y,Z]$ – adaptation parameter,

N_{ss} – elements of the diagonal matrix $\mathbf{N}$,

a_{ss} – elements of the diagonal matrix $\mathbf{A}$ of the quadratic form of kinetic energy,

$w(t)$ – white gaussian noise [21],

$$M\left[\mathbf{w}_k^{(j)}\cdot\left(\mathbf{w}_k^{(j)}\right)^T\right]=\mathbf{Q}^{(j)}\delta_k \tag{6}$$

where δ_k – Kronecker symbol,

$\mathbf{Q}$ – non-negative definite matrix of size 2×2.

Let us consider the formulation of the problem of estimating the spatial movement trajectory of the observation object in the operating zone of the LBL system.

The input data for the trajectory tracking algorithm are the position marks at each data reception cycle. A mark is understood to be three coordinates of the object $\left(x_1^X,x_1^Y,x_1^Z\right)$, obtained as a result of the primary processing of hydroacoustic signals [38]. As the observation model at time k for each coordinate of the object, we take:

$$\mathbf{z}_k^{(j)}=\mathbf{H}\mathbf{x}_k^{(j)}+\mathbf{v}_k^{(j)},\ j\in[X,Y,Z],\ k=\overline{1,K}, \tag{7}$$

where K – number of marks in the observed episode,

$\mathbf{H}=\begin{bmatrix}1&0\\0&0\end{bmatrix}$ – transition observation matrix,

$\mathbf{z}_k^{(j)}=\begin{bmatrix}z_{1,k}^{(j)}\\ z_{2,k}^{(j)}\end{bmatrix}$ – observation vector,

$\mathbf{v}_k^{(j)}=\begin{bmatrix}v_{1,k}^{(j)}\\ v_{2,k}^{(j)}\end{bmatrix}$ – vector of observation errors,

$$M\left[\mathbf{v}_k^{(j)}\cdot\left(\mathbf{v}_k^{(j)}\right)^T\right]=\mathbf{R}^{(j)}\delta_k, \tag{8}$$

$\mathbf{R}$ – non-negative definite matrix of size 2×2,

it is assumed that random processes $\mathbf{v}$ and $\mathbf{w}$ are independent

$$M\left(\mathbf{v}_k^{(j)}\left(\mathbf{w}_k^{(j)}\right)^T\right)=0,\ k=\overline{1,K}.$$

Thus, at each processing cycle for the tracked trajectories the following set of input data is generated:

- measured coordinate values obtained at the current processing cycle;
- estimates of coordinates and their change rates obtained at previous processing cycles;

Let us consider the problem of tracking the trajectory of an underwater object: at the moment of the *k*-th data reception cycle, estimate the values of each spatial coordinate $\hat{x}_{1,k}^{(j)}$ and the rate of its change $\hat{x}_{2,k}^{(j)}$.

4 MATHEMATICAL DESCRIPTION OF THE ALGORITHM FOR TRACKING THE TRAJECTORY OF AN UNDERWATER OBJECT

For smoothing and step-by-step extrapolation of the trajectory based on the results of observation of the motion parameters available for measurement, the Kalman filter is traditionally used, the structure of which is determined by the model (4), and for rectilinear uniform motion

$$\mathbf{F}=\begin{bmatrix}0&0\\0&1\end{bmatrix},\ \mathbf{G}=\begin{bmatrix}0\\1\end{bmatrix}. \tag{9}$$

The implementation of tracking systems using digital information processors implies the operation of estimation algorithms in discrete time, which leads to an algorithm for updating the estimates of the $\hat{\mathbf{x}}_k$ object in the form [25]

$$\begin{gathered}\hat{\mathbf{x}}_{k|k-1}^{(j)}=\mathbf{\Phi}^{(j)}\hat{\mathbf{x}}_{k-1}^{(j)},\\ \hat{\mathbf{x}}_k^{(j)}=\hat{\mathbf{x}}_{k|k-1}^{(j)}+\mathbf{P}_{k-1}^{(j)}\mathbf{H}^T\left(\mathbf{R}^{(j)}\right)^{-1}\left[\mathbf{z}_k^{(j)}-\mathbf{H}\hat{\mathbf{x}}_{k|k-1}^{(j)}\right],\\ \mathbf{P}_{k|k-1}^{(j)}=\mathbf{Q}^{(j)}+\mathbf{\Phi}^{(j)}\mathbf{P}_{k-1}^{(j)}\left(\mathbf{\Phi}^{(j)}\right)^T,\\ \mathbf{P}_k^{(j)}=\mathbf{P}_{k|k-1}^{(j)}-\mathbf{P}_{k|k-1}^{(j)}\mathbf{H}^T\left[\mathbf{H}\mathbf{P}_{k|k-1}^{(j)}\mathbf{H}^T+\mathbf{R}^{(j)}\right]^{-1}\mathbf{H}\mathbf{P}_{k|k-1}^{(j)},\\ j\in[X,Y,Z],\ k=\overline{1,K},\end{gathered} \tag{10}$$

where $\mathbf{R}^{(j)}=\begin{bmatrix}\left(\sigma^{(j)}\right)^2&0\\0&\left(\sigma^{(j)}\right)^2\end{bmatrix}$,

$\mathbf{P}_{k|k-1}^{(j)}$ – extrapolation error covariance matrix,

$\mathbf{P}_k^{(j)}$ – filter error covariance matrix,

$$\mathbf{Q}^{(j)}=\begin{bmatrix}\dfrac{\Delta t^3}{4}&\dfrac{\Delta t^2}{2}\\ \dfrac{\Delta t^2}{2}&\Delta t\end{bmatrix} \tag{11}$$

$$\mathbf{\Phi}^{(j)}=\begin{bmatrix}1&\Delta t\\0&1\end{bmatrix}\text{ – state transition matrix} \tag{12}$$

$\hat{\mathbf{x}}_{k|k-1}^{(j)}$ – extrapolated value of the state vector.

Δt – period of receipt of marks.

The Kalman filter works acceptably [21,22] in estimating the parameters of uniform rectilinear motion. However, the actual motion of underwater objects cannot be described with sufficient accuracy by the model (10) – (12). Numerous maneuvers determine the feasibility of using adaptive tracking algorithms. Let us consider the use of model (4), (5) in the procedure for synthesizing algorithm (10), which involves carrying out a procedure for its finite-dimensional approximation. The motion of an object in discrete time can be described by the equation [25]:

$$\mathbf{x}_k^{(j)}=\mathbf{\Phi}^{(j)}\mathbf{x}_{k-1}^{(j)}+\mathbf{\Gamma}^{(j)}w_{k-1}^{(j)},\ j\in[X,Y,Z],\ k=\overline{1,K},$$

where

$$\mathbf{\Phi}^{(j)}=\mathbf{I}-\mathbf{F}^{(j)}\Delta t,\quad \mathbf{\Gamma}^{(j)}=\int_{t_{k-1}}^{t_k}\mathbf{\Phi}^{(j)}\mathbf{G}^{(j)}d\tau,\ j\in[X,Y,Z],\ k=\overline{1,K}, \tag{13}$$

where $\mathbf{I}$ – identity matrix.

For small values of Δt equations (13) take the form [24]

$$\mathbf{\Phi}^{(j)}=\begin{bmatrix}1 & \Delta t\\ 0 & 1-\sqrt{\alpha^{(j)}\Delta t}\end{bmatrix},\ \mathbf{\Gamma}^{(j)}=\begin{bmatrix}\dfrac{\alpha^{(j)}\Delta t^{2}}{2}\\ \alpha^{(j)}\Delta t\end{bmatrix},\ j\in[X,Y,Z],\ k=\overline{1,K}. \qquad (13)$$

State noise intensity matrix:

$$\mathbf{Q}^{(j)}=\frac{1}{\Delta t}\mathbf{\Gamma}^{(j)}\left(\mathbf{\Gamma}^{(j)}\right)^{T}=\begin{bmatrix}\dfrac{\left(\alpha^{(j)}\right)^{2}\Delta t^{3}}{4} & \dfrac{\left(\alpha^{(j)}\right)^{2}\Delta t^{2}}{2}\\ \dfrac{\left(\alpha^{(j)}\right)^{2}\Delta t^{2}}{2} & \left(\alpha^{(j)}\right)^{2}\Delta t\end{bmatrix},\ j\in[X,Y,Z]. \qquad (13)$$

The obtained matrices (14) and (15) determine the structure of the adaptive tracking algorithm (10) based on model (4), which can be used to estimate the state vector of underwater objects.

5 MATHEMATICAL MODELING OF THE PROCEDURE OF TRAJECTORY DATA PROCESSING OF THE LONG BASE LINE SYSTEM

To determine the quality of the algorithm, a simulation was performed, using the example of the task of tracking the trajectory of an underwater object using an LBL system with acoustic beacons (Fig. 1). The system functions as follows: on the underwater object, the transceiver provides a request for an acoustic signal (A), and at least 3 acoustic beacons are submerged in a fixed position on the bottom. An acoustic signal is generated at time T_0, and is received by beacons (B), (C) and (D), which in turn emit an acoustic response signal (including a known response time ΔT), which the underwater object receives at times $T_{(B)}$, $T_{(C)}$ and $T_{(D)}$. After which the distance to each of the beacons is calculated considering the response time ΔT and the speed of sound in water [39]. The beacons are synchronized and transmit acoustic pulses at a set emission time T^E. GPS coordinates of three beacons $\left[X_{(B)},Y_{(B)},Z_{(B)}\right]$, $\left[X_{(C)},Y_{(C)},Z_{(C)}\right]$ and $\left[X_{(D)},Y_{(D)},Z_{(D)}\right]$ are known.

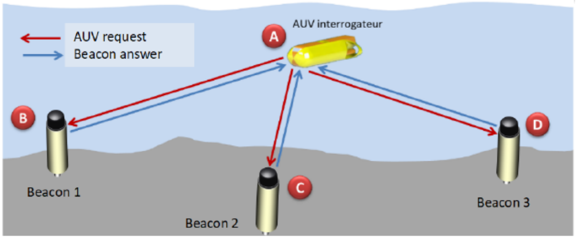

Figure 1 Illustration of the LBL acoustic system.

The underwater object must be synchronized with the same time reference of the beacons. Thanks to the acoustic transceiver on board the object, the acoustic pulses from the beacons are detected and recognized, comparing the arrival time T^A with T^E. Knowing the speed of sound in water V, which depends on the depth $\hat{x}_1^Z$ (Fig. 2), the distances $d_{(B)}$, $d_{(C)}$ and $d_{(D)}$ to the beacons are determined by the equation

$$d_{(n)}=\left(T_{(n)}^{A}-T_{(n)}^{E}\right)\cdot V\left(\hat{x}_1^Z\right),\ n\in[B,C,D]. \qquad (16)$$

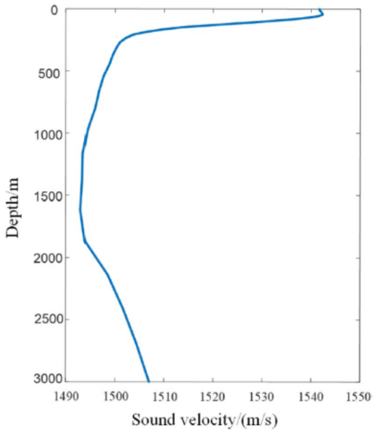

Figure 2 Dependence of the speed of sound on depth

After measuring the distance between the underwater object and three beacons, the absolute position can be calculated using the trilateration method [40]. The $z_{1,k}^X, z_{1,k}^Y, z_{1,k}^Z$ coordinates of an underwater object are determined by solving the equations for a sphere

$$\begin{cases}\left(X_{(B),k}-z_{1,k}^X\right)^2+\left(Y_{(B),k}-z_{1,k}^Y\right)^2+\left(Z_{(B),k}-z_{1,k}^Z\right)^2=d_{(B),k}^2,\ k=\overline{1,K},\\ \left(X_{(C),k}-z_{1,k}^X\right)^2+\left(Y_{(C),k}-z_{1,k}^Y\right)^2+\left(Z_{(C),k}-z_{1,k}^Z\right)^2=d_{(C),k}^2,\ k=\overline{1,K},\\ \left(X_{(D),k}-z_{1,k}^X\right)^2+\left(Y_{(D),k}-z_{1,k}^Y\right)^2+\left(Z_{(D),k}-z_{1,k}^Z\right)^2=d_{(D),k}^2,\ k=\overline{1,K}.\end{cases} \qquad (17)$$

Thus, the measured distances $d_{(B)}$, $d_{(C)}$ and $d_{(D)}$ to beacons (B), (C) and (D) determine the measured Cartesian coordinates $z_{1,k}^X, z_{1,k}^Y, z_{1,k}^Z$ of the underwater object, which are the input data of the tracking algorithm.

In the paper, a tactical episode that determines the trajectory of an underwater object depending on time is considered. The parameters of the object's motion are formed in such a way as to ensure the quality check of the tracking algorithm according to the criterion of the minimum standard deviation of estimates relative to the reference trajectory. The episode duration is 18 s, the period of receiving measurement data is $\Delta t = 0.1$ s. The trajectory of the underwater object was obtained using the MATLAB software package (built-in function *trajectory()* with the *waypoints* parameter) and is shown in figure 3.

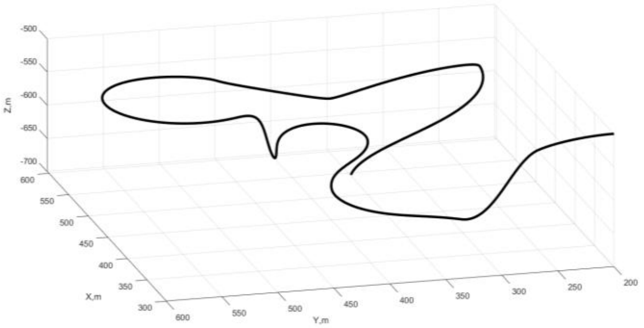

Figure 3 Model trajectory of an object in Cartesian coordinates.

The input data for the trajectory processing task are presented in the form of an array, containing the measured values of the Cartesian coordinates $z_{1,k}^{X}, z_{1,k}^{Y}, z_{1,k}^{Z}$, $k=\overline{1,K}$ the object, and the standard deviation $\sigma_{z_1^X}=\sigma_{z_1^Y}=\sigma_{z_1^Z}=60$ m (Figs. 4 and 5).

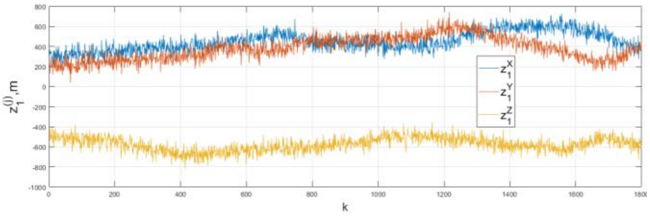

Figure 4 Measured coordinate values at Δt = 0.1 s.

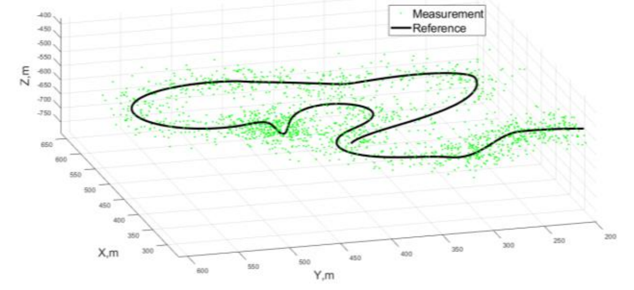

Figure 5 Trajectory marks at Δt = 0.1 s.

Based on statistical modeling, a series of numerical experiments were conducted to implement the classical Kalman filter (10) – (12) and the proposed algorithm (10), (14) – (15) with preliminary adaptation of the parameter according to the criterion

$$\varepsilon^{(j)} = K^{-1}\sum_{k=1}^{K}\left[\hat{x}_{1,k}^{(j)} - x_{1,k}^{(j)}\right]^2 \to \min,\ j\in\left[X,Y,Z\right], \qquad (18)$$

$$\alpha_{m+1}^{(j)} = \alpha_m^{(j)} + \eta_m^{(j)}\alpha_m^{(j)}\left(\frac{\left(\varepsilon\left(\alpha_m^{(j)}+c_m^{(j)}\right)-\varepsilon\left(\alpha_m^{(j)}-c_m^{(j)}\right)\right)}{2c_m^{(j)}}\right),\ j\in\left[X,Y,Z\right], \qquad (19)$$

where $\left\{c_m^{(j)}\right\}$ and $\left\{\eta_m^{(j)}\right\}$ – positive sequences such that

$$c_m^{(j)} \to 0$$

$$\sum_{i=0}^{\infty}\eta_i^{(j)} = \infty\ ,\ \sum_{i=0}^{\infty}\eta_i^{(j)}c_i^{(j)} < \infty\ ,\ \sum_{i=0}^{\infty}\left(\eta_i^{(j)}\right)^2\left(c_i^{(j)}\right)^{-2} < \infty\ .$$

An illustration of the process of adaptation of the algorithm (10), (14), (15) by the Kiefer-Wolfowitz method [41] for the parameter α^X is shown in figure 6.

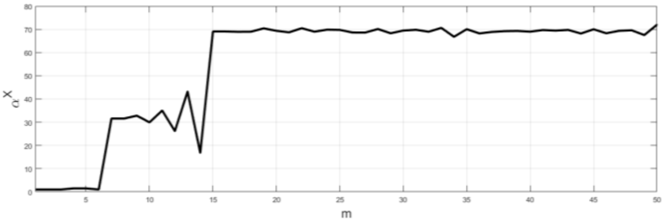

Figure 6 The process of adaptation of the proposed algorithm

Estimates of the trajectory on the interval of the considered tactical episode are presented in Figure 7.

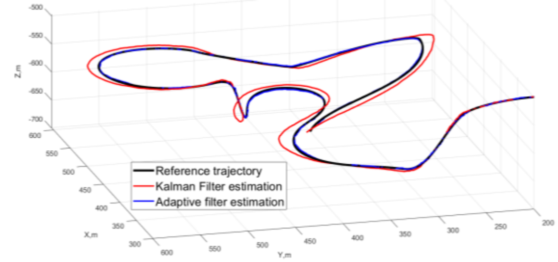

Figure 7 Estimates of the trajectory for $\sigma_{z_1^X}=\sigma_{z_1^Y}=\sigma_{z_1^Z}=60$ m, $\Delta t = 0.1\ s$, $\alpha = 70$

The black line indicates the true value of the coordinate, and the red and blue lines indicate the marks, obtained on the basis of the simulation data using a set of developed algorithms for estimating the Kalman filter and the adaptive algorithm, respectively. It was found that in certain sections of the trajectory, the proposed algorithm provides an increase in the accuracy of determining the X coordinate by 40%; the Y coordinate by 50%; the Z coordinate by 40% (Figs. 9–10). At the same time, over the entire observed interval, the mean square error of the coordinates estimated by the proposed algorithm is 15% lower, compared to the classical Kalman filter. This allows to state, that the adaptation of the parameters of the motion model allows to consider the dynamic characteristics of the motion of various classes of targets, compared to objects whose motion is uniform and rectilinear.

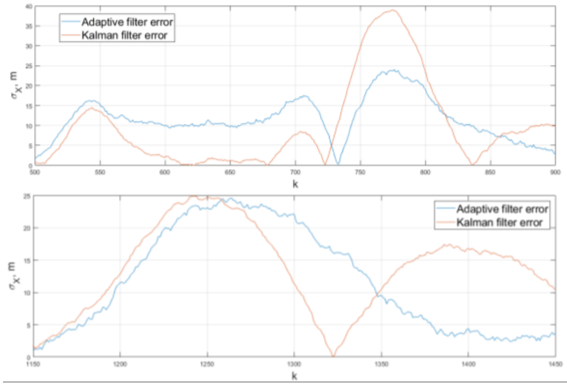

Figure 8 Average errors in estimating the X coordinate at maneuver intervals $k\in[500,900]$ and $k\in[1150,1450]$

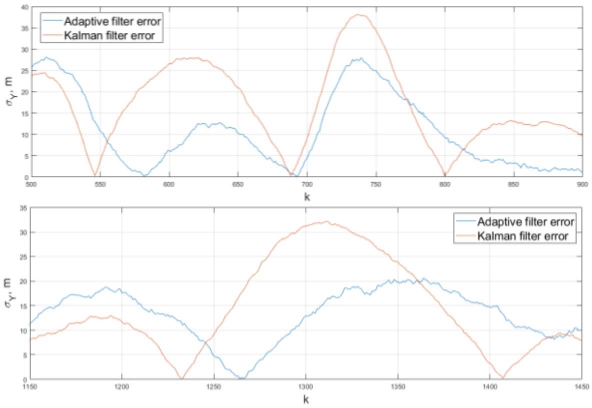

Figure 9 Average errors in estimating the Y coordinate at maneuver intervals $k\in[500,900]$ and $k\in[1150,1450]$

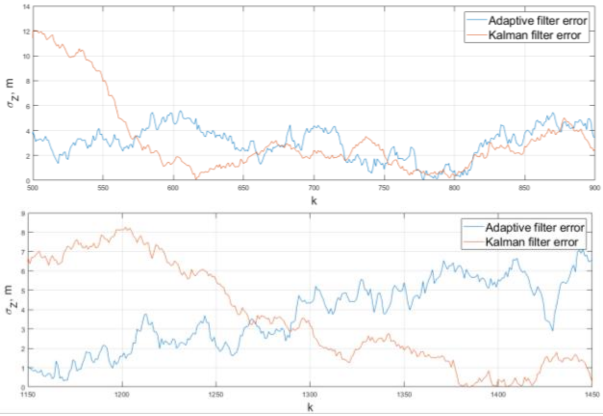

Figure 10 Average errors in estimating the Z coordinate at maneuver intervals $k \in [500, 900]$ and $k \in \left[1150, 1450\right]$

Analysis of the simulation results under various noise conditions demonstrates an increase in the accuracy of trajectory estimation by the adaptive algorithm in comparison with the Kalman filter for different values of the standard deviation of observation noise (figure 11).

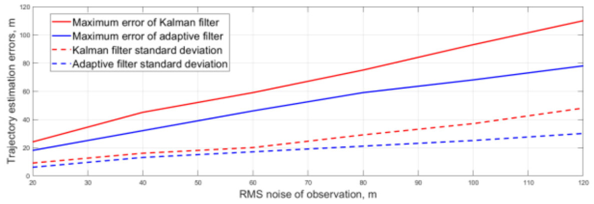

Figure 11 Averaged dependencies of the standard deviation of the trajectory estimate on the intensity of the observation noise

Figure 12 shows the trajectory estimates for different values of the measurement data receipt period.

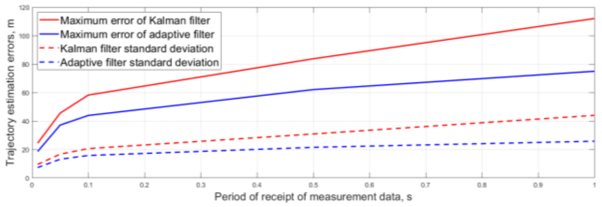

Figure 12 Dependence of the standard deviation of the trajectory estimate on the period of receipt of measurement data

In the considered tactical episode, the proposed algorithm allows to increase the accuracy of tracking the trajectory of an underwater object by an average of 5 – 20 % depending on the type of maneuver with the same computational costs as the traditional Kalman algorithm.

6 CONCLUSIONS

In the work, an algorithm for tracking objects based on acoustic positioning data using an adaptive motion model is synthesized, and its efficiency is analyzed using numerical simulation.

To improve the accuracy of trajectory parameter estimation, the model of a moving object obtained using the decomposition principle is adapted based on the Kiefer-Wolfowitz stochastic approximation procedure, which makes it possible to consider the dynamic characteristics of underwater object motion according to the acoustic positioning system data. Comparison of the efficiency of the proposed algorithm with the Kalman filter makes it possible to talk about an increase in the accuracy of estimating the Cartesian coordinates of a maneuvering underwater object in a wide range of observation noise intensity and different periods of measurement data receipt. The developed approach can serve as a basis for constructing a new class of algorithms for estimating the parameters of dynamic processes that consider physical laws using a particle filter, which ensures their fundamental appeal in a wide range of applied problems. In the future, it is planned to conduct research aimed at solving the problem of synthesizing hybrid algorithms for information processing based on the integrated use of the adaptive Kalman filter and neural networks through the implementation of a two-stage processing procedure:

- at the first stage, parametric adaptation of the mathematical model is performed using real datasets and synthetic data, characterizing typical modes of operation of the considered class of objects, which ensures that the regular properties of the model are taken into account and the power of the input data set is reduced for the second stage of processing;
- the second stage is associated with the construction of hybrid adaptive algorithms for information processing, that use the results of the first stage of processing and the accumulation of current data for training neural networks in real conditions, taking into account the non-stationarity of external and internal processes.

Preliminary studies by the authors show that the combination of adaptive algorithms for estimating motion parameters with neural networks provides increased accuracy of the spatial position of moving objects. The use of the neural network approach in this case is due to the ability to take into account a wide range of input data, such as the specified motion mode, the magnitude of the control action, the intensity and type of maneuver, the state of the environment, the operating mode and accuracy of the measuring system, and many others.

REFERENCES

[1] Yang Y., Liu Y., Sun D., Xu T., et al., Seafloor geodetic network establishment and key technologies. *SCES. Science China Press*, Vol. 63, No. 8, pp. 1188-1198, 2020.

[2] Wu L., Jing Z., Chen X., Li C., et al., Marine science in China: Current status and future outlooks. *Frontiers in Earth Science*, Vol. 29, No. 1, 2022.

[3] Li Z., Wang N., Liu A., Li A., et al., Progress of Geodesy Related Ionosphere from Chinese Scientists in the Period of 2019-2023. *Journal of Geodesy and Geoinformation Science*, Vol. 6, No. 3, pp. 115-123, 2023.

[4] Liu Y., Sun Y., Li B., Wang X., et al., Experimental Analysis of Deep-Sea AUV Based on Multi-Sensor Integrated Navigation and Positioning: 1. *Remote Sensing. Multidisciplinary Digital Publishing Institute*, Vol. 16, No. 1, p. 199, 2024.

[5] Yuanxi Y., Concepts of Comprehensive PNT and Related Key Technologies. *Acta Geodaetica et Cartographica Sinica*, Vol. 45, No. 5, p. 505, 2016.

[6] Yang Y., Li J., Xu J., Tang J., et al. Contribution of the Compass satellite navigation system to global PNT users. Chinese Science Bulletin. Vol. 56, No. 26, pp. 2813-2819, 2011.

[7] Xing Y., Wang J., Hou B., He Zh., et al., Underwater Long Baseline Positioning Based on B-Spline Surface for Fitting Effective Sound Speed Table. *Journal of Marine Science and Engineering (JMSE)*, Vol. 12, No. 8, p. 1429, 2024.

[8] Wu Y., Ta X., Xiao R., Wei Y., et al., Survey of underwater robot positioning navigation. *Applied Ocean Research*, Vol. 90, p. 101845, 2019.

[9] Liu Y., Li M., Liu Y., Chen G., et al., Sequential GNSS-Acoustic seafloor point positioning with modeling of sound speed variation. *Journal of Geodesy*, Vol. 97, No. 12, p. 115, 2023.

[10] Cario G., Casavola A., Gagliardi G. and Lupia M., Accurate Localization in Acoustic Underwater Localization Systems. *Sensors*, Vol. 21, No. 3, p. 762, 2021.

[11] Leonard J.J., Benett A.A., Smith C.M. and Feder H.J.S., Autonomous Underwater Vehicle Navigation. *Springer handbook of ocean engineering*, Vol. 98, No. 1, pp. 341–358, 2016.

[12] Wu P., Nie W., Liu Y., Xu T. Improving the underwater navigation performance of an IMU with acoustic long baseline calibration. *Satellite Navigation*, Vol. 5, No. 1, p. 7, 2024.

[13] Zhao S., Wang Z., He K. and Ding N., Investigation on underwater positioning stochastic model based on acoustic ray incidence angle. *Applied Ocean Research*, Vol. 77, pp. 69-77, 2018.

[14] Kebkal K.G. and Mashoshin A.I., AUV acoustic positioning methods. *Gyroscopy and navigation*, Vol. 8, No. 1, pp. 80-89, 2017.

[15] Zhang J., Han Y., Zheng C. and Sun D., Underwater target localization using long baseline positioning system. *Applied Acoustics*, Vol. 111, pp. 129-134, 2016.

[16] Yang H., Gao X., Huang H., Li B., et al., An LBL positioning algorithm based on an EMD–ML hybrid method. *EURASIP J. Adv. Signal Process*, Vol. 2022, No. 1, p. 38, 2022.

[17] Xiong K., Wei C. and Zhang H., Q-learning for noise covariance adaptation in extended KALMAN filter. Asian Journal of Control, Vol. 23, No. 4, 2020.

[18] Bauden M., Langer R., Kubjatko T. and Schweiger H.-G., Post-Processing Kalman Filter Application for Improving Cooperative Awareness Messages' Position Data Accuracy. *Sensors*, Vol. 24, No. 24, p. 7892, 2024.

[19] Konovalov A.A., Fundamentals of trajectory processing of radar information. Part 2. *St. Petersburg: ETU "LETI"*, p. 180, 2014.

[20] Risti B., Arulampalam M. and Gordon A., *Beyond Kalman Filters: Particle Filters for Target Tracking*. 2004.

[21] Bar-Shalom Y. and Li X.R., *Multitarget-multisensor tracking: principles and techniques*. Storrs: YBS Publishing, Vol. II, p. 615, 1995.

[22] Blackman S.S. and Popoli R.F., *Design and Analysis of Modern Tracking Systems*. Boston: MA: Artech House, p. 1229, 1999.

[23] Kostoglotov A.A., Method of Quasi-Optimal Synthesis of Control Laws Based on the Reduction of the Lagrange Problem to the Isoperimetric Problem Using Asynchronous Variation / A.A. Kostoglotov, S. V. Lazarenko. *Journal of Computer and Systems Sciences International*, Vol. 60, No. 6, pp. 843-852, 2021.

[24] Kostoglotov A.A. and Penkov A.S., Synthesis method of algorithms for dynamic state estimation of maneuvering objects based on quasi-optimal motion models using reduction of the Lagrange problem. *International Journal of Mechanics and Control*, Vol. 25, No. 2, pp. 77–85, 2024.

[25] Matveev V.V. and Raspopov V.Y., *Fundamentals of constructing strapdown inertial navigation systems*. St. Petersburg: JSC "Concern "TsNII "Elektropribor, p. 280, 2009.

[26] Conte G., Zanoli S.M., Scaradozzi D., et al., Robotics techniques for data acquisition in underwater archeology. *International Journal of Mechanics and Control*, Vol. 10, pp. 45-51, 2009.

[27] Kis L., Prohaszka Z. and Regula G., Calibration and testing issues of the vision, inertial measurement and control system of an autonomous indoor quadrotor helicopter. *International Journal of Mechanics and Control*, Vol. 09, pp. 1-10, 2008.

[28] Stevanovic I., Cosic A., Rodić A. and Rašuo, B., Biologically inspired design and hydrodynamic analysis of a remotely operated vehicle for river underwater tasks. *International Journal of Mechanics and Control*, Vol. 17, No. 1, pp. 13-22, 2016.

[29] Ambrozic L., Gorsic M., Slajpah S., Kamnik, R. and Munih, M., Wearable Sensory System for Robotic Prosthesis. *International Journal of Mechanics and Control*, Vol. 15, No. 1, pp. 269-275, 2014.

[30] Costa D., A Novel Class of Bio-Inspired Underwater Robots. *International Journal of Mechanics and Control*, Vol. 23, No. 2, pp. 23-36, 2022.

[31] Pyatnitsky E.S., The decomposition principle in the control of mechanical systems. *Reports of the USSR Academy of Sciences*, Vol. 300, No. 2, pp. 300-303, 1988.

[32] Kostoglotov A.A., Penkov A.S. and Lazarenko S.V., Structural-parametric synthesis of a tracking filter based on decomposition by the target functional with adaptation to trajectory disturbances. *Information measuring and control systems*, Vol. 19, No. 2, pp. 14-25, 2021.

[33] Kostoglotov A.A., Kuznetsov A.A. and Lazarenko S.V., Synthesis of a process model with non-stationary disturbances based on the maximum of the generalized power function. *Mathematical Modeling*, Vol. 28, No. 12, pp. 133-142, 2016.

[34] Pyatnitsky E.S., Synthesis of hierarchical control systems for mechanical and electromechanical objects based on the decomposition principle. I. *Automation and Telemechanics*, Vol. 50, No. 1, pp. 87-99, 1989.

[35] Kostoglotov A., Lazarenko S. and Pugachev I., Method of synthesis of multi-mode control under the expected uncertainty using the analysis of the phase-space decomposition on the basis of the generalized power maximum condition. *AIP Conference Proceedings*, Vol. 2188, p. 030005, 2019.

[36] Kostoglotov A.A., Penkov A.A., Lazarenko S.V. and Pavlov V.M., Analysis of the possibility of intellectualization of algorithms for estimating the parameters of dynamic systems based on adaptive model of motion. *Lecture Notes in Networks and Systems*, Vol. 330 LNNS, pp. 589-600, 2022.

[37] Kostoglotov A.A., Penkov A.S. and Lazarenko S.V., Synthesis method of adaptive algorithms for estimating dynamic systems parameters based on the decomposition principle and the methodology of the combined maximum principle: 4 (208). *News of higher educational institutions. North Caucasian region. Series: Natural sciences,* Vol. 4, No. 208, pp. 22-28, 2020.

[38] Konovalov A.A., Fundamentals of trajectory processing of radar information. Part 1. *St. Petersburg: ETU "LETI"*, p. 164, 2013.

[39] Es-Sadaoui R., Khallaayoune J. and Brizard T., Embedded acoustic long baseline localization system for autonomous underwater vehicles. *Indonesian Journal of Electrical Engineering and Computer Science*, Vol. 24, No. 3, pp. 1445-1453, 2021.

[40] Toky A. and Singh R., Localization schemes for Underwater Acoustic Sensor Networks - A Review. *Computer Science Review*, Vol. 37, p. 100241, 2024.

[41] Vazan M., *Stochastic approximation*. Moscow: Mir Publishing House, p. 298, 1972.

ISSN 1590-8844
International Journal of Mechanics and Control, Vol. 26, No. 2, 2025
https://doi.org/10.69076/jomac.2025.0023

SELECTION OF THE WORKING BODY OF THE SAILING WPP AND PROOF OF THE IMPLEMENTATION OF REVERSE OSCILLATION TO OBTAIN ELECTRIC CURRENT

Berik Mirzabayev*

* M. Auezov South Kazakhstan University, Taukehan street 5, 16000, Shymkent, Kazakhstan

ABSTRACT

At present, alternative energy, technologies are experiencing a dynamic stage of development, with wind energy playing a particularly significant role in reducing and potentially eliminating dependence on conventional energy sources that contribute to global warming. However, the stable performance of traditional turbine-based wind power plants typically requires wind speeds to remain steady and above 10 m/s. Consequently, ongoing research is focused on enhancing the efficiency of wind power systems to achieve a higher conversion rate of wind's kinetic energy into useful electrical power. This study introduces a low-capacity sail-type wind power plant (WPP). Unlike conventional WPPs, where rotor blades generate rotation primarily through aerodynamic lift, the sail-based configuration operates on a different principle. In this design, the working body undergoes oscillatory motion, converting wind energy into electricity by harnessing not only the lift force but also the drag force. Notably, the oscillatory motion of the working body is initiated at wind speeds as low as 2.5 m/s, which makes sail-type WPPs especially suitable for deployment in regions with varying or relatively moderate wind conditions.

Keywords**:** wind power plant, toroidal sail, dynamic model, parallel manipulator, computer modeling

1 INTRODUCTION

In the contemporary world, the environmental situation, increasingly aggravated by global climate change driven by excessive greenhouse gas emissions, underscores the urgent need to gradually abandon fossil fuels in favor of renewable energy sources (RES). Among the most accessible and promising options within this domain, wind energy stands out as a particularly viable alternative. According to current estimates, the total energy potential of wind flows near the Earth's surface exceeds global energy consumption by nearly twentyfold [1,2], which theoretically makes it possible to fully meet humanity's energy demands. Nevertheless, the challenge of efficiently converting the kinetic energy of wind into electricity remains highly relevant.

Systems designed for this purpose are generally referred to as wind power plants (WPP). The most widespread solutions are turbine wind power plants (TWPS), which operate with either a horizontal [3,4] or a vertical axis of rotation, including the well-known Darrieus and Savonius designs [5,6]. Recent research in wind energy has largely focused on the enhancement of TWPS. In particular, the following directions have gained momentum in recent years:

- Minimizing fluctuations in generated power output [7];
- Integrating big data technologies for environmental monitoring and adaptive control [8];
- Modernizing control systems through disturbance-based sensors and intelligent controllers [9];
- Advancing aerodynamic studies of blade profiles [10].

While these efforts provide valuable partial solutions, several critical technological barriers persist. For all types of TWPS, the following challenges remain unresolved:

- The inherent variability of wind speed and power;
- Abrupt directional shifts in airflow over short time spans;
- A relatively high cut-in wind speed (around 10 m/s) combined with a modest peak efficiency factor of approximately 0.3 [11–13].

Contact author: Berik Mirzabayev
M. Auezov South Kazakhstan University, Taukehan street 5, 16000, Shymkent, Kazakhstan
E-mail: berik.mirza@mail.ru

A noteworthy and promising development in recent years has been the introduction of small-scale sailing wind power plants (SWPP), equipped with automatic control mechanisms [14, 15]. These systems employ spatial oscillations with dynamically adjustable surface area exposed to airflow, combined with a specialized aerodynamic profile that is simultaneously sensitive to drag and lift forces. The core component of SWPS is a manipulator-converter (MC) developed based on the Sholkor parallel mechanism [16-17]. Owing to its unique topology, the MC enables the transformation of the spatial motion of the working body-comprising the sail, mast, and the manipulator's upper platform-into electrical energy, thereby paving the way for a new level of efficiency in wind energy systems.

2 EXPERIMENTAL

The sailing WPP consists of three components figure 1, which are: toroidal sail 11, mast 10 and platform manipulator 9. Toroidal sail is the working body of 11 sailing WPP. The Shape of the sail is toroidal. The reason for taking the shape of the sail as a toroidal shape is that it can knock out the kinetic energy of the wind from any direction and does not require special additional tools to turn in the direction of the wind, like a traditional WPP. Due to the structural feature of the toroidal sail, it converts the energy blown by the wind into oscillatory energy. The horizontal section of the toroidal sail is the same as the cross section of the Aircraft Wing, which is twisted by 18 degrees, and the shape is toroidal. The dimensions of the toroidal sail increase and decrease by a constant approximate. These measurements were tested in a virtual aerodynamic test and had a higher buoyancy and drag force compared to other toroidal sails. It is light in weight and solid in construction. The mast is a working body of 10 and connects the toroidal sail and the platform manipulator transducer. The format is made of solid material, light in weight, like a long rod. The bottom of the mast is rigidly connected to the moving side of the platform transducer. Depending on the wind speed, several toroidal sails are located along the mast and toroidal sails move up or down along the mast. Platform manipulator converter 9, named after Sholkor [10] is built on the basis of the platform manipulator. The sholkor platform manipulator differs from other platform manipulators in that in the Sholkor platform manipulator, 3-8 of the six engines can all work freely independently of each other, so this platform manipulator has six degrees of freedom of movement. The Sholkor platform manipulator was obtained for such properties as a platform manipulator converter for a sailing WPP [14]. The manipulator transducer (MT) consists of two platforms top 2 and bottom 1. the bottom platform 1 is rigidly connected to the ground layer, and the top platform 2 is movable. The upper and lower platform are connected to each other by six telescopic connections (cylinders) 3-8 with contact points A_1,B_1,C_1, and a_2,b_2,c_2. The toroidal sail converts the kinetic energy knocked out of the wind into oscillatory energy by MT into oscillatory energy, and MT converts oscillatory energy into electrical energy.

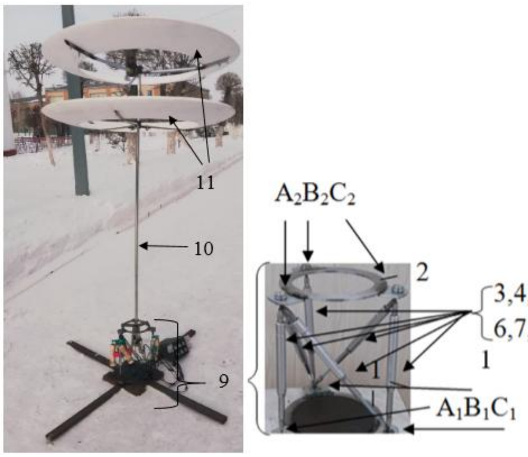

Figure 1 General view of the Zaboratory sailing wind power plant.

The main work of a sailing WPP is to convert the kinetic energy of the wind into electrical energy. That is, the working body of a sailing WPP converts the kinetic energy of the wind into vibrational energy, and vibrational energy into electrical energy MT. The work of a sailing WPP is directly proportional to the coefficient of beneficial effect of the working body, therefore, the choice of a toroidal sail is one of the main research works.

3 RESULTS AND DISCUSSION

3.1 SELECTION OF TOROIDAL SAILS FOR SAILING WPP

Nine types of sails were selected for laboratory selection of high-speed toroidal sails. The main part of it was a toroidal sail and a single ball-shaped sail. All sails were modeled in the SOLIDWORKS computer program Figure 2 and we obtained that the outer diameter of each lattice is equal to 7.5 meters. Simulated toroidal sails were tested on a virtual aerodynamic pipe by the computer program Autodesk Flow Design, Figure 3 shows the test progress of nine sails. Of the nine sails tested, only three toroidal sails had buoyancy and drag power. Of the other three toroidal sails, only one had high buoyancy and drag power. It was built on the basis of the wing profile of the aircraft P-II-14% (TsAGI-718)_[14] and had a toroidal sail with a cross-section of 18 degrees.

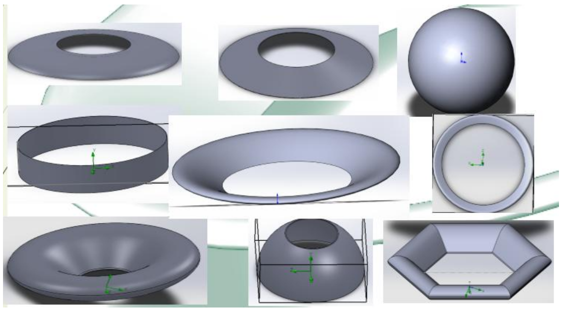

Figure 2 Types of sails modeled in the SolidWorks 2017 computer program.

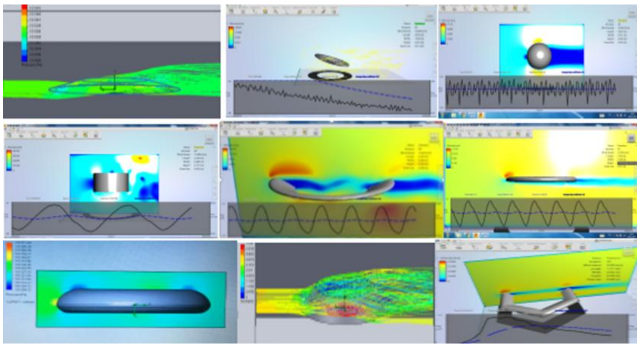

Figure 3 Autodesk Flow Design test course of sails on a virtual aerodynamic pipe

Since the working body of the sailing WPP performed oscillatory work, the following tests were carried out to determine the change in the lifting force and drag force of the selected toroidal sail at different turning angles. The computer program Autodesk Flow Design assumes that the toroidal sail selected in the virtual aerodynamic pipe is initially in a stable position in space, that is, at 0 degrees, and in this case the Test begins. In each subsequent test, we turn the position of the toroidal sail by 2 degrees, at the end of the test, the toroidal sail is turned by 16 degrees. During the test, we changed not only the position of the toroidal sail, but also the wind speed in the virtual aerodynamic pipe. The wind speed varies between 3 m/s, 5 m/s, 10 m/s, 15 m/s and 20 m/s. At each wind speed, the toroidal lattice is studied at all angles of rotation in space, blowing in the wind. Figure 4 shows the test progress of the toroidal lattice on the Autodesk Flow design virtual aerodynamic pipe.

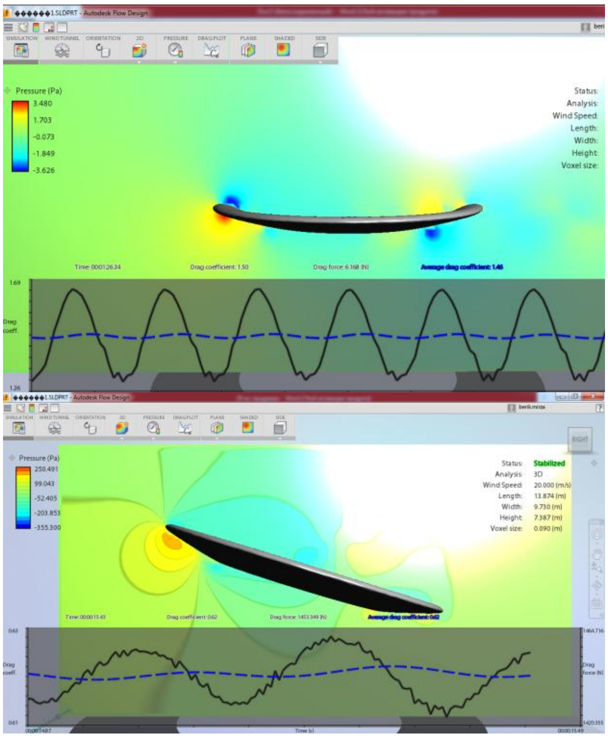

Time: 00:01:26.34 Drag coefficient: 1.50 Drag force: 6.168 (N) Average drag coefficient: 1.46

Time: 00:00:15.43 Drag coefficient: 0.62 Drag force: 1453.349 (N) Average drag coefficient: 0.62

Figure 4 The Test progress of the toroidal lattice in the Autodesk Flow design virtual aerodynamic pipe

The information from the test is transmitted as a color gamut on the left side of the program window, and the resistance force and the program automatically calculates resistance factor of the toroidal mesh being tested at the bottom of the program window. By placing the information obtained from the test in the table, in figures 5-6, we obtain a graph of the coefficient of resistance and resistance of the toroidal lattice in relation to the angle of rotation in space and wind speed.

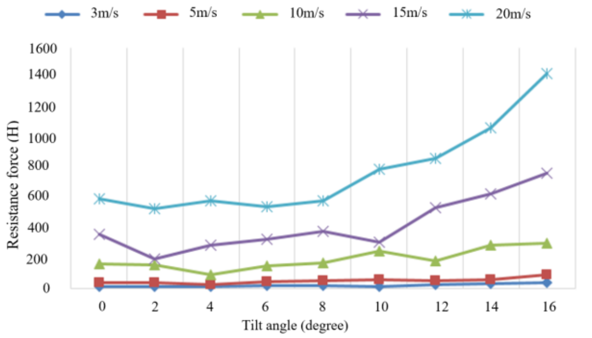

Figure 5 The resistance force of the toroidal lattice

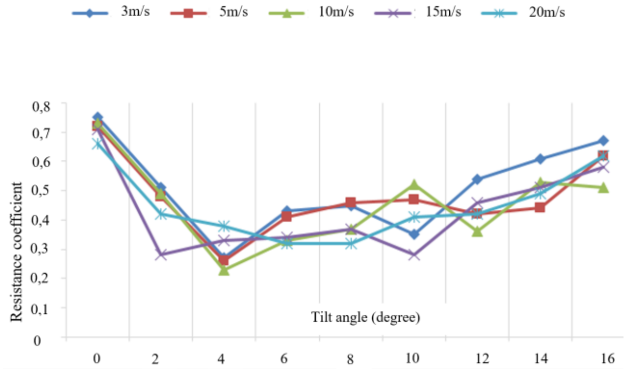

Figure 6 Resistance coefficient of the toroidal lattice

Looking at Figures 5 and 6 and comparing them with the color gamut in the program window shown in Figure 4, we can observe that the law governing the variation of aerodynamic drag and lift forces of the toroidal lattice is consistent with the ratio of drag to lift forces for aircraft wings described in aviation literature [14]. A computational test was performed in Autodesk CFD 2019 to demonstrate that the toroidal lattice generates lift and to additionally verify that, when it is deflected at a certain angle, the drag force increases while the lift force decreases. In Figure 7.A), the toroidal lattice was tested in a straight position within the plane. The resulting graph indicates that the lift force exceeded the drag force. In contrast, in Figure 7.B), the lattice was tilted backward at an angle of 15 degrees relative to the wind direction. The graph from this test shows that the lift force in the deflected position decreased, while the drag force became dominant. Based on these results, it was established that during the operation of the sailing WPP specifically, during the oscillation of the toroidal lattice a deflection of approximately 6 degrees from the Oz coordinate provides the maximum lift force while minimizing drag. When the deflection exceeds 6 degrees, the lift force decreases and drag increases. At this stage, due to the reduction in lift acting on the lattice, it naturally returns to its initial position. A manipulator transducer ensures the restoration of the working body to its original coordinate during oscillation.

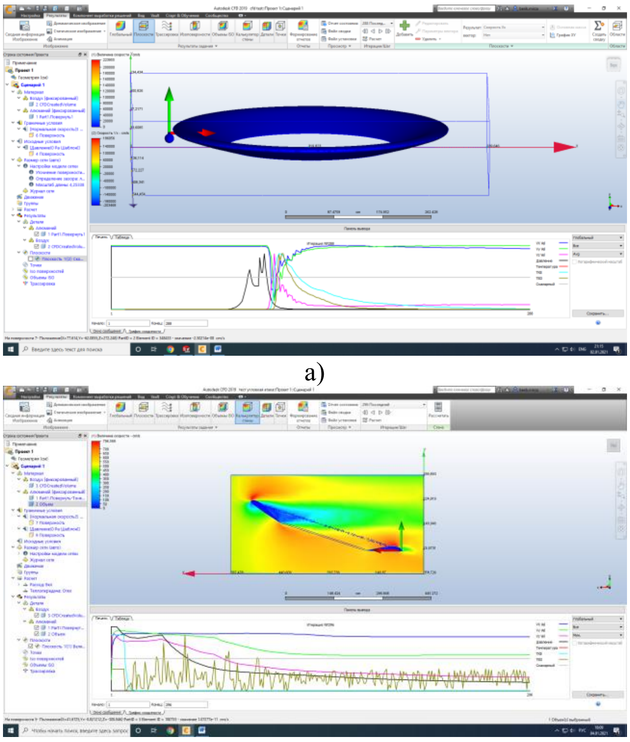
a)

b)

Figure 7 Progress of toroidal lattice testing in the computer program Autodesk CFD 2019.

3.2 The study of the regularity of changes in the speed of the network over time.

Due to the specifics of the principle of operation, coupled with the structural features of the sailing WPP, there is a need to study the wind speed in time. A sailing WPP oscillates over time with a certain period, and this period largely depends on the magnitude of the change in wind speed, that is, on the whim of the wind. The following articles provide graphs of changes in wind speed over time. Analyzing the same graphs, it was seen that the change in wind speed over time changes in wind speed according to the stiffness of the blow. If the average wind speed is in the range of 15-20 m/s [18], then the period of wind speed drop and increase oscillation oscillates about 1-2 times in 10 seconds in Figure 8, and if the average wind speed is in the range of 3-10 m/s [19-21] oscillates about 3-4 times in 10 seconds in figure 9.

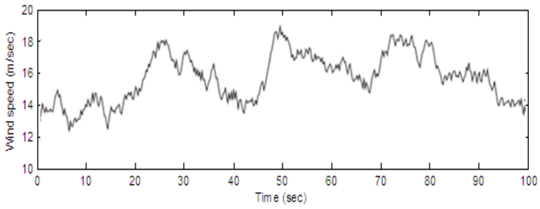

Figure 8 Wind oscillation pattern when the average wind speed is between 15-20 m/s.

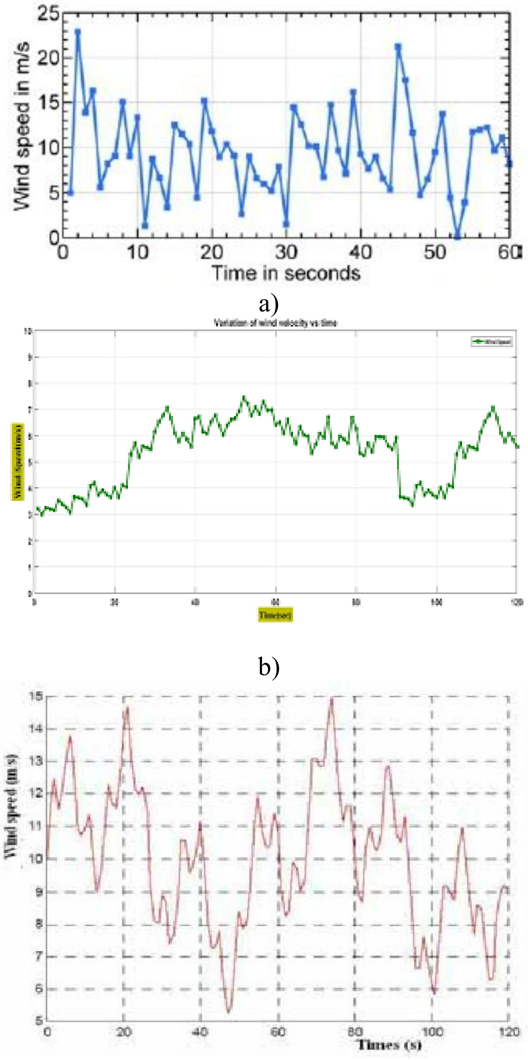

a)

b)

c)

Figure 9 Wind oscillation pattern when the average wind speed is between 3-10 m/s

Arine wind speed oscillations largely depend on the flatness of the Earth's crust. The more the Earth's crust is not flat, the more wind speed oscillates. Looking at the graph above, we determine the period of oscillation of a sailing WPP with a wind speed of 15-20 m/s or 3-10 m/s by the following formula.

$$T_1 = \frac{t}{N} = \frac{10}{2} = 5s$$

$$T_2 = \frac{t}{N} = \frac{10}{4} = 2.5s$$

The wind speed is 15-20 m/s, and the time is t=10s., if the oscillation number is N=2, the oscillation period is T_1 = 5s. The wind speed is 3-10 m/s, and the time is T=10s., the oscillation period is equal to T_2 = 2.5 s if the oscillation number is N = 4. This indicator indicates favorable conditions for the operation of a sailing WPP at low wind speeds.

4 DYNAMIC ANALYSIS OF THE OPERATION OF A SAILING WPP

Figure 10 shows the calculation scheme for the purpose of dynamic analysis of sailing WPP. The calculation scheme considers the issue of returning the sailing WPP to its original position after a deviation. We write a mathematical model of the operation of a sailing WPP only in a simplified and simplified form. This is because several nonlinear dynamic models that are related to each other characterize mathematical models of sailing WPP operation, and some nonlinear dynamic models have not yet found a problem with mathematical laws. At the same time, the phenomena of the relationship of the outer layer material and wind blowing of the working bodies of the sailing WPP have not yet found a complete solution.

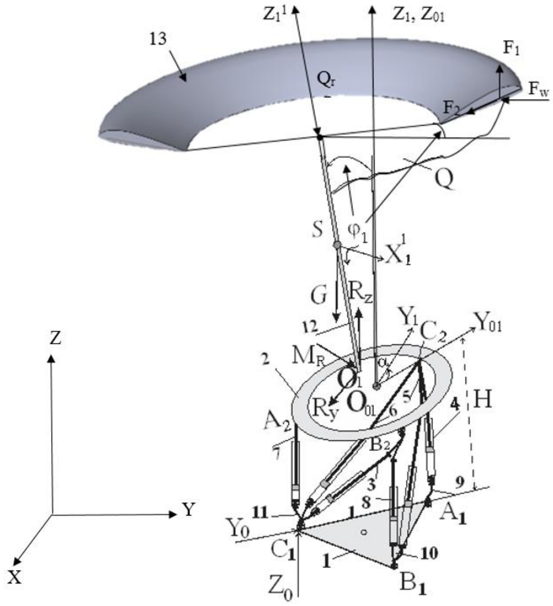

Figure 10 Calculation scheme

To derive a dynamic analysis of the working body, we take two coordinate systems. The stationary coordinate system is connected to the $C_1X_0Y_0Z_0$ stationary manipulator platform. The C_1Z_0 axis is directed vertically upwards, and the c1u0 axis runs along the c1a1 side. The head of the stationary coordinate system subsystem is associated with the initial position of O_{01} in the center of the moving platform of the manipulator. The axis $O_{01}Z_1$ is parallel to the axis C_1Z_0. To write a simplified mathematical model of a sailing WPP, we consider that the work of a sailing WPP located in space is being performed in one plane, which is a plane Q located in the plane $O_{10}Y_1Z_1$, Figure 10. The wind resistance force and wind lift force caused by the impact of the wind on a sailing WPP located in the Q plane, the force of gravity, the reaction force of actuators and the mast of the working body of the o1or O_1O_r are located. The total sum of the forces is concentrated in the mass centigrade S, which is located at a distance $O_1S = L$ from the coordinate head of the sailing WPP. The forces of wind action are located at a distance R from the coordinate head. The position of the $O_{10}Y_1Z_1$ plane depends on the direction of the wind speed and C_1Y_0 between the $O_{01}Y_{01}$ Oster with the c1u0 axis. $O_{10}Y_1Z_1$ makes a plane parallel motion in the plane and makes a circular motion along the $O_{01}X_1$axis parallel to the SX_1^1. The law of poinsettia performs the concentration of total forces at one point.

In a sailing WPP, the force of gravity F_a=m·g is affected by The Force F_{az}=m·g·sin(φ) sin(φ) at coordinate Z_1 and F_{ay}=m·g·cos(φ) at coordinate Y_1. The lifting force of the wind and the drag force vary depending on the speed of the wind and the position of the toroidal sail in space. Since the lifting force of the wind is directed vertically upwards, the lifting force F_1 of the wind is located along the coordinate Z_1. In addition, the wind resistance F_2 is located along the Y_1 coordinate. The lifting force and drag force of the wind are determined by formula 1 [14].

$$
\begin{aligned}
&F_1 = c_A \cdot \frac{1}{2} \cdot \rho \cdot S_P \cdot v_W^2, \\
&F_2 = c_W \cdot \frac{1}{2} \cdot \rho \cdot S_P \cdot v_W^2
\end{aligned}
\tag{1}
$$

here c_A, c_W, ρ, S_P, v_W the coefficient of lifting force of the wind, determined experimentally, is the coefficient of drag force of the wind, air density, surface volume of the toroidal Lattice and the average wind speed.

The force sum of the actuators returns the working body of a sailing WPP deviated from its coordinate at an angle φ to its original position. Therefore, the power direction of the manipulator transducer will be directly proportional to the direction of movement of the working body of the sailing WPP from the place F_{z1} to the starting position F_z along the plane Q, that is, perpendicular to the mast along the plane Q. We denote the force direction of MT as ΣN_i, and the complete mathematical model of MT is fully written in the article [14]. $O_{10}Y_1Z_1$ in connection with the development of a dynamic model of the operation of a sailing WPP in its plane and the operation of a sailing WPP in its plane, we have written three equations.

$$
\sum_{i=3}^{i=8} N_{ix} = 0; \qquad \sum_{i=3}^{i=8} M_x(\mathbf{N}_i) + M_{Rx} = 0;
$$

$$
\sum_{i=3}^{i=8} N_{iy} + R_y = 0; \qquad \sum_{i=3}^{i=8} N_{iz} + R_z = 0;
$$

In Equation 2 Y_1 sum of forces in coordinates, in Equation 3 Z_1 the equation of forces in coordinates and the equation of moment of forces in Equation 4 were written.

$$
m\frac{d^2 y_s}{dt^2} = \sum_{i=3}^{i=8} N_{iy} + R_y + F_{ay} - F_2 \tag{2}
$$

$$
m\frac{d^2 z_s}{d^2 t} = F_1 + \sum_{i=3}^{i=8} N_{iz} + R_z - F_{az} \tag{3}
$$

$$
J_{OX}\ddot{\varphi} = \sum_{i=3}^{i=8} M_x(\mathbf{N}_i) + M_{Rx} - F_2 \cdot R \tag{4}
$$

Where m- is the mass of the working body, y_s, z_s, φ the coordinates of the mass value and the maximum angle of departure of the working body from its own coordinate.

If we explain and complement the forces in the 2nd 3rd and 4th equations, we get the following 5th, 6th and 7th equations.

$$m\frac{d^2y_s}{dt^2}=\left(\sum_{i=3}^{i=8}N_{iy}+R_y\right)\cdot\cos(\varphi)+m\cdot g\cdot\cos(\varphi)-c_W\cdot\frac{1}{2}\cdot\rho\cdot S_P\cdot\left(\frac{dy_s}{dt}\right)^2 \qquad (5)$$

$$m\frac{d^2z_s}{d^2t}=c_A\cdot\frac{1}{2}\cdot\rho\cdot S_P\cdot\left(\frac{dy_s}{dt}\right)^2+\left(\sum_{i=3}^{i=8}N_{iz}+R_z\right)\cdot\sin(\varphi)-m\cdot g\cdot\sin(\varphi) \qquad (6)$$

$$J_{OX}\ddot{\varphi}=\left(\sum_{i=3}^{i=8}N_{ix}+R_x\right)\cdot L-c_W\cdot\frac{1}{2}\cdot\rho\cdot S_P\cdot\left(\frac{dy_s}{dt}\right)^2\cdot R \qquad (7)$$

The above equations are a complete dynamic model of the operation of a sailing WPP. The purpose of our work is to return to its place where it deviates from its coordinate to the limit point. The working body of a sailing WPP deviating from its coordinates is returned to its original position by a manipulator transducer.

MT Figure 11 consists of six actuators, three of which 4,8,7 are located vertically the other three are located diagonally 3,5,6. Vertically standing actuators are connected to the electric generator and, together with the remaining oblique actuators, return the working body deviated from its coordinate to its original position.

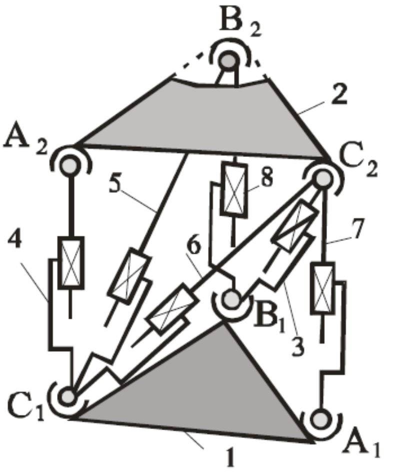

Figure 11 Platform manipulator analysis scheme

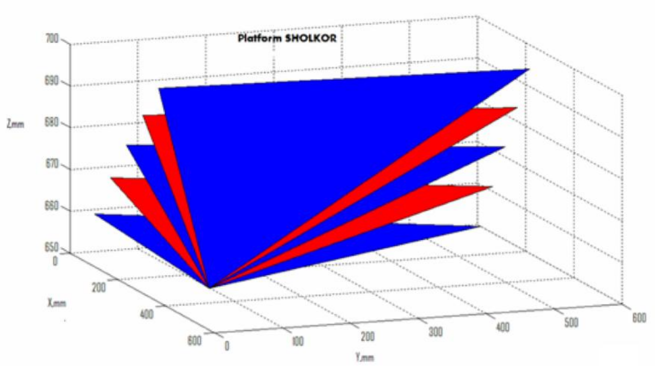

Figure 12 Graph of the displacement of the upper platform

Figure 12 shows one of the methods of displacement of the upper moving platform. Looking at figure 12, it can be seen that the actuators connecting the two platforms move the upper platform up and down separately, either vertically in pairs or alone. In this regard, we assume that the reaction force MT moves with the coordinate Z_1, since the projection force applied to the coordinate Y_1 is low, we get it equal to zero.

$$\sum N = k\cdot\Delta x \qquad (8)$$

Here: k – the coefficient of elasticity of the actuator,
x – break and decrease in the spring located on the actuator.

In formula (8), the reaction force of a vertically positioned actuator in the manipulator transducer is normally equal to the elastic force of the same actuator. If the elastic force of the actuator is insufficient, an additional spring compression force R is added.

To restore the working body of the sailing WPP from its deviated position back to the normal coordinate, we consider Equation (7). If the reaction force of the actuator exceeds the product of the wind resistance force and the lever arm of the toroidal lattice, the working body returns to its original position. Consequently, the condition for returning the deviated working body to its initial coordinate must satisfy Equation (9).

$$\left(\sum_{i=3}^{i=8}N_{ix}+R_x\right)\cdot L > c_W\cdot\frac{1}{2}\cdot\rho\cdot S_P\cdot\left(\frac{dy_s}{dt}\right)^2\cdot R \qquad (9)$$

Modeling equation 7 in Matlab and proving the theory of equation 9. To model equation 7 in Matlab, we bring equation 7 to equation 10 by simple mathematical processing.

$$\ddot{\varphi}=\frac{(k\cdot\Delta x+R_X)\cdot L-c_W\cdot\frac{1}{2}\cdot\rho\cdot S_P\cdot\left(\frac{dy_s}{dt}\right)^2\cdot R}{m\cdot L^2} \qquad (10)$$

Here: k=300, Δx=0.05м, L=1.5м, c_W=0.3, S_p=50м^3, R=2м ρ=1.293kg/m^3, m=4 kg. we get a value of.

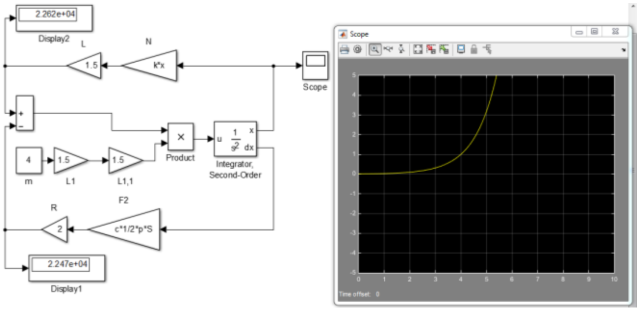

Figure 13 7 modeling the equation in the MATLAB computer program

In the figure 13, the process of returning the working body deviated from its coordinates to its place of the sailing WPP is shown in the position of a half-parabola graph raised to the top.

5 CONCLUSION

As the working element of the sail-type wind power system (SWPS), a novel toroidal sail was developed through aerodynamic investigations. This design is based on the R-II-14% (TsAGI-718) aircraft wing profile and incorporates a 18° twisted cross-section, providing enhanced lift characteristics while maintaining drag resistance. The resulting toroidal sail effectively converts the kinetic energy of the wind into oscillatory motion of the working body through its interaction with the mast and manipulator-transformer (MT). A mathematical dynamic model was established to describe the return-to-equilibrium process of the oscillating working body after displacement from its initial position. The moment of inertia during the reverse oscillatory phase of the SWPS was analyzed and verified using the MATLAB computational environment. The obtained graphical results clearly demonstrated the presence of reverse oscillations of the working element, thereby validating the theoretical assumptions.The findings confirm that the research objectives have been successfully achieved, providing a solid foundation for further development of advanced aerodynamic working bodies in sail-type wind power systems.

6 ACKNOWLEDGEMENTS

This research was funded by Non-public joint stock company "South Kazakhstan University named after M.Auezov, grant number: SKU2024-014 "Study of the integrated operation of a sailing wind power plant and a gas-petrol electric generator"

7 REFERENCES

[1] Tong W., Fundamentals of wind energy. *WIT Transactions on State of the Art in Science and Engineering*, vol. 44, pp. 3–48, 2010.

[2] Carbone G., Laribi M.A., Bouraoui T., Znaidi A., Benameur T., Moussa N.B., Zemzmi F., Ennetta R., Aifaoui N., PREFACE FOR THE SPECIAL ISSUE OF THE INTERNATIONAL JOURNAL OF MECHANICS AND CONTROL DEDICATED TO THE SIXTH INTERNATIONAL TUNISIAN CONFERENCE ON MECHANICS (COTUME 2023). *International Journal of Mechanics and Control,* 25 (2), pp. 1 – 2, 2024.

[3] Ye Z., Wang X., Chen Z., and Wang L., Unsteady aerodynamic characteristics of a horizontal wind turbine under yaw and dynamic yawing. *Acta Mechanica Sinica*, vol. 36, no. 2, pp. 320–338, 2020.

[4] 3 Shkara Y., Cardaun M., Schelenz R., and Jacobs G., Aeroelastic response of a multi-megawatt upwind horizontal axis wind turbine (HAWT) based on fluid-structure interaction simulation. *Wind Energy Science*, vol. 5, no. 1, pp. 141–154, 2020.

[5] Gitifar S., Zahedi R., Ziaie S., Mirzaei A. M., and Forootan M. M., Reviewof different vertical axis wind turbine modeling methods. *Future Energy*, vol. 3, no. 1, pp. 23–33, 2024.

[6] Didane D. H., Maksud S. M., Zulkafli M. F., Rosly N., Shamsudin S. S., and Khalid A., Performance investigation of a small savonius-darrius counter-rotating vertical-axis wind turbine. *International Journal of Energy Research*, vol. 44, no. 12, pp. 9309–9316, 2020.

[7] Dhoska K., Dumishllari E., Sulejmani A., Çejku M., Koça O., ASSESSING ENERGY CONSUMPTION IN PRIVATE RESIDENTIAL BUILDING AREA. *International Journal of Mechanics and Control*, 25 (1), pp. 3 – 8, 2024

[8] Canizo M., Onieva E., Conde A., Charramendieta S., and Trujillo S., Real-time predictive maintenance for wind turbines using big data frameworks. *IEEE International Conference on Prognostics and Health Management (ICPHM),* pp. 70–77, 2017.

[9] Cheon J., Kwon S., and Choi Y., Design of a pitch controller using disturbance accommodating control for wind turbines under stochastic environments. in *IEEE 23rd International Symposium Industrial Electronics (ISIE), IEEE*, Istanbul, Turkey, pp. 2572–2577, 2014.

[10] Sholanov K.S., Abzhaparov K.A., Zhumasheva Zh.T., Ceccarelli M.. A new parallel manipulator hydraulically actuated. *International Journal of Mechanics and Control,* Vol. 17, No. 01, pp 49-57. 2016.

[11] Traiteur J. J. and Roy S. B., Impacts of wind farms on weather and climate at local and global scales. *in Alternative Energy and Shale Gas Encyclopedia. Wiley*, pp. 88– 103, , 2016.

[12] Dai K., Bergot A., Liang C., Xiang W.-N., and Huang Z., Environmental issues associated with wind energy—a review. *Renewable Energy*, vol. 75, pp. 911–921, 2015.

[13] Sholanov K. S., Kabanbayev A., and Abzhaparov K. M., Study and selection of parameters of automatically controlled wind power station with swaying sails, *International Journal of Renewable Energy Research*, vol. 11, no. v10i2, pp. 723–737, 2020.

[14] Sholanov K. S., Mirzabayev B. I., and Ceccarelli M., Expansibility of electric power production by sail wind power stations, *International Journal of Mechanics and Control,* vol. 22, no. 2, pp. 117–126, 2021.

[15] Sholanov K., Omarov A., and Ceccarelli M., Improving efficiency of converting wind energy in modified sail wind power station. *International Journal of Mechanics and Control*, vol. 23, no. 2, pp. 101–110, 2022.

[16] K. S. Sholanov, Parallel Manipulators of Robots: Theory and Applications, *Springer*, p. 164, 2020.

[17] Toibekov Z., Baigabylova D., Markabaeva D., Mirzabayev B., Automatic system of generation of electricity of autonomous wind power plant with sailing working body. *E3S Web of Conferences*, 614, art. no. 01005, 2025.

[18] Dr.Emad Q. Hussien, AN OPTIMAL DESGSIN FOR VARIABLE SPEED WIND TURBINES BASED ON LQG. *The Iraqi Journal For Mechanical And Material Engineering*, Vol.14, No1, 2014.

[19] Akshay Kumar Saha; Rudiren Pillay Carpanen, Characterisation of wind speed series and power in Durban. *J. energy South*. Afr.vol.28, n.3, Cape Town, Aug. 2017.

[20] Hemanth Kumar M. B.6 and Saravanan B., Impact of global warming and other climatic condition for generation of wind energy and assessing the wind potential for future trends. *Innovations in Power and Advanced Computing Technologies (i-PACT)*, Vellore, pp. 1-5, 2017.

[21] Belakehal, S., Benalla, H., Bentounsi, A., Power maximization control of small wind system using permanent magnet synchronous generator. *Revue des Energies Renouvelables*, Vol. 12 N°2 pp. 307 – 319, 2009.

ISSN 1590-8844
International Journal of Mechanics and Control, Vol. 26, No. 02, 2025
https://doi.org/10.69076/jomac.2025.0024

AN ENGINEERING STUDY OF THE HUMAN PELVIS USING MODELS AND DATA FROM THE LITERATURE

Gabriella Eula*, Federico Gorraz**, Luigi Mazza*, Terenziano Raparelli*
* Department of Mechanical and Aerospace Engineering, Politecnico di Torino, Torino, Italy
** Cogne Acciai Speciali S.p.A, Italy

ABSTRACT

The paper presents a human pelvis study, building on data and methods sourced from the literature. The study provided a better understanding of the main pelvic parameters, including Sagittal Pelvic Thickness (SPT), that can be applied in designing industrial trunk support exoskeletons and their test benches. In addition, the study improved on the methods presented in the literature by developing models capable of calculating various human pelvic dimensions from different data. Electronic spreadsheets were also developed to calculate SPT from a variety of available information. Trigonometric methods proposed in the literature were used to calculate SPT, and the results were compared with those obtained from literature data. This study will make it possible to optimize the pelvis simulator in the Politecnico di Torino Department of Mechanical and Aerospace Engineering (DIMEAS) industrial exoskeleton test bench prototype. This prototype replicates the human body by means of a trunk simulator and a pelvis simulator which currently has a non-adjustable SPT. As a result of the study, a new pelvis simulator can be designed with provision for anthropometric adjustments to simulate different adult human bodies. This information will also be used to design and construct a human pelvis model featuring all its geometric parameters.

Keywords: human pelvis analysis; human pelvis geometrical characteristics; calculation methods for human pelvis dimensions; human pelvis study for industrial exoskeleton trunk design; engineering methods to study human pelvis.

1 INTRODUCTION

Wearable exoskeleton design entails extensive testing. The prototype must be tested for functionality, performance and wearer safety. It is also necessary to carry out a risk analysis [1-3]. Exoskeleton performance is also studied to prevent joint strain or chafed skin [3]. Performance metrics must be compared with the baseline for human subjects not wearing the exoskeleton. Test benches are often designed to test a single exoskeleton performance characteristic, e.g., flexural strength, actuators, resistance limits of joints or structural elements, etc. In some cases, dummies are used to replicate human features, size and body weight [4].

A number of rehabilitation and industrial exoskeleton prototypes have been designed and constructed at the Politecnico di Torino Department of Mechanical and Aerospace Engineering (DIMEAS) [5-8].Work on designing a test bench for industrial trunk support exoskeletons started in 2019. While design initially focused on a test bench featuring a trunk simulator, it became apparent that an appropriate pelvis simulator was also needed, with provision for anthropometric adjustments to simulate different adult exoskeleton wearers. Accurate measurement of pelvic parameters is essential in many clinical and research fields and is particularly important in this case in the optimization of a prototype test bench for industrial exoskeletons [9-15]. Among these parameters, the line connecting the axis of the femoral head and the midpoint of the sacral plate, on the sagittal plane (defined as sagittal pelvic thickness or SPT), plays a crucial role in understanding the anatomical variations of the pelvis and in practical application in the industrial context. This study aims to calculate the value of the SPT through two distinct methods: the use of values from the literature and the calculation based on a geometric transposition of the pelvis, integrating additional pelvic parameters and using trigonometric methods from the

---

Contact author: Gabriella Eula[1]

[1] Dept. of Mechanical and Aerospace Engineering, Politecnico di Torino, Torino, Italy
E-mail: gabriella.eula@polito.it

literature [9-21]. The data analysis was conducted on a representative sample, presenting the results in the form of mean, standard deviation and maximum and minimum values for three confidence intervals. Before proceeding with the analysis, several case studies and scientific articles were examined, from which the pelvic parameters necessary for the calculation were extracted. This research not only aims to provide a precise definition of the SPT but also to contribute to the existing literature with empirical data that can be used for future scientific investigations. The combination of tabular and geometric methods [9-21] offers a potentially more accurate perspective for the measurement of this parameter, ensuring a comparison between different assessments and increasing the probability that the defined range reflects real values. The examination of the SPT involved a lot of parameters and methods, both experimental and numerical [11, 12, 14-16]. The parameters were often analysed using standing radiographic imaging then compared with normal subjects. All the main study carried out on the human pelvis demonstrate that SPT and S1 (sacral tilt) can be considered reflecting the action lever arm of the spinopelvic muscles and capable of expressing the ability of the subject to compensate a possible sagittal unbalance. The study presented here is useful both as an engineering study of the human pelvis and in improving the DIMEAS exoskeleton test bench. In fact through these considerations and literature data and methods elaboration, authors succeeded to know the proper SPT range variation that allows to realize in the DIMEAS test bench a pelvis simulator with important anthropometric regulations. In the future, it will be possible to interact with doctors involved in these studies, but always with engineering-based research purposes in mind. The human pelvis represents a crucial link between the upper and lower body, and it plays a key role in trunk motion and in the static and dynamic balance of the entire body. Therefore, future interactions with doctors will be important both to improve knowledge of this part for balance and rehabilitation, including cerebral rehabilitation, and to better design exoskeletons to assist the trunk. To date, the study of the pelvis has focused mainly on data and literature research in order to allow the authors to improve their knowledge and engineering modeling for subsequent interdisciplinary studies.

2 AIM OF THE STUDY

The study analyzes the range of variation in the Sagittal Pelvic Thickness (SPT) of adult subjects in order to determine pelvis simulator dimensions. The DIMEAS test bench prototype is pneumatically controlled (Figures 1). Hip joint (H) and the lumbo-sacral joint (L) axis are separate, as in the physiological human pelvis.

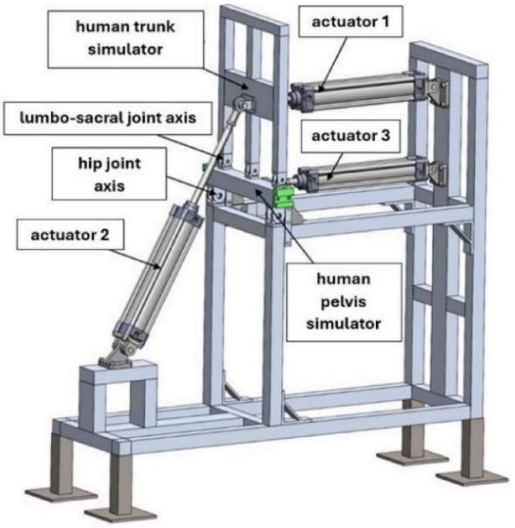

Figure 1a A scheme of the DIMEAS exoskeleton test bench prototype.

Figure 1b Some details of the current pelvis simulator.

Figure 1c Photographs of test bench in operation.

Pneumatic actuator 3 moves the pelvis simulator during trunk flexion and extension, while cylinders 1 and 2 respectively simulate the trunk weight effect and muscle action during trunk movement. The pelvis simulator features two flat hinges, simulating joints H and L. The current SPT value is 102 mm and it is a fixed dimension.

3 MAIN GEOMETRIC PARAMETERS

The main pelvis nomenclature for the human pelvis study is shown in Table I. These parameters are illustrated in Figure 2. Specifically, parameters include: length of S1 (line joining the anterior and posterior sacral plate points); offset of S1 (the distance between the femoral head axis and the midpoint of the sacral base S1 projection on the horizontal); pelvic angle (between the pelvic radius and the vertical through the femoral head axis; pelvic radius (line joining the center of the femoral head to the posterior point of the sacral plate); angle α_1 (the complementary angle to pelvic incidence) [9,10]. Several values are directly linked to SPT. They include: PI (the angle between the perpendicular to the sacral plate at its midpoint and line connecting this point to the femoral head axis); SS (sacral angle [10] between the sacral plane and the horizontal); PT (angle between SPT and the vertical through the femoral head axis; PR-S1 (Jackson's angle [11] or pelvic lordosis), angle between the sacral plate plane and line joining the sacral plate posterior point and the femoral head axis.

Table I – Main pelvis nomenclature

Name	Abbreviation
Sagittal pelvic thickness	SPT, PTH
Pelvic incidence	PI
Pelvic tilt	PT
Pelvic angle	PA
Sacral angle	SS
Jackson's angle	PR-S1, α_2
Half of the length of vertebra S1	d
Pelvic radius	PR
Overhang or offset of vertebra S1	OVS1, PO
Femoral head diameter	D
Femoral axis	HA
SPT projection on the vertical	A, DYp
SPT projection on the horizontal	B, DZp
Length b + length d	c
Complement of PI	α_1
Lumbar lordosis angle	LLA, LL
Sacropelvic angle	PSA
Lumbosacral angle	LSA
Sacral tilt	S1

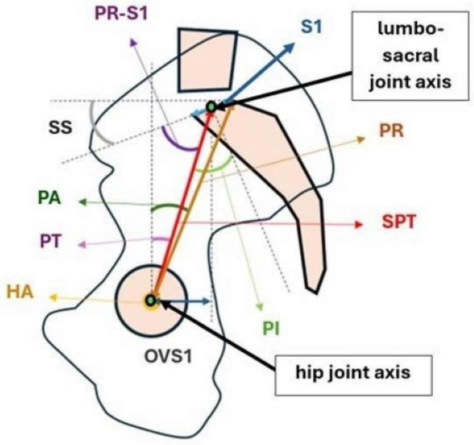

Figure 2 Main nomenclature.

3.1 FACTORS INFLUENCING SPT

As a number of studies [9,12-22] have shown, SPT is influenced by pathologies, age, gender and ethnicity. Analysis of many lateral radiographs of the pelvis has shown how pathologies such as lumbago and spondylosis can influence pelvic incidence, Jackson's angle and the length of vertebra S1. Significant changes in pelvic incidence and Jackson's angle (α_2) also lead to a significant changes in SPT. Pelvic thickness is around 130 mm for healthy subjects and those with relatively minor pathologies, with a pelvic incidence of around 50° and Jackson's angle from 32° to 38° and PI between 60° and 70° (PR-S1 between 17° and 25°), corresponding to an SPT between 108 and 116 mm for subjects affected by more serious pathologies [16]. Several studies have addressed changes in pelvic parameters as a function of the subjects' age, using computed tomography to determine pelvic incidence, pelvic thickness and vertebra S1 width. With advancing age, pelvic incidence increases, while sagittal pelvic thickness decreases. Japanese researchers have also analyzed the increase in pelvic incidence with age using linear regression equations to evaluate subjects' parameters [10,13,14]. Studies have investigated differences between men and women with respect to fundamental pelvic parameters [9-11]. One such study evaluated a group of subjects [11] consisting of 55 men and 53 women. For the men, average age was 49.3 ± 30.1, height 166.0 ± 11.4 cm, and body weight 63.3 ± 16.6 kg, while for the women, average age was 49.1 ± 29.6, height 151.9 ± 12.1 cm, body weight 52.4 ± 14.6 kg. The study found no substantial difference between males and females for all examined parameters, though on average SPT was relatively higher in women considering the difference in body height in particular [11]. In another study [13], radiographic measurements were taken with subjects aged between 18 and 80 years belonging to different ethnic groups across five countries (France, Japan, United States, Singapore and Tunisia). It was found that pelvic parameters vary considerably among ethnicities. SPT was higher among the Asian population than among Arabo-Bèrbère subjects, while Caucasians had a higher pelvic incidence than Asians [9-16].

4 STATE-OF-THE-ART: PELVIS ANALYSIS METHODS IN THE LITERATURE

Some pelvis analysis methods from the literature are presented. In one method, radiographic angles were measured for pelvic incidence [17,20], vertebra S1 offset, and pelvic tilt, which can provide a tool for calculating SPT and sagittal balance. Trigonometric models have also been used to determine pelvic radius and Jackson's angle [12], where sometimes the pelvic thickness is the hypotenuse of a triangle formed by a and b (Figure 3). Geometric relations for calculating SPT as a function of the other parameters developed using Figure 3 will be illustrated in the following sections. Standing lateral radiographs can also be used to calculate SPT from the pelvic radius and PR-S1 defined by Jackson in his studies of 1998,18 200019 and 2003,20 analyzing pelvic morphology (pelvisacral angle, pelvic incidence, and pelvic lordosis) and calculating the combined angles. In a 2005 study [14] two different methods were used to determine the relationship between sagittal pelvic thickness and pelvic incidence in 12 subjects, and the results of each method were compared. The first method consisted of direct anatomical measurement of incidence and thickness by means of an electromagnetic system. The second method used measurements from radiographs in the sagittal plane.

In a study from 2006 [21] pelvic parameters were measured on standing lateral radiographs of 145 adults without vertebral problems and 35 adults with spondylosis in order to assess sagittal spinal balance. Specifically, pelvic thickness was determined by calculating pelvic incidence (PI) and Jackson's angle (PR-S1), defining angles α_1 and α_2. Sagittal spinal balance has also been assessed using the pelvic radius technique [17]. In this case, pelvic radius and Jackson's angle were analyzed in 75 healthy subjects, 75 subjects with spondylolisthesis, 194 subjects with spinal deformity, and 60 subjects with scoliosis, for a total study population of 40

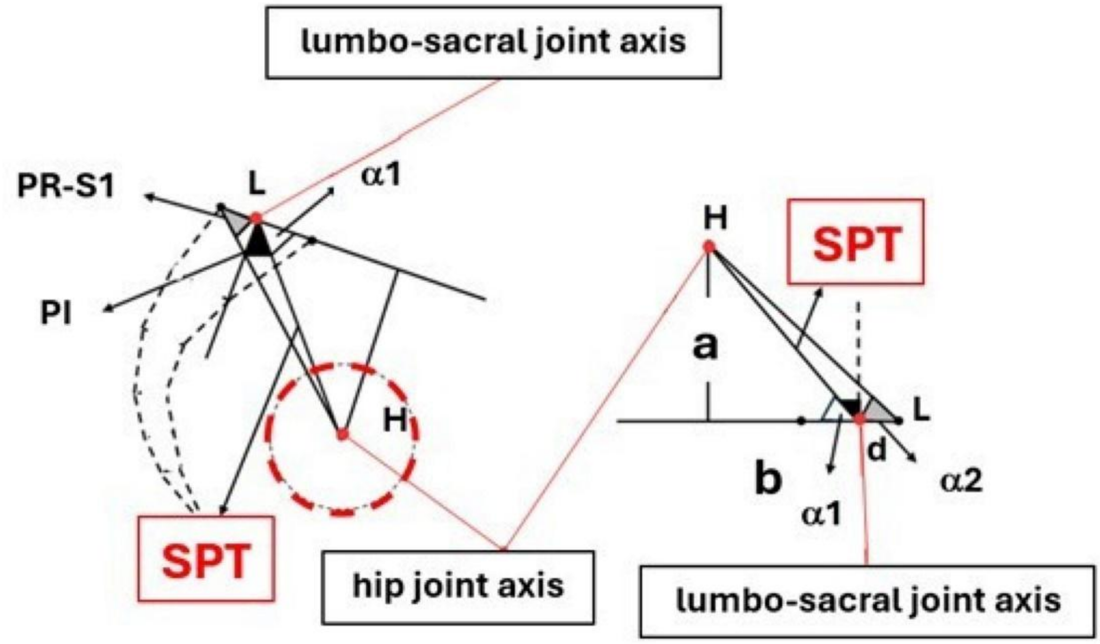

Figure 3 Details of the trigonometric method [12].

The study cites a number of published measures: Jackson et al. (1998) with N = 50, age 39.4 ± 9.5, PR (mm) 135 ± 8.6, PRS1 (°) 31.2 ± 7.9; Jackson et al. (2000) with N = 20, age 46, PRS1 (°) 31± 8.7; Jackson et al. (2003) with N = 75, age 39, PR (mm) 136,8 ± 8.9, PRS1 (°) 30.9 ± 9.8; Legaye (2007) with N = 145, age 40.7 ± 18.7, PRS1 (°) 35.2 ± 9.6.

Studies carried out by Japanese researchers [13] use linear regression equations to determine correlations among radiographic parameters in order to support the hypothesis that pelvic incidence increases with age. The study cohort consisted of 126 healthy adult volunteers (without spinal pathologies), 30 males and 96 females, aged between 20 and 69 years, for an average age of 39.4 years. These equations will also be used by the present authors. S1 offset and the pelvic tilt angle were also indicated. A 2022 study [22] compared pelvic parameter measurements from 43 subjects affected by spondylosis before and after they received spondylodesis. The following parameters were measured to evaluate sagittal lumbar alignment: segmental lordosis (SL); ventral (vDH) and dorsal (dDH) disc height as distances of the ventral and dorsal edge of the treated vertebral disk; lumbar lordosis (LL); pelvic incidence (PI); pelvic tilt (PT); and sacral slope (SS). A study published in 1998 [16] measured anatomical parameters on orthogonal plane

radiographs of individuals in a standing position. The data were then processed by means of a software package used to reconstruct the spinal column and pelvis in three dimensions and perform statistical analysis. Subjects were divided into two categories: normotypes (49 in total, 28 men and 21 women) and those affected by scoliosis (66 individuals).
Some physical characteristics are also indicated: the population consisting of healthy individuals has an average age of 24 years (19-50), height of 173 cm and body weight of 65.8 kg; the subjects with scoliosis have an average age of 33 years, height of 161 cm and body weight of 55 kg [20-27].

5 AUTHORS' STUDIES

On the basis of the studies outlined above, the authors used trigonometric models [12-16] and direct numerical values from the literature [9-29] to calculate SPT from a range of initial information. Data from the literature [9-29] were also used to validate the trigonometric models' results.

5.1 SPT FROM TRIGONOMETRIC MODELS

Using the two main trigonometric methods [12] illustrated in Figures 4 and 5, the authors calculate the SPT length for different subjects. The trigonometric models were as follows:

- method 1: authors used the trigonometric model shown in Figure 3 [12] and calculated SPT via pelvic incidence and via pelvic radius;
- method 2: authors used a simpler model deriving SPT from pelvic tilt and S1 offset using a trigonometric formula (Figure 4 [12]).
- Average SPTs from the literature were then analyzed for healthy subjects and subjects affected by pathologies. These aspects will be described below.

5.1.1 SPT from Trigonometric Models: Method 1

In this analysis, SPT was calculated starting from the trigonometric model shown in Figure 3 [12] and then using pelvic incidence and pelvic radius, using the expressions proposed in the literature [12] and sometimes also reformulated them:

$$\alpha_1 = 90 - PI \tag{1}$$

$$\tan\alpha_1 = a/b; \quad \tan\alpha_2 = a/c \tag{2}$$

where c = b+d (Figure 3)

$$SPT = a/\sin(\alpha_1); \; SPT = b/\cos(\alpha_1) \tag{3}$$

It should be borne in mind that d=S1/2.
From the measurement of the pelvic radius, we obtain (Figure 4):

$$a = PR \cdot \sin\alpha_2 \tag{4}$$

SPT was calculated using dimensions a and b (Figure 3).

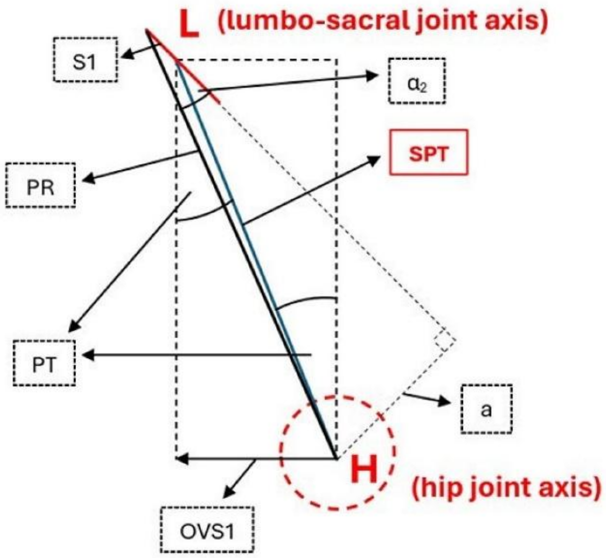

Figure 4 Relationship between SPT, pelvic tilt (PT) and S1 (OVS1) offset in the sagittal plane [12].

5.1.2 SPT from Trigonometric Models: Method 2

With method 2, the authors determined SPT from pelvic tilt and S1 offset using a trigonometric formula, starting from the diagram shown here in Figure 4 [12]:

$$SPT = OVS1/\sin(PT) \tag{5}$$

Further details of these calculation results will be illustrated below.

5.2 SPT CALCULATED FROM LITERATURE DATA

To verify the SPT values obtained using methods 1 and 2 described above, the authors analyzed a number of articles [9-15,18-20] obtaining a sizable quantity of SPT values for different subjects which were then compared with the authors' calculations.

5.2.1 Healthy Subjects

One of authors' first calculations from literature data [12] was the general determination of SPT using pelvic incidence and pelvic thickness measurements. Table II shows the results obtained from analyzing subjects presented in the literature [9-15,18-20] while Table III illustrates the results for PI and α_1. The goal was to derive a defined interval from all measurements, regardless of the subjects' demographic characteristics. In all of the tables, the numbers in bold at the bottom are the overall average measurements for each column. Referring to Table II e III, the total values (in bold) are the average of the values of all the measures based on the number of samples in the study (N = 1657 for SPT, N = 1600 for PI) designated with N. The maximum and minimum are either extreme values of the analyzed population or statistical limits given by doubling the measure of the calculated standard deviation, representing a 95% confidence interval for the total population.

Table II - SPT values analyzed from literature [9-15,18-20]

Average (mm)	Min (mm)	Max (mm)
132.0	103.9	160.1
95.2	7.6	113.8
85.3	64.2	106.4
104.9	87.7	122.1
107.0	87.1	126.9
108.4	91.4	125.4
109.0	95.0	123.0
109.0	89.0	130.0
102.1	100.5	103.7
107.3	106.3	108.3
105.6	104.4	106.8
116.9	98.1	135.7
116.9	99.0	147.0
120.0	105.0	135.0
155.5	136.2	174.8
133.1	117.8	148.4
113.3	**97.9**	**129.1**

Table III - PI and α1 values from literature [9-15,18-20]

PI			α_1		
Average (°)	Min (°)	Max (°)	Average (°)	Min (°)	Max (°)
48.3	28.1	68.5	41.7	21.5	61.9
58.6	37.2	80.1	31.4	9.93	52.8
59.7	39.8	79.6	30.3	10.43	50.
47.6	27.2	68.0	42.4	22	62.8
46.2	27.0	65.4	43.8	24.6	63.0
47.0	30.7	63.3	43.0	26.7	59.3
52.3	30.1	74.5	37.7	15.5	59.9
52.3	26.9	82.1	37.7	7.9	63.1
52.0	49.6	54.3	38.0	35.7	40.4
51.0	49.4	52.5	39.0	37.5	40.6
52.5	51.0	54.1	37.5	35.9	39.0
48.5	30.5	66.5	41.5	23.5	59.5
48.5	33.0	69.0	41.5	21.0	57.0
49.8	**34.5**	**65.6**	**40.2**	**24.4**	**55.5**

5.2.2 For Different Conditions

The authors then analyzed SPT in various types of subjects and situations presented in the literature [9-11, 23, 24]. For example, Table IV illustrates the analysis conducted for different genders (M = male, F = female). As can be seen, there is in general a slight difference (in the order of 1°) in pelvic incidence between the female (F) and male (M) population. The gender difference is even smaller for STP, as the average, minimum and maximum figures are practically identical in a population of 238 subjects. Table V and VI show results for non-elderly subjects. As can be seen from the analysis of variations in pelvic incidence angle, the mean values do not vary significantly; here again, the range of values increases on both sides. By contrast, the trend for angle α_1 is the inverse of that for PI (being its complement) and the angle is thus directly proportional to SPT.

Table IV - Selected SPT values by gender [10-12,15]

SPT					
M			F		
Average (mm)	Min (mm)	Max (mm)	Average (mm)	Min (mm)	Max (mm)
104.5	87.3	121.7	105.4	87.6	123.2
108.9	89.8	128.0	110.2	90.4	127.0
119.0	99.5	138.5	114.1	97.5	130.6
107.2	**89.3**	**125.1**	**107.3**	**89.1**	**124.7**

Table V - Average, minimum and maximum SPT excluding distributions with individuals aged over 65 years [9-13]

SPT		
Average (mm)	Min (mm)	Max (mm)
132.0	103.9	160.1
104.9	87.7	122.1
108.9	89.8	128.0
110.2	92.4	128.0
109.0	95.0	123.0
109.0	89.0	130.0
116.9	98.1	135.7
116.9	99.0	147.0
120.0	105.0	135.0
155.5	136.2	174.8
133.1	117.8	148.4
117.1	**96.4**	**138.3**

Table VI - Average, minimum and maximum PI and α_1 excluding distributions with individuals aged over 65 years [9-13]

PI			α_1		
Average (°)	Min (°)	Max (°)	Average (°)	Min (°)	Max (°)
48.3	28.1	68.5	41.7	21.5	61.9
47.6	27.2	68.0	42.4	22.0	62.8
46.1	25.5	66.7	43.9	23.3	64.5
45.8	29.1	62.5	44.2	27.5	60.9
52.3	30.1	74.5	37.7	15.5	59.9
52.3	26.9	82.1	37.7	7.9	63.1
48.5	30.5	66.5	41.5	23.5	59.5
48.5	33.0	69.0	41.5	21.0	57.0
48.9	**28.2**	**70.4**	**41.1**	**19.6**	**61.8**

6 SOME PROCEDURES FOR DETERMINING SPT

As described below, electronic spreadsheets were developed that can be used to determine the SPT range for the DIMEAS pelvis simulator. An example will also be presented of calculating trends for pelvic incidence and pelvic thickness as a function of subjects' age using two linear regression equations. The example involves a total of 6 subjects (3 male and 3 female) divided into 3 ethnic categories.

The SPT values considered in determining the adjustment range of the pelvis simulator section of the DIMEAS exoskeleton test bench are discussed below.

6.1 AUTHORS' ELECTRONIC SPREADSHEETS

The following procedure was used to calculate the pelvic thickness values shown in Table VII from pelvic parameter measurements and geometric/trigonometric models, developing the electronic spreadsheets such as that shown in Table VII as a tool for examining literature data and calculating results, obtaining the corresponding SPT. In Table VII, when a and b are indicated, SPT values are derived from method 1, while when a and b are not indicated, SPT derives from method 2. All values in Table VII were determined with method 1 or 2. Length d (Figure 3) is assumed to be a constant 18 mm, given the limited literature on the subject and given that its between-subjects variation is negligible compared to that of the other parameters [12,24,25]. From the perspective of statistical analysis, it should be borne in mind that the SPT measurements are given by the averages of the different distributions presented, since values of the pelvic parameters associated with an individual are not readily available in the literature.

6.1.1 SPT Filtered by Age and Pathologies

Further spreadsheets whereby SPT can be obtained under different conditions were developed by filtering for values associated with elderly subjects and those with more serious spinal pathologies. The resulting data will be used statistically to define the range of values. To that end, the mean of the distribution will be calculated as a weighted mean based on the number of subjects, the variance (again based on N) and the associated standard deviation. The maximum and minimum are defined by the deviation of twice the standard deviation from the mean of the values, as here defined: average value 115.20 mm; minimum value 93.92 mm; maximum value 136.47 mm; variance 113.17 mm^2 ; standard deviation 10.64 mm.

6.1.2 PI and SPT Trends Using Linear Regression Equations

Some of the articles cited in this study [9,10,13] are useful in investigating how pelvis parameters vary as a function of age, and provide linear regression equations that can also be used to visualize pelvic parameter variation. Specifically, the two equations to define pelvic incidence and SPT based on age and the subjects' gender and ethnicity [9,10,13] are as follow:

$$PI = 44.3 + 0.2 * age \tag{6}$$

$$SPT = (115.2 - 0.05 * age + 1.07 * gender - 1.68 * a + 0.63 * b - PI)/0.55 \tag{7}$$

In the SPT equation, gender can be male (zero) or female (one), the letter a designates Arab ethnicity, b designates Asian ethnicity, while if both are set to zero the ethnicity is Caucasian. Further electronic spreadsheets (not shown for space reasons) were constructed whereby the influence of subjects' ages and ethnicities on PI and SPT can be examined. Average SPT for each year of age was then generated and graphed together with PI as shown in Figure 5.

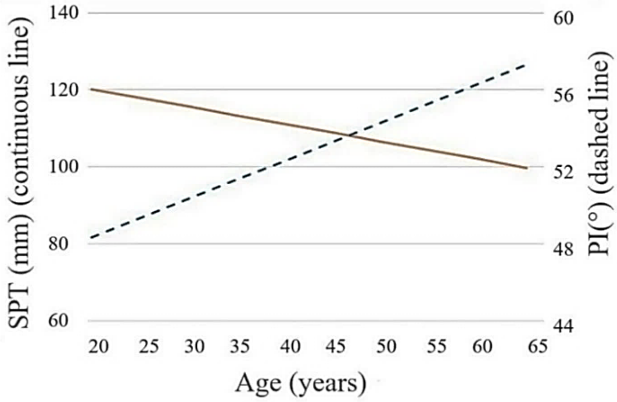

Figure 5 PI and SPT as a function of age.

Estimated variation in pelvic thickness is about 20 mm, while that of pelvic incidence is about 10°. The variation in the two measures is inversely proportional: pelvic thickness tends to decrease with age, while pelvic incidence increases. The electronic spreadsheets shown in Figure 7 allows to obtain the SPT values starting from different information from the literature data or calculated from the models proposed. SPT values are important both for the proper design of automatic devices applied to the human trunk (active or passive) and for a general study and knowledge of the human pelvis. The key for reading Table VII is: referring to the trigonometric models illustrated above and the two methods proposed by the authors. In fact the SPT can be calculated in various ways, depending on the known parameters (PI, PRS1, PR, PT, etc.). Therefore, where there are blank spaces in the columns of the respective parameters (Table VII), it means that the parameter is unknown, but the SPT can still be calculated using the other available parameters.

7 COMPARISON AND ANALYSIS OF RESULTS

Calculated and literature data for STP and other pelvic parameters, including pelvic incidence and Jackson's angle in particular, were compared to improve this study. It should also be borne in mind that the issue of measurement uncertainty cannot be addressed here, as the study draws on data and literature analysis. However, it is an important study, as it is difficult to find information on SPT and construct, as the authors did, useful tools for its calculation.

7.1 CALCULATED AND LITERATURE DATA FOR SPT

In comparing the means and standard deviations of the SPT values from the literature data and resulting from calculation, it was found that the two distributions have a very similar means: 117.01 mm for the literature data, and 115.20 mm for the calculated values, resulting in a delta of 1.8 mm. The delta for the standard deviation, on the other hand, tends to zero, as the two values are practically identical (around 10.6 mm).

Table VII - SPT values calculated from pelvic parameters from literature data or using trigonometric models [16-29]

PI (°)	PRS1 (°)	PR (mm)	PT (°)	OVS1 (mm)	α_1 (°)	α_2 (°)	a (mm)	b (mm)	SPT (mm)
50.2	35.2		11.5		39.8	35.2	82.8	69.0	107.8
49.6	35.8		10.6		40.4	35.8	85.1	72.4	111.7
62.0	24.3		14.7		28.0	24.3	53.9	28.7	61.1
58.0	32.0	137.0			32.0	32.0	72.6	98.2	122.1
76.0	14.0	137.0			14.0	14.0	33.1	114.9	119.6
66.0	24.0	135.0			24.0	24.0	54.9	105.3	118.8
60.0	30.0	138.0			30.0	30.0	69.0	101.5	122.7
			11.9	22.6					109.6
			10.3	19.2					107.4
			12.3	22.4					105.2
			16.0	25.0					90.7
			12.6	20.8					95.4
			14.0	24.6					101.7
54.3	31.2	135.0			35.7	31.2	69.9		119.8
54.7	30.9	136.8			35.3	30.9	70.3		121.6
60.8	34.3				29.2	34.3	55.7	99.6	114.1
39.6	45.5				50.4	45.5	115.8	95.8	150.3
52.6	33.2				37.4	33.2	81.7	106.9	134.6
48.3	36.9				41.7	36.9	85.9	96.4	129.2
52.8	32.5				37.2	32.5	71.4	94.0	118.0
47.3	38.1				42.7	38.1	93.9	101.8	138.5
60.5	25.9				29.5	25.9	61.7	109.0	125.2
70.6	17.2				19.4	17.2	46.1	130.8	138.7
			10.3	18.8					105.1
			10.0	18.3					105.4
			11.5	21.7					108.6
			12.3	21.3					99.9
			11.9	22.4					108.5
			12.9	24.1					107.8
46.3	38.9				43.7	38.9	94.2	98.6	136.3
51.6	34.4				38.4	34.4	89.5	112.8	144.0
			9.3	18.2					112.7
48.5	37.1	128.9			41.5	37.0	85.4	84.9	120.4

This indicates that the distributions have practically identical behavior, with widths that are approximately equal and means with a very small deviation. The value that differentiates the two measures is the number of subjects in the sample population, 1138 for the literature data and 2156 for the calculated data, almost double. Individual SPT values can also be compared graphically, analyzing their dispersion (Figure 6). The curves for the two series of data differ (given that different subjects are analyzed), but the extremes coincide and the curves meet at a point close to the average values.

It can thus be concluded that the literature values for SPT are comparable to the calculated values, and the calculation model is consistent.

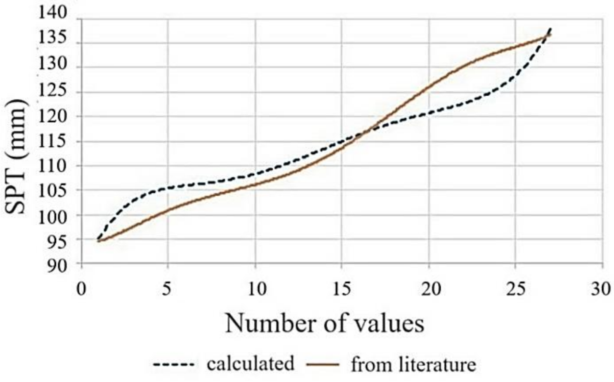

Figure 6 SPT versus number of results for the two distributions.

7.2 FINAL SPT RANGE

A preliminary possible proposal for studying these data is presented here. Table VIII was compiled to define the range of pelvic thickness variation. It illustrates the mean and the standard deviation calculated for the parameter. Values were divided into three confidence intervals (a confidence interval provides a range of values within which a population parameter, such as a mean or proportion, is believed to lie with a certain probability or "confidence," typically expressed as a percentage (e.g., 95% or 99%)) based on standard deviation. Standard deviation (the standard deviation (or root mean square) is a statistical measure of dispersion that indicates how much the values in a set of data deviate from their arithmetic mean) is here indicated as SD. The ranges of 1, 2 or 3 standard deviations represent the confidence intervals (in the order 68.6, 95.4 and 99.7). These intervals represent the percentage probability (it is the most common way to express the probability of an event, converting the fraction (favorable cases / possible cases) into a percentage. To do this, divide the numerator by the denominator to obtain a decimal, and then multiply this decimal by 100, adding the "%" symbol) of finding a subject within the range represented by the SD: for example, the interval obtained from 2*SD represents a 95.4% probability that a subject will fall within that interval.

Table VIII - SPT values for three confidence intervals.

SPT					
Confidence interval	Average value (mm)	Min value(mm)	Max value (mm)	SD (mm)	Probability (%)
SD	115.2	105	126	10.64	68.6
2*SD	115.2	94	136	10.64	95.4
3*SD	115.2	83	147	10.64	99.7

By calculating the minimum and maximum values and deviation from the mean, the probability that a subject has a pelvic thickness that falls within that range is approximately 68%. This increases to 99% by deviating by three standard deviations (SD). It is also interesting to introduce the distribution of pelvic thickness (Figure 7).

This normal distribution indicates the probability considered on N=33 subjects in the sample population here from SPT values calculated and not from the literature data. On the other hand the whole number of subjects examined by the authors was N = 115. It follows that an average useful range of SPT variations for the DIMEAS pelvis simulator is from 80 mm to 190 mm.

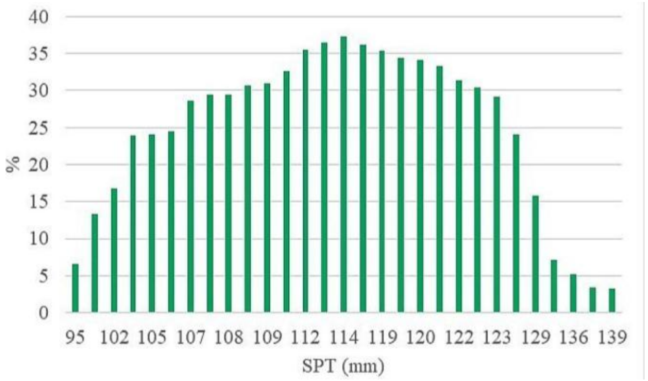

Figure 7 Normal distribution of SPT.

In the future, all these analyses may be refined through studies conducted in collaboration with physicians in the field. The study presented here is useful for improving engineering knowledge of the human pelvis and thus future interactions with clinicians [30-32].

8 DIMEAS PELVIS SIMULATOR MODIFICATION

The study presented here was the basis for developing a new configuration of the DIMEAS exoskeleton test bench pelvis simulator. SPT can be adjusted by varying the dimension either along the hypotenuse of the right triangle shown in Figure 3 or along the sides. Figure 8 shows a possible preliminary design solution. The SPT regulation is in this case obtained using commercial recirculating ball guides for all movements. Each regulation is currently foreseen in manual mode. Future work will focus on optimizing this configuration to arrive at the final test bench layout featuring an SPT adjustment range of 80 mm to 190 mm.

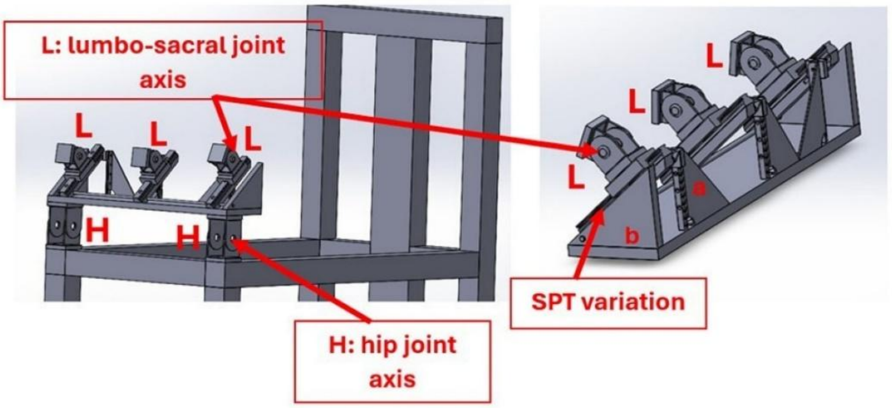

a) b)

Figure 8 A possible configuration of the new pelvis simulator in the DIMEAS test bench: a) overall view; b) details.

9 CONCLUSIONS

The study presents an original analysis of data from the literature that can help in gaining a better understanding of human pelvis dimensions and geometry.

Starting from a literature review, the authors developed a method for calculating several main human pelvis parameters, including sagittal pelvic thickness.

The analysis also resulted in a human pelvis engineering study that can be fruitfully applied in designing industrial trunk support exoskeletons and their test benches.

The study and construction of a 3D-printed scale model of the human pelvis (95% ile of which is Italian male) is currently underway. This will allow both to improve understanding of this part of the human body and to present and explain it to students in the field.

A physical model of the human pelvis will also be constructed, perhaps with movable parts, in order to analyze pelvic function and characteristics.

ACKNOWLEDGEMENTS

The authors would like to thank Eng.s F.G. Pietrafesa, S. Seminara, C. Vigenti, L. Carchia, A. Sabatino and Z. Reguig for their help in this study.

Authors underline that Figures 3 and 4 were partially modified by the authors from the original ones for exigence of the study here presented and are from the paper [12]

Legaye J. The sagittal pelvic thickness: A determining parameter for the regulation of the sagittal spinopelvic balance. ISRN Anatomy 2013; 4: 1–9, were in the beginning is this note: *“Copyright © 2013 Legaye Jean. This is an open access article distributed under the Creative Commons Attribution License, which permits unrestricted use, distribution, and reproduction in any medium, provided the original work is properly cited”.*

REFERENCES

[1] Bostelman R. and Hong T., Test Methods for Exoskeletons – Lessons Learned from Industrial and Response Robotics. *National Institute of Standards and Technology*, Gaithersburg, MD 20899, USA, Le2i, Université de Bourgogne, BP 47870, 21078 Dijon, France, https://api.semanticscholar.org/CorpusID: 56454435, 2018.

[2] Huysamen K., de Looze M.P., Bosch T., Ortirz J., Toxiri S.C. and O’Sullivan L.W., Assessment of an active industrial exoskeleton to aid dynamic lifting and lowering manual handling tasks. *Applied Ergonomics*, Vol. 68, pp. 125 – 131, 2018.

[3] de Looze M.P., Bosch T., Krause F., Stadler K.S. and O’Sullivan L.W., Exoskeletons for industrial application and their potential effects on physical work load. *Ergonomics*, Vol. 59, No. 5, pp. 671-81, 2016.

[4] Nabeshima C., Ayusawa K., Hochberg C. and Yoshida E., Standard Performance Test of Wearable Robots for Lumbar Support. *IEEE Robotics and Automation Letters*, Vol. 3, No. 3, pp.1-8, 2018.

[5] Belforte G., Eula G., Appendino S. and Sirolli S., Pneumatic Interactive Gait Rehabilitation Orthosis: design and preliminary testing. *Proceedings of the Institution of Mechanical Engineers, Part H: Journal of Engineering in Medicine*, Vol. 225, No. 2, pp.158-169, 2011.

[6] Belforte G. and Eula G., Design of an active-passive device for human ankle movement during functional magnetic resonance imaging analysis. *Proc. IMechE, Part H: Journal of Engineering in Medicine*, Vol. 226, No. 1, pp. 21-32 2011.

[7] Raparelli T., Eula G., Mazza L., Ivanov A., Pietrafesa F., Mala R. and Pontin M., A preliminar prototype of an industrial exoskeleton for the operator’s trunk support. *International Journal of Mechanics and Control*, Vol. 23, No. 2, pp. 37-52, 2022.

[8] Raparelli T., Eula G., Mazza L., Ivanov A., Pietrafesa F., Mala R. and Pontin M., The design of an innovative active exoskeleton prototype for industrial application with a pneumatic actuation. *International Journal of Mechanics and Control*, Vol. 23, No. 2, pp. 61-72, 2022.

[9] Hasegawa K., Hatsushikano S., Le Huec J-C., Sardar Z., Wong H.K., Hey H.W.D., Liu G., Bourret S., Kelly M., Riahi H., Chelli-Bouaziz M. and Lenke L.G., Pelvic thickness, sex, ethnicity, and age affect pelvic incidence in healthy volunteers of multi-ethnic alignment normative study (MEANS) database. *European Spine Journal*, Vol. 31. No. 6, pp. 1421-1430, 2022.

[10] Vrtovec T., Janssen M.M.A., Likar B., Castelein R.M. and Pernus F., Evaluation of pelvic morphology in the sagittal plane. *The Spine Journal*, Vol. 13, No. 11, pp. 1500–1509, 2013.

[11] Imai N., Suzuki H., Nozaki A., Miyasaka D., Tsuchiya K., Ito T., Minato I. and Endo N., Evaluation of anatomical pelvic parameters between normal, healthy men and women using three-dimensional computed tomography: A cross-sectional study of sex-specific and age-specific differences. *Journal of Orthopaedic Surgery and Research*, Vol. 14, No. 126, pp. 1-7, 2019.

[12] Legaye J., The sagittal pelvic thickness: A determining parameter for the regulation of the sagittal spinopelvic balance. *ISRN Anatomy*, Vol. 4, pp. 1–9, 2013.

[13] Hasegawa K., Okamoto M., Hatsushikano S., Shimoda H., Ono M. and Watanabe K., Normative values of

spino-pelvic sagittal alignment, balance, age, and health-related quality of life in a cohort of healthy adult subjects. *European Spine Journal,* Vol. 25, No. 11, pp. 3675–3686, 2016.

[14] Boulay C., Tardieu C., Hecquet J., Benaim C., Mitulescu A., Marty C., PratPradal D., Legaye J., Duval-Beaupere G. and Pèlissier J., Anatomical reliability of two fundamental radiological and clinical pelvic parameters: Incidence and thickness. *European Journal of Orthopedic Surgery & Traumatology*, Vol.15, No. 3, pp. 197–204, 2005.

[15] Singh R., Yadav S.K., Sood S., Yadav R.K. and Rohilla R., Spino-pelvic radiological parameters in normal Indian population. *Sicot-J 2018*, Vol. 4, No. 14, pp. 1-9, 2018.

[16] Legaye J., Duval-Beaupere G., Marty C. and Hecquet J., Pelvic incidence: A fundamental pelvic parameter for three-dimensional regulation of spinal sagittal curves. *European Spine Journal*, Vol. 7, No. 2, pp. 99–103, 1998.

[17] Sergides I.G., McCombe P.F., White G., Makhtar S. and Sears W.R., Lumbo-pelvic lordosis and the pelvic radius technique in the assessment of spinal sagittal balance: Strengths and caveats. *European Spine Journal*, Vol. 20, No. S5, pp. 591–601, 2011.

[18] Jackson R.P., Peterson M.D., McManus A.C., and Hales C., Compensatory spinopelvic balance over the hip axis and better reliability in measuring lordosis to the pelvic radius on standing lateral radiographs of adult volunteers and patients. *Spine*, Vol.23, No.16, pp.1750–1767, 1998.

[19] Jackson R.P., Kanemura T., Kawakami N. and Hales C., Lumbopelvic lordosis and pelvic balance on repeated standing lateral radiographs of adult volunteers and untreated patients with constant low back pain. *Spine,* Vol. 25, No. 5, pp. 575–586, 2000.

[20] Jackson R.P., Phipps T., Hales C. and Surber J., Pelvic lordosis and alignment in spondylolisthesis. *Spine*, Vol. 28, No. 2, pp. 151–160, 2003.

[21] Legaye J., The femoro-sacral posterior angle: An anatomical sagittal pelvic parameter usable with dome-shaped sacrum. *European Spine Journal*, Vol. 16, No. 2, pp.219–225, 2006.

[22] Hohenhaus M, Volz F, Merz Y, Watzlawick R., Scholz C., Hubbe U. and Klingler J.H., The challenge of measuring spinopelvic parameters: Inter-rater reliability before and after minimally invasive lumbar spondylodesis. *BMC Musculoskeletal Disorders*, Vol. 23, No. 104, pp. 1-8, 2022.

[23] Morfotipologia. (s.d.). CECV France, https://www.demauroy.net/SFIMO/cecv_france.htm.

[24] Tiwari A., Sonone S.V. and Jaiswal N.P., New classification of S1 pedicle morphometry impacting pedicle screw insertion technique. *International Journal of Research in Orthopaedics*, Vol. 8, No. 6, pp. 694-700, 2022.

[25] Van der Houwen E.B., Baron P., Veldhuizen A.G., Burgerhof J.G., van Ooijen P.M.A. and Verkerke G.J., Geometry of the intervertebral volume and vertebral endplates of the human spine. *Annals of Biomedical Engineering*, Vol. 38, No. 1, pp.33–40, 2009.

[26] Duval-Beaupère G., Schmidt C. and Cosson P., A barycentremetric study of the sagittal shape of spine and pelvis: The conditions required for an economic standing position. *Annals of Biomedical Engineering*, Vol. 20, No. 4, pp. 451–462, 1992.

[27] Lee C.S., Chung S.S., Kang K.C., Park S.J. and Shin S.K., Normal patterns of sagittal alignment of the spine in young adults radiological analysis in a Korean population. *Spine*, Vol. 36, No. 25, pp. E1648—E1654, 2011.

[28] Rajnics P., Pomero V., Templier A., Lavaste F. and Illes T., Computer-Assisted assessment of spinal sagittal plane radiographs. *Journal of Spinal Disorders*, Vol. 14, No. 2, pp.135–142, 2001.

[29] Vialle R., Levassor N., Rillardon L., Templier A., Skalli W. and Guigui P., Radiographic analysis of the sagittal alignment and balance of the spine in asymptomatic subjects. *The Journal of Bone & Joint Surgery,* Vol. 87. No. 2, pp. 260–267, 2005.

[30] Fellag R., Guiatni M., Hamerlain M. and Achour N., Exoskeleton robust control using adaptive finite time homogeneous higher order sliding modes. *International Journal of Mechanics and Control*, Vol. 22, No. 2, pp. 95-106, 2021.

[31] Abane A., Guiatni M., Ababou N., Amine Alouane M. and Bouzid Y., Mechatronics design and control of a transformed upper limb rehabilitation exoskeleton. *International Journal of Mechanics and Control*, Vol. 21, No. 1, pp. 75-90, 2020.

[32] Ben Hariz N. and Ayadi M., The influence of 3D printing process parameters in the dimension accuracy, roughness, and weight. *International Journal of Mechanics and Control*, Vol. 25, No. 2, pp. 47-52, 2024.

ISSN 1590-8844
International Journal of Mechanics and Control, Vol. 26, No. 02, 2025
https://doi.org/10.69076/jomac.2025.0025

MODELING IMPACT ON MECHANICAL CONVERSION IN AN INVERTED DOUBLE PENDULUM ENERGY HARVESTER

Seif Eddine Chebbi Fethi Aloui Charfeddine Mrad Rachid Nasri

National Engineering School of Tunis (ENIT), University of Tunis el Manar (UTM),
BP 37 Le Belvedere, 1002, Tunis, Tunisia

ABSTRACT

Green and clean energy harvesting has been of interest owing to exploit renewable energies and to avoid pollutant sources. The literature proposes significant devices to convert ambient energies into usable energies such as double pendulums. Double pendulums have high potential for energy harvesting due to their nonlinear dynamics and especially their chaotic behaviour. In this study, an inverted double pendulum energy harvester is proposed to harness vibration energy for mechanical applications. First, we present the inverted double pendulum design and the governing equations, in free and forced regimes. Second, we analyse the inverted double pendulum oscillations and bifurcations. Third, we conduct a parametric study to explore the effect of varying the inverted double pendulum parameters: first pendulum mass and length, second pendulum mass and length, and double pendulum total length. Last, we present the produced optimal energies, in free and forced regimes. The double pendulum nonlinearity leads to quasiperiodic and chaotic responses. The findings reveal that it is possible to tune the double pendulum parameters toward maximizing the converted energy.

Keywords: Inverted double pendulum, Energy conversion, Nonlinear dynamics, parametric analysis, optimal energy.

1 INTRODUCTION

Energy harvesting is the method of gathering and converting energy from ambient environment[1]. It has been in the focus list in recent years as a promising solution for providing clean, decentralized, and sustainable power. There are several ways to harness different ambient energies, such as wave movement[2], mechanical vibration[3, 4], and dynamic oscillation[5, 6]. Substantial volume of literature have been devoted to development and efficiency optimization of different systems and methodologies to convert these vibrational energies into electricity, paying particular attention to efficiency optimization and compatibility with differing operational environments[7, 8, 9].Among the many mechanical tools investigated for energy harvesting, pendulums have been among effective classes. These mechanisms, especially those involving nonlinear dynamic phenomena, are more suitable for energy harvesting from low-frequency, irregular, and multidirectional vibrations.

Double pendulum is a famous example of these nonlinear systems. Its capacity to exhibit sophisticated dynamic properties, including large and stable oscillations for some excitations, renders it a promising contender for energy harvesting[10]. Several design advancements have been proposed to exploit the potential of pendulum-based systems. As an example, [11] proposes an asymmetric conical pendulum involving a piezoelectric cantilever beam with multidirectional energy harvesting functionality. In[12], a model of a two-degree-of-freedom (2-DOF) system was developed to demonstrate how quasiperiodicity and energy harvesting stabilization is induced by a passive pendulum. However, despite improvements in motion control, the power output under this method averaged frequently lower than in uncontrolled instances. While chaotic responses have been associated with higher energy output. Yet another creative solution is presented in[13], where a hybrid pendulum-beam

---

Contact author: Seif Eddine Chebbi[1]

[1]National Engineering School of Tunis (ENIT), University of Tunis el Manar (UTM), BP 37 Le Belvedere, Tunis, 1002, Tunisia
E-mail: seifeddine.chebbi@enit.utm.tn

system, modelled by Euler-Bernoulli theory and Hamilton's principle, was discovered to achieve optimal harvesting performance with regard to pendulum mass and length. Similarly, [14] introduced a quad-stable energy harvester comprising a nonlinear pendulum and magnetic forces that can harvest ultra-low-frequency motion and translate it into useful electrical power. A magnet-coil configuration within a double pendulum system was proposed in [8], which facilitated efficient energy harvesting in both linear and nonlinear motion regimes. The integration of pendulum structures with elastic elements has also been encouraging. In [15], a pendulum-elastic beam configuration was seen to exhibit good performance under low excitations, producing high power output.

Pendulum systems have also been studied for offshore structures. The dynamic nature of ocean waves with varying amplitudes and frequencies creates a best possible scenario for such systems [16, 17, 18]. A floating pendulum platform coupled with a DC generator shaft was optimized by a particle swarm algorithm in order to show power output sensitivity to pendulum parameters [19]. Another study [20] examined a parametrically excited pendulum that was designed to enhance performance at low wave amplitudes and frequencies using both heaving and surging motions. A pendulum-type harvester capable of harvesting multidirectional wave energy consisted of a combination of a triboelectric nanogenerator (TENG) and an electromagnetic generator (EMG) as reported in [4]. The system was effective in charging capacitors for use in wireless monitoring in marine scenarios. Further, [21, 22] proposed pendulum-based underwater systems, achieving maximum energy conversion at specific conditions of resonance. An integrated electromagnetic energy harvester magnetic spring mechanism was proposed in [23], which showed good efficient performance under variable accelerations.

Nonlinear dynamics also widen the application of pendulum systems in vibration control, as can be seen from [24], in which a pendulum-type Electromagnetic Tuned Mass Damper (ETMD) was proposed for the mitigation of structural vibrations and power harvesting. In wearable devices, pendulum-type harvesters have been used successfully for the harvesting of human motion energy. Research [1] showed that these systems were several orders of magnitude better than traditional methods in specific body joints. High-performance quality piezoelectric ceramics have also encouraged the application of such systems in low-frequency human motion, leading to useful power outputs [25]. Apart from practical applications, pendulum systems have also been treated with numerical simulations and theoretical mathematics. A simple pendulum model based on a Lagrange equation was constructed in [26] to calculate optimal power output angles and periods and display them in efficiency maps that can aid system design. A chaotic triple pendulum was modelled in another study with consideration of its use as a secure pseudo-random number generator (PRNG), exhibiting double usability in the uses of both energy harvesting and cryptography [27]. The spectrum of pendulum dynamics from rotation to oscillation and chaotic modes influences heavily the energy harvester design. For instance, [28, 29] addressed ideal and non-ideal pendulum models and provided evidence that the parameters in energy balance determined the form of prevailing motion type and connected power output. Further research on tunable double-mass pendulum structures created better frequency adaptability and power output in response to varying conditions [30, 31]. Chaos-activated energy harvesting was also investigated in [32], which investigated transitions among oscillatory, centrifugal equilibrium, and chaotic modes in a double pendulum system.

The goal of this study is to investigate a novel double pendulum energy harvester. The double pendulum is inverted and is explored in free and forced regimes. First, we present the double pendulum design and the governing equations, in free and forced regimes. Second, we analyse the double pendulum oscillations and bifurcations. Third, we conduct a parametric study to explore the effect of varying the double pendulum parameters: masses and lengths. Last, we present the produced optimal energies, in free and forced regimes.

2 PENDULUM PRESENTATION

The inverted double pendulum energy harvester is presented in the current section. The fundamental design, modelling, and equations are presented with a particular attention to the pendulum motion.

2.1 PENDULUM CONFIGURATION

Figure 1a presents the inverted double pendulum energy harvester layout in free regime. It is composed of two coupled pendulums: first pendulum and second pendulum. When the second pendulum oscillates, it pivots into a frame, the frame is embedded on the output axis, hence the first pendulum oscillates, since it is also embedded on the output axis. The first pendulum is of mass M_1 and length L_1, the rod mass is m_1. Its angular displacement is denoted θ_1. The second pendulum is of mass M_2 and length L_2, the rod mass is m_2. Its angular displacement is denoted θ_2. The motion of the first pendulum (Ellipsoid 1) is driven by the oscillation of the second pendulum (Ellipsoid 2). The total length of the inverted double pendulum energy harvester is L.

The masses geometry is elliptical instead of spherical to reduce aerodynamic friction [33]. The pivot links are to be with bearings to decrease mechanical friction. To the output axis, an electric generator with a motion accumulating device are to be mounted. Aerodynamic and mechanical frictions are to be negligible to enhance the double pendulum responsiveness and its motion durability.

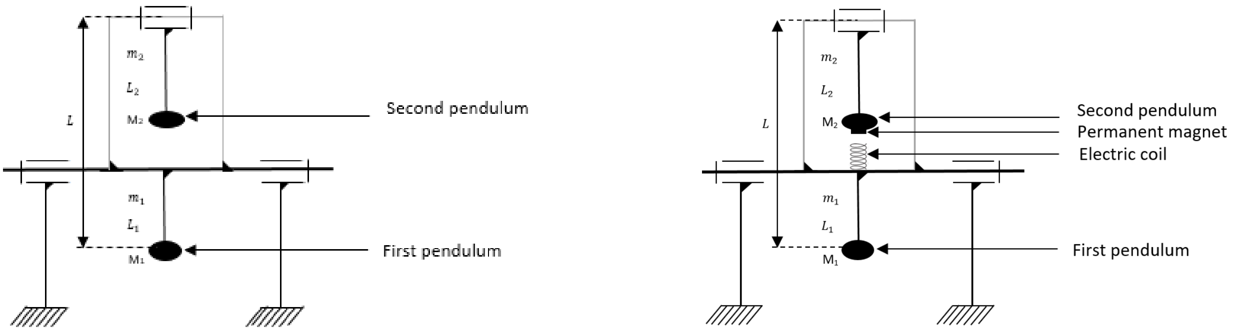

(a) Free regime.

(b) Forced regime.

Figure 1 Inverted double pendulum layout.

To explore the subsequent behaviour of the pendulums, we consider a case in which the coupled pendulums are subjected to forcing source. We apply a magnetic excitation force to the second pendulum. It enables sustainable energy, to pass from free regime to forced regime.

The source of excitation consists of an electric coil, mounted on the output axis and carries current to generate a magnetic field. Depending on the relative position of the circular-permanent magnet, mounted on the second pendulum mass, from the electric coil, the magnet-magnetic field interaction generates attractive and repulsive forces. The electric coil current direction is changed accordingly to avoid electromagnetic damping.

2.2 LAGRANGE FORMULATION

The dynamics of the inverted double pendulum energy harvester can be described using the Lagrange formulation L, which is obtained from the difference between the kinetic energy T and the potential energy V ($L = T - V$). In this study, the effects of friction in the joints and other damping effects are neglected to simplify the equations of motion.

$$T = \frac{1}{2}J_1\dot{\theta_1}^2 + \frac{1}{2}M_2 v_B^2 + \frac{1}{2}m_2 v_G^2 + \frac{1}{2}I_{bG}\dot{\theta_2}^2 \tag{1}$$

$$J_1 = J_{M_1} + J_{m_1} \tag{2}$$

$$J_{M_1} = M_1 L_1^2 + \frac{m_1 L^2}{12} + m_1\left(\frac{L}{2} - L_1\right)^2 \tag{3}$$

$$J_{m_1} = \frac{m_1 L^2}{12} + m_1\left(\frac{L}{2} - L_1\right)^2 \tag{4}$$

$$\vec{v_B} = \begin{pmatrix} (L - L_1)\sin(\theta_1)\dot{\theta_1} - L_2\sin(\theta_2)\dot{\theta_2} \\ -(L - L_1)\cos(\theta_1)\dot{\theta_1} - L_2\cos(\theta_2)\dot{\theta_2} \end{pmatrix} \tag{5}$$

$$\vec{v_G} = \begin{pmatrix} (L - L_1)\sin(\theta_1)\dot{\theta_1} - L_2\sin(\theta_2)\dot{\theta_2} \\ -(L - L_1)\cos(\theta_1)\dot{\theta_1} - \frac{L_2}{2}\cos(\theta_2)\dot{\theta_2} \end{pmatrix} \tag{6}$$

$$I_{bG} = \frac{m_2 L_2^2}{12} \tag{7}$$

$$\begin{aligned} T = {} & \frac{1}{2}(M_1 L_1^2 + \frac{m_1 L^2}{12} + m_1(\frac{L}{2} - L_1)^2)\dot{\theta}_1^2 \\ & + \frac{1}{2}M_2((L - L_1)^2\dot{\theta}_1^2 + L_2^2\dot{\theta}_2^2 + 2(L - L_1)L_2\dot{\theta}_1\dot{\theta}_2\cos(\theta_1 + \theta_2)) \\ & + \frac{1}{2}m_2((L - L_1)^2\dot{\theta}_1^2 + \frac{L_2^2}{4}\dot{\theta}_2^2 + (L - L_1)L_2\dot{\theta}_1\dot{\theta}_2\cos(\theta_1 + \theta_2)) + \frac{1}{2}m_2\frac{L_2^2}{12}\dot{\theta}_2^2 \end{aligned} \tag{8}$$

$$V = g\cos\theta_1((M_2 + m_2)(L - L_1) - m_1(\frac{L}{2} - L_1) - M_1 L_1) - g\cos\theta_2(M_2 + \frac{m_2}{2})L_2 \tag{9}$$

2.3 FREE OSCILLATIONS

The Lagrangian function provides a means of obtaining the equations of motion. That are obtained through the Euler-Lagrange equation[29]. Its general form in case of free pendulums is as the following:

$$\frac{d}{dt}\left(\frac{\partial L}{\partial \dot{\theta}_i}\right) - \frac{\partial L}{\partial \theta_i} = 0,\ i \in \{1, 2\} \tag{10}$$

Equation 10 combined to 8 and 9 forms the following governed equations that describe the dynamics of pendulums. They take into account the interactions between the two pendulums as well as their respective angles, velocities and accelerations.

$$\begin{aligned}
&\left(M_1 L_1^2 + \frac{m_1 L^2}{12} + m_1\left(\frac{L}{2} - L_1\right)^2 + (M_2 + m_2)(L - L_1)^2\right)\ddot{\theta}_1 \\
&+ (M_2 + \frac{m_2}{2})(L - L_1)L_2\left(\ddot{\theta}_2 \cos(\theta_1 + \theta_2) - \dot{\theta}_2^2 \sin(\theta_1 + \theta_2)\right) \\
&+ \left(M_1 L_1 + m_1\left(\frac{L}{2} - L_1\right) - (M_2 + m_2)(L - L_1)\right) g \sin\theta_1 = 0 \\
\\
&(M_2 + \frac{m_2}{3})L_2^2\ddot{\theta}_2 \\
&+ (M_2 + \frac{m_2}{2})(L - L_1)L_2\left(\ddot{\theta}_1 \cos(\theta_1 + \theta_2) - \dot{\theta}_1^2 \sin(\theta_1 + \theta_2)\right) \\
&+ (M_2 + \frac{m_2}{2})L_2 g \sin\theta_2 = 0
\end{aligned} \tag{11}$$

2.4 FORCED OSCILLATIONS

In order to obtain equations of motion for the pendulums in forced oscillations, we apply the following equation:

$$\frac{d}{dt}\left(\frac{\partial L}{\partial \dot{\theta}_i}\right) - \frac{\partial L}{\partial \theta_i} - \frac{\partial P_{\text{ex}}}{\partial \dot{\theta}_i} = 0 \tag{12}$$

P_{ex} is the excitation power and could be giving by:

$$P_{ex} = \kappa \frac{\mu_0 I N r^2}{2(r^2 + a^2)^{\frac{3}{2}}} \sin(\phi)\, a\dot{\theta}_2 \tag{13}$$

We define μ_0 as the vacuum permeability ($\mu_0 = 4\pi \times 10^{-7}$ T·m/A). The electrical current flowing through the coil is denoted by I. We notice r, N, and l_c specify respectively the diameter of the electric coil, its number of turns, and its length.

The magnetic moment κ of the permanent magnet is defined as $\kappa = M_r V$, where M_r represents the magnetization of the material and V is the volume of the permanent magnet. While e and R represent its thickness and radius, respectively, κ can thus be expressed as:

$$\kappa = M_r \pi e R^2 \tag{14}$$

We present ϕ as the angle of orientation between the electric coil axis and the magnetic moment. It can be expressed as follows:

$$\phi = \arctan\left(\frac{(L - L_1)\sin(\theta_1) + (L_2 + e + \frac{b_2}{2})\sin(\theta_2)}{(L - L_1)\cos(\theta_1) - (L_2 + e + \frac{b_2}{2})\cos(\theta_2) - \frac{l_c}{2}}\right) \tag{15}$$

We notice b_2 is the length of the vertical semi-axis of the second pendulum. The parameter a corresponds to the axial separation distance between the center of the electric coil and the permanent magnet. It can be written as:

$$a = [((L - L_1)\cos(\theta_1) - (L_2 + e + \frac{b_2}{2})\cos(\theta_2) - \frac{l_c}{2})^2 \tag{16}$$

$$+((L - L_1)\sin(\theta_1) + (L_2 + e + \frac{b_2}{2})\sin(\theta_2))^2]^{\frac{1}{2}} \tag{17}$$

The following governing equations describe the motion of the inverted double pendulum:

$$\begin{aligned}
&\left(M_1 L_1^2 + \frac{m_1 L^2}{12} + m_1\left(\frac{L}{2} - L_1\right)^2 + (M_2 + m_2)(L - L_1)^2\right)\ddot{\theta}_1 \\
&+ (M_2 + \frac{m_2}{2})(L - L_1)L_2\left(\ddot{\theta}_2 \cos(\theta_1 + \theta_2) - \dot{\theta}_2^2 \sin(\theta_1 + \theta_2)\right) \\
&+ \left(M_1 L_1 + m_1\left(\frac{L}{2} - L_1\right) - (M_2 + m_2)(L - L_1)\right) g \sin\theta_1 = 0 \\
\\
&(M_2 + \frac{m_2}{3})L_2^2\ddot{\theta}_2 \\
&+ (M_2 + \frac{m_2}{2})(L - L_1)L_2\left(\ddot{\theta}_1 \cos(\theta_1 + \theta_2) - \dot{\theta}_1^2 \sin(\theta_1 + \theta_2)\right) \\
&+ (M_2 + \frac{m_2}{2})L_2 g \sin\theta_2 = \kappa \frac{\mu_0 I N r^2}{2(r^2 + a^2)^{\frac{3}{2}}} \sin(\phi)\, a
\end{aligned} \tag{18}$$

3 OSCILLATIONS ANALYSIS

In the current section, we study the dynamic behaviour of the inverted double pendulum energy harvester in both free and forced oscillations by numerically resolving the equations of motion for each scenario with simulation software using fourth-order Runge-Kutta method.

The governing equations are strongly related to different physical conditions and external excitation, which have significant influence on the pendulums dynamics with the following initial conditions: $\theta_1(0) = -0.1 rad$, $\theta_2(0) = 0.2 rad$, $\dot{\theta}_1(0) = 0 rad/s$, and $\dot{\theta}_2(0) = 0 rad/s$. These conditions are taken in both free and forced vibrations in order to emphasis the coupling effect between θ_1 and θ_2, and to induce an oscillatory motion to pendulums, even when the excitation force is present. The following table resumes the different parameters used in our simulation:

3.1 FREE REGIME

In free regime, the inverted double pendulum displays the intrinsic dynamic by itself. Figure 2 illustrates the dynamic

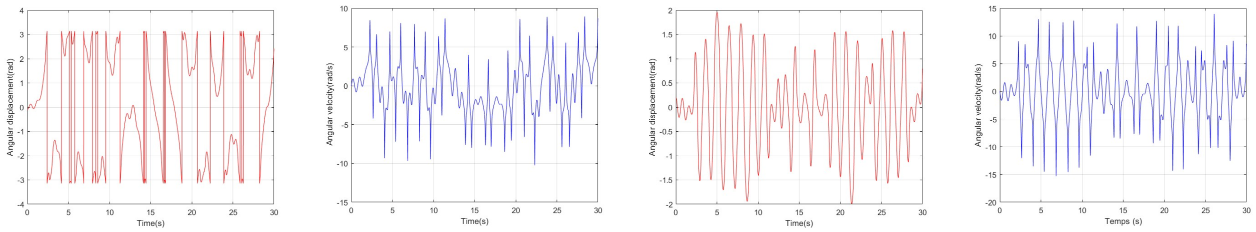

(a) $\theta_1(rad)$.
(b) $\dot{\theta}_1(rad/s)$.
(c) A$\theta_2(rad)$.
(d) $\dot{\theta}_2(rad/s)$.

Figure 2 Free pendulums oscillations.

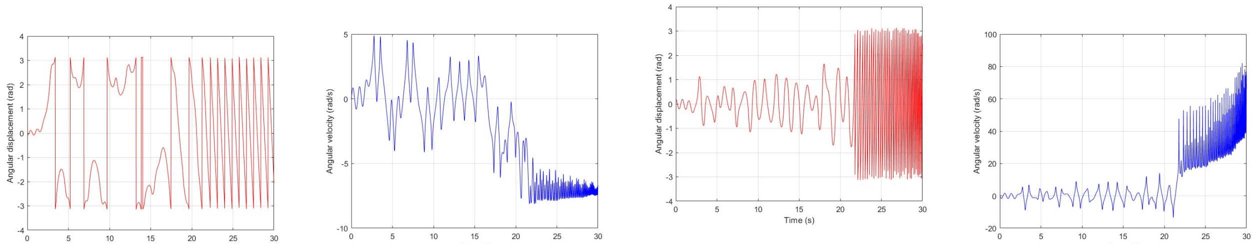

(a) $\theta_1(rad)$.
(b) $\dot{\theta}_1(rad/s)$.
(c) Angular displacement $\theta_2(rad)$.
(d) Angular velocity $\dot{\theta}_2(rad/s)$.

Figure 3 Forced pendulums oscillations.

Table I - Inverted double pendulum physical and excitation parameters

Physical parameters			Excitation parameters		
Parameter	Value	Unit	Parameter	Value	Unit
M_1	1	kg	l_c	0.075	m
M_2	1.3	kg	N	350	-
m_1	0.05	kg	I	2	A
m_2	0.08	kg	e	0.005	m
L_1	0.4	m	R	0.005	m
L_2	0.5	m	r	0.005	m
L	1.033	m	μ_0	$4\pi 10^{-7}$	TmA^{-1}
b_2	0.05	m	M_r	1.2	A/m

behaviour of the double pendulum being analysed. It shows both angular displacements (θ_1 and θ_2) and angular velocities ($\dot{\theta_1}$ and $\dot{\theta_2}$). The angular displacement θ_1 (figure 2a) presents quasiperiodic oscillations and chaotic motion. The amplitudes fluctuate between $\pm\pi rad$, abrupt reversals to indicate energy transfer among links. The angular velocity (figure 2b) $\dot{\theta_1}$ consist of spikes $\approx \pm 8rad/s$ of swift directional reversals, denoting spikes in kinetic energy.

The angular displacements of second pendulum θ_2 do exhibit less important oscillations amplitudes. Whereas $\dot{\theta_2}$ might attain extremes $\approx 14rad/s$ during chaotic motions due to nonlinear coupling effect (figure 2d).

3.2 FORCED REGIME

Figure 3a shows the angular displacement θ_1 dominated by quasiperiodic oscillations. Their amplitudes are slightly maintained then enhanced with time. Figure 3b displays the angular velocity $\dot{\theta_1}$ that is dominated by cyclical surges in kinetic energy ($\dot{\theta_1}$ between $+5.0(rad/s)$ and $-8.1(rad/s)$) that indicate momentum transfer intensified by external driving with an increase in the oscillation amplitudes afterwards $t = 21s$.

Besides, figure 3c presents the displacement of second pendulum. It oscillates around zero, with higher frequency oscillations and a significant phase lag relative to θ_1. This reflect the result of the nonlinear coupling effect between the pendulums. Whereas figure 3d deciphers the corresponding angular velocity $\dot{\theta_2}$, during the chaotic phase. When $\dot{\theta_2}$ fluctuates around zero, it shows irregular variations between $t = 0s$ and $t = 22s$. After this, a second regime appears that makes $\dot{\theta_2}$ begin to increase dramatically. It shows rapid oscillations with increasing amplitude ($> 80rad/s$).

3.3 BIFURCATION DIAGRAMS

Figure 4 illustrates the dynamics of the investigated pendulums in free and forced regimes. In fact, free vibration (figures 4a and 4b) exhibit chaotic motions leading to Hamiltonian dynamics. This means that bifurcations in the free double pendulum energy harvester are dominated mainly by energy-dependent transitions, such as libration-to-rotation changes and parameter-induced stability changes.

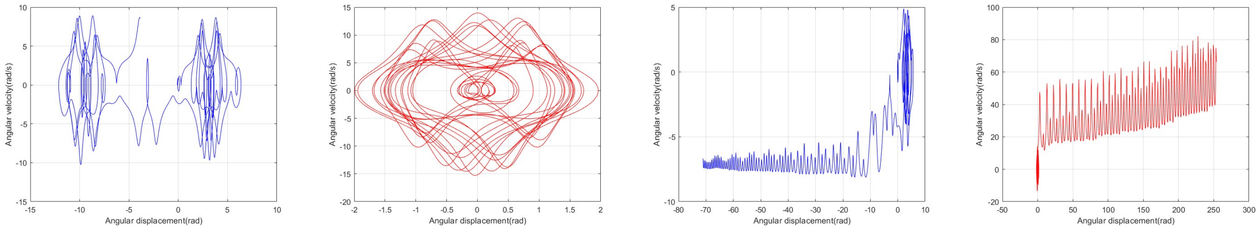

(a) $\dot{\theta}_1$ vs. θ_1.　(b) $\dot{\theta}_2$ vs. θ_2.　(c) $\dot{\theta}_1$ vs. θ_1.　(d) $\dot{\theta}_2$ vs. θ_2.

Figure 4 Phase portraits illustrating the angular velocity versus the angular displacement of the double pendulum in free vibration.

In contrast, forced regime (figures 4c and 4d) includes external energy input and leads to more structured dynamics. The phase portraits signify limit cycles which correspond to more regular responses to forcing and correspond to chaotic behaviour. Moreover the coupled motions between first and second pendulum under forced conditions show mixed-mode oscillations and intermittent chaos, with trajectories asymmetry hinting at nonlinear resonance effects as seen in the dramatic acceleration in figure 4c and the increasing amplitude of oscillations in figure 4d. The inverted double pendulum energy harvester is consequently not only governed by external excitation but also by its own parameters, such as mass distribution and link lengths, which are responsible for defining its overall behaviour.

These structural characteristics influence the nonlinear interactions of the pendulums that define their stability and capacity to maintain oscillations. In the next section we discuss how they could affect the dynamics of the inverted double pendulum energy harvester.

4 PARAMETRIC ANALYSIS

This study is based on a detailed parameters analysis in free and forced regimes. This elucidates the influence of changes in the physical parameters; pendulums masses (M_1 and M_2) and pendulums lengths (L_1, L_2 and L) on the dynamics of the inverted double pendulum energy harvester. The parameters of excitation remain the same as detailed in table I.

4.1 DOUBLE PENDULUM MASSES

4.1.1 EFFECT OF THE FIRST PENDULUM MASS

To start by considering the mass of the first pendulum, we vary M_1 while keeping all other parameters fixed in the simulations with the same initial conditions. This varying method allows us to isolate and study the influence of M_1 on the dynamic behaviour of pendulums. The simulation parameters, as outlined in the table below, include the fixed values of the physical parameters of the pendulums as well as the range of mass values that were used for the first pendulum:

Table II - Analysis of the first pendulum mass

Parameter	Value/Range	Unit
M_1	From 1.1 to 1.5(step$=0.1$)	kg
M_2	1.3	kg
m_1	0.05	kg
m_2	0.08	kg
L_1	0.4	m
L_2	0.5	m
L	1.03	m

By plotting both the curves of angular displacement and angular velocity for various masses of the first pendulum $(\theta_1, \dot{\theta}_1)$ and the second pendulum $(\theta_2, \dot{\theta}_2)$, we aim to determine how different variations in mass affect the natural dynamics and stability of the double pendulum.

In free regime, figure 5a demonstrates that increasing M_1 from $1.1kg$ to $1.5kg$ leads to smaller angular displacement of the first pendulum excepting in the case when $M_1 = M_2$.This specific value leads to chaotic movement. Figure 5b shows that the angular velocity $\dot{\theta}_1$ follows a similar trend in decrease when M_1 decreases. The angular velocity is $\dot{\theta}_1 = 9.3rad/s$ for $M_1 = 1.1kg$ and $6rad/s$ in the case of M_1.

Besides, figure 5c demonstrates that θ_2 amplitudes decrease from $1.6rad$ to $1.1rad$ when M_1 increases. Also, figure 5d indicates that $\dot{\theta}_2$ undergoes a corresponding drop in peak velocity (from $\pm 12rad/s$ to $\pm 8rad/s$). This reflects the coupled nature of the first and second pendulum.

In forced regime, figure 5e deciphers that the first pendulum has a greater angular displacement when its mass increase and attend value of $26rad$ at $M_1 = 1.5kg$. Moreover, figure 5f displays that $\dot{\theta}_1$ follows the inverse proportionality of M_1 with maximum velocities decreasing from $\pm 6rad/s$ to $\pm 4rad/s$, respectively for $M_1 = 1.1kg$ and $M_1 = 1.5kg$. Similarly, figures 5g and 5h show the decrease in displacement and velocity of the second pendulum with inverse mass-dependent phase.

4.1.2 EFFECT OF THE SECOND PENDULUM MASS

After the analysis of the effect of the mass M_1, now we analyse the effect of the mass M_2 on the dynamics of the

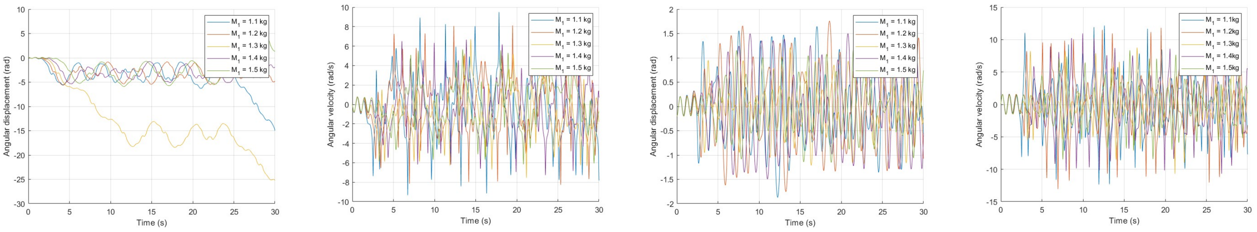

(a) θ_1. (b) $\dot{\theta}_1$. (c) θ_2. (d) $\dot{\theta}_2$.

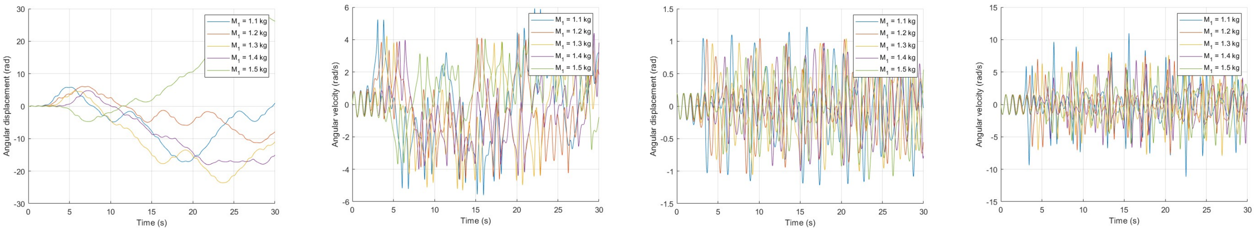

(e) θ_1. (f) $\dot{\theta}_1$. (g) θ_2. (h) $\dot{\theta}_2$.

Figure 5 Impact of varying M_1 on the double pendulum dynamics in free vibration (top row), and forced vibration (bottom row).

double pendulum. The table below provides the parameters used in this study:

Table III - Analysis of the second pendulum mass

Parameter	Value/Range	Unit
M_2	From 1.1 to 1.5(step= 0.1)	kg
M_1	1.3	kg
m_1	0.05	kg
m_2	0.08	kg
L_1	0.4	m
L_2	0.5	m
L	1.03	m

The following figures illustrate the angular displacements (θ_1, θ_2) and resulting angular velocities ($\dot{\theta}_1$, $\dot{\theta}_2$) of the double pendulum for various values of M_2.

In free regime, figure 6a illustrates that with increasing M_2 from $1.1kg$ to $1.5kg$, the angular displacement amplitude θ_1 decreases. For instance, it increases when $M_2 = M_1 = 1.3kg$ with to chaotic type of behaviour. Figure 6b shows that the angular velocity ($\dot{\theta}_1$) has little sensitivity to M_2. Furthermore, $\dot{\theta}_1$ reaches a maximum of $6rad/s$ for $M_2 = 1.1kg$, $6.9rad/s$ for $M_2 = 1.3kg$, and $9rad/s$ for $M_2 = 1.5kg$, so $\dot{\theta}_1$ increases slightly when M_2 increases. In addition, figure 6c presents at $t = 10$ s, the maximum angular displacement which is $0.27rad$ for $M_2 = 1.3kg$ and $0.19rad$ for $M_2 = 1.1kg$. So θ_2 is propositional to M_2. The angular velocity of the second pendulum $\dot{\theta}_2$ is plotted in figure 6d. It is shown that the angular velocity increases by increasing M_2. Since M_2 increases, the response becomes more intense, with maximum peaks at $M_2 = 1.5kg$, indicating greater oscillations ($\pm 12rad/s$) and energy production.

In forced regime, figure 6e presents that higher values of M_2 result in larger and longer oscillations of angular displacement (θ_1) and leads to chaotic behaviour. For example, $M_2 = 1.5kg$ has larger amplitude oscillations ($27rad$) compared to $M_2 = 1.1kg$. In addition, figure 6f indicates that higher values of M_2 create larger and more persistent oscillations in $\dot{\theta}_1$, with peaks at approximately $5.6rad/s$ for $M_2 = 1.5kg$ and $3.8rad/s$ for $M_2 = 1.1kg$.

Figure 6g also shows that higher values of M_2 produce more amplitude and longer-duration oscillations in the angular displacement θ_2 with peaks of approximately $8rad$ for $M_2 = 1.5kg$ and $0.5rad$ for $M_2 = 1.1kg$. Figure 6h demonstrates that higher values of M_2 give significant values of $\dot{\theta}_2$ and reach of around $12rad/s$ for $M_2 = 1.5kg$ and $5rad/s$ for $M_2 = 1.1kg$.

4.2 DOUBLE PENDULUM LENGTHS

4.2.1 EFFECT OF THE FIRST PENDULUM LENGTH

Having gained insight into the influence of pendulums masses on their dynamic responses, we no move on to study the effect of their lengths. Starting with investigation L_1 on the double pendulum behaviour, we use parameters values provides in the following table:

Next we plot the angular displacements (θ_1, θ_2) and angular velocities ($\dot{\theta}_1$, $\dot{\theta}_2$) of the double pendulum for each value of L_1.

In free regime, figure 7a demonstrates that when L_1 increases from $0.3m$ to $0.7m$, the angular displacement amplitudes of θ_1 increase, where peaks range from $-5rad$ to $6rad$. However θ_1 reaches its maximum ($24.5rad$) when $L_1 =$

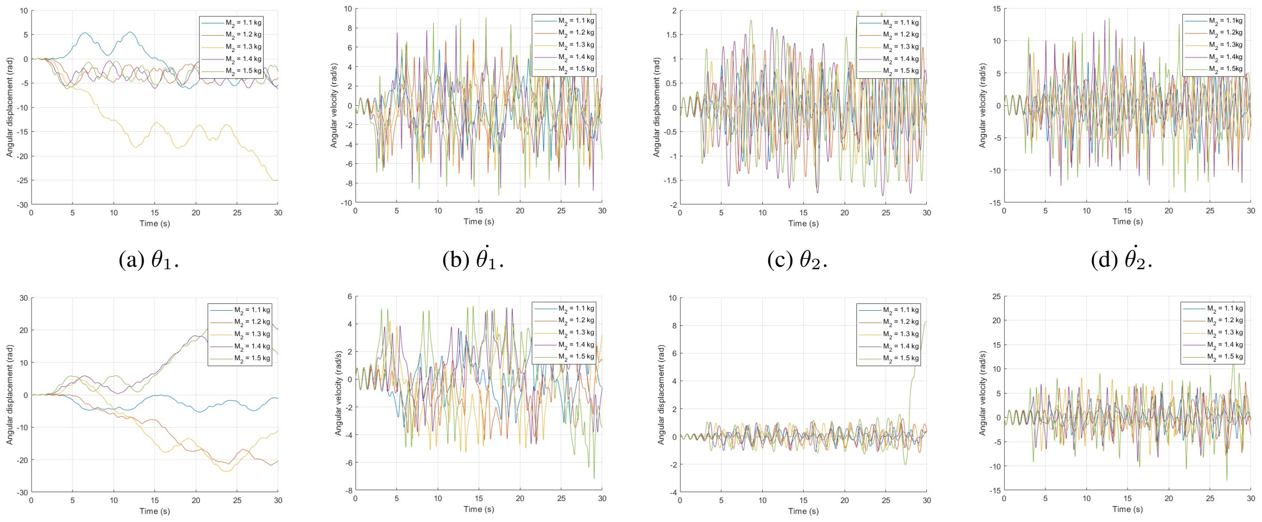

(a) θ_1. (b) $\dot{\theta}_1$. (c) θ_2. (d) $\dot{\theta}_2$.

(e) θ_1. (f) $\dot{\theta}_1$. (g) θ_2. (h) $\dot{\theta}_2$.

Figure 6 Impact of varying M_2 on the double pendulum dynamics in free vibration (top row), and forced vibration: (bottom row).

Table IV - Analysis of the first pendulum length

Parameter	Value/Range	Unit
M_1	1	kg
M_2	1.3	kg
m_1	0.05	kg
m_2	0.08	kg
L_1	From 0.3 to 0.7(step= 0.1)	m
L_2	0.5	m
L	$L_1 + L_2 + 0.13$	m

$L_2 = 0.5m$. Figure 7b illustrates that the angular velocity $\dot{\theta}_1$ is inversely proportional to L_1 with peaks increasing from $4rad/s$ for $L_1 = 0.7m$ to $15\,rad/s$ for $L_1 = 0.3m$. The oscillations for intermediate lengths, such as $L_1 = 0.4m$ and $L_1 = 0.5m$, exhibit peaks, respectively, around $10.3rad/s$ and $6\,rad/s$. Also, figure 7c shows that the angular displacement θ_2 grows with less values of L_1, with peaks increasing from $1,8rad$ for $L_1 = 0.7m$ to around $3rad$ for $L_1 = 0.3m$. Likewise, figure 7d outlines that the angular velocity $\dot{\theta}_2$ peaks at $22rad/s$ for $L_1 = 0.3m$ and $5rad/s$ for $L_1 = 0.7m$, showing that smaller lengths produce more extreme oscillations. In forced regime, figure 7e shows that larger values of L_1 result in less sustained oscillations. For instance, $L_1 = 0.3m$ exhibits larger amplitude swings up to $25rad$ compared to $L_1 = 0.7m$ at $-5, rad$. In addition, figure 7f indicates that the angular velocity $\dot{\theta}_1$ follows the same trend as θ_1, where $L_1 = 0.7m$ reaches $2rad/s$, whereas $L_1 = 0.3m$ reaches a maximum of $7.7rad/s$. Furthermore, figure 7g illustrates that the angular displacement θ_2 also grows with decreasing L_1, peaks rising for small values of L_1. In addition, figure 7h shows that the angular velocity $\dot{\theta}_2$ is increasing for a shorter length of the first pendulum. The second pendulum leads to chaotic behaviour when its displacement and velocity reach huge values when $L_1 = 0.3m$.

4.2.2 EFFECT OF THE SECOND PENDULUM LENGTH

For more investigation of the dynamics of the double pendulum, we take into account the impact of the second pendulum length L_2 on the pendulums responses. The parameters employed in this research are as summarized in the table below:

Table V - Analysis of the second pendulum length

Parameter	Value/Range	Unit
M_1	1	kg
M_2	1.3	kg
m_1	0.05	kg
m_2	0.08	kg
L_2	From 0.3 to 0.7(step= 0.1)	m
L_1	0.5	m
L	$L_1 + L_2 + 0.13$	m

Figure 8 shows the angular displacements (θ_1, θ_2) and angular velocities ($\dot{\theta}_1$, $\dot{\theta}_2$) of the double pendulum for each value of L_2.

In free regime, the angular displacement of the first pendulum θ_1 is visualized in figure 8a. It is shown that its maximum is approximately equal to $24rad$ for $L_2 = 0.5m$. When L_2 increase, θ_1 became more significative while we have the greatest range of displacement for $L_2 = 0.7m$. Additionally, figure 8b demonstrates the angular velocity $\dot{\theta}_1$ is at its highest level between $6rad/s$ and $9.3rad$,

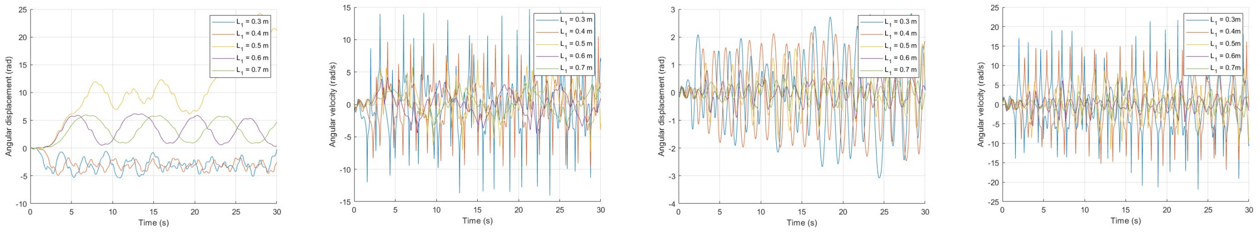

(a) θ_1. (b) $\dot{\theta_1}$. (c) θ_2. (d) $\dot{\theta_2}$.

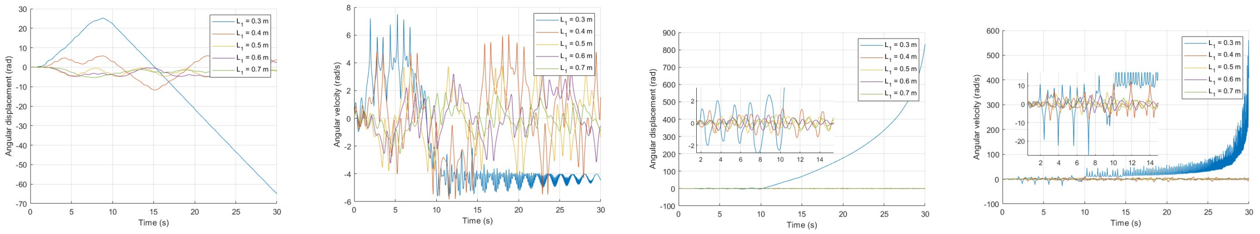

(e) θ_1. (f) $\dot{\theta_1}$. (g) θ_2. (h) $\dot{\theta_2}$.

Figure 7 Impact of varying L_1 on the double pendulum dynamics in free vibration (top row), and forced vibration: (bottom row).

with longer lengths sustaining higher angular velocities. Similarly, the angular displacement of the second pendulum θ_2 (figure 8c) is at its highest level for the greatest value of L_2. The motioned figure shows the maximum of θ_2 is $1.6rad$ for $L_2 = 0.7m$. However its minimum $0.3rad$ for $L_2 = 0.3m$. Likewise, the angular velocity of the second pendulum $\dot{\theta_1}$ has its maximum between $10rad/s$ and $12rad/s$ confirming that larger lengths foster the dynamic behaviour of the pendulums. In forced regime , the angular displacement of the first pendulum (θ_1) has a maximum value more than $40rad$ for $L_2 = 0.7m$ (figure 8e), indicating that external forcing actually enhances oscillations. Furthermore, figure 8g shows the displacement of the second pendulum θ_2 which has a maximum value of $5.2rad$ for the highest value of L_2 with the same trend of enhanced oscillation for longer lengths. The angular velocity of the primary pendulum $\dot{\theta_1}$ (figure 8f) achieves peaks between $5.5rad/s$ and $4rad$ for $L_2 = 0.7m$.

4.2.3 EFFECT OF THE PENDULUM TOTAL LENGTH

We exam the influence of the total length L of the double pendulum on its dynamic response. The following table resumes the parameters used in the current study:

Table VI - Analysis of the pendulum total length

Parameter	Value/Range	Unit
M_1	1	kg
M_2	1.3	kg
m_1	0.05	kg
m_2	0.08	kg
L_2	0.5	m
L_1	0.4	m
L	From 1.03 to 1.11(step= 0.02)	m

Figure 9 illustrates the angular displacements (θ_1, θ_2) and angular velocities ($\dot{\theta_1}$, $\dot{\theta_2}$) for each value of L.

In free regime, figure 9a shows an increase in angular displacement of first pendulum θ_1 amplitudes when $L = 1.05m$ and $L = 1.09m$ lead to chaotic motion. The angular velocity $\dot{\theta_1}$ are given respectively $-17.7rad$ and $8.36rad$. For the rest of the values of L; the first pendulum oscillates between $-0.0rad$ and $-5.9rad$. However, angular velocity of the first pendulum is less sensible in varying L then its displacement when $\dot{\theta_1}$ fluctuates between $-10.7rad/s$ and $+10.7rad/s$ for all values of L. The figure 9c demonstrates that the highest value of θ_2 is equal to $\pm 2.5rad$ for $L = 1.11m$. When $L = 1.03m$, $\theta_2 = \pm 2.4rad$ and the minimum values of θ_2 are given for $L = 1.05m$. The angular velocity $\dot{\theta_2}$ is also less sensible to the pendulum total length. Meanwhile, figure 9d shows $\dot{\theta_2}$ varying between $\pm 10rad/s$ for $L = 1.09m$ and $\pm 18.8rad/s$ for $L = 1.11m$. In forced regime, figure 9e demonstrates that increasing L leads θ_1 to become higher. It then reaches $-63.2rad$ when $L = 1.11m$ and leads to an unstable and chaotic motions. In contrast, figure 9f shows that $\dot{\theta_1}$ is inversely proportional to L ([when $L = 1.03m$ that $\dot{\theta_1} = \pm 6rad/s$] and [when $L = 1.11m$ that $\dot{\theta_1} = -6.2rad/s$ and $+4.2rad/s$]).

The dynamic of the second pendulum is also inversely proportional to L when θ_2 reaches its maximum at $\pm 1.74rad$ (figure 9g) and $\dot{\theta_2}$ vary between $-10rad/s$ and $+17.12rad/s$ (figure 9h) when $L = 1.11m$.

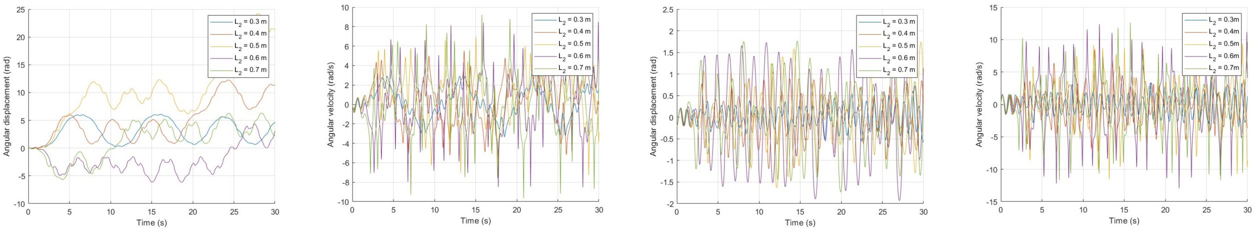

(a) θ_1. (b) $\dot{\theta}_1$. (c) θ_2. (d) $\dot{\theta}_2$.

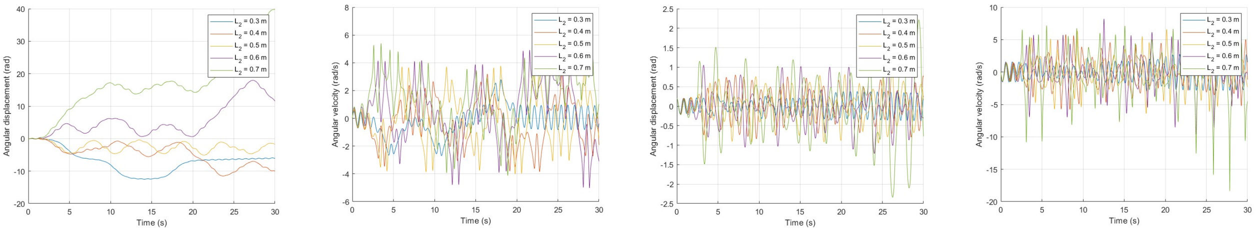

(e) θ_1. (f) $\dot{\theta}_1$. (g) θ_2. (h) $\dot{\theta}_2$.

Figure 8 Impact of varying L_2 on the double pendulum dynamics in free vibration (top row), and forced vibration (bottom row).

4.3 OPTIMAL ENERGY

The parameters analysis of the inverted double pendulum energy harvester indicates that the masses and lengths have a significant impact on its response. An increase in the mass of the first pendulum (M_1) from $1.1kg$ to $1.5kg$ reduces amplitudes oscillations of both first and second pendulums, and chaotic motion is observed when $M_1 = M_2 = 1.3kg$. The dynamics of the second pendulum are also affected with θ_2 and $\dot{\theta}_2$ experiencing lower amplitudes and velocities as M_1 increases. Add to that, in free vibration, (M_2) dominates the dynamic of pendulums, with increasing values of M_2 influencing energy transfer and oscillations intensity. For instance, $\dot{\theta}_1 = 9rad/s$ for $M_2 = 1.5kg$, but $\dot{\theta}_1 = 6rad/s$ for $M_2 = 1.1kg$, while θ_2 and $\dot{\theta}_2$ exhibit more intense oscillations. Forced pendulums experience chaotic behaviour when M_2 assumes higher values. By introducing lower values of $L_1(0.3m)$ in free vibration we obtain greater angular velocities ($\dot{\theta}_1 = 15rad/s$). Greater lengths ($L_1 = 0.7m$) sustain oscillations longer but reduce peaks velocities and amplitudes. Forced vibration exhibits chaotic motion for lower values of L_1. The dynamic behaviour of the double pendulum is also enhanced by the L_2, where the highest value of θ_1 was $24rad$ when $L_2 = 0.5m$ and $\dot{\theta}_2 = 22rad/s$ when $L_2 = 0.3\,\text{m}$. Forced vibration exhibits more intense oscillations, with $\theta_1 > 40rad$ when $L_2 = 0.7m$. The pendulum total length L has a lesser effect on the pendulums responses compared to the rest of physical parameters. Indeed, for the free vibrations, the larger the length L, the smaller the angular displacement and angular velocity. However, for the forced inverted double pendulum energy harvester, this tendency is reversed, where angular displacement and angular velocity reach their highest values when $L = 1.11m$. This is because of the proportionality of the excitation force to the pendulum length total L. Furthermore, increasing L leads to increasing the distance a, which justifies the relation between L and pendulum angular displacement and velocity. In our research, we analysed the impact of the physical parameters of the double pendulum: M_1, M_2, L_1, L_2, and L. Five values were retained for each parameter, and angular displacement and angular velocity were plotted for every case. If we seek the optimal energy with the relevant parameters using the same way, 55 combinations are to be explored. To facilitate the task, we directly try the optimal values found previously to seek the double pendulum optimal energies. According to the above findings, it is evident to make the convenient selection of the optimal parameters that yield to maximum mechanical energy in both the free and forced inverted double pendulum energy harvester configurations. The mechanical energy is the sum of kinetic and potential energy. It is described by the following equation:

$$
\begin{aligned}
E = {} & \frac{1}{2}(M_1 L_1^2 + \frac{m_1 L^2}{12} + m_1(\frac{L}{2} - L_1)^2)\dot{\theta_1}^2 \\
& + \frac{1}{2}M_2((L-L_1)^2\dot{\theta_1}^2 + L_2^2\dot{\theta_2}^2 \\
& + 2(L-L_1)L_2\dot{\theta_1}\dot{\theta_2}\cos(\theta_1+\theta_2)) \\
& + \frac{1}{2}m_2((L-L_1)^2\dot{\theta_1}^2 + \frac{L_2^2}{4}\dot{\theta}_2^2 \\
& + (L-L_1)L_2\dot{\theta_1}\dot{\theta_2}\cos(\theta_1+\theta_2)) + \frac{1}{2}m_2\frac{L_2^2}{12}\dot{\theta}_2^2 \\
& + g\cos\theta_1((M_2+m_2)(L-L_1) - m_1(\frac{L}{2} - L_1) - M_1 L_1) \\
& - g\cos\theta_2(M_2 + \frac{m_2}{2})L_2
\end{aligned}
\tag{19}
$$

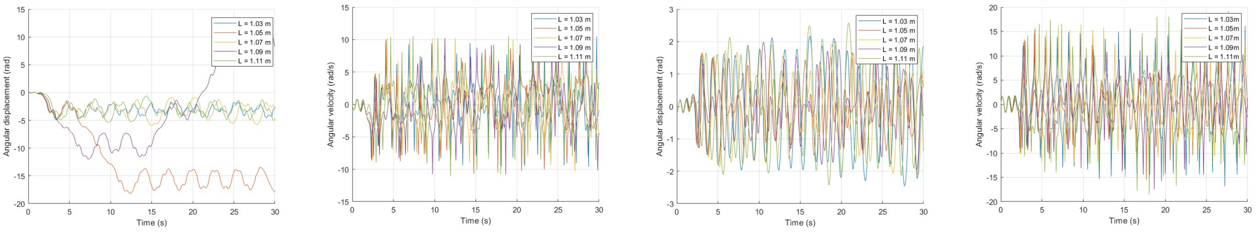

(a) θ_1. (b) $\dot{\theta_1}$. (c) θ_2 (d) $\dot{\theta_2}$.

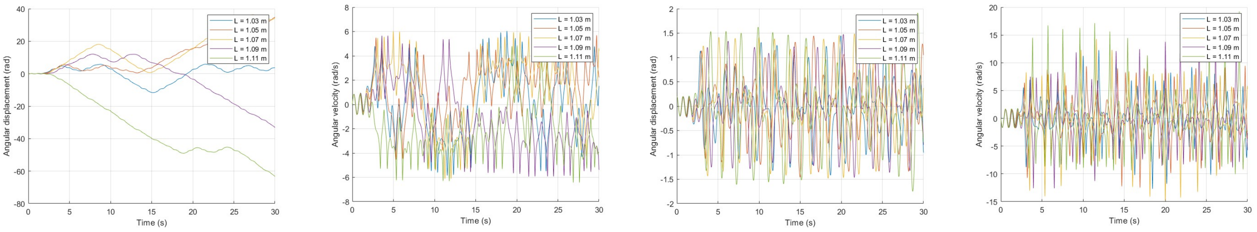

(e) θ_1. (f) $\dot{\theta_1}$. (g) θ_2. (h) $\dot{\theta_2}$.

Figure 9 Impact of varying L on the double pendulum dynamics in free vibration (top row), and forced vibration: (bottom row).

Equation 19 shows that the mechanical energy is a function ultimately of the square of the angular velocities and $\dot{\theta_1}\dot{\theta_2}$. Contrary to this, the angular displacement have lesser impact than angular velocities because they essentially influence the dynamical behaviour of double pendulum as well as the coupling effect on first and second pendulum. Their contribution appears mainly within cosine function ($cos(\theta_1 + \theta_2)$). This justify optimal parameters shown in the following table and used to achieve maximum mechanical energy in free and forced vibrations.

Table VII - The optimal values of the double pendulum parameters

Free vibration			**Forced vibration**		
Parameter	**Value**	**Unit**	**Parameter**	**Value**	**Unit**
M_1	1.1	kg	M_1	1.1	kg
M_2	1.5	kg	M_2	1.5	kg
L_1	0.3	m	L_1	0.3	m
L_2	0.7	m	L_2	0.7	m
L	1.03	m	L	1.11	m

The following simulations illustrate the produced energy by the inverted double pendulum for both free and forced vibrations that its physical parameters indicated in table VII: The plots above illustrate that the kinetic energy T controls the entire mechanical energy derived from the inverted double pendulum energy harvester. In free regime, T reaches $23.89J$, while the total mechanical energy E takes the maximum value of $26.3J$. In contrast, the potential energy V does not exceed $3.11J$. The same relation- ship remains in the case of forced vibration. That is, the total energy E is $643.61J$ with $T = 642.61J$, while the maximum value of V is $2J$. The excitation force does not only influence the dynamics of the pendulums but also their total mechanical energy. Indeed, the produced energy in the forced vibration is approximately 26.94 times greater than that of the free regime. In forced regime, the produced energy has a clear tendency to increase with time. In fact, the kinetic energy peaks increase more and more steeply for each successive peak, and with it, the total mechanical energy increases correspondingly. This trend is particularly evident if we examine minimum points of kinetic energy following each successive peak. They increase with time and tend to do so more and more steeply, since they interval between successive peaks tends to become shorter.

5 CONCLUSION

Green and clean energy harvesting has been of interest owing to exploit renewable energies and avoid pollutant sources. Double pendulums have high potential for energy harvesting due to their nonlinear dynamics and especially their chaotic behaviour. The goal of this study was to investigate a novel double pendulum energy harvester. The double pendulum is inverted and is explored in free and forced regimes. First, we presented the double pendulum design and the governing equations, in free and forced regimes. Second, we analysed the double pendulum oscillations and bifurcations. Third, we conducted a parametric study to explore the effect of varying the double pendulum parameters: masses and lengths. Last, we presented the produced optimal energies, in free and forced regimes. The double pendulum was described in free and forced regimes. An electric coil and a permanent magnet were used in forced regime. The

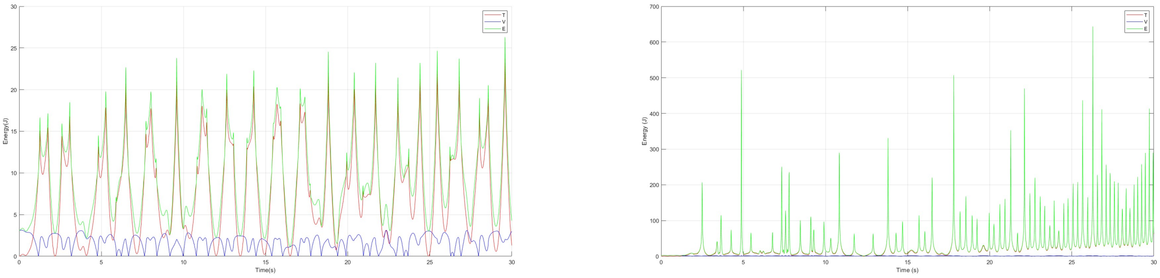

(a) Free vibration for $M_1 = 1.1\,\mathrm{kg}$, $M_2 = 1.5\,\mathrm{kg}$, $L_1 = 0.3\,\mathrm{m}$, $L_2 = 0.7\,\mathrm{m}$, and $L = 1.03\,\mathrm{m}$.

(b) Forced vibration for $M_1 = 1.1\,\mathrm{kg}$, $M_2 = 1.5\,\mathrm{kg}$, $L_1 = 0.3\,\mathrm{m}$, $L_2 = 0.7\,\mathrm{m}$, and $L = 1.11\,\mathrm{m}$.

Figure 10 Converted energy by the double pendulum.

equations of motion were discussed in terms of Euler-Lagrange formalism. The equations were solved numerically with computation software by fourth-order Runge-Kutta method under the same conditions. Results showed the coupling effect on pendulums dynamic behaviour. In free oscillation, angular displacement and velocity revealed quasiperiodic and chaotic behaviours with unstructured and unstable dynamics. In forced oscillation, double pendulum motion is more structured and stable, it is of two phases: quasiperiodic at the beginning, and chaotic after that. The behaviour is well illustrated in the bifurcations. The parameters analysis indicates that the pendulums masses and lengths variation have a major impact on the dynamics of the double pendulum. The increase of the first pendulum mass significantly decreases angular velocity amplitudes. Whereas increasing the second pendulum mass increases angular velocity amplitudes. Similarly, short first pendulum length yields to higher angular velocities. Also, long second pendulum length leads to higher angular velocities. Studying the effect of each physical parameter leads to the optimal produced energies. The results show that kinetic energy dominates potential energy. At free and forced regimes, the converted energy experiences peaks due to chaos, while the forced regime produced energy is neatly promising than the free regime produced energy. The double pendulum nonlinearity leads to quasiperiodic and chaotic responses. The findings reveal that it is possible to tune the double pendulum parameters toward maximizing the converted energy. The variability analysis is to be followed by a sensitivity analysis to investigate the impact of the optimal parameters possible uncertainties. Furthermore, an experimental study is to be conducted to confirm the analytical modelling and the numerical analysis. These two important issues will be addressed in the future.

REFERENCES

[1] Montoya, J. A., Mariscal, D. M., and Romero, E., *Energy harvesting from human walking to power biomedical devices using oscillating generation*, in *2016 38th Annual International Conference of the IEEE Engineering in Medicine and Biology Society (EMBC)*, 2016, pp. 4951–4954.

[2] Viñolo, C., Toma, D., Mànuel, A., and del Rio, J., *Sea motion electrical energy generator for low-power applications*, in *2013 MTS/IEEE OCEANS-Bergen*, 2013, pp. 1–7.

[3] Abbas Hassan, S., Osman, T., Khattab, A., Arafa, M., and Abdelnaby, M. A., *Design of a self-tunable, variable-length pendulum for harvesting energy from rotational motion*, *Journal of Vibroengineering*, 2020, vol. 22, no. 6, pp. 1309–1325.

[4] Hao, C., He, J., Zhang, Z., Yuan, Y., Chou, X., and Xue, C., *A pendulum hybrid generator for water wave energy harvesting and hydrophone-based wireless sensing*, *AIP Advances*, 2020, vol. 10, no. 12.

[5] Geisler, M., Boisseau, S., Perez, M., Gasnier, P., Willemin, J., Ait-Ali, I., and Perraud, S., *Human-motion energy harvester for autonomous body area sensors*, *Smart materials and structures*, 2017, vol. 26, no. 3, pp. 035028.

[6] Kecik, K., and Mitura, A., *Nonlinear dynamics of a vibration harvest-absorber system. Experimental Study*, in *Dynamical Systems: Modelling: Łódź, Poland, December 7-10, 2015*, Springer, 2016, pp. 197–208.

[7] Caliò, R., Rongala, U. B., Camboni, D., Milazzo, M., Stefanini, C., De Petris, G., and Oddo, C. M., *Piezoelectric energy harvesting solutions*, *Sensors*, 2014, vol. 14, no. 3, pp. 4755–4790.

[8] Kumar, R., Gupta, S., and Ali, S. F., *Energy harvesting from chaos in base excited double pendulum*, *Mechanical Systems and Signal Processing*, 2019, vol. 124, pp. 49–64.

[9] Xu, P., Chen, Y., Wu, H., Dai, Y., and Li, K., *Chaotic motion behaviors of liquid crystal elastomer pendulum under periodic illumination*, *Results in Physics*, vol. 56, p. 107332, 2024.

[10] Khan, M. Z. A., Khan, H. A., and Aziz, M., *Harvesting energy from ocean: Technologies and perspectives*, *Energies*, 2022, vol. 15, no. 9, p. 3456.

[11] Zhang, Y., Wang, W., Zheng, R., Nakano, K., and Cartmell, M. P., *A piezoelectric cantilever-asymmetric-conical-pendulum-based energy harvesting under multi-directional excitation*, *Journal of Sound and Vibration*, 2024, vol. 569, p. 118080.

[12] Rocha, R. T., Balthazar, J. M., Tusset, A. M., and Piccirillo, V., *Using passive control by a pendulum in a portal frame platform with piezoelectric energy harvesting*, *Journal of Vibration and Control*, 2018, vol. 24, no. 16, pp. 3684–3697.

[13] Li, H., and Qin, W., *Nonlinear dynamics of a pendulum-beam coupling piezoelectric energy harvesting system*, *The European Physical Journal Plus*, 2019, vol. 134, no. 12, p. 595.

[14] Fu, H., Jiang, J., Hu, S., Rao, J., and Theodossiades, S., *A multi-stable ultra-low frequency energy harvester using a nonlinear pendulum and piezoelectric transduction for self-powered sensing*, *Mechanical Systems and Signal Processing*, 2023, vol. 189, p. 110034.

[15] Pan, J., Qin, W., Deng, W., Zhang, P., and Zhou, Z., *Harvesting weak vibration energy by integrating piezoelectric inverted beam and pendulum*, *Energy*, 2021, vol. 227, p. 120374.

[16] Chen, X., Gao, L., Chen, J., Lu, S., Zhou, H., Wang, T., Wang, A., Zhang, Z., Guo, S., Mu, X., and others, *A chaotic pendulum triboelectric-electromagnetic hybridized nanogenerator for wave energy scavenging and self-powered wireless sensing system*, *Nano Energy*, 2020, vol. 69, p. 104440.

[17] Ren, Z., Liang, X., Liu, D., Li, X., Ping, J., Wang, Z., and Wang, Z. L., *Water-wave driven route avoidance warning system for wireless ocean navigation*, *Advanced Energy Materials*, 2021, vol. 11, no. 31, p. 2101116.

[18] Zhang, C., He, L., Zhou, L., Yang, O., Yuan, W., Wei, X., Liu, Y., Lu, L., Wang, J., and Wang, Z. L., *Active resonance triboelectric nanogenerator for harvesting omnidirectional water-wave energy*, *Joule*, 2021, vol. 5, no. 6, pp. 1613–1623.

[19] Janzen, F. C., Tusset, A. M., Balthazar, J. M., Rocha, R. T., Lima, J. J. de, and Nabarrete, A., *Offshore energy harvesting of a marine floating pendulum platform model*, *Latin American Journal of Solids and Structures*, 2019, vol. 16, no. 01, p. e118.

[20] Yurchenko, D., and Alevras, P., *Parametric pendulum based wave energy converter*, *Mechanical Systems and Signal Processing*, 2018, vol. 99, pp. 504–515.

[21] Ding, W., Song, B., Mao, Z., and Wang, K., *Experimental investigations on a low frequency horizontal pendulum ocean kinetic energy harvester for underwater mooring platforms*, *Journal of Marine Science and Technology*, 2016, vol. 21, pp. 359–367.

[22] Li, Y., Guo, Q., Liu, H., Chen, T., Sun, L., Ma, X., and Chen, Z., *Design and experiment of an ultra-low frequency pendulum-based wave energy harvester*, in *2019 IEEE 14th International Conference on Nano/Micro Engineered and Molecular Systems (NEMS)*, 2019, pp. 101–104.

[23] Castagnetti, D., *A simply tunable electromagnetic pendulum energy harvester*, *Meccanica*, 2019, vol. 54, no. 6, pp. 749–760.

[24] Shen, W., Zhu, S., and Xu, Y., *An experimental study on self-powered vibration control and monitoring system using electromagnetic TMD and wireless sensors*, *Sensors and Actuators A: Physical*, 2012, vol. 180, pp. 166–176.

[25] Wu, Y., Qiu, J., Ji, H., and Zhou, S., *Piezoelectric spring pendulum oscillator for animal/human motion energy harvesting*, *2018 IEEE/ASME International Conference on Advanced Intelligent Mechatronics (AIM)*, 2018, pp. 774–779.

[26] Kim, H., and Lee, S., *A study on the efficiency in the energy harvesting device using resonance of pendulum*, *Applied Sciences*, vol. 12, no. 22, p. 11862, 2022.

[27] Paul, B., Pal, S., Agrawal, A., and Trivedi, G., *Triple pendulum based nonlinear chaos generator and its applications in cryptography*, *IEEE Access*, vol. 10, pp. 127073–127093, 2022.

[28] Avanço, R. H., Tusset, A. M., Suetake, M., Navarro, H. A., Balthazar, J. M., and Nabarrete, A., *Energy harvesting through pendulum motion and DC generators*, *Latin American Journal of Solids and Structures*, vol. 16, e150, 2019.

[29] Avanço, R. H., Balthazar, J. M., Tusset, Á. M., and Ribeiro, M. A., *Short comments on chaotic behavior of a double pendulum with two subharmonic frequencies and in the main resonance zone*, *ZAMM-Journal of Applied Mathematics and Mechanics/Zeitschrift für Angewandte Mathematik und Mechanik*, 2021, vol. 101, no. 12, e202000197.

[30] Cai, Q., and Zhu, S., *Applying double-mass pendulum oscillator with tunable ultra-low frequency in wave energy converters*, *Applied Energy*, vol. 298, 117228, 2021.

[31] Cai, Q., and Zhu, S., *Nonlinear double-mass pendulum for vibration-based energy harvesting*, *Nonlinear Dynamics*, vol. 112, no. 7, pp. 5109–5128, 2024.

[32] Zaouali, E., Najar, F., and Kacem, N., *Nonlinear dynamics of a double pendulum energy harvesting device for continuously rotating systems*, *Physica Scripta*, vol. 99, no. 6, 065273, 2024.

[33] Jia, J., and Zhang, Y., *Heat flux and pressure reduction using aerospike and counterflowing jet on complex hypersonic flow*, *International Journal of Aeronautical and Space Sciences*, 2020, vol. 21, no. 2, pp. 337–346.

ISSN 1590-8844
International Journal of Mechanics and Control, Vol. 26, No. 02, 2025
https://doi.org/10.69076/jomac.2025.0026

CFD-BASED DESIGN AND OPTIMIZATION OF A CRYOGENIC PISTON VALVE FOR LIQUID HYDROGEN FLOW CONTROL

Arash Safaei* Matteo Davide Lorenzo Dalla Vedova* Paolo Maggiore*

* Department of Mechanics and Aerospace Engineering, Politecnico di Torino, Italy

ABSTRACT

Thanks to their reliability and accuracy, piston valves are widely used in pressure regulation systems. This is especially true in the aerospace sector, where cryogenic fluids such as liquid hydrogen are commonly handled, making the design and operation of these valves particularly critical. However, the development of piston valve technology for cryogenic applications is still relatively limited, mainly because of the challenges involved in creating systems that can operate reliably in such harsh conditions. This highlights the need for more detailed studies and simulations using CFD tools and predictive models. To achieve efficient and stable performance of a piston pressure-regulating valve in a cryogenic environment, it is essential to understand both the strengths and the limitations of this technology under extreme thermal and mechanical loads. The work presented here focuses on a preliminary analysis and optimization of a piston valve operating with liquid hydrogen for pressure control purposes. Special attention is given to the dynamic behavior of the piston body, particularly regarding the robustness and controllability of its response. The study explores the motion of the piston in a low-viscosity flow, as well as the thermodynamic and fluid-dynamic characteristics of the valve system. Flow field simulations are carried out using CFD tools, and the results are combined with system response data obtained from a Simulink dynamic model. Finally, the outcomes are critically analysed to identify the regions where the valve is most affected by thermal and mechanical stresses, suggesting possible design improvements.

Keywords: aerospace systems, CFD analysis, cryogenic hydrogen, fluids, simplified fluid dynamic numerical models

1 INTRODUCTION

Piston valves are fundamental components in pressure regulation systems across various sectors, including aerospace, aeronautics, and energy. Their capacity to maintain accurate control over fluid pressure is particularly critical when dealing with cryogenic media such as liquid hydrogen, which exhibits extremely low temperatures and distinctive fluid-dynamic behaviour. Nonetheless, operating piston valves under such extreme conditions introduces several engineering challenges, primarily related to the handling and control of cryogenic fluids. Liquid hydrogen, widely employed as a propellant in aerospace propulsion systems, exhibits thermophysical properties that differ substantially from those of fluids at ambient temperature.

When gases are cooled to cryogenic levels, they condense into highly dense liquids, resulting in pronounced variations in parameters such as density, viscosity, and thermal expansion. These specific features constitute fluid dynamic challenges for pressure piston valves designed for fluids with more conventional properties. In addition, thermal contraction of valve components can affect tolerances and clearances, thereby compromising the functionality of the valve. Furthermore, liquid hydrogen has an exceedingly low viscosity compared to fluids at ambient temperature. This low-viscous fluid has the potential to influence the fluid's flow behavior within the valve, resulting in flow restrictions, pressure drops, and increased wear and strain on valve components. In such circumstances, maintaining precision pressure control becomes even more crucial.

Cryogenic fluids have a natural tendency to boil and vaporize when exposed to higher temperatures. This can occur during the pressure reduction procedure or even when the flow reaches high velocities, resulting in phase changes within the valve itself. These phase changes can destabilize the flow control mechanisms and make it difficult to maintain precise pressure regulation.

Contact author: Arash Safaei[1]

[1] C.so Duca degli Abruzzi 24, 10129, Turin, Italy.
E-mail: arash.safaei@polito.it

This study therefore concentrates on a preliminary CFD-based analysis and optimization of a piston valve operating with liquid hydrogen, aimed at addressing the complex fluid-dynamic phenomena associated with cryogenic conditions. A simplified dynamic model of the piston's response is subsequently developed for both the optimized and non-optimized configurations, allowing a comparative evaluation of the valve's regulating performance and overall efficiency. The analysis begins by creating a simplified geometry, suitable for the CFD analysis, of the main piston body of a generic pressure regulating valve. By simulating the behaviour of liquid hydrogen flow across the piston's body, it is then shown how the results of the performed CFD simulations provide a clear visualization of the critical aspects such as flow patterns, pressure distribution, velocity flow field and recirculating zones.

2 PROBLEM ANALYSIS AND OPTIMIZATION

The analysis and optimization of the simplified piston valve architecture (Fig. 1) carried out in this work are grounded in fundamental fluid-dynamic principles and in the physics governing flow through constricted passages. To optimize a conventional pressure-regulating valve for cryogenic applications, a thorough understanding of its individual components, along with their respective advantages and limitations, is essential. A pressure regulating valve can govern the fluid pressure of a feeding system using the mechanical forces acting on a control spring and the relative movement of the commanded piston. This is accomplished by adjusting the valve's opening to balance the forces operating on the piston itself, thereby maintaining a stable and controlled outlet port pressure. This kind of valve is commonly used in numerous industries to maintain the desired pressure levels in fluid systems. If the pressure at the outlet port fluctuates, owing to recirculation zones or chaotic velocity field downstream the control surfaces, the piston's position will start to change continuously to maintain the desired pressure. If the outlet pressure falls below the set pressure, the piston will move to allow more fluid to pass and increase the pressure. Instead, if the outlet pressure exceeds the specified pressure set value, the piston will move to restrict the flow and therefore to counterbalance this perturbation. The formation of flow recirculation regions and pronounced local pressure drops within a pressure-regulating valve represents a critical phenomenon, as it can strongly influence the system's thermal behaviour and dynamic stability, ultimately affecting the overall performance of the regulating mechanism. Complex fluid dynamics, valve geometry, and operational conditions frequently give rise to these two phenomena, which are closely related. Understanding the impact of these criticalities is essential for comprehending their potential effects on operating efficiency, safety, and valve's integrity. Fluid recirculation zones are regions within and around the valve where fluid flow reverses or becomes stagnant, instead of passing smoothly through the valve. Such regions may develop due to several factors, including suboptimal valve geometry, unsuitable flow conditions, or specific fluid properties that promote turbulence and flow separation [1]. These effects can, in turn, generate localized heat transfer issues within the system. Fluids that are stagnant or move slowly can cause temperature stratification, leading to the freezing or overheating of valve components. These thermal variations can compromise the structural integrity and functionality of the valve and its surrounding components [2]. In addition, fluid recirculation zones frequently cause pressure fluctuations and instability downstream of the valve. As the fluid flow becomes erratic, pressure levels may fluctuate, influencing the valve's overall pressure regulation performance. These fluctuations may lead to pressure levels outside of the designed range, compromising the safety and reliability of the system. The stagnant or reversing flow can transport abrasive particles or contaminants that damage the valve's internal surfaces. This erosion may reduce the valve's efficiency and performance over time, necessitating maintenance and possible component replacement, particularly when dealing with cryogenic fluids such as liquid hydrogen. Large localized pressure drops can induce cavitation, which occurs when the fluid pressure falls below the vapor pressure, resulting in the formation and disintegration of vapor bubbles. This process of cavitation generates intense pressure waves and vibrations that can cause damage to the valve and adjacent components [3-4]. In addition, a significant localized pressure drop might interfere with the controllability of the valve. As unexpected pressure drops occur, the valve may struggle to maintain its desired pressure setpoint, resulting in system instability and fluctuations [5]. For the aforementioned reasons, it is crucial to develop valve architectures and mechanisms capable of minimizing the effects of these critical phenomena. As a starting point for the present analysis, a pressure drop of 23 bar is imposed across the entire system, with liquid hydrogen serving as the working fluid. The initial geometry of the piston valve, together with the specified boundary pressure drop and the no-slip wall condition, define and close the fluid-dynamic problem. Subsequently, the key parameters are evaluated, including the total force acting on the piston, F, as well as the pressure and velocity distributions along the piston body, obtained from the CFD analysis.

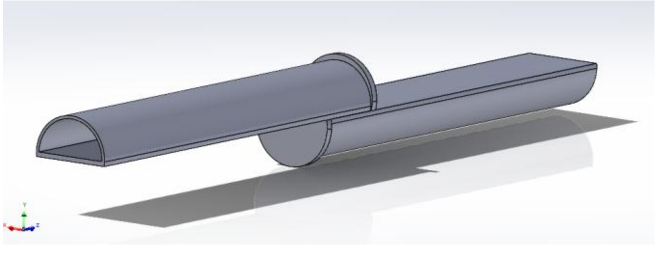

Figure 1 Three-dimensional representation of the simplified valve geometry.

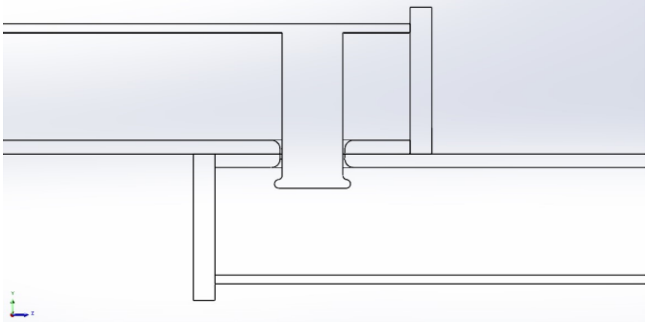

Figure 2 Cross section of the simplified valve geometry.

Determining the total force *F* acting on the piston body is a key step in evaluating the dynamic response of the system, particularly in terms of the position and velocity of the regulating mechanism. This force serves as input parameter for the Simulink-based dynamic model; therefore, its accurate estimation through CFD fluid-dynamic simulations is essential to ensure the reliability and precision of the modelling outcomes. Regarding the piston body, an effective aspect of the fluid-dynamic and mechanical optimization involves the thickness of its stem. A thicker piston stem provides the advantage of reducing the traction force exerted by the fluid flow, since the effective area of the annular surface on which the flow acts is smaller. Consequently, the piston experiences lower mechanical stress, which contributes to improved durability and operational lifespan. Moreover, having a thicker stem gives more inertia to the piston, and its robustness contribute to making it less sensitive to possible imbalance of forces with respect to a thinner and less inert piston. In addition, the distributed load of the flow along the stem, which causes a bending moment on the stem itself, causing it to deflect, is smaller if the resistant section of the stem is larger. For this reason, the proposed simplified architecture features a central piston body designed with a robust and carefully optimized geometry, allowing the cryogenic fluid to flow through it smoothly without encountering sharp edges or abrupt geometric variations. Such design considerations help prevent flow separation or the formation of recirculation zones near the crown orifice, which plays a key role in governing the pressure reduction process. Another optimization performed in this work on the valve design is the piston body passing through the conventional orifice which divides downstream from upstream, to create a circular crown-shaped zone for the passage of the flow (Fig. 3). This area shall be designed in such a way that the flow has a reduction of pressure equal to that set by design: in this way, if the piston regulating mechanism is to suffer a damage and therefore no longer work efficiently, the piston would still remain in axis providing the demanded area to reduce the upstream flow pressure to the desired value of downstream. This solution, properly implemented from an engineering point of view (i.e. by connecting the piston axis to a guide to maintain the axis straight), allows for a more robust and reliable pressure regulating mechanism, decoupling the pressure reduction function from that of regulation in case of system failures.

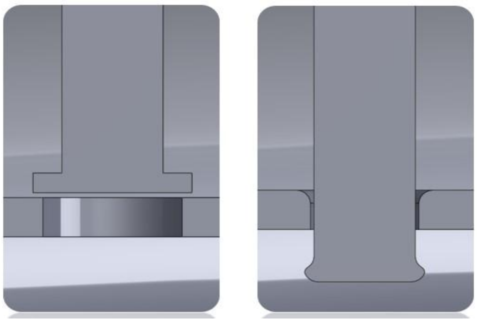

Figure 3 Comparison between the non-optimized piston body (left) and the optimized design (right).

As demonstrated by the CFD analysis results, the optimized piston configuration, which is featuring a body that passes through the circular crown orifice, experiences a lower overall force acting upon it, which is also significantly more stable over time compared to the total force observed in the conventional design, where the piston pushes directly toward the orifice (Fig. 3, left). A more constant force acting on the piston results in reduced oscillations during the pressure regulation phase, thereby improving the valve performance. Furthermore, if the total force acting on the piston is small enough, the piston inertia, combined with the action of the control spring and the viscous force of the flow, more effectively dampen the movement of the piston itself, reaching the desired equilibrium position with a contained number of oscillations compared to the non-optimized case.

2.1 NUMERICAL MODEL

In valve design, dedicated damping devices are seldom employed, as the combined influence of flow resistance and viscous effects inherently provides sufficient damping action [6]. For this reason, damping effect will not be considered as caused by a physical damper in the model, but from the viscous action of the liquid hydrogen flow.

In the mathematical differential model of the problem, the effect of the downstream and upstream flow acting on the piston body is taken into consideration. To assess the performance of the valve, it is mandatory to calculate the time required for the piston to reach its equilibrium position, which is a function of the resultant total force *F*, input of the model. The characteristic time of the system is the time it takes for the piston to reach the equilibrium position required to achieve the set pressure reduction and maintain that value. Therefore, a pressure regulating valve with high performance is desired to respond quickly to a pressure perturbation while maintaining the shortest possible characteristic time. The simplified model of the optimized pressure-regulating valve can be idealized as a mass–spring–damper system, where the mass corresponds to the piston body, the damping effect arises from the viscous action of the flow passing through the valve, and the spring represents the mechanical element governing the piston position during the regulation phase. Consequently, the overall system can be described by a second-order differential equation of the classical form:

$$M\ddot{x} + C\dot{x} + Kx = F_{tot} \tag{1}$$

where M represents the mass of the piston, C the viscous coefficient, K the stiffness of the control spring, while the variable x represents the position of the piston under the action of the total force F_{tot}. It must be clearly considered that the displacement of the piston governs the relationship between the volume flow rate and the pressure drop across the valve, through the relation:

$$Q = C_d A\sqrt{\frac{2\,\Delta p}{\rho}} = C_d 2\pi r x\sqrt{\frac{2\,\Delta p}{\rho}} \tag{2}$$

where C_d is the discharge coefficient of the valve, r is the radius of the orifice, x is the displacement of the piston (which can be considered as the height of the geometrical cylinder which stands between the piston's plate and the orifice opening), Δp the pressure drop across the orifice and ρ the density of the fluid, in this case liquid hydrogen. The above equation shows how the maximum value of the volume flow rate Q is directly proportional to the displacement x the piston undergoes during the pressure regulation. This means that to each displacement x of the piston corresponds a maximum volume flow rate Q that can cross the circular crown orifice of the valve with a resulting drop of Δp. Therefore, if the downstream volume flow rate drops below the maximum value reported in Eq. (2), the downstream pressure will consequently rise, and this will cause the piston to move toward the closure of the valve, with a decrease in its displacement x as well as the flow passage area A. This displacement will directly lead to a further pressure decrease below the set value of Δp, hence regulating the pressure level as a function of the downstream flow condition of the valve. The objective of the implemented numerical model is therefore to compute the piston displacement x during the pressure regulation process, as obtained from the solution of the differential equation reported in Eq. (1). If the computed value x is consistent with the solution of Eq. (2), then the model will be able to forecast faithfully the physics of the system, allowing further assessments on the real dynamics of the valve's response starting from the theoretical implemented numerical model. To set properly the input total force F_{tot} in Eq. (1), a CFD analysis should be carried out, calculating the force contributions that act on the piston's body. These contributions can be then put into the model implemented on Simulink, which will simulate the dynamics of the system. For the complete definition of the dynamic model, the parameters of mass M, damping coefficient C, and spring stiffness K must be appropriately specified. Regarding the piston mass M, this parameter can be readily determined from the piston's geometry and material properties, which, in cryogenic environments, are typically selected from Inconel alloys or austenitic stainless steels [7-8]. The static model of the system gives the value of the stiffness K, by setting a starting suitable equilibrium position x_{eq} of the piston:

$$x_{eq} = \frac{F_{tot}}{K} \quad \rightarrow \quad K = \frac{F_{tot}}{x_{eq}} \tag{3}$$

The value of x_{eq} can be set equal to the piston's position in fully open valve's configuration, i.e., when the maximum volumetric flow passes through it. This position corresponds to the distance between the exit edge of the orifice and the bottom surface of the piston, value that can be estimated through Eq. (2) by setting the desired Δp, the required volume flow rate Q and the geometry of the orifice. The final parameter required to complete the dynamic model setup is the viscous coefficient C. Particular attention must be given to its accurate estimation, as the first-order differential term $C\dot{x}$ plays a critical role in defining the damping behaviour of the system. The C coefficient binds the viscous force acting on the piston to the velocity of the piston itself, and it is dependent on the fluid dynamic properties. Given the very low viscosity of liquid hydrogen [9], the viscous action of the flow may be insufficient to dampen significantly the response of the piston, leading to a slow dynamic of the system with many oscillations until the equilibrium position is reached. Describing the mechanism of dissipation in a mathematical way is very difficult. The dampening effects are usually represented by idealized mathematical formulas. For many cases, these complex effects are adequately described by viscous equivalent damping. Therefore, the actual damping contribution of the liquid hydrogen flow, represented by the viscous coefficient C, can be accurately determined only through experimental measurements or CFD simulations, as it depends on inherently complex physical phenomena [10]. Analytically, this coefficient is computed as the ratio of the force acting on the piston and its related velocity. Since the only unknown value within the modeled system turns out to be the value of the viscous coefficient C, an initial guess value will be considered, moving preliminarily to a parameterized analysis. It is possible to calculate the critical value of the system, known the mass of the piston and the stiffness of the control spring (these values have been obtained through a prior lumped-parameter analysis here not reported), using the following formula:

$$C_{crit} = 2\sqrt{M * K} = 156.2 \quad \left[\frac{kg}{s}\right] \tag{4}$$

If the viscous coefficient C is below the critical value C_{crit}, then the system will be under-dampened, resulting in wide oscillations of the piston. The closer the value of the coefficient C to the critical one, the more important the fluid's dampening effect will be on the dynamics of the piston, which will reach the equilibrium position x_{eq} with gradually more contained oscillations. The Simulink-implemented model is schematically illustrated in Fig. 4. It is worth noting that a highly complex model is not required to perform a preliminary analysis of the piston dynamics within a liquid hydrogen flow. The main objective of this study is to provide a comparative assessment of valve performance and robustness between the optimized and non-optimized architectures, from both fluid-dynamic and dynamic perspectives.

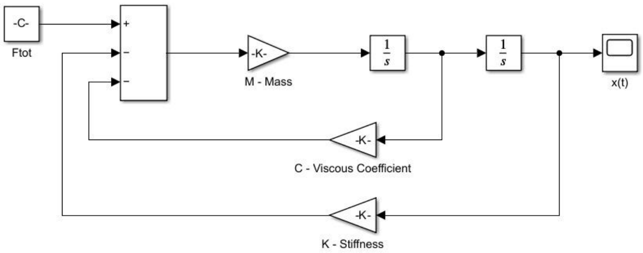

Figure 4 Schematic of the simplified Simulink model of the piston dynamics.

For the sake of this analysis, it is sufficient the computation of the coefficients of the differential model, together with the velocity and pressure field of the flow, in order to establish with accuracy, the total force F_{tot} acting on the piston of the valve and the contribution of the viscous effect of the liquid hydrogen carrying fluid, estimated directly through the CFD analysis. The complete dynamic model is solved in Simulink using sequential (waterfall) integrations, based on the differential equation derived from Eq. (1):

$$\frac{d^2x}{dt^2} = \frac{1}{M}\left(F_{tot} - C\dot{x} - Kx\right) \tag{5}$$

3 CFD SIMULATION

The CFD-driven optimization aims to refine the conventional piston valve design, enhancing its operational efficiency and reliability in managing low-viscosity fluids such as liquid hydrogen. This iterative process of analysis and optimization empowers the aerospace and cryogenic industries to develop piston valve designs that meet the stringent demands of cryogenic applications, ensuring safety, efficiency, and precise pressure control in extreme low-temperature environments. The purpose of the performed CFD's simulation is to provide an accurate and reliable fluid dynamic results in terms of velocity and pressure fields across the main body of the valve, in order to better understand and localize flow regions which may have a negative impact on the performance of the valve, in terms of localized high pressure drops, recirculating zones and high flow velocities. Particular attention must be given to the definition of the boundary layer, as accurately capturing the viscous effects along the wall is essential to ensure both convergence and fluid-dynamic accuracy of the simulations. Therefore, an adequate number of layers must be specified. To create a suitable and reliable mesh, it is necessary to ensure a good geometry's tessellation (as shown in Fig. 5), to approximate as much as possible the shape of the orifice to that of a circular crown rather than of a polygon. In this way it is possible to capture with high resolution the pressure and velocity field of the fluid in the proximity of the orifice small area avoiding singularities near sharp edges.

3.1 GEOMETRY AND MESHING

A 3D cross-sectional model of the simplified main body of the valve is presented in Fig. 5. The CFD simulations were performed using SimScale, covering all stages from meshing to post-processing.

A patch-independent, tetra-dominant shell mesh was employed, together with tetra/mixed volume meshing based on the tetrahedral method. The volume mesh in the region surrounding the piston is illustrated in Fig. 7. To accurately capture the boundary layer, a prism mesh was applied along all wall surfaces. The smooth transition inflation method was adopted, with a growth ratio of 1.3 across 20 layers, as shown in Fig. 8. Mesh quality was assessed to verify element integrity and the absence of negative volumes. The minimum element quality was 0.03, with a maximum of 1.0, and an average quality of 0.88, for a total of approximately 9.7 million elements. The maximum precision of the model and its entities is 5e-07 m, which means that the mesh can capture the curvatures and small edges inside the geometry of the presented simplified design. Therefore, the mesh is suitable for the simulation.

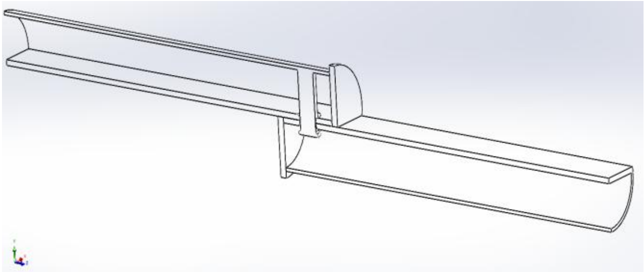

Figure 5 Cross section of the CAD model.

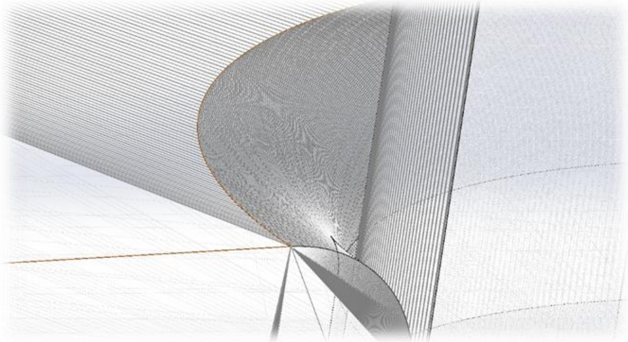

Figure 6 Tessellation of the piston body of the valve.

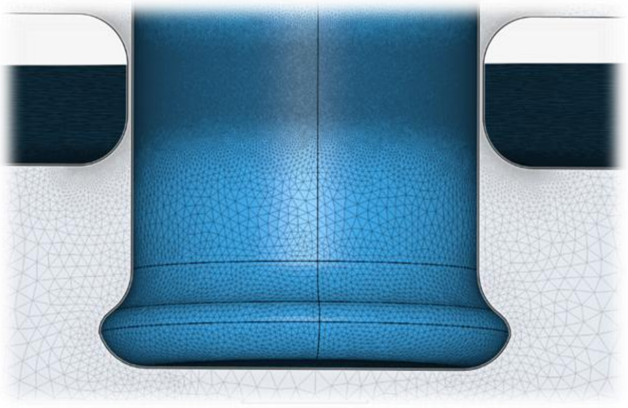

Figure 7 Volume Mesh with Tetrahedral cells.

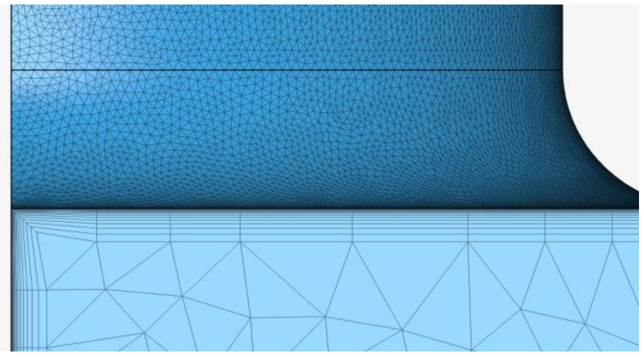

Figure 8 Boundary Layer inflation during meshing phase.

3.1 SOLVER SETTING

SimScale was used to solve the Reynolds-Averaged steady-state Navier–Stokes equations employing the k–ω SST turbulence model under inviscid flow conditions. The wall boundaries were defined as no-slip, while pressure-driven boundary conditions were applied at the inlet and outlet. The selection of an appropriate turbulence model is crucial for achieving reliable simulation results. Among the most widely adopted approaches in CFD analysis are the k–ω and k–ε models. The main distinction between these two lies in their treatment of the viscous sublayer, with the k–ε model providing a less accurate resolution compared to the k–ω formulation [11]. Moreover, the k-ω model is effective at resolving internal flows, separated flows and jets, flows with a high-pressure gradient, and internal flows through curved geometries [12] such as the orifice of the presented simplified valve. The realizable k-ε model is an alternative that differs from the standard k-ε model in two respects. Firstly, it contains a novel formulation for turbulent viscosity. The second difference is a new transport equation for the dissipation rate ε, which is derived from an exact equation for the transport of the mean-square vorticity fluctuation. As a result, it mainly yields improved predictions for the spreading rate of jets, a superior ability to capture the mean flow of complex structures and for flows involving rotation, boundary layers under strong adverse pressure gradients, separation and recirculation. Both k-ε and realizable k-ε adopt wall functions. Therefore, regardless of which model is chosen for the simulation, the $y+$ values in the first cell near the wall must not be less than 30 or excessively greater than 100. If the mesh does not meet these criteria, the geometry must be meshed again to achieve reasonable results. Switching to a different turbulence model cannot compensate for a poor-quality mesh, especially when the selected model also relies on wall functions. The turbulent viscosity is calculated in a less complex manner in the standard k-ε model, making it more stable. However, if the mesh captures the boundary sub-viscous layer appropriately, stability should not be an issue in either instance. Considering the respective advantages and limitations of the previously discussed models, the k–ω SST turbulence model was ultimately selected for the simulations, as it effectively integrates the strengths of both the k–ω and k–ε formulations [13-14].

4 RESULTS AND DISCUSSION

All simulations met the convergence criterion within fewer than 1000 iterations, as illustrated in Fig. 9. The residuals of the computed solutions ranged between 10^{-3} and 10^{-5}, indicating that the CFD results can be regarded as practically steady, with only minor fluctuations. The figures that follow show the main differences between the optimized and non-optimized architecture of the piston: these significant differences are expressed in terms of pressure drop distribution of the fluid flow from the inlet to the outlet of the orifice, the local peaks of pressure, the flow's velocity field across the piston body as well as the main direction of the velocity vector, the recirculating zones and the instantaneous volume mesh rendering of the velocity particles motion across the piston. As far as concerns the interaction between the fluid flow with the smooth wall of the valve, the viscosity effect causes a decrease in the flow's velocity close to the walls, leading to the formation of the boundary layer shown in Fig. 14. The CFD simulations highlight the critical role of the geometric optimization performed on the piston body in shaping the fluid flow through the valve. The specific configuration of the piston and the surrounding circular crown orifice maintains the flow in a coherent, column-shaped jet, as illustrated in Figs. 12 and 16. This behaviour arises because the fluid is constrained to pass through the narrow yet elongated gap between the orifice wall and the piston stem, from the upstream to the downstream region. Consequently, this specific geometric arrangement promotes flow laminarization, preventing the pronounced pressure recovery typically observed downstream of a single orifice [15-19], and enabling a smooth and well-distributed pressure drop from the inlet to the outlet, as shown in Fig. 10. The non-optimized architecture is instead characterized by a huge localized pressure drop across the orifice, as can be noticed from Figs. 11, 13 and 15.

If the pressure drop is confined in a very small area, thus not having enough space to smoothly transition between a high pressure zone to a lower one, this will inevitably lead to a faster and more energetic turbulent flow, which translates into higher thermal exchange between the extremely cold liquid hydrogen flow with the wall and the piston itself. This will cause a continuous wear and thermal stress corrosion of the valve's regulating mechanism, causing the system failure during the valve's expected lifetime. Another significant difference between the optimized and non-optimized valve's architecture can be highlighted by comparing the pressure and viscous forces acting on the y-axis of the piston at equilibrium, which is the main axis along which the regulating mechanism acts. As can be clearly seen from Fig. 19 and 20, the non-optimized configuration involves a higher-pressure force with respect to the optimized one, and a lower viscous effect. This means that in the case of the non-optimized geometry, the piston must withstand a higher force ($\bar{F}_{tot} = 190\ N$), which is almost four times the average force that the optimized piston must deal with ($\bar{F}_{tot} = 54\ N$).

Therefore, an increase in the pressure force requires a more rigid control spring to maintain the piston's equilibrium position; consequently, the critical value C_{crit} of the system will increase, making it much more difficult for the liquid hydrogen flow to damp the piston's motion during the pressure regulation phase. Interpreting it in an alternative way, a greater force acting on the piston implies a greater amount of energy that must be dissipated over time, and since liquid hydrogen has a very low viscosity, the optimal solution would be to design the system so that the piston withstands a small total force, so as to have few oscillations and be able to dissipate the incoming energy from the flow over time. Furthermore, the time history of the pressure force in the case of the non-optimized piston, shown in Fig. 19, presents several large fluctuations around its average value, and this is due to the fact that the flow field under the piston surface is strongly irregular and chaotic, with the presence of vortices and recirculation zones that contribute to a continuous variation of the total acting force on the piston. The pressure regulating mechanism becomes clearly more complicated and less efficient, since the control spring is forced to work continuously to maintain the desired position of the piston. In the case of the optimized piston, however, it is noticeable from the plot reported in Fig. 19 that the time history of the pressure force is almost constant, with fluctuations much more contained than the non-optimized case, therefore representing a better and more effective piston dynamic response. Regarding the response time required for the piston to reach the desired equilibrium position, it can be seen from the plot reported in Figs. 21 and 22 how the optimized solution reaches the equilibrium position with a lower number of oscillations, about half of the oscillations performed by the non-optimized piston. These oscillations are clearly due to the low viscous effect of liquid hydrogen, which results in an extremely low viscous coefficient, below the critical value of the system $C_{crit} = 156.2$. Therefore, the optimized piston exploits fewer oscillations. Specifically, when considering a higher viscosity fluid like Oil SAE 120, the dynamic model implemented on Simulink confirms the validity of the analysis and optimization performed on the valve. It is evident that the optimized piston, when operating with high viscous fluids, displays a considerably reduced number of oscillations and a more significant damping effect compared to the non-optimized piston. The dynamic simulations performed in Simulink, solving the piston's differential model, reveal repeated oscillations that asymptotically approach a steady-state value. This behaviour occurs because the only damping contribution considered in the analysed system is the viscous action of liquid hydrogen, which alone is insufficient to fully attenuate the piston's motion. Furthermore, the piston mass is set to $M = 0.038\ kg$ in the model simulation, so very little inertia opposes the motion of the piston, thus leading to continuous oscillations. As far as concerns the viscous C coefficient, it is computed through an iterative process starting from a guess value arbitrarily set equal to 10.

By taking the distribution of the piston's velocity from the solution of Eq. (1) implemented on Simulink, whose analytical behavior is shown in Fig. 21, and averaging over time this distribution in terms of amplitude of the velocity peak values [20], it is thus estimated the system's viscous coefficient, initially unknown. Combining the value of the total force acting along the piston axis in steady state configuration, obtained through CFD and shown in Fig. 20, and the average value of piston velocity, the following viscous coefficient is obtained:

$$C = \frac{F_{tot}}{\dot{x}_{piston}} = \frac{1.40\ N}{0.14\ m/s} = 10 \quad \left[\frac{kg}{s}\right] \tag{6}$$

If this simple procedure is repeated iteratively, the convergence value of $C = 4.75$ [*kg/s*] is obtained after four iterations with a residual error of 0.3 %, as shown in Table 1. This analytical procedure allows an estimation of the viscous coefficient based on the dynamics of the system. Nevertheless, in order to calculate a more reliable value of the viscous coefficient C of the real system, an experimental test is required, which is extremely expensive and complicated due to the fact that it would involve the measurement of the friction force between the piston's body and the walls of the valve (this friction contribution has been neglected for this preliminary study), as well as the piston's velocity caused by an applied force within liquid hydrogen environment, which is dangerous if not handled carefully within a dedicated experimental test bench.

Table I - Iterative computation of viscous coefficient *C*

Iteration n°	***C* [kg/s]**	***Error %***
1	10.00	88.0
2	5.31	10.2
3	4.81	1.3
4	4.75	0.3
Final value	**4.75**	**0.3**

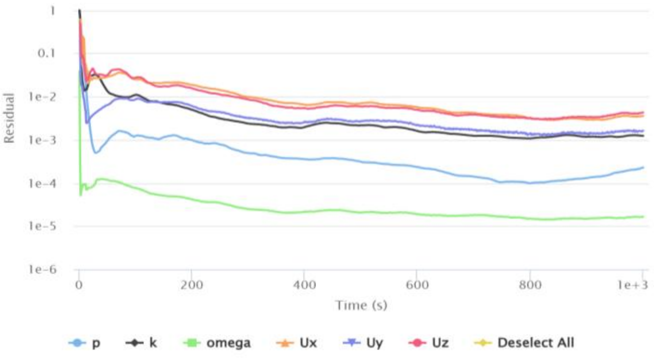

Figure 9 Residual convergence plot obtained from the simulation performed in SimScale.

Figure 10 Pressure field variation across the optimized piston body.

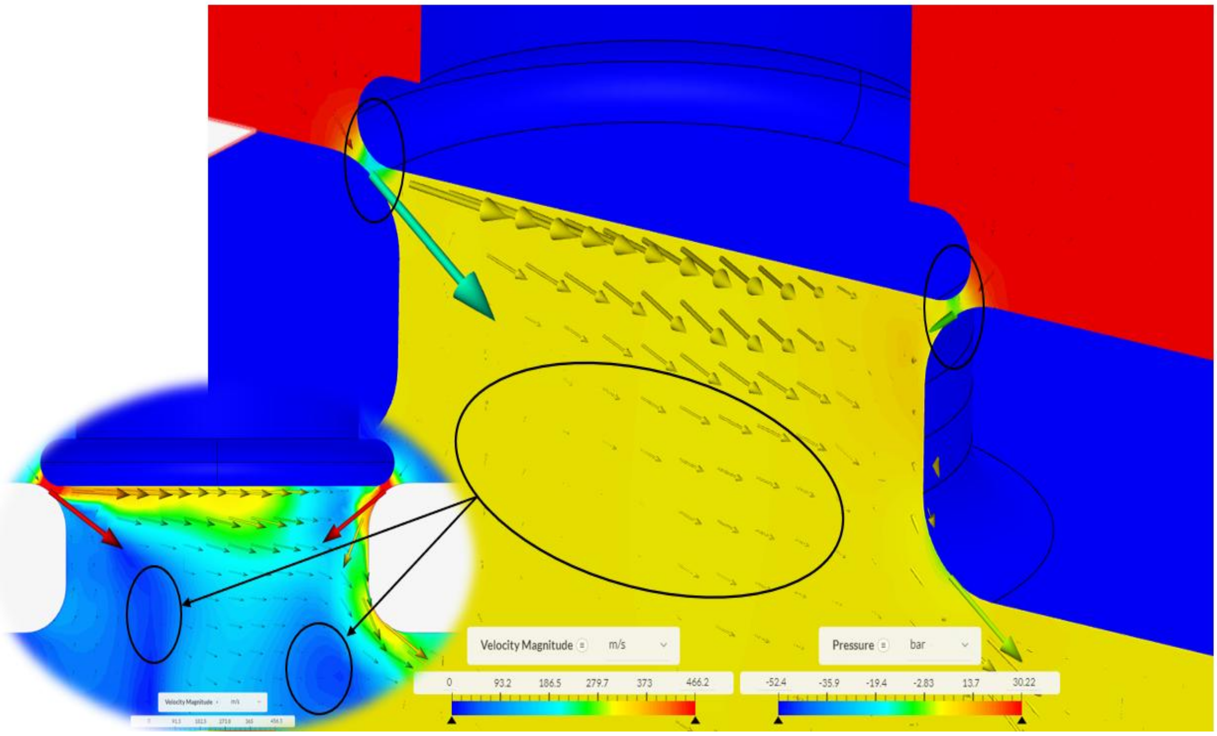

Figure 11 Pressure field variation across the non-optimized piston body.
On the left the recirculation zones, on the top the localized pressure drops.

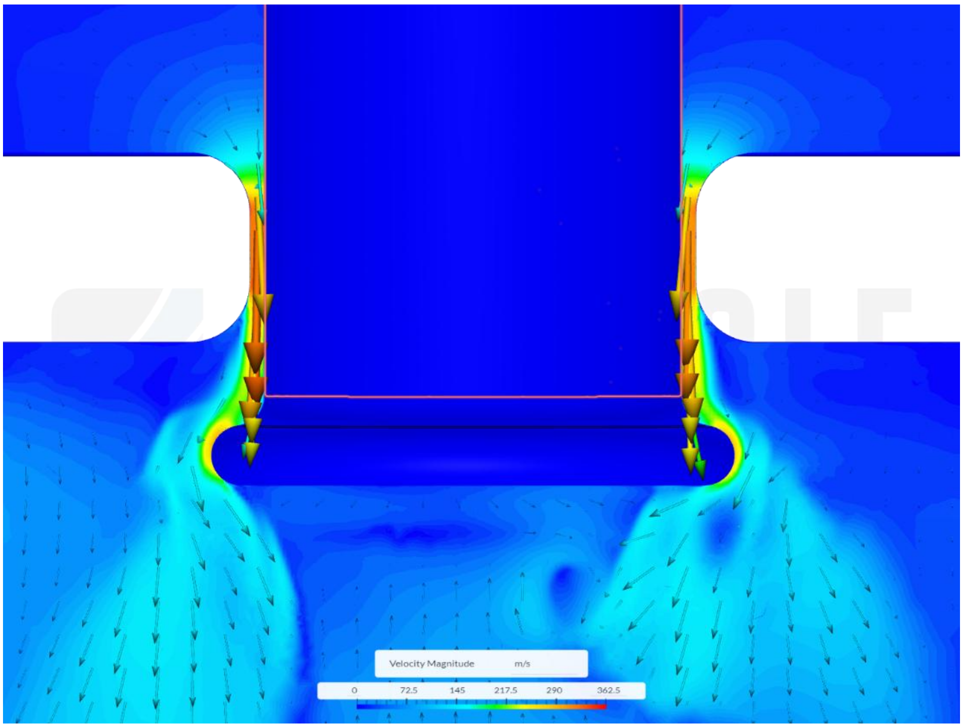

Figure 12 Computed velocity field of liquid hydrogen around the optimized piston body.

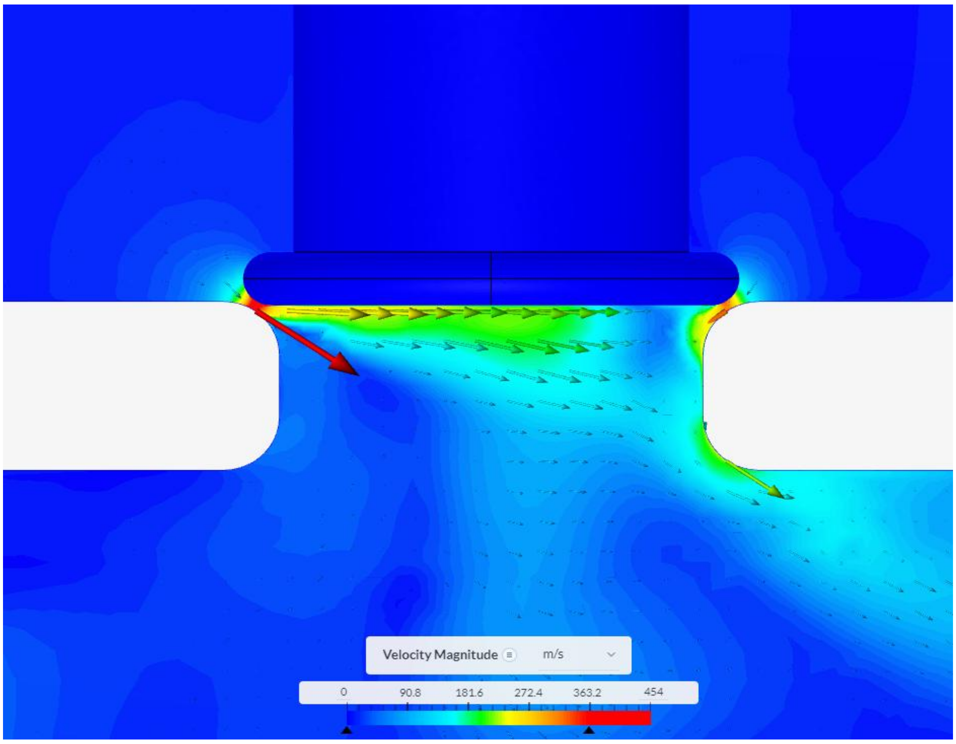

Figure 13 Velocity field of the LH2 flow around the non-optimized piston body.

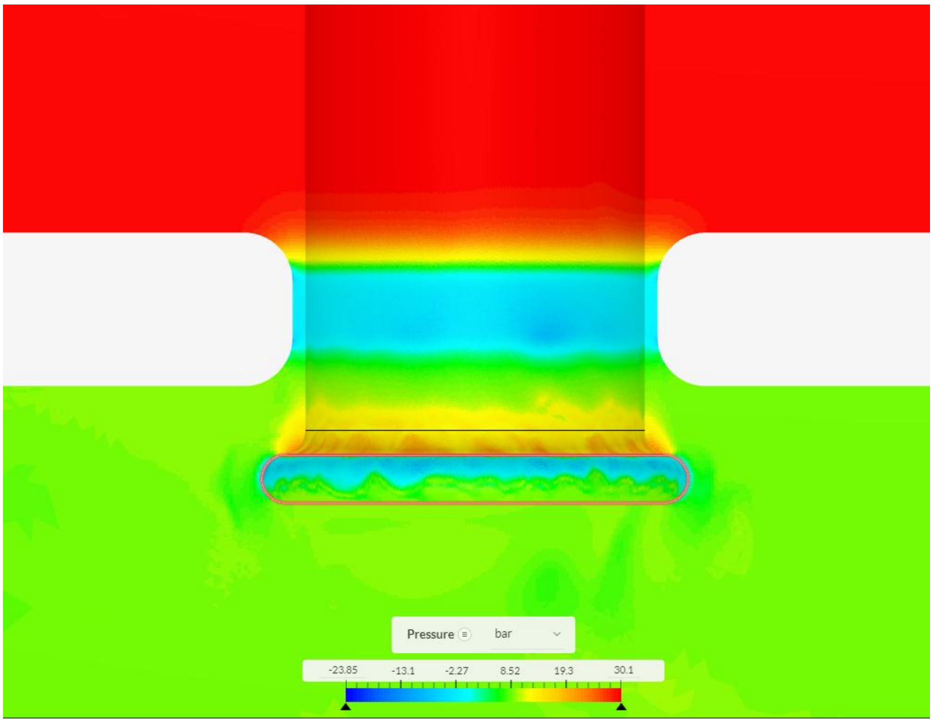

Figure 14 Pressure field of the LH2 flow around the optimized piston body.

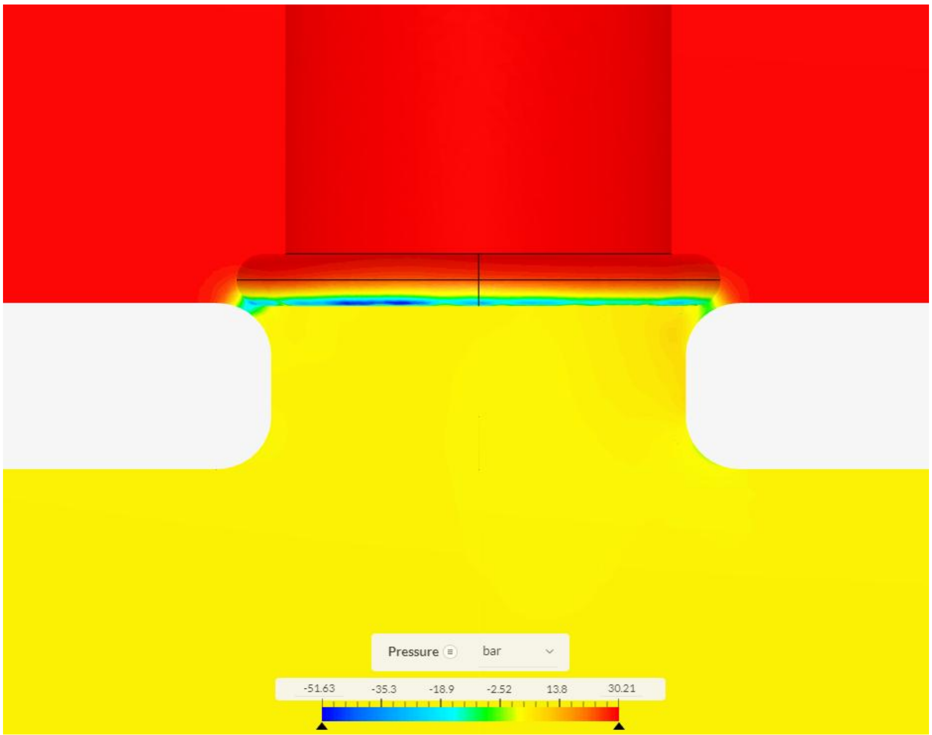

Figure 15 Pressure field of the LH2 flow around the non-optimized piston body.

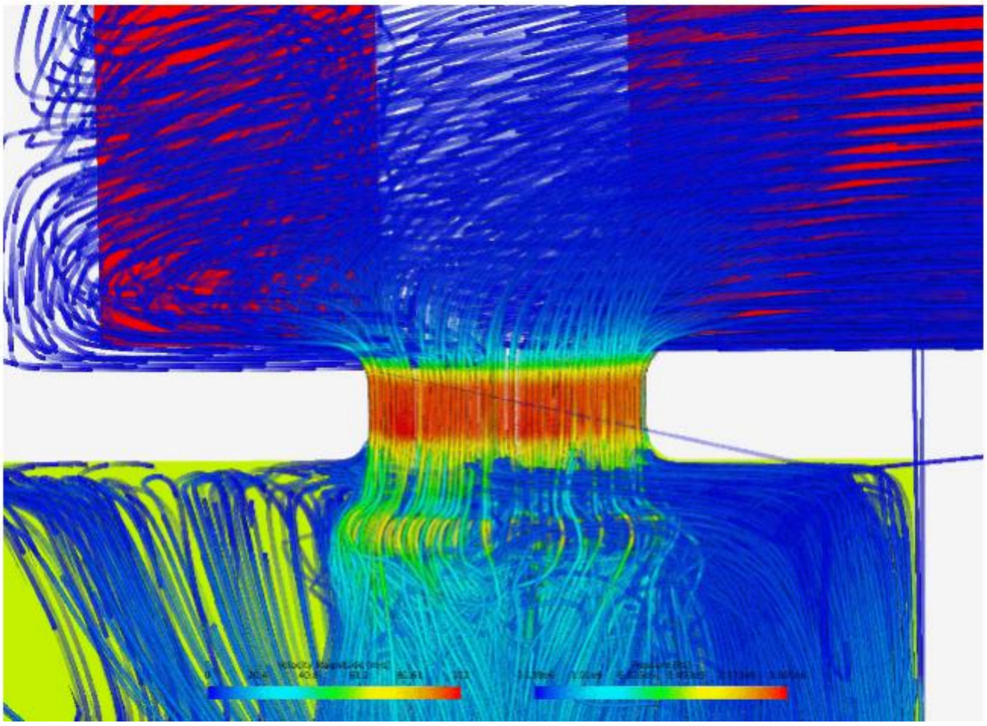

Figure 16 Laminarization of the flow jet across the optimized piston body of the valve.

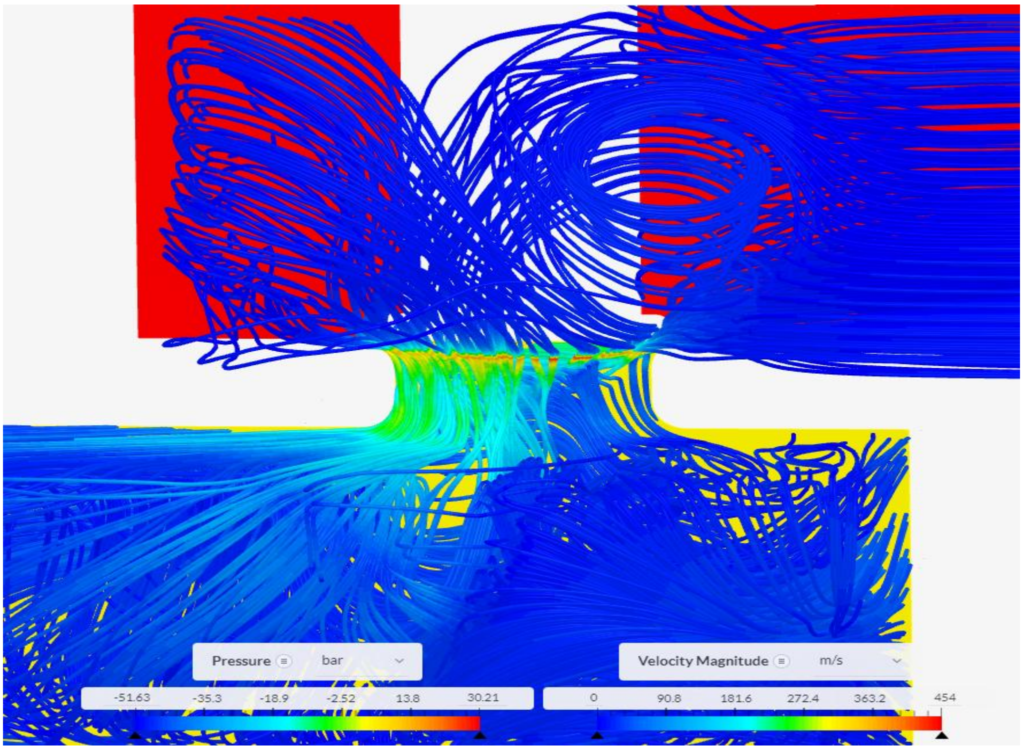

Figure 17 Laminarization of the flow jet across the non-optimized piston body of the valve.

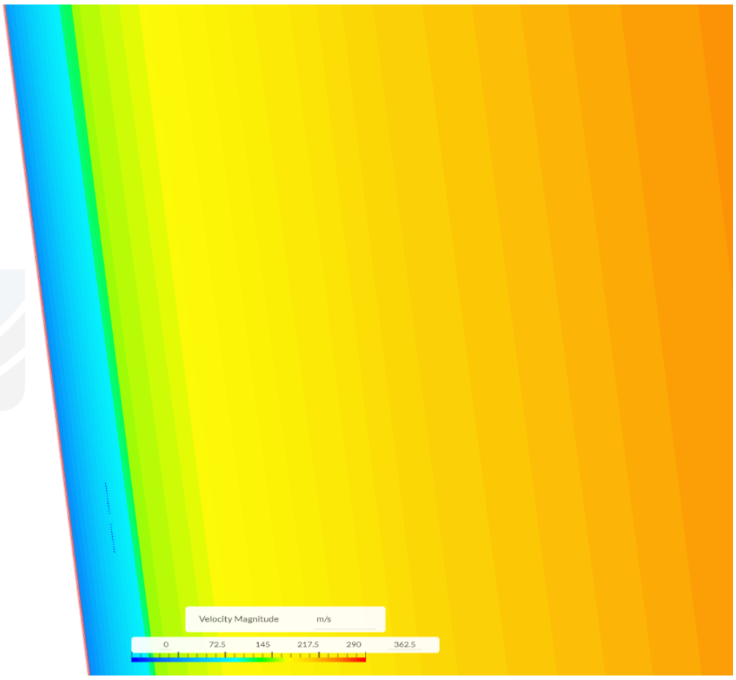

Figure 18 Boundary layer's capture in the proximity of the wall.

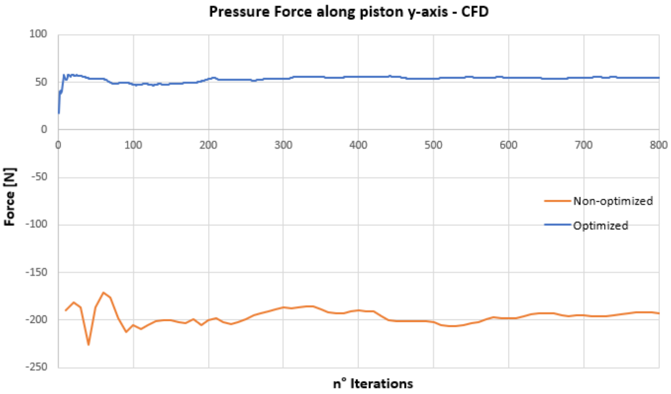

Figure 19 Pressure force along the *y*-axis of the piston body.

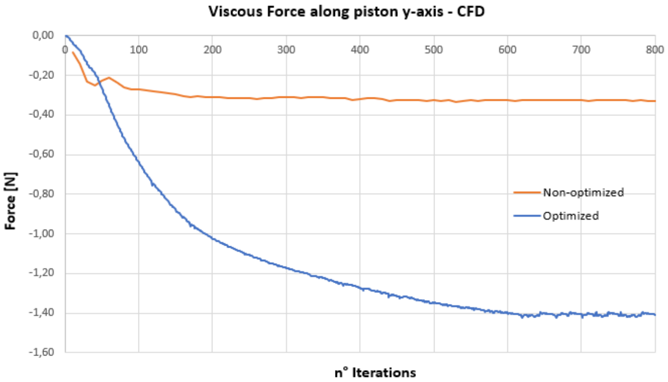

Figure 20 Viscous force along the *y*-axis of the piston body.

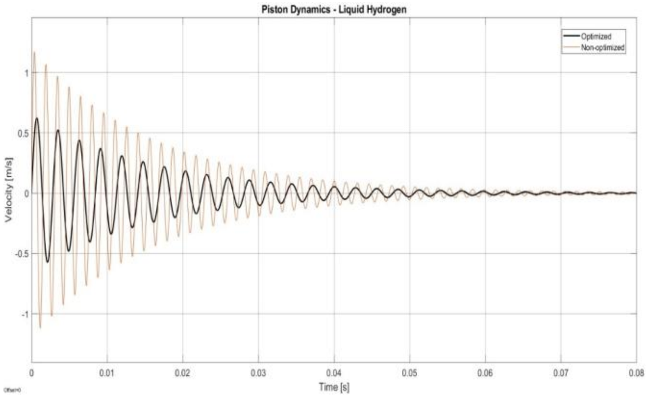

Figure 21 Comparison of the optimized and non-optimized piston dynamics with liquid hydrogen.

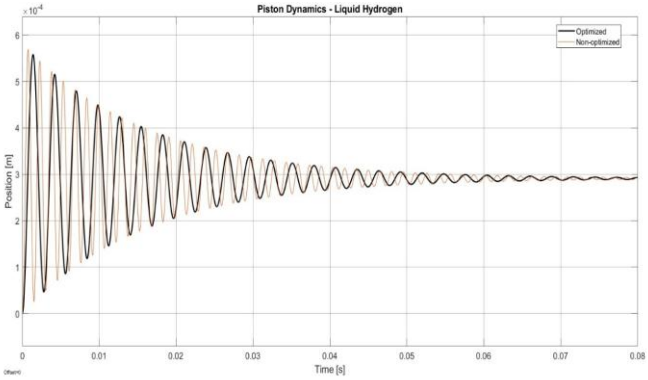

Figure 22 Comparison of the optimized and non-optimized piston dynamics with liquid hydrogen.

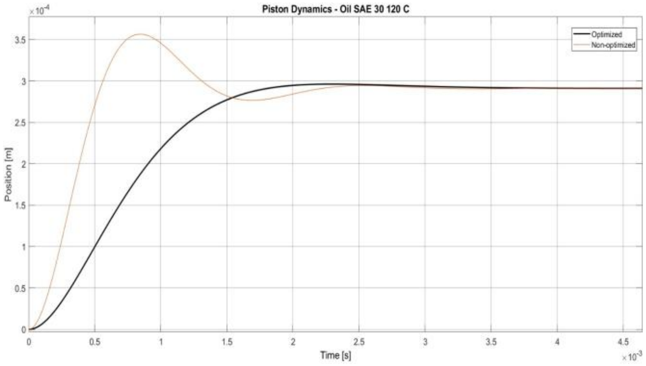

Figure 23 Comparison of the optimized and non-optimized piston motion with oil SAE 30.

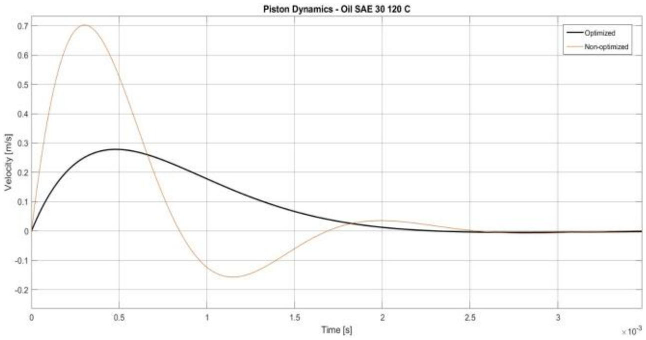

Figure 24 Comparison of the optimized and non-optimized piston motion with oil SAE 30.

5 CONCLUSIONS

A CFD-based preliminary study on a simplified liquid hydrogen pressure-regulating valve has demonstrated the benefits of geometric optimization in enhancing flow stability and valve performance. The optimized design reduces pressure losses and recirculation effects, while a simplified Simulink model successfully predicts the piston's dynamic response based on its geometry. The performed analysis and optimization via CFD are therefore able to assess and capture the main differences concerning the flow field between the presented architectures with good accuracy, thus validating the robustness and performance of the optimized piston's body. The proposed simplified pressure-regulating valve highlights the influence of liquid hydrogen flow on the piston's dynamic behaviour, particularly in terms of its position and velocity. Due to the extremely low viscosity of this cryogenic fluid, the system exhibits a lightly damped response with pronounced oscillations, which can be effectively controlled only through careful geometric and dynamic optimization. Moreover, the developed analysis framework can be readily extended to fluids with different viscosities and operating pressures, making the simplified valve concept a versatile solution for a wide range of fluid-dynamic applications. Future work will focus on manufacturing and testing the proposed optimized geometry in different fluid dynamic environments and pressure conditions, ranging from low to high-viscous fluids, to validate the real response of the piston with respect to the dynamic response of the numerical model.

REFERENCES

[1] Tabrizi A.S., Asadi M., Xie G., Lorenzini G. and Biserni C., Computational fluid-dynamics-based analysis of a ball valve performance in the presence of cavitation. *Journal of Engineering Thermophysics,* pp. 23, 27-38, February 2014.

[2] Jin H., Zheng Z., Ou G., Zhang L., Rao J., Shu G. and Wang C., Failure Analysis of a high pressure differential regulating valve in coal liquefaction. *Engineering Failure Analysis*, Vol. 55, pp. 115-130, September 2015.

[3] Niola V., Spirto M., Savino S. and Cosenza C., Vibrational analysis to detect cavitation phenomena in a directional spool valve. *International Journal of Mechanics and Control*, Vol. 22, No. 1, pp. 11-16, 2021.

[4] Niola V., Savino S., Quaremba G., Cosenza C., Spirto M., Nicolella A., Romagnuolo L. and Frosina E., Classification of different cavitation conditions in a proportional spool valve through vibrational analysis. *International Journal of Mechanics and Control*, Vol. 24, No. 1, pp. 53-60, 2023.

[5] Wang Y. and Yang V., Central recirculation zones and instability waves in internal swirling flows with an annular entry. *Physics of Fluids*, Vol. 30, No. 1, January 2018.

[6] Turgut S.S., *Wave Forces on Offshore Structures: Hydrodynamic Damping*. Cambridge University Press, pp. 265-284, July 2014.

[7] Kendall E.G., *Metals and Alloys for Crygenic Applications – A review*. Defense Documentation Center for Scientific and Technical Information, United States Air Force, January 1964.

[8] MIL-HDBK-5J, *Metallic Materials and Elements for Aerospace Vehicle Structures*. Department of Defense Handbook, United States of America, January 2003.

[9] Kim H.I., Han K.Y. and Park J.H., *Liquid Hydrogen Properties*. HANARO Utilization Technology Development Div, p. 32, 2004.

[10] Lesieutre G.A., *Damping in FE Models*. Encyclopedia of Vibration, pp. 321-327, 2001.

[11] Minsheng Z., Decheng W. and Yangyang G., Comparative Study of Different Turbulence Models for Cavitational Flows around NACA0012 Hydrofoil. *Journal of Marine Science and Engineering*, MDPI, 2021.

[12] Thakare H.R. and Parekh A.D., CFD analysis of energy separation of vortex tube employing different gases, turbulence models and discretisation schemes. *International Journal of Heat and Mass Transfer*, Vol. 78, pp. 360-370, November 2014.

[13] Menter F.R., Zonal Two Equation k-ω Turbulence Models for Aerodynamic Flows. *AIAA Paper*, No. 93-2906, 1993.

[14] Menter F.R., Two-Equation Eddy-Viscosity Turbulence Models for Engineering Applications. *AIAA Journal*, Vol. 32, No 8, pp. 1598-1605, 1994.

[15] Shivarudrappa K.B., Sargunar E.V.M. and Sakthivadivel R., An Experimental Investigation of Pressure Recovery Factor in Discharging Manifolds. *6th Australasian Hydraulics and Fluid Mechanics Conference*, Adelaide, Australia, 5-9 December 1977.

[16] Dalla Vedova M.D.L. and Alimhillaj P., Study of new fluid dynamic nonlinear servovalve numerical models for aerospace applications. *Proceedings 2018 2nd European Conference on Electrical Engineering and Computer Science Eecs 2018*, pp. 483-490, 8910132, 2018.

[17] Dalla Vedova M.D.L., Berri P.C., Corsi C. and Alimhillaj P., New synthetic fluid dynamic model for aerospace four-ways servovalve. *International Journal of Mechanics and Control*, Vol. 20, No. 2, pp. 105-112, 2019.

[18] Dalla Vedova M.D.L. and Berri, P.C., A new simplified fluid dynamic model for digital twins of electrohydraulic servovalves. *Aircraft Engineering and Aerospace Technology*, Vol. 94, No. 1, pp. 79-88, 2022.

[19] Poçari S., Alcani M., Alimhillaj P., Londo A. and Hoxha A., Numerical and experimental study of the pressure-compensated flow control valve in an hydraulic system using, mathematical model and LabVIEW. *International Journal of Mechanics and Control*, Vol. 25, No. 1, pp. 69-76, 2024.

[20] Ponzo F.C. and DiTommaso R., *Valutazione della capacità dissipativa di un sistema strutturale*. Corso di Laurea Magistrale in Ingegneria Civile, Università degli Studi della Basilicata, 2011.

ISSN 1590-8844
International Journal of Mechanics and Control, Vol. 26, No. 02, 2025
https://doi.org/10.69076/jomac.2025.0027

REMOTE ASSESSMENT OF CARDIODYNAMIC CHANGES IN COMPETITIVE CYCLISTS DURING AN INCREMENTAL CYCLE-ERGOMETER TEST TO EXHAUSTION: A PILOT STUDY

Tocco F[1,8], Manuello Bertetto A[2], Velluzzi F[1], Roux A[2], Rosadelli S[2], Fois A[3], Deledda A[1], Cappai EA[1], Melis S[1,4,8], Dell'Osa AH[5], Cerina A[6], Marcello R[7], Concu A[7,8]

[1]Department of Medical Sciences and Public Health, University of Cagliari, Italy
[2]Department of Mechanical and Aerospace Engineering, Politecnico di Torino, Turin, Italy
[3]Nomadyca Ltd, Remote Biosignals Acquisition Unit, Mulago Hospital, Kampala, Uganda
[4]Sardinia's Schools Direction Office, Physical and Sports Education Unit, Ministry of Education and Merit, Cagliari, Italy
[5]Laboratorio de Electrónica Aplicada y Biomedicina, Universidad Nacional de Tierra del Fuego, Ushuaia, Argentina
[6]Acquaforte Thalasso & Spa Medical Team, Forte Village Resort, Santa Margherita di Pula, Cagliari, Italy
[7]AC Technologies Ltd, Bioimpedance Devices Manufacturing, Cagliari, Italy
[8]Sporting Life & Medicine Lab, Sardegna Ricerche, Cagliari, Italy

ABSTRACT

Seven male competitive road cyclists (22.3 ± 3.2 years; 73.9 ± 5.5 kg; 185 ± 7.9 cm), with 7.0 ± 6.8 years of racing experience and approximately 7 hours per week of specific training, participated in a laboratory-based cardiopulmonary incremental test to exhaustion. Each cyclist performed the test on their personal bicycle, with the rear wheel replaced by an electromechanical system that allowed real-time measurement of the mechanical power output generated during pedaling. Throughout the test, beat-by-beat cardiovascular variables—including stroke volume, heart rate, and cardiac output—were continuously assessed noninvasively using a custom-designed wearable device based on electrical impedance cardiography. Using proprietary telemedicine software, bioimpedance data collected during the tests were transmitted for remote acquisition and processing by an expert medical team. The experimental sessions were conducted in a dedicated laboratory of the Department of Mechanical and Aerospace Engineering at the Polytechnic University of Turin, Italy. The results demonstrated a progressive increase in cardiac output up to exhaustion, driven by concurrent increases in heart rate and stroke volume. The rise in stroke volume was attributed to enhanced myocardial contractility and the maintenance of ventricular preload. Mean arterial blood pressure remained stable until the end of the test, despite a substantial decrease in diastolic pressure.

Keywords: road cyclists, cardiopulmonary test, impedance cardiography, cardiac output

1 INRODUCTION

In cycling sports, one of the main objectives is to accurately measure the power output developed on the bicycle during training or competition. In the 1980s, Ulrich Schoberer developed the "SRM spider" device [1], which, when mounted on a bicycle, allows the mechanical power produced during cycling performance to be measured with very high precision [2]. These technological innovations made it possible to investigate how the various physiological systems involved in cycling performance interact, by enabling the formulation of rigorous mathematical correlations between the stimulus variable—namely, the mechanical power applied to the pedals—and circulatory, respiratory, and metabolic responses. Advances in modern wearable technologies now make it possible not only to improve the quality of life of individuals affected by severe disabling pathologies [3–7], but also to enable real-time, quantitative assessment of the respiratory and metabolic

---

Contact authors: Filippo Tocco[1], Alberto Concu[2]
[1]Dept of Medical Sciences and Public Health, University Cittadella, Provincial Road 8 – 09042 Monserrato (CA), Italy;
[2]AC Technologies Ltd, Via Pais 12- 09128 Cagliari, Italy.

adjustments [8–10] of athletes during laboratory simulations of different racing conditions. However, precise measurement of cardiodynamic variables during motion has remained challenging, as current techniques still lack sufficient accuracy under dynamic conditions. Nevertheless, a non-invasive method has been available for some time: electrical impedance cardiometry (EIC) [11, 12]. This technique enables the beat-to-beat assessment of cardiac output along with the cardiodynamic variables on which it depends, even in moving subjects through the use of wearable devices [13–16]. In the present study, competitive road cyclists employed the EIC method to monitor progressive changes in their cardiodynamic profile. Specifically, they wore a custom-made EIC wearable device, the E-Physio Tool [16–18], while performing a cardiopulmonary incremental exercise test to exhaustion in a laboratory setting. The test was conducted using each cyclist's own bicycle, with the rear wheel replaced by an ergometer capable of precisely measuring the mechanical power applied to the pedals. Some of the data presented here have been previously reported in a master's thesis in Mechanical Engineering at the *Politecnico di Torino*, Italy [19].

Figure 1 Promotional image from an advertising flyer illustrating the use of the Elite Direto XR-T power meter. The device replaces the rear wheel of the athlete's bicycle and connects directly to the cassette, which interacts with the derailleur and chain to enable gear shifting and maintain optimal pedalling efficiency across various terrains.

2 METHODS

2.1 SUBJECTS

Seven road racing competitive skilled cyclists were engaged and their characteristics are shown in table I.

Table I – Morphological and training data

Age (years)	BM (kg)	BH (cm)	$\text{Cycle}_{\text{Pract}}$ (years)	$\text{Time}_{\text{weecly}}$ (h:min)
22.3 ±3.2	73.9 ±5.5	185 ±7.9	7.0 ±6.8	6:45 ±0:21

BM: body mass; BH: body height; $\text{Cycle}_{\text{Pract}}$: practice of cycling; $\text{Time}_{\text{weecly}}$: time at week spent in cycling training in hours and minutes. Each athlete was made aware about the experimental procedure and all of they declared their informed consent.

2.2 INSTRUMENTATION

2.2.1 Mechanical equipment.

The Elite Direto XR-T power meter (Elite Ltd., Italy) was selected for this study. This device replaces the bicycle's rear wheel, allowing the bike to connect directly to its cassette (Figure 1). A constant resistance torque mode was employed, and the cyclists self-regulated their cadence and gear ratios during the trials. Each athlete used their own bicycle to prevent improper pedaling mechanics that could result from an incorrectly sized frame [20]. This mechatronic system communicates with smartphones via ANT+ technology (ANT-Productions, Belgium), a wireless communication standard commonly used for data transmission between fitness devices. Through this connection, the system recorded the cyclist's speed, pedaling cadence, and power output. The acquired data were stored on a Garmin cycle computer (Garmin, Lenexa, KS, USA) and subsequently

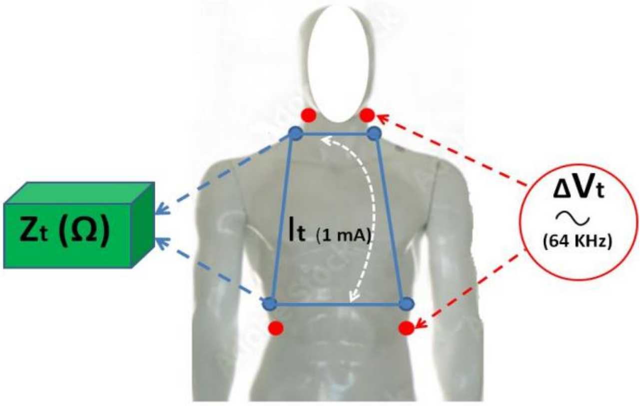

Figure 2 Schematic representation, on a mannequin, of the application of the E-Physio Tool to the human thorax. The device models an inverted truncated cone whose smaller circumference lies in the plane of the roots of the neck muscles, while the larger circumference lies in the plane of the xiphoid process. The blue trapezium represents the core of the volume of electrically participating tissues (VEPT) contributing to the thoracic impedance. Two pairs of disposable electrodes (blue circles), positioned respectively at the smaller and larger circumferences, enable the acquisition of beat-to-beat thoracic electrical impedance values (Zt) using the impedance measurement device (indicated by blue dotted arrows). This measurement is made possible by the E-Physio Tool, which applies an electrical potential difference (ΔVt) through two additional pairs of disposable electrodes (red circles and red dotted arrows), placed a few centimetres outside the measurement electrodes. This configuration generates within the thorax an alternating electrical current (It) of constant amplitude (1 mA at 64 kHz), symbolised by the white dotted line within the trapezium.

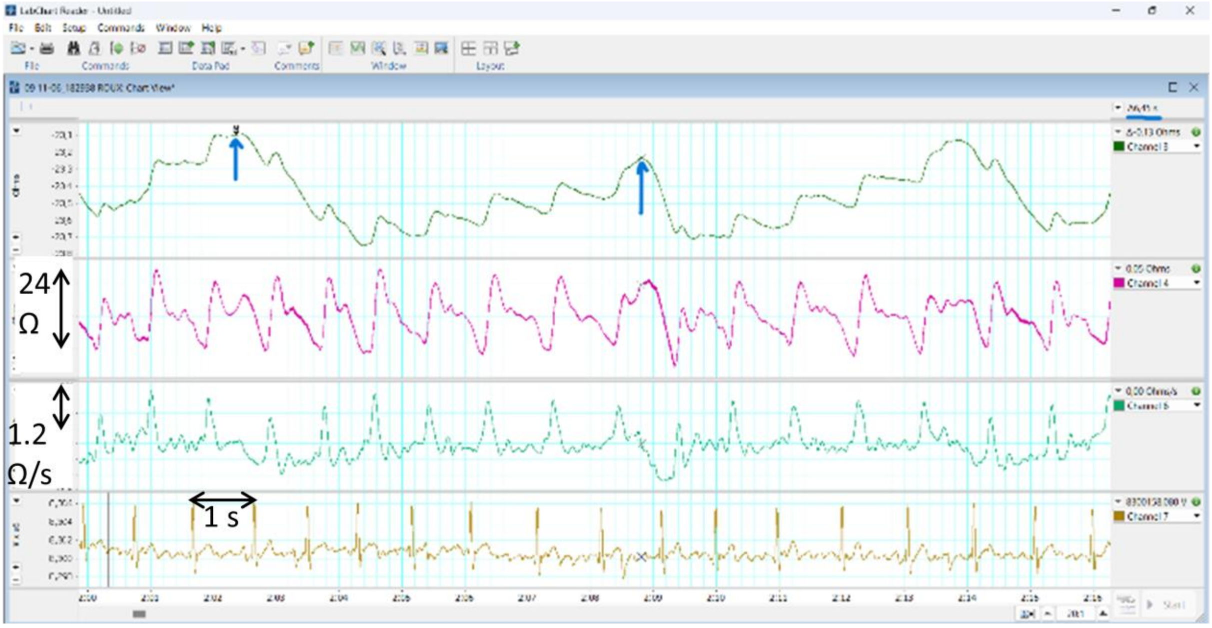

Figure 3 Analog traces of bioimpedance variables recorded by the LabCart Reader from a cyclist at rest. From top to bottom, the plots show: (1) beat-to-beat thoracic bioimpedance signals, in which the main, broader, and slower harmonic corresponds to the respiratory rate (see the two blue arrows marking the beginning and end of a breath), while the superimposed, narrower harmonic—synchronous with the cardiac cycle—represents the beat-to-beat variations in thoracic bioimpedance, which are clearly isolated in the second trace; (2) the first mathematical derivative of thoracic bioimpedance in the third trace; and (3) the beat-to-beat electrocardiogram in the fourth trace.

analyzed using the *Strava software* (Strava Inc., San Francisco, CA, USA).Strava is a widely used fitness-tracking and social networking application for athletes that records workouts such as running, cycling, and swimming using GPS data. The use of this mechatronic equipment is supported by previous validation studies [21, 22]. In this study, the software integrated into the mechatronic device enabled the assessment of mechanical power output during cycling performance at each pedaling phase.

2.2.3 Biomedical equipment.

The E-Physio Tool is a device that, as shown in Figure 2, applies a low-intensity, high-frequency alternating electrical current (I = 1 mA, 64 kHz), powered independently by a power bank supplying up to 2 mA at 5 V, along the planes corresponding to the roots of the neck muscles and the xiphoid process. The resulting difference in electric potential between these two points (ΔVt) is then measured.

The reliability of data acquired using this EIC device was demonstrated in a previous study [23], where it was compared with a validated EIC (NCCOM3-R7, BoMed, CA, USA) previously cited in the scientific literature (see references 15 and 16 in [23]). Stroke volume (SV) values were obtained by both instruments in 18 male participants at rest and during exercise up to 70% of their age-predicted maximum heart rate (220 – age).

Agreement between the two measurement methods was assessed using the Bland–Altman analysis from the ICT wearable device and the NCCOM3, both at rest and during exercise. The limits of agreement were within +7.01 and –8.12 mL at rest, and +6.77 and –9.86 mL during exercise.

Thus, this approach allowed the calculation of the real component of thoracic impedance (Zt) using the following equation, as the imaginary capacitive reactance was effectively nullified by the very high frequency of the alternating electrical current.

$$Zt = \Delta Vt / It \quad (1)$$

Thanks to the open-source LabChart Reader, both the Zt and ECG signals could be acquired non-invasively on a beat-to-beat basis using electrodes placed on the athletes' thorax and visualized in real time on a PC screen. As shown in Figure 3, the LabChart software enabled the acquisition of the following conditioning variables related to left ventricular SV: TFI (Zt^{-1}, or thoracic fluid index), representing the electrical equivalent of left ventricular preload (LVPL); EVI (electrical equivalent of left ventricular ejection velocity peak), here considered as the myocardial contractility index (MCI); and ventricular ejection time (VET). The Sramek-Bernstein equations (2 and 3) allow indirect calculation of SV as follows [24, 25]:

$$SV = TFI \ x \ EVI \ x \ VET \ x \ VEPT \quad (2)$$

$$SV = (\Omega^{-1}) \ x \ (\Omega \ s^{-1}) \ x \ (s) \ x \ (cm^3) = cm^3 \quad (3)$$

Equation (2), in addition to three multipliers of purely bioimpedance origin, includes a fourth multiplier: the volume of electrically participating tissues in the thoracic impedance (VEPT). VEPT was derived from a nomogram based on the subject's anthropometric characteristics weight, height and sex, as described by Donald Bernstein experimental tests [24]. Equation (3) further demonstrates that, from a dimensional perspective, the product of these four variables on the right-hand side of the equation yields a volume (cm³), corresponding to the volume of blood ejected by the left ventricle into the aorta during each systole.

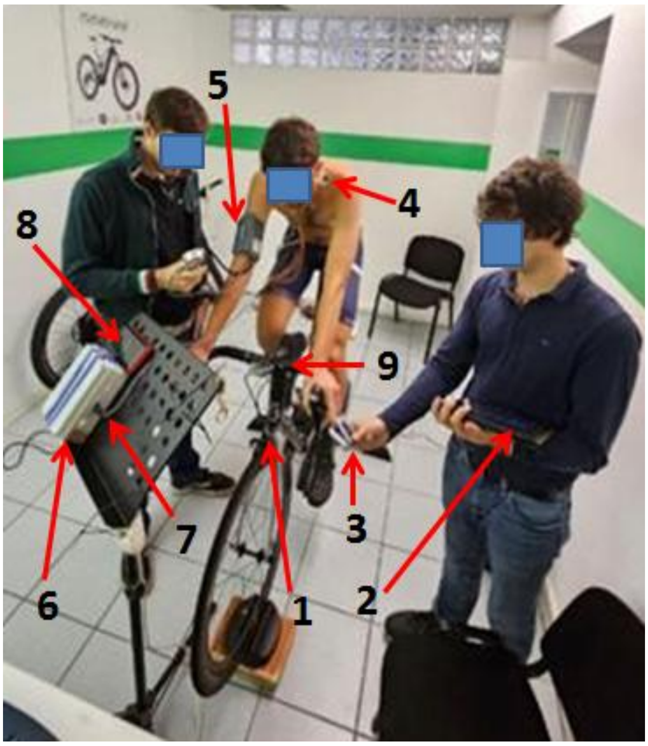

Figure 4 Image of a tested cyclist, assisted by two skilled operators from the Polytechnic University of Turin, Italy, while pedaling on his bike. (1) The rear wheel has been replaced with an Elite Direto XR-T power meter (not visible in the image). (2) Tablet organizer held by one of the operators for acquiring mechanical and biomedical measurements, the latter manually recorded by both operators. (3) Finger pulse oximeter. (4) Disposable ECG electrode visible here, attached at the roots of the neck muscles. (5) Inflatable sphygmomanometer cuff with stethoscope, used by the other operator to auscultate brachial artery sounds. (6) Box containing the E-Physio impedance cardiograph hardware and electronics. (7) Five-pin connection cable linking the athlete's chest electrodes to the impedance cardiograph. (8) Power bank providing 5 V, 2.4 A DC supply to the impedance cardiograph. (9) Garmin Edge cycle computer.

As is known, multiplying SV to the heart rate per minute (HR), it can be calculated the CO as:

$$CO = SV\,(ml) \times HR\,(beats\ min^{-1}) = mL\ min^{-1} \tag{4}$$

2.3 EXPERIMENTAL PROTOCOL

Each recruited cyclist performed an incremental test, pedaling their bicycle connected at the rear to the Elite Direto XR-T cycle-ergometer power meter (see Figures 1 and 4) until they were unable to continue. Cyclists self-selected their pedaling cadence, while the pedal load, starting at 0 W, increased by 30 W every 2 minutes. At each stage of the test, systolic and diastolic blood pressures were measured using a manual sphygmo-manometer (PB Pharma, Metal Deluxe, Italy) via the auscultatory Riva-Rocci-Korotkoff method [26] with a stethoscope (Figure 6). Arterial oxygen saturation (SO_2) was simultaneously recorded using a commercial fingertip device. For each athlete, the workload measured during the last minute of each stage was considered the maximal workload (W_{max}). Data collected remotely through the E-Physio Tool required careful review and selection to obtain accurate values for the variables of interest. Impedance cardiography recordings were provided in ".txt" format, and to visualize them as time-analogous traces, the "LabChart Reader" program was used [27]. Once opened, the software allowed visualization (Figure 3) of the beat-to-beat evolution of two primary variables: Zt and ECG.

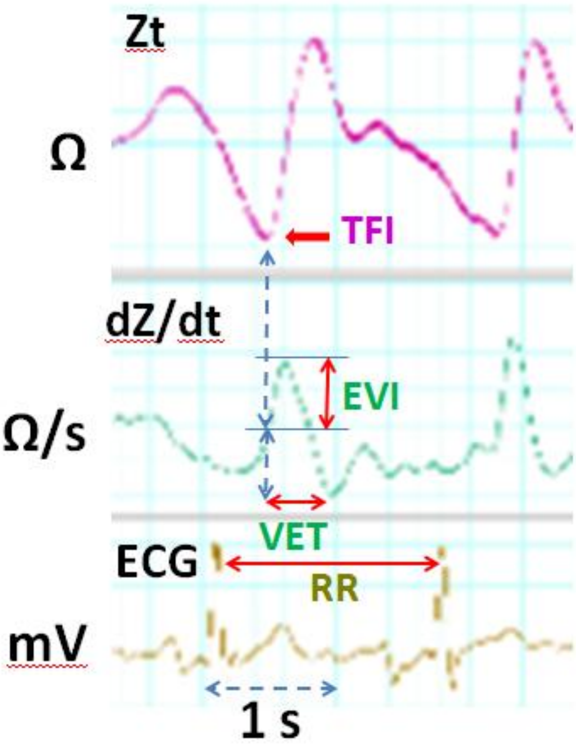

Figure 5 The graphs in the figure are enlarged segments of the impedance recordings obtained with the LabCart Reader during a cardiac cycle in one of the tested cyclists. The top panel shows the thoracic impedance (Zt) variations, where the minimum value (indicated by a red arrow) represents the thoracic fluid volume index (TFI). The reciprocal of this value corresponds directly to the left ventricular end-diastolic volume (ventricular preload). The subsequent dicrotic wave corresponds to the closure of the aortic valve at the end of ventricular ejection. The middle panel displays the first derivative of Zt (dZ/dt), where the peak corresponds to the maximum impedance index of the EVI, and the VET indicates the left ventricular ejection time. The bottom panel shows the ECG trace, with the R-R interval corresponding to the duration of the cardiac cycle analyzed.

Figure 6 On the left, the manual sphygmomanometer is shown, comprising three main components: an inflatable arm cuff, a rubber bulb with a valve for air inflation and deflation, and an aneroid manometer for displaying pressure readings. On the right, the stethoscope is depicted, consisting of a small, disc-shaped chest piece (diaphragm or bell) placed over the brachial artery beneath the cuff to capture sounds, which are then transmitted through flexible tubing to the earpieces worn by the user.

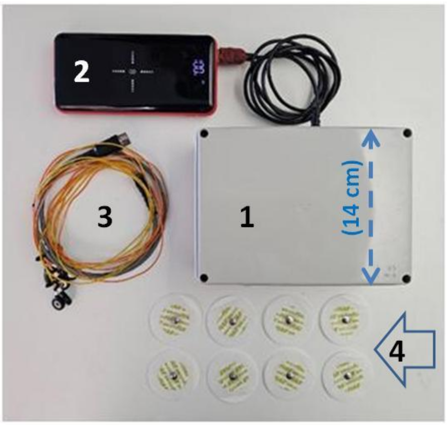

Figure 7 The custom designed "E-Physio Tool" is shown, with the main device unit (1) connected by a cable to its power bank (2). The patient connection cable (3) is shown coiled; it connects to the device via a 5-pin plug and terminates in 8 snap connectors on the opposite end, which attach to the eight disposable electrodes (4) placed on the patient's chest.

Using LabChart, the first derivative of Zt (dZt/dt) was also analyzed. With a specific graphical cursor (Figure 5), both the EVI and VET were calculated beat-to-beat from the dZt/dt trace. Together with the reciprocal of Zt, these represent the three impedance-based components of the Sramek-Bernstein equation. From the ECG trace, heart rate (HR) per minute was calculated based on the R-R interval, and breath-by-breath respiratory rate (BR) was also determined (Figure 3). For each measurement interval corresponding to a test stage, variables of interest were averaged over 10 consecutive beats, starting from the first beat after the midpoint of the stage, to minimize the influence of inaccurate measurements. Special care was taken to eliminate outliers, which are common at high workloads. For each stage, from W_0 to W_{max}, 20 consecutive measurements were initially recorded. Outliers and values most deviant from the mean were removed, and the remaining 10 measurements were averaged. This procedure also substantially reduced the standard deviation of stage-specific variables.

2.4 REMOTE DATA ASSESSMENT

A key feature of the E-Physio tool (Figure 7) is that it functions as an Internet of Things (IoT) device with the capability to connect to the internet. This connectivity enables real-time data transmission and reception, facilitating interaction and communication with other remote devices and systems. Another important aspect of the E-Physio tool is its ability to be managed and controlled remotely via web-based platforms. Thus, the E-Physio tool is an IoT system equipped with sensors and actuators that allow it to both collect data from the physical environment and interact with it. Specifically, it can detect multiple cardiorespiratory variables in subjects tested remotely, providing detailed information on their cardiovascular and respiratory profiles. In these experiments, skilled physicians and researchers operating in the biomedical laboratory of AC Technologies Ltd. (ACTlab, Italy) remotely acquired cardiodynamic data transmitted from the biomechanics laboratory at the Department of Mechanical and Aerospace Engineering, Polytechnic University of Turin (DIMlab, Italy), via the E-Physio tool and other connected devices. The data were obtained from a cyclist undergoing an incremental test, continuously monitored by two expert technicians (see Figure 4). During both the athletes' pre-test preparation and the test execution, a continuous real-time audio-visual communication was maintained between the two remote research units, located in the ACTlab and the DIMlab, to ensure proper adherence to the experimental protocol.

3 RESULTS

To better illustrate the functional adjustments observed in the cyclists during the test, the step-by-step changes of each selected variable are graphically represented below, using one of the subjects as a reference. In these graphs, the standard deviations (previously shown to be negligible) were omitted for each workload increment, in order to make the characteristic curves clearer and easier to interpret, thereby emphasizing their descriptive value. Figure 8 shows that the breathing rate (BR) initially increased almost linearly with the progressive workload, starting from approximately 13 breaths/min at 90 W (W0, 6th minute) up to the 24th minute (1th step), which was of 330 W. Beyond this point, the slope of the increase became steeper, reaching the maximum BR at Wmax (390 W) after only two additional workload increments. The figure also indicates that after about 10 minutes of recovery, the BR nearly returned to its resting value (13.5 vs. 17.8 breaths/min, respectively). In Figure 9, HR increased sharply from 62 b/min at W_0 to 110 b/min at the fourth workload step, corresponding to the 10th minute from the beginning of the test. After this point, HR continued to rise at a nearly steady rate, reaching 163 b/min at W_{max}, although with a gentler slope of approximately 3 b/min per step. In contrast to the behavior observed for breathing rate (BR), after the de-fatiguing pedaling period HR did not return to its pre-test value, remaining instead at 102 b/min. Figure 10 illustrates the workload-induced behavior of the athlete's systolic (SABP) and diastolic (DABP) arterial blood pressures. The SABP increased in a pattern similar to that observed for heart rate (HR), rising from 122 Torr at W_0 to a peak of 185 Torr at W_{max}. In contrast, the DABP exhibited an opposite trend, decreasing progressively from 80 Torr at W_0 to a minimum of 15 Torr at W_{max}. During the recovery pedaling period, the SABP nearly returned to its resting value (118 Torr), whereas the DABP did not fully recover, stabilizing instead at 60 Torr. The blue curves in Figures 11, 12, and 13 illustrate the workload-dependent changes in three bioimpedance-derived variables contributing to the SV generation: the Thoracic Fluid Index or TFI, the Ejection Velocity Index or EVI, and the Ventricular Ejection Time or VET, respectively.

In Figure 11, the TFI curve shows an initial increase in the LVPL, rising from its resting value of 41.8 $m\Omega^{-1}$ up to 43.8 $m\Omega^{-1}$ at the fourth workload step—an increase of approximately +5%. Beyond this point, TFI remained stable until the peak workload was reached. However, during the post-exercise (de-fatiguing) pedalling period, TFI decreased to 40.8 $m\Omega^{-1}$, corresponding to about –2.8% relative to its resting value. In contrast, the blue curve in Figure 12, which represents the workload-induced changes in the cyclist's EVI (here considered as the left ventricular MCI), displays an increasing trend similar to that observed in the BR. From rest (W_0, 1.21 $\Omega \cdot s^{-1}$) up to the 22^{ht} minute of pedalling (2.49 $\Omega \cdot s^{-1}$), EVI increased almost linearly, at a rate of approximately 0.13 $\Omega \cdot s^{-1}$ per step. After this point, the slope steepened, leading to a peak value of 3.07 $\Omega \cdot s^{-1}$. As shown by the blue curve in Figure 13, the cyclist's VET during the incremental test behaved, as expected, inversely to HR. Specifically, compared to the resting value (0.182 s), VET decreased markedly during exercise, reaching 0.138 s at maximal workload (Wmax)—a reduction of approximately 24%. The blue curve in Figure 14, representing the stroke volume (SV) adjustments observed in this athlete during the test effort — resulting from the integrated responses of TFI, EVI, and VET — displays a triphasic pattern.

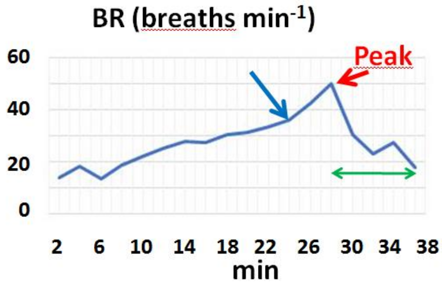

Figure 8 In the representative subject selected as a reference, the blue curve illustrates the breathing rate (BR), measured every 2 minutes from the beginning of the incremental test until exhaustion. The interval between the two tips of the double green arrow indicates the de-fatiguing pedalling period. The blue arrow marks the time point from the beginning of the test when the curve slope sharply increased (approximately at the 23^{ht} minute), up to the workload peak indicated by the red arrow.

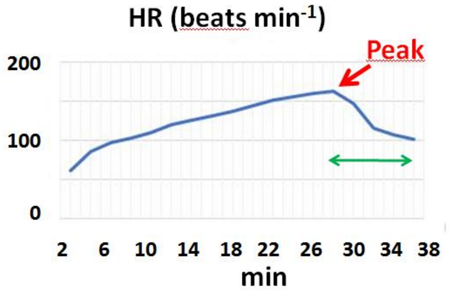

Figure 9 In the tested subject, the blue curve shows the heart rate (HR), measured every 2 minutes from the start of the incremental test until exhaustion. The interval between the two tips of the double green arrow indicates the de-fatiguing pedalling period. The red arrow marks the time point at which the peak mechanical power output occurred. From the 6th minute up to the peak workload, no significant changes in the curve slope were observed.

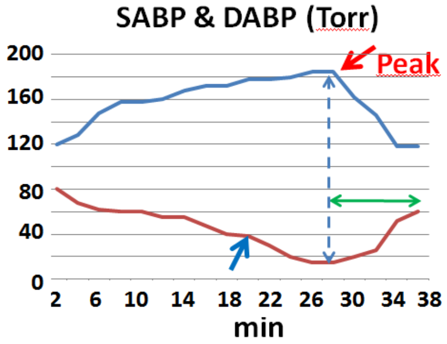

Figure 10 In the same subject, the blue and red curves represent the systolic (SABP) and diastolic (DABP) arterial blood pressures, respectively, measured every 2 minutes from the beginning of the incremental test until exhaustion. The blue vertical dotted line indicates the coincidence of both pressures at the peak workload step, marked by the red arrow. The blue arrow highlights the point (around the 20th minute) at which the DABP curve showed an increase in its negative slope. The interval between the two tips of the double green arrow represents the de-fatiguing pedalling period for both arterial pressure variables.

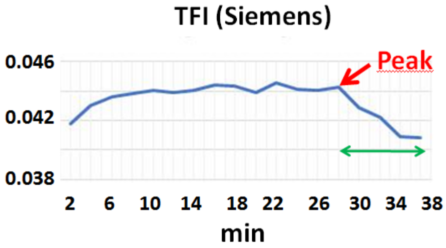

Figure 11 In the tested subject, the blue curve represents the thoracic fluids index (TFI)—that is, the left ventricular preload index—measured in Siemens as thoracic electrical conductance, assessed every 2 minutes from rest up to the peak workload during the incremental test to exhaustion. The interval between the two tips of the double green arrow indicates the de-fatiguing pedalling period. The red arrow marks the time at which the peak mechanical power output occurred.

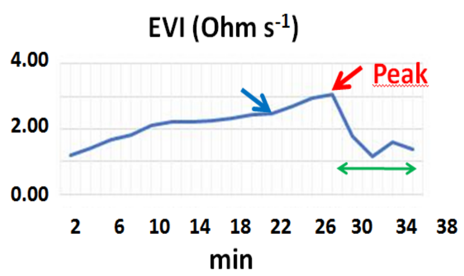

Figure 12 In the representative cyclist, the blue curve illustrates the left ventricular ejection velocity index (EVI), assessed every 2 minutes from the beginning of the incremental test until exhaustion. The interval between the two tips of the double green arrow indicates the de-fatiguing pedalling period. The blue arrow marks the time point when the curve slope visibly increased (approximately at the 22th minute), while the red arrow indicates the time corresponding to the peak mechanical workload.

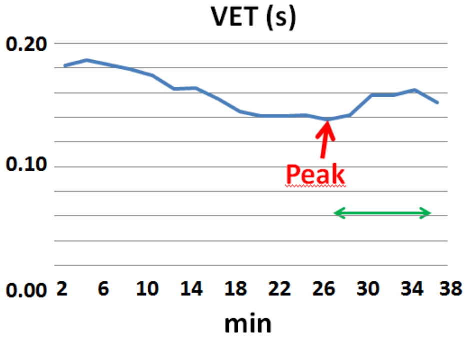

Figure 13 In the here tested cyclist, the blue curve shows the left ventricular ejection time (VET), measured every 2 minutes from the beginning of the incremental test until exhaustion, indicated by the red arrow. The interval between the two tips of the double green arrow indicates the de-fatiguing pedalling period.

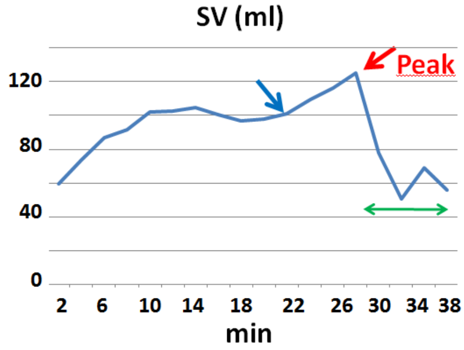

Figure 14 In this cyclist, the blue curve represents the left ventricular stroke volume (SV), measured every 2 minutes from the beginning of the incremental test until exhaustion. The interval between the two tips of the double green arrow indicates the de-fatiguing pedalling period. The blue arrow marks the point where an increase in the curve slope occurred, while the red arrow indicates the time at which the peak mechanical power output was reached.

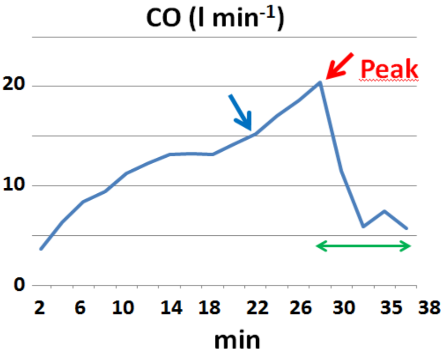

Figure 15 In the representative cyclist, the blue curve illustrates the cardiac output (CO), measured every 2 minutes from the beginning of the incremental test until exhaustion. The interval between the two tips of the double green arrow indicates the de-fatiguing pedalling period. The blue arrow marks a small but evident increase in the curve slope, while the red arrow indicates the time corresponding to the peak mechanical power output.

From rest to the 10th minute of exercise (corresponding to the 5th workload step), SV increased from 59.7 ml to 102.5 ml, 100 ml, fluctuating between a minimum of 96.6 ml and a maximum of 104.5 ml. Subsequently, as indicated by the blue arrow in figure, at approximately the 22th minute, SV rose sharply again, with a mean slope of about 8.5 mL per step during the final three workload increments, ultimately reaching a peak value of 125.2 ml. However, by the end of the recovery (de-fatiguing) phase, SV returned to its resting value, even dropping slightly below it. As is well known, CO depends on both an inotropic component (SV) and a chronotropic component (HR), being mathematically defined as their product (see Eq. 4). Indeed, as shown in Figure 15, the morphology of the cyclist's CO curve as a function of workload increase resembles the shape of the SV curve, albeit with less pronounced variations in slope, due to the smoothing effect of HR. Nevertheless, as highlighted by the blue arrow in Figure 15, a small but noticeable increase in the CO curve slope also occurred when the workload reached the 22th minute from W_0. At the end of the post-test recovery period, however, CO did not return to its resting value, remaining at 5.7 l min^{-1} compared to the resting level of 3.7 l min^{-1}. Table II reports the mean ± SD values of all selected cardiorespiratory variables measured in the seven cyclists, both at W_0 and at W_{max}. A statistically significant increase was observed at W_{max} compared with W_0 for HR, BR, SABP, EVI, SV, and CO, whereas DABP, and VET significantly decreased. In contrast, no statistically significant change was found in TFI between W_{max} and W_0. Furthermore, a slight reduction in peak SO_2 was observed (−2%), although this variation remained within the range of physiological variability. Nevertheless, due to the small sample size of the tested subjects, the only statistically significant differences observed between mean resting and peak values (i.e., W_0 and W_{max}; $P < 0.5$ or $P > 0.5$) may not fully capture the true effect size produced by the incremental test performed to exhaustion.

Table II – Mean ± SD values of cardiorespiratory variables among seven tested athletes

STEP	W (watt)	HR (Beat/min)	BR (Breath/min)	SABP (Torr)	DABP (Torr)	SO_2 (%)	TFI (Siemens)	EVI (Ω/s)	VET (s)	SV (ml)	CO (l/min)
W_0	0	67	17	122	74	98	0.044	1.12	0.22	74.3	4.6
±SD		±11	±2	±10	±8	±1.0	±0.002	±0.11	±0.03	±1.1	±0.2
W_{max}	360	182*	56*	194*	38*	96*	0.043	3.27*	0.14*	131.4*	21.3*
±SD	±36	±11	±8	±12	±19	±1.4	±0.004	±0.29	±0.01	±26.5	±5.5
Δ%		+172	+229	+59	-49	-2	-2.3	+192	-36	+77	+363

W_0: rest; W_{max}: maximum workload; HR: heart rate; BR: breath rate; SABP: systolic arterial blood pressure; DABP: diastolic arterial blood pressure; SO_2: arterial blood oxygen saturation; TFI: thoracic fluids index; EVI: ejection velocity index; VET: ventricular ejection time; SV: stroke volume; CO: cardiac output; Δ%: changes in percentage of maximum versus rest values; *: $P<0.05$ or statically significant compared to rest (the Student's *t* parametric test for paired data was here utilized).

Table III – Effect sizes amplitude of the W_{max} versus W_0 mean values comparisons for each selected variable

Variables	Means difference (W_{max}-W_0)	Pooled SD	Cohen's "d" index
HR Beats/min	115	11.00	10.45
BR Breaths/min	39	5.83	6.69
SABP Torr	72	11.04	6.52
DABP Torr	-36	14.58	12.11
SO_2 %	2	1.22	1.64
TFI mSiemens	1	3.46	0.29
EVI mΩ/s	2150	219	9.82
VET ms	-80	22.36	3.58
SV ml	57.10	18.75	3.04
CO l/min	16.7	3.90	3.89
Workload W	360	25.46	14.14

HR: heart rate; BR: breath rate; SABP: systolic arterial blood pressure; DABP: diastolic arterial blood pressure; SO_2: arterial blood oxygen percentage; TFI: thoracic fluids index; EVI: peak of left ventricle ejection velocity index; VET: ventricular ejection time; SV: left ventricle stroke volume; CO: cardiac output.

Therefore, the Cohen's "d" index [28]—calculated as the difference between the two means divided by the pooled standard deviation—was employed. For each cardiorespiratory and power-related variable considered, table III reports the magnitude of this effect when comparing values at W_0 and W_{max}. A "d" value greater than 0.8 was interpreted as indicating a strong physiological response of the variable to maximal exercise, which was the case for all but one of the variables analyzed. Conversely, a "d" value around 0.2, as observed for TFI, suggests a negligible effect size between W_{max} and W_0, implying that these two conditions are practically similar for this variable.

4 DISCUSSION

Data presented in Table II clearly demonstrate that the group of competitive road cyclists investigated in this study were characterized by cardiodynamic profiles typical of well-trained athletes engaged in this sport. Recent evidence indicates that the functional adaptations occurring during exercise in such athletes are characterized by increased hemodynamic force generation during systole and enhanced relaxation during early diastole [29].Indeed, the cardiovascular variables that primarily determined the cyclists' oxygen consumption—and consequently their muscular power output—namely the cardiac output "CO", which was in turn dependent on the SV and, more specifically, on the EVI, all reached peak values significantly higher than those observed at rest. These differences were statistically significant both in terms of "P" and "d" values here calculated. Furthermore, in the representative athlete's graphs showing the changes in these three cardiodynamic variables with increasing workload, a marked increase in the slope of the curves becomes evident at approximately 77% (300 W) of the maximal workload (W_{max} = 390 W). Simultaneously, the curve describing the BR as a function of workload also shows a noticeable increase in slope beginning around 330 W compared with the W_0 condition.

Considering that during exercise pulmonary ventilation (PV) is mainly driven by BR [30], and that during incremental exercise PV increases its slope when carbon dioxide volume (VCO_2) production exceeds that of oxygen uptake (VO_2)—that is, when the so-called aerobic threshold (AT) is reached [31]—the observed increase in the slope of the BR curve in the studied athlete can reasonably be interpreted as an indicator of having reached the AT. Sendra-Perez et al. [32], studying skilled cyclists and triathletes performing an incremental test on a cycle ergometer, reported that muscle oxygen saturation—corresponding to the attainment of the AT—in the biceps femoris occurred at approximately 77% of Wmax. This percentage closely matched the workload at which an increased slope was observed in the cardiodynamic variables of our tested cyclist. Accordingly, the cyclist's CO and its generating cardiodynamic components—namely, EVI and SV—all exhibited slope increases in their respective characteristic curves around the workload corresponding to a metabolic substrate shift. This shift reflects the point at which anaerobic pathways begin to play a crucial role in supplying energy for the mechanical power produced by the pedalling muscles. From this observation, it can be inferred that this experimental protocol allows for the detection of the percentage of W_{max} at which AT occurs in competitive road cyclists directly from the morphology of the cardiodynamic response curves during an incremental test. Thus, it eliminates the need for bulky and expensive calorimetric equipment for measuring O_2 consumption and CO_2 production in performing athletes. In this context, it is well known that just above the AT, enhanced sympathetic activity promotes the secretion of hormones (e.g., epinephrine) that increase heart rate and blood pressure to sustain oxygen delivery to the tissues. Moreover, a recent study demonstrated a strong relationship between the rapid repolarisation of the cardiac ventricles—triggered by the heightened sympathetic drive—and the attainment of AT. Specifically, upon reaching AT during an incremental test, the surge in sympathetic activity required for faster ventilation induces rapid changes in sympathetically modulated ventricular repolarisation [33]. It is therefore reasonable to hypothesize that, in our exampled cyclist, the rapid electrical event of ventricular repolarisation was followed by an equally rapid mechanical response of the ventricle—manifested as an increase in myocardial contractility, which translates into a higher velocity of left ventricular ejection. In our study, the blue arrows in the EVI, followed by SV and then CO characteristic curves plotted against increasing workload, indicate a steeper slope after the subject's AT, or approximately at 80% of W_{max}. When extrapolated from individual athletes to the average of all seven tested subjects, these data confirm that all participants had excellent aerobic capacity, efficiently supplying energy to the muscles involved in sustaining high pedal workloads. This performance was further supported by a cardiodynamic contribution, as CO increased post-AT, thereby enhancing oxygen delivery to the working muscles. However, considering the heterometric contribution of ventricular preload (see the TFI graph in Figure 11) to SV and consequently to CO, it is evident that TFI initially increased by approximately 5% above the resting value with workload rising to 120 W and then remained essentially unchanged up to W_{max}. In summary, the two central/cardiac determinants of SV—the homeometric component, reflecting sympathetic nervous system-mediated myocardial contractility as represented by EVI, and the heterometric component, reflecting mechanical volumetric properties as represented by end-diastolic ventricular volume index by TFI—both increased during exercise on the laboratory bicycle. This dual contribution explains the progressive increase in SV despite a gradual reduction in VET, which decreased from 0.18 s at W_0 to approximately 22% below the resting value around 70% of W_{max}, and remained stable thereafter until peak workload (see Figure 13). The resultant SV, together with the nearly linear increase in HR, substantially contributed to the observed progressive rise in CO. During acute aerobic exercise, left ventricular diastolic function, and consequently ventricular filling, increase to ensure adequate cardiac output. This represents a significant challenge for the myocardium because exercise-induced tachycardia shortens ventricular diastolic time, even as cardiac output must rise to meet physiological demands [34]. In contrast to acute exercise, chronic exercise training, as observed in the exampled cyclist in our study, has been shown to enhance myocardial diastolic function [35]. As diastolic time shortens with increasing exercise intensity, the diastolic filling rate must rise to maintain the balance between left ventricular filling and ejection. This increase in diastolic filling rate is achieved primarily by augmenting the trans-mitral diastolic pressure gradient between the left atrium and left ventricle. The trans-mitral flow rate rises due to a relative decrease in intra-left ventricular pressure during early diastole [35], effectively creating a left ventricular suction effect across the mitral valve that enhances the trans-mitral pressure gradient. Several mechanisms contribute to this left ventricular diastolic suction:

1. Increased systolic contractile force (inotropic effect) enhances early diastolic elastic recoil of the myocardium [36].
2. Greater systolic fiber shortening during exercise results in smaller end-systolic volumes and lower intra-left ventricular pressures during early diastolic filling [37].
3. Enhanced relaxation of individual cardiomyocytes which occurs due to increased sarcoplasmic reticulum (SR) calcium reuptake [38], which is further stimulated by exercise-induced beta-adrenergic activation [39].
4. Beta-adrenergic stimulation increases cyclic AMP, which phosphorylates phospholamban, a regulatory of the SR membrane protein. This phosphorylation accelerates SR calcium reuptake, thereby enhancing cardiomyocyte relaxation and increasing the rate of diastolic filling [39,40].

Since the normal heart can increase trans-mitral diastolic flow during exercise through enhanced ventricular contraction and relaxation (ventricular suction), it can be reasonably inferred that, in the present sample of cyclists, the maintenance—or even increase—of left ventricular preload during the test, despite the progressive shortening of diastolic time, reflects a coordinated set of morpho-functional adaptations.

These adaptations are characteristic of athletes extensively trained for long-duration aerobic activities such as road cycling. Moreover, in this type of cyclist, the potential contribution of reduced total peripheral vascular resistance (TPVR)—i.e., left ventricular afterload—to the increase in SV) during intense exercise should not be overlooked. TPVR at a given workload can be estimated as the ratio between mean arterial blood pressure (MABP) and CO. MABP can, in turn, be calculated as [41]:

$$MABP = DABP + 1/3\ (SABP - DABP) = Torr \qquad (5)$$

thus the TPVR could be obtained as [41]:

$$TPVR = MABP : CO = Torr\ min\ l^{-1} \tag{6}$$

Concerning our reference cyclist, data from Figure 10 indicate that the MABP at W_0 was 90 Torr, and data from Figure 15 show that the corresponding CO was 3.7 l min⁻¹. Consequently, the TPVR at W_0 was approximately 24.3 Torr min l⁻¹. At W_{max}, his MABP remained at 90 Torr, while the corresponding CO increased to about 20 l min⁻¹, resulting in a TPVR of 4.5 Torr min l⁻¹—roughly 18% of its value at W_0.

This marked reduction in TPVR with increasing workload may appear paradoxical, given that exercise generally induces a widespread increase in sympathetic tone, leading to α_1-adrenergic receptor-mediated vasoconstriction across most vascular beds. However, it has been shown [42] that α_1 receptors are predominantly located in large upstream arteries of the muscles and are less sensitive, or even insensitive, to inhibitory factors generated by muscle metabolism. This distribution contributes to the maintenance of high MABP values as exercise intensity increases, as described by the following equation:

$$MABP = TPVR\ x\ CO \tag{7}$$

Thus, maintaining—or at least not allowing a decrease in—MABP during incremental exercise (as was observed in our tested cyclist) helps ensure adequate arterial blood flow to the working muscles by sustaining sufficient CO values, as illustrated by the following equation:

$$CO = MABP : TPVR \tag{8}$$

At the same time, due to the high density of α_2-type adrenergic receptors in intramuscular arteries—which serve a nutritive function and are highly sensitive to inhibition by muscle-derived agents/catabolites such as prostaglandins, adenosine, thromboxanes, and others—there is consequent intramuscular vasodilation aimed at supplying nutrients to the myocytes [43]. In the reference cyclist analyzed here, the graphs in Figure 10 clearly show two opposing events as workload increased: (a) a progressive rise in SABP resulting from increasing α_1-mediated stimuli in the large vessels outside the muscles, which ensured adequate peripheral transmission of a sufficient fraction of cardiac output; and (b) a mirror-like decrease in intramuscular TPVR due to inhibition of α_2 receptors, leading to a progressive drop in DABP while still ensuring nourishment of the muscles engaged in the escalating pedalling effort. Notably, in this subject, mean arterial blood pressure (MABP) remained at a good level despite the marked reduction in TPVR, with MABP around 90 Torr in both W_0 and W_{max} conditions. Furthermore, these adaptations provided a clear advantage for the heart mechanics, allowing it to deliver adequate oxygen to the working muscles at a lower energetic cost. Extending the observations from the reference cyclist to the seven athletes tested—whose mean ± SD values are reported in Table II—it is evident that the mean TFI, reflecting left ventricular preload impedance, reached a peak value at the end of the test that was not significantly different from the pre-test value. This finding indicates that, in all athletes, despite the progressive and substantial reduction in VET, preload continued to contribute to the volumetric component of stroke output until the conclusion of the test. Regarding the omeometric contributor index for stroke volume increase, namely the EVI, the peak increase observed in the graph of Figure 12 was approximately 154% of the resting value. This was lower than the mean peak value recorded across all tested subjects at W_{max}, which reached +192%. However, since the peak EVI value of the reference athlete (3.07 $\Omega\cdot s^{-1}$) fell within the range of the standard deviation of the group mean (minimum SD from the mean = 2.98 $\Omega\cdot s^{-1}$), it can reasonably be stated that the beat-to-beat pattern of EVI in the reference athlete can be considered representative of the mean behaviour observed across all participants. With respect to the peak values of the main bioimpedance-derived cardiodynamic variables—heart rate, stroke volume, and cardiac output—the percentage differences between the group mean and the representative subject were +10%, +5%, and +4%, respectively. As all three differences fall within the ±SD calculated for each mean, it is reasonable to consider the workload-dependent cardiodynamic adjustments observed in the exemplar cyclist as representative of those occurring in the entire group of athletes studied.

6 CONCLUSIONS

In the competitive road cyclists tested in this study, cardiovascular adaptations similar to those observed in long-distance runners may have occurred, leading to improved exercise efficiency. In fact, their hearts appeared to function more efficiently by increasing stroke volume as workload rose, thereby delivering more oxygen to the working muscles at a relatively lower overall heart rate. These adaptations could be further supported by a possible increase in the capillary network of the leg muscles [44], as suggested by the marked decrease in mean value of TPVR observed during the test. This indicates that the amount of blood pumped per heartbeat increased, meaning that less pumping effort was required to circulate the same volume of blood—i.e., the mechanical efficiency of the heart was enhanced. Moreover, since in these cyclists the peak value of the left ventricular preload index (TFI) did not decrease compared with W0, as previously reported in skilled long-distance runners after maximal treadmill exercise [45], this finding reinforces the conclusion that well-trained competitive road cyclists develop specific cardiovascular morpho-functional adaptations. These adaptations provide an advantage in maintaining high and prolonged levels of mechanically generated power at the pedals, primarily of aerobic origin, as also suggested by the high workload (77% of the peak value) at which their anaerobic threshold occurred during the exhaustive test.

7 STUDY LIMITATIONS

Unfortunately, this study is subject to several limitations. In particular, its small, all-male, single-session sample limits the generalizability of the findings. For these reasons, the present work should be regarded as a preliminary study. The authors are committed to collecting additional experimental data in the near future to address these limitations and thereby ensure the full applicability of the proposed method. Nevertheless, despite the restricted sample size and gender composition, the effect size statistics reported here provide substantial evidence of a robust physiological response to maximal exercise in this specific group of athletes.

REFERENCES

[1] Gardner A.S., Stephens S., Martin D.T., Lawton E., Lee H. and Jenkins D., Accuracy of SRM and power tap power monitoring systems for bicycling. *Med Sci Sports Exerc,* Vol. 36, No. 7, pp. 1252–1258, 2004.

[2] Bouillod A., Soto-Romero G., Grappe F., Bertucci W., Brunet E. and Cassirame J., Caveats and recommendations to assess the validity and reliability of cycling power meters: A systematic scoping review. *Sensors*, Vol. 22, No. 1, pp. 386, 2022.

[3] Belforte G., Bonisoli E., Eula G., Ivanov A. and Sirolli S., Design and Tests of Textile Pneumatic Muscles for Active Suits, *International Journal of Mechanics and Control*, Vol. 17, No. 01, pp. 37-48, 2016.

[4] Belforte G., Raparelli T., Eula G., Sirolli S., Appendino S., Geminiani G.C., Geda E., Zettin M., Virgilio R. and Sacco K., Study and Realisation of a preliminary control system for the active exoskeleton called P.I.G.R.O., suitable for unloaded robotic neurorehabilitation treatments, *International Journal of Mechanics and Control*, Vol. 22, No. 01, pp. 125-142, 2021.

[5] Garrosa M., Ceccarelli M. and V. Díaz, Biomechanics in vehicle accidents for risk analysis, *International Journal of Mechanics and Control*, Vol. 24, No. 01, pp. 43-52, 2023.

[6] Shepertycky M., Burton S., Dickson A., Liu Y.F. and Li, Q., Removing energy with an exoskeleton reduces the metabolic cost of walking. S*cience*, Vol. 80, No. 372, pp. 957–960, 2021.

[7] Mohammadzadeh Gonabadi A., Pipinos I.I., Myers S.A. and Fallahtafti F., Optimizing hip exoskeleton assistance pattern based on machine learning and simulation algorithms: a personalized approach to metabolic cost reduction. *Front Robot AI.* Vol. 12, pp. 1669600, 2025.

[8] Wu W.C., Concu A., Solinas R., Meloni L., Manuello-Bertetto A., Fois A., Loviselli A., Deledda A. and Velluzzi F., Metabolic power and energy cost of mechanical work carried out by a sailor engaged in a solo ocean race: a case study. *International Journal of Mechanics and Control*, Vol. 19, No. 02, pp. 19-32, 2018.

[9] Garau M., Ruggiu M., Manuello M. and Concu A., Correlation between mechanical and metabolic energy during the gait cycle with and without jumping stilts. *International Journal of Mechanics and Control*, Vol. 19, No. 02, pp. 33-38, 2018.

[10] Sheridan D., Jaspers A., Viet Cuong D., Op De Beéck T., Moyna N.M., de Beukelaar T.T. and Roantree M., Estimating oxygen uptake in simulated team sports using machine learning models and wearable sensor data: A pilot study. *PLoS One*, Vol. 20, No. 4, 2025.

[11] Concu A. and Marcello C., Stroke volume response to progressive exercise in athletes engaged in different training modes. *Eur J Appl Physiol*, Vol. 66, pp. 11-17, 1993.

[12] Kumari P.D., Singh K.M., Mayaluri Z.L., Sahoo P.K., Lenka S., Panda G. and Agir S.K., A hybrid variational mode decomposition framework for enhanced cardiac output estimation using impedance cardiography. *Sci Rep*, Vol. 15, No. 1, pp. 25784, 2025.

[13] Marongiu E., Crisafulli A., Ghiani G., Olla S., Roberto S., Pinna M., Pusceddu M., Palazzolo M., Sanna I., Concu A. and Tocco F., Cardiovascular Responses during free-diving in the sea. *Int J Sports Med*, Vol. 36, pp. 297-301, 2015.

[14] Campagna M., Lecca L.I., Velluzzi F., Serra C., Bianco P., Manuello Bertetto A., Dell'Osa A.H., Fanni B., De Pau A., Fois A., Melis L., Kalb A., Marcello R., Melis S., Concu A. and Tocco F., A mechatronic simulator of an aircraft cockpit to study, by a virtual flight test, cardiovascular fitness in airline pilots banned to fly since covid-19 lockdown. *International Journal of Mechanics and Control*, Vol. 23, No. 02, pp. 85-99, 2022.

[15] Metshein M., Krivošei A., Abdullayev A., Annus P. and Märtens O., Non-Standard Electrode Placement Strategies for ECG Signal Acquisition. *Sensors (Basel)*, Vol. 22, No. 23, pp. 9351, 2022.

[16] Tocco F., Mattana D.V., Solinas R., Velluzzi F., Usai P., Fois A., Melis L., Bianco P., Serra C., Manuello Bertetto A., Dell'Osa A.H., Pereira A.F., Cerina A., Loviselli L., Marcello R., Melis S. and Concu A., Cardiometabolic benefits from a coastal sailing in a radical cystectomy patient remotely controlled by an internet of thing mechatronic tool: a case study. *International Journal of Mechanics and Control*. Vol. 24, N. 02, pp. 39-61, 2023.

[17] Tocco F., Solinas R., Velluzzi F., Massidda M., Mattana D.V., Fois A., Melis L., Manuello Bertetto A., Bonisoli E.[†], Venturini S., Bianco P., Dell'Osa A.H., Pereira A.F., Melis S., Cerina A., Loviselli L., Marcello R. and Concu A., A mechatronic tool for revealing inverse relationships among heart's stroke volume and head's linear acceleration induced by moored boats rolling in elderly sailors with unchanged body sizes: a non-drug anti-hypertensive advantage?. *International Journal of Mechanics and Control,* Vol. 25, No. 01, pp. 133-142, 2024.

[18] Dell'Osa A.H., Fois A., Cerina A., Pili F., Manuello Bertetto A., Velluzzi F., Bellomi G., Palmas M., Ruggiu M., Melis S., Tocco F., and Concu A., Impedance cardiography assessment during body immersion in a high concentrated water solution of magnesium chloride simulating space microgravity: a pilot study. *Journal of Physics: Conference Series*, Vol. 3014, pp. 012006, 2025.

[19] Roux A., Optimal integration between mechanical and physiological quantities to maximize the performance of competitive cyclists. *Graduate thesis in Mechanical Engineering,* Referees: Proff. Manuello Bertetto A, Concu A, Politecnico di Torino, Italy, 2024.

[20] Digo E., Ingrosso L., Vargas M., De Vito C. and Gastaldi C., A computational methodology for recumbent bicycle fitting to optimize aerodynamic efficiency while ensuring rider comfort. *International Journal of Mechanics and Control*, Vol. 25, No. 01, pp. 105-113, 2024.

[21] Charvátová H, Procházka A. and Vyšata O., Motion assessment for accelerometric and heart rate cycling data analysis. *Sensors (Basel)*, 2020 Vol. 20, No. 5, pp.1523, 2020.

[22] Salas-Montoro J.A., Valdivia-Fernández I., Rozas A., Reyes-Sánchez J.M., Zabala M. and Pérez-Díaz J.J., Do power meter data depend on the device on which they are collected? Comparison of eleven different recordings. *Sensors (Basel)*, Vol. 25. No. 2, pp. 295, 2025.

[23] Tocco F., Crisafulli A., Marongiu E., Milia R., Kalb A. and Concu A., A portable device to assess underwater changes of cardiodynamic variables by impedance cardiography. *Journal of Physics: Conference Series*, Vol. 407, pp. 012026, 2012.

[24] Bernstein D.P., A new stroke volume equation for thoracic electrical bioimpedance: theory and rationale. *Crit Care Med*, Vol. 14, No. 10, pp. 904-909, 1986.

[25] Concu A., Respiratory and cardiac effect of passive limb movements in man. *Pflugers Arch Eur J Physiol*, Vol. 412, pp. 548-550, 1988.

[26] Eeftinck Schattenkerk D.W., van Lieshout J.J., van den Meiracker A.H., Wesseling K.R., Blanc S., Wieling W., van Montfrans G.A., Settels J.J., Wesseling K.H. and Westerhof B.E., Nexfin noninvasive continuous blood pressure validated against Riva-Rocci/Korotkoff. *Am J Hypertens*, Vol. 22, No. 4, pp. 378-383, 2009.

[27] Ruedisueli I., Ma J., Nguyen R., Lakhani K., Gornbein J. and Middlekauff H.R, Optimizing ECG lead selection for detection of prolongation of ventricular repolarization as measured by the Tpeak-end interval. *Ann Noninvasive Electrocardiol*, Vol. 27, No. 4, pp. e12958, 2022.

[28] Eren-Zengin F., Tuncer D., Senaran H. and Uzer G., Effects of isolated gastrocnemius tightness on foot posture, strength, function, and balance in children aged 7-16: a case-control study. *BMC Sports Sci Med Rehabil*, Vol. 17, No. 1, pp. 289, 2025.

[29] Pellegrino A., Toncelli L., Vanni S., Modesti A., Pedrizzetti G. and Modesti P.A., Structural and functional remodeling for elite cyclists during exercise; pressure-volume loops and hemodynamic forces analysis. *Am J Physiol Heart Circ Physiol*, Vol. 328, No. 3, pp. H393-H400, 2025.

[30] Hoshi D., Fukuie M., Tomoto T., Qin W., Tarumi T., Sugawara J. and Watanabe K., Respiratory regulation and lung volume during aquatic and land-based exercise in healthy young adults. *Physiol Rep*, Vol. 13, No. 19, pp. e70564, 2025.

[31] Sun X.G., Hansen J.E., Garatachea N., Storer T.W. and Wasserman K., Ventilatory efficiency during exercise in healthy subjects. *Am J Respir Crit Care Med*, Vol. 166, No. 11, pp. 1443-1448, 2002.

[32] Sendra-Pérez C., Encarnacion-Martinez A., Salvador-Palmer R., Murias J.M. and Priego-Quesada J.I. Profiles of muscle-specific oxygenation responses and thresholds during graded cycling incremental test. *Eur J Appl Physiol*. Vol. 125, No. 1, pp. 237-245, 2025.

[33] Milagro J., Hernández-Vicente A., Hernando D., Casajús J.A., Garatachea N., Bailón R. and Pueyo E., Estimation of the second ventilatory threshold through ventricular repolarization profile analysis. *Scand J Med Sci Sports*, Vol. 31, No. 2, pp. 339-349, 2021.

[34] Libonati J.R., Myocardial diastolic function and exercise. *Med Sci Sports Exerc*, Vol. 31, No. 12, pp. 1741-1747, 1999.

[35] George K., Oxborough D., Forster J., Whyte G., Shave R., Dawson E., Stephenson C., Dugdill L., Edwards B. and Gaze D., Mitral annular myocardial velocity assessment of segmental left ventricular diastolic function after prolonged exercise in humans. *J Physiol*, Vol. 15, No. 569(Pt 1), pp. 305-313, 2005.

[36] Cheng, C.P., Igarashi Y. and Little W.C., Mechanism of augmented rate of left ventricular filling during exercise. *Circ Res*, Vol. 70, pp. 9–19, 1992.

[37] Little, W.C. and Cheng C.P., Modulation of diastolic dysfunction in the intact heart. In : *Diastolic Relaxation of the Heart,* 2nd edition, B. H. Lorell and W. Grossman, Boston: Kluwer Academic Publishers, pp. 167–176, 1994.

[38] Tate C.A., Taffet G.E., Hudson E.K., Blaylock S.L., McBride R.P. and Michael L.H., Enhanced calcium uptake of cardiac sarcoplasmic reticulum in exercise-trained rats. *Am J Physiol Heart Circ Physiol*, Vol. 258, No. 27, pp. H431-H435, 1990.

[39] Katz A.M., *Physiology of the Heart*. New York: Raven Press, pp. 178–195, 1992.

[40] Apstein C.S., Libonati J.R., Varma N., and Eberli F.R., *Exercise, Diastolic Function, and Dysfunction: Exercise and Heart Failure,* Eds. G. Balady and J. P. Armonk, NY: Futura Publishing, pp. 39–83, 1997.

[41] Manuello Bertetto A.,Tocco F., Bellomi G., Mulargia L., Ruggiu M., Palmas M., Massidda M., Ghiani G., Velluzzi F., Melis S., Fois A., Dell'Osa A.H., Cerina A., Bertelli U., Carta M.G., Bianco P.R. and Concu A., Cardiovascular and metabolic engagement after an endurance race in pilots driving motorboats electrically powered by green Energy. *International Journal of Mechanics and Control*, Vol. 26, No. 01, pp. 221-230, 2025.

[42] Wray D.W., Fadel P.J., Smith M.L., Raven P. and Sander M., Inhibition of alpha-adrenergic vasoconstriction in exercising human thigh muscles. *J Physiol*, Vol. 555 No. 2, pp. 545-563, 2004.

[43] Concu A., Cardiovascular adjustments during exercise: points and counterpoints, *New insight into cardiovascular apparatus during exercise*, Eds. Crisafulli A. and Concu A., Research Signpost, Kerala, India, pp. 61-84, 2007.

[44] Saltin B., Kim C.K., Terrados N., Larsen H., Svedenhag J. and Rolf C.J., Morphology, enzyme activities and buffer capacity in leg muscles of Kenyan and Scandinavian runners. *Scand J Med Sci Sports*, Vol. 5, No. 4, pp. 222-230, 1995.

[45] Percy R.F., Conetta D.A. and Miller A.B., Echocardiographic assessment of the left ventricle of endurance athletes just before and after exercise. *Am J Cardiol*, Vol. 65, No. 16, pp. 1140-1144, 1990.

ISSN 1590-8844
International Journal of Mechanics and Control, Vol. 26, No. 02, 2025
https://doi.org/10.69076/jomac.2025.0028

REMOTE MONITORING OF DAILY CHANGES IN CARDIAC MECHANICAL EFFICIENCY AND OTHER CARDIAC PARAMETERS IN A COASTAL KAYAKER OVER ONE-MONTH OF PADDLING

FilippoTocco[1,10], Giovanna Ghiani[1], Marco Palmas[1,10], Michele Ruggiu[1,10], Fernanda Velluzzi[1], Deledda A[1], Alberto Masala[2], Andrea Fois[3], Andrea Manuello Bertetto[4], Antonio Hector dell'Osa[5], Angelo Cerina[6], Cristiana Cappagli[7], Salvatore Melis[1,8,10], Valentina Loi[9], Ricardo Marcello[9], Alberto Concu[9,10]

[1]Department of Medical Sciences and Public Health, University of Cagliari, Italy
[2]Sports Medicine Association of Sassari, Sassari, Italy
[3]Nomadyca Ltd, Remote Biosignals Acquisition Unit, Mulago Hospital, Kampala, Uganda
[4]Department of Mechanical and Aerospace Engineering, Politecnico di Torino, Turin, Italy
[5]Laboratorio de Electrónica Aplicada y Biomedicina, Universidad Nacional de Tierra del Fuego, Ushuaia, Argentina
[6]Acquaforte Thalasso & Spa Medical Team, Forte Village Resort, Santa Margherita di Pula, Cagliari, Italy
[7]Kpurple, individual company, Cagliari, Italy
[8]Sardinia's Schools Direction Office, Physical and Sports Education Unit, Ministry of Education and Merit, Cagliari, Italy
[9]AC Technologies Ltd, Internet of Things Unit, Cagliari, Italy
[10]Sporting Life & Medicine Lab, Sardegna Ricerche, Cagliari, Italy

ABSTRACT

A male kayaker covered approximately 1,000 km along a sea coast over a period of ~40 days. Each night, after setting up camp, he noninvasively self-recorded at rest several systemic variables and transmitted them to a remote medical center via a telemedicine platform developed by the research team. This system employed a custom-built wearable device based on electrical impedance to acquire beat-to-beat cardiodynamic variables. Additional measurements included arterial blood pressure, expiratory peak flow, maximal handgrip force, tympanic temperature, and urine specific gravity. Over the course of the expedition, cardiac output linearly increased by 65 ml min^{-1} per day, primarily due to a rise in stroke volume and a concomitant reduction in total peripheral vascular resistance which, in turn, led to a decrease in mean arterial pressure. The mechanical work of the heart showed no significant variation during navigation. However, towards the end of the journey, the rate–pressure product—an indicator of myocardial oxygen consumption—rose exponentially, indicating a progressive decline in cardiac mechanical efficiency. This trend paralleled a decrease in maximal handgrip strength and an increase in perceived exertion. Overall, the kayaking expedition promoted an improvement in oxygen delivery capacity and blood pressure lowering, although signs of cardiac and muscular fatigue became evident toward the end of the trip.

Keywords: kayaking, cardiodynamics, remote data assessing, heart mechanical efficiency

1 INTRODUCTION

Nautical motion activities performed with a paddle, i.e. kayaking, are characterized a motor pattern that leads to the activation of numerous muscle groups. Specifically, to execute the technical paddling movement—which primarily involves the muscles of the arms and shoulders—the paddler also engages the muscles of the back responsible for trunk rotation, as well as the core muscles, including the abdominals, which contribute to maintaining balance and proper spinal alignment. The legs are likewise involved, as they are subjected to a condition of isometric hypertonia during motion-specific performance. Therefore, kayak-specific functional training integrates aerobic conditioning —to enhance endurance—with muscular strengthening and toning, aimed at improving overall performance. From a biomechanical standpoint, kayak technique is a cyclical

Contact authors: Filippo Tocco[1], Alberto Concu[2]
[1]Dept of Medical Sciences and Public Health, University Cittadella, Provincial Road 8 – 09042 Cagliari, Italy
[2]AC Technologies Ltd, Internet of Things Unit, Via Pais 12- 09128 Cagliari, Italy
E-mail: aconcu44@gmail.com, filippo.tocco@tiscali.it

movement characterized by alternating right- and left-side strokes. During each stroke, the kayak exhibits fluctuations in acceleration because the paddler's dynamic motion, together with the varying magnitudes of propulsive and resistive forces, gives rise to oscillations in boat velocity. Consequently, the ability to achieve a high stroke rate is inversely proportional to stroke duration, such that greater kayak speed can be attributed to an increased stroke frequency. With the aim of investigating the systemic adaptations that characterise the body's response to long-duration physical activity training in a kayak carried out in a coastal marine environment, in a male kayaker who covered approximately 1,000 km along the coast over ~40 days, maximal kayak-ergometer tests to exhaustion after the trip has been found that VO_2peak normalized to body mass increased by 13%, the respiratory exchange rose by 16%, and estimated energy expenditure increased by 12%. Moreover, in this athlete echocardio-graphic assessment revealed a 32% increase in resting left ventricular stroke volume following the trip [1]. Since during his coastal voyage, this athlete was able each night—after dinner and after making camp—to noninvasively at rest self-record several systemic variables and transmit them to a remote specialized medical centre (RSMC) using a telemedicine device developed by the research team [2], in this study, it has been investigated the daily adjustments in the engagement of the athlete's physiological systems induced by paddling. This approach elucidated the time-dependent intrinsic adaptations underlying the morpho-functional changes that were previously observed following completion of the trip [1].

2 METHODS

2.1 THE SUBJECT AND HIS KAYAK

The participant was a highly skilled 47-year-old male kayaker who served as a federal-level rowing instructor at an Italian sports club. He frequently undertook long coastal kayak trips for both athletic and recreational/touristic purposes. For this study he circumnavigated the island of Sardinia (Italy) by kayak (Diana Canoe Manufacturers, model 535), covering 969 km over 41 days (see Figure 1). After each day of paddling he searched for a coastal site in which to camp overnight; if weather conditions precluded further navigation, he sometimes sheltered during the day as well. These circumstances resulted in prolonged stops during the trip, sometimes lasting several days.

2.2 INSTRUMENTATION

As shown in Figure 1, a flexible photovoltaic panel (Energy Flyer, Solbian, Turin, Italy) was installed on the stern of the boat; its specifications are reported in Figure 2. The compact panel weighs 360 g and which comprises four solar cells, delivering a maximum power of 12.5 W and a maximum current of 2.4 A at a nominal voltage of 5 V. While the kayak was underway and exposed to sunlight, the Energy Flyer panel charged a power bank via a standard USB port.

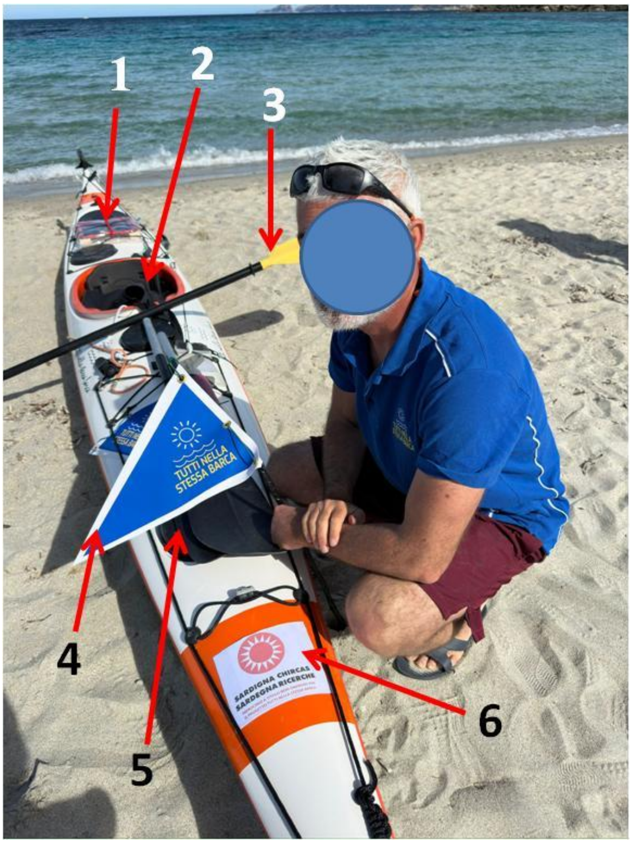

Figure 1 The kayak and its kayaker. (1) photovoltaic panel; (2) cockpit; (3) paddle; (4) pennant bearing the expedition name; (5) watertight bow locker containing scientific instruments; (6) adhesive panel bearing the logo of Sardegna Ricerche, the Italian research institution that provided patronage for the experiments together with the Polytechnic University of Turin in Italy.

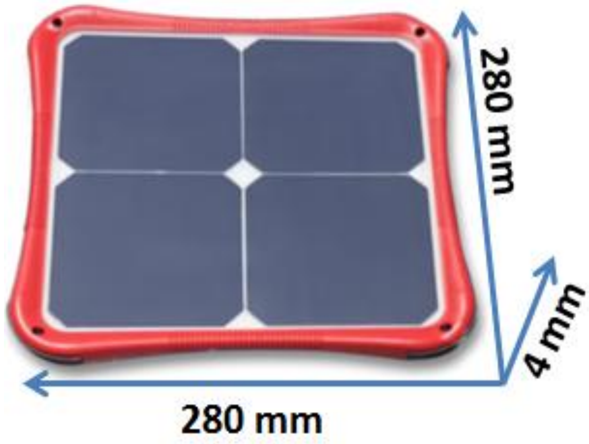

Figure 2 The flexible, square photovoltaic panel (model Energy Flyer) mounted on the stern of the kayak. Its three spatial dimensions—length, width, and thickness—are indicated by blue axes, with values shown in millimetres (mm). A protective red rubber frame with one anchoring hole at each corner surrounds the panel's active area, which consists of four black photovoltaic cells.

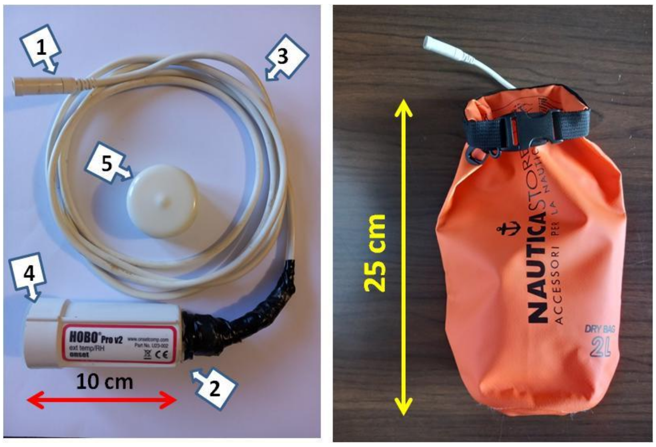

Figure 3 On the left a photo of the sensing device to record environment's temperature and humidity. 1) sensors tip, 2) device body with dedicated electronics for data recording, 3) 175 cm long connection cable between the tip and the body of the device, 4) optical emitter interface for the transmission of the stored signals, 5) protective cap of the optical interface. On the right the closed waterproof nautical bag from which only the sensorized head emerged.

The power bank then supplied power to the electronic devices used for functional measurements once the kayaker landed to set up the night camp. During navigation, all equipment was enclosed in a waterproof casing that was transparent to sunlight. The kayak was also fitted with a waterproof data logger (HOBO Pro v2, LI−COR, Lincoln, USA) shown in Figure 3 that recorded ambient air temperature (*°C*) and relative humidity (%) at 30−second intervals. The logger was housed in a 2 litter waterproof nautical bag with only the sensor tip protruding, and was secured daily in the cockpit by attaching it to the sides of the seat. Upon disembarking, the athlete brought the bag containing the HOBO into the overnight camp to enable a continuous 24-hour recording. Instrumental traces in Figure 4 illustrate a representative day of these measurements. When inserted into a splash−resistant docking station, this interface permits data transfer from the HOBO logger via an optical USB connection.

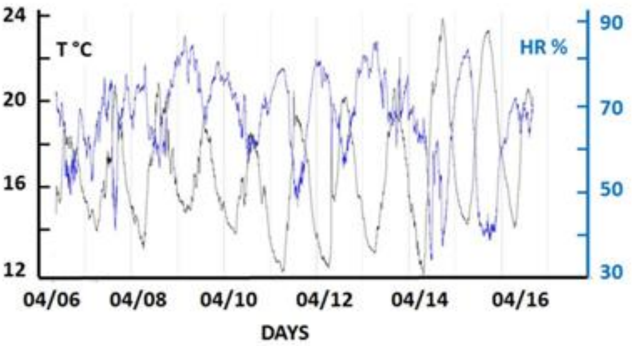

Figure 4 Time series of environmental temperature (T, *°C*; black) and relative humidity (RH %; blue) recorded by the HOBO logger from 6 to 16 April. Both the lowest temperatures and highest relative humidity were observed at night.

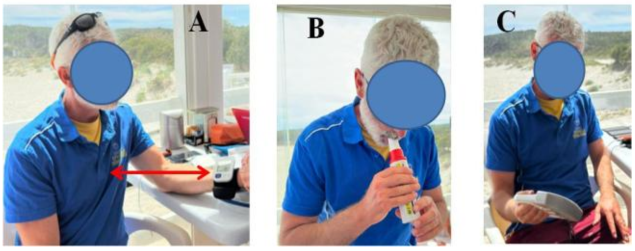

Figure 5 Photographs illustrate examples of the kayaker performing daily physiological measurements after landing: (A) arterial blood pressure measured with an automatic wrist sphygmomanometer, ensuring that the device was kept at heart level (indicated by the double red arrow); (B) peak expiratory flow assessed using a graduated tube inserted into the mouth and held with both hands, taking care not to obstruct the sliding cursor along the scale ($l\ min^{-1}$) and (C) handgrip strength measured with the dominant hand using a dynamometer, displaying the maximum contraction force in *kg* on its screen.

Inside a waterproof nautical bag stored in the kayak's bow locker (see Figure 1), the athlete kept the equipment used to self-record noninvasive data, which he transmitted to the RSMC each night after dinner and after establishing camp. The instrumentation included:

- a custom-built wearable device [3] for acquiring thoracic electrical impedance (Zt in Ω), which reciprocal also represents the thoracic fluid index (TFI in Ω-1), enabled the use of impedance cardiography (ICG) to non invasively obtain beat-to-beat cardiodynamic variables together with an ECG trace (E-Physio Tool, AC Technologies Ltd, Cagliari, Italy), the device requires a 5 V DC power supply capable of deliver 2A.
- a miniaturized automatic wrist sphygmomanometer (Omron HEM-6181, Kyoto, Japan), shown in Figure 5, was used to acquire systolic (SABP) and diastolic (DABP) arterial blood pressures (in *Torr*) together with heart rate (HR; bpm), the device has been validated
- according to the ANSI/AAMI/ISO 81060-2:2013 protocol [4];
- a manual device for measuring peak expiratory flow (PEF), expressed in l min-1, which consisted of a graduated cylinder to be inserted into the mouth through into which the subject performed a maximal forced;
- exhalation (Mini-Wright, Clement Clarke International, UK) (see Figure 5) [5];
- a device for assessing maximal force output during the handgrip maneuver (HAG), measured in kg and performed with the dominant hand (Gripx, Vatmaster Consulting, Germany), is shown in Figure 5 [6];
- a fingertip pulse oximeter (Pheartcare; Shenzhen Lepu Intelligent Medical Equipment Ltd., Shenzhen, China) was used to measure beat-to-beat arterial blood oxygen saturation (SO2 %) [7];
- an electronic tympanic thermometer (Gima, Italy) was chosen to measure Body temperature (BT) in °C [8];
- a tool to measure urine specific gravity (USG) through multifunction reagent strips (Combi Screen, Germany) [9].

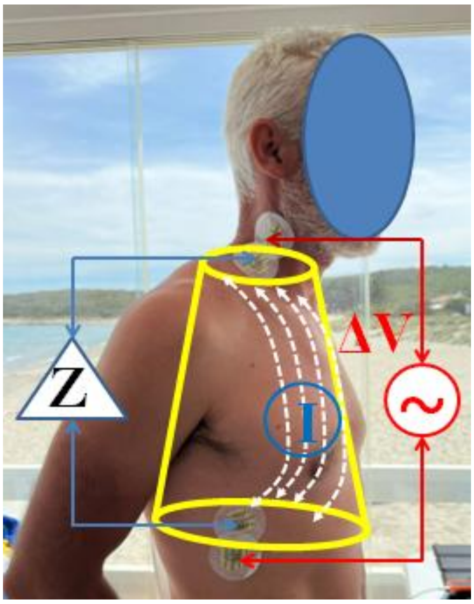

Figure 6 Schematic representation of thoracic electrical bioimpedance assessment in the athlete's chest using the E-Physio Tool. The inverted cone-shaped trunk, shown in yellow, symbolically represents the volume of tissues contributing to the electrical impedance (VEPT). The smaller base of this anatomical solid lies at the level of the neck muscle roots, while the larger base corresponds to the plane of the xiphoid process. Two disposable electrodes are positioned on the right side of the neck and thorax (with four additional electrodes symmetrically placed on the left side). The outer electrodes, connected by red cables, are linked to the voltage generator (ΔV), whereas the inner electrodes, connected by blue cables, are linked to the impedance meter (Z). The impedance measurements dependon an electrical current (I) of 1 *mA* at 65 *kHz* passing through the thorax, represented here by white dotted lines.

All acquired functional data were transmitted via a proprietary information and communication technology (ICT) platform implementing the E-Physio Tool together with telemedicine software [2] to the RSMC, where experienced researchers performed detailed analyses.

The electronic and informatics characteristics of this ICT platform have been described extensively elsewhere [2,3,10–12]. Left ventricular stroke volume (SV) was therefore estimated on a beat-to-beat basis (*ml*) from the following variables directly derived from impedance measurements [13]:

- - left ventricular preload index (LVPLI), also called the central (cardiac) heterometric stroke-volume–modulating factor, defined as TFI (1/Zt, units: Ω^{-1});
- - left ventricular myocardial contractility index (LMCI), also called the central (cardiac) homeometric stroke-volume–modulating factor, defined as the ventricular peak systolic ejection velocity (EVI) (units: $\Omega\ s^{-1}$);
- - ventricular ejection time, defined as the interval between aortic valve opening and closing, which is directly related to SV (VET) (units: *s*).

According to the Sramek–Bernstein equation [14], a subject's SV can be estimated by the volume of thoracic tissues contributing to the impedance (VEPT, ml) [15] together with the three impedance-dependent variables described above. VEPT comprises all thoracic tissues contained within the geometric solid shown in Figure 6 and can be obtained from a dedicated nomogram that relates three variables—gender, body mass, and height—using a set of scales arranged so that the value of one variable is determined by drawing a straight line through the corresponding points on the other scales [14].

That following is the Sramek-Bernstein equation:

$$SV = VEPT\{ml\} * TFI\{\Omega^{-1}\} * EVI\{\Omega s^{-1}\} * VET\{s\} = ml \qquad (1)$$

Equation (1) is valid because, when the cardiovascular system is modelled as a simple closed hydraulic circuit with a reciprocating plunger pump in series (the heart), each suction–delivery cycle of the pump (diastole and systole respectively) yields multiplicative terms that correspond dimensionally to the electrical analogs of the four hydraulic variables that characterize the system. In this formulation, the volume ejected per pump cycle is directly related to the peak ejection velocity and the duration of ejection. Accordingly, the four variables on the right-hand side of (1) represent, respectively: the pump's hydraulic volume (blood volume) or VEPT; the suction volume or LVPLI (measured as TFI); the peak delivery velocity or LVMCI (measured as EVI); and the delivery duration or VET.

2.3 ESPERIMENTAL PROTOCOL

Due to unexpected atmospheric and technical problems at the start of the trip, remote acquisition of the daily data transmitted by our kayaker to the RSMC was delayed by 10 days. Consequently, the ICT platform's daily analysis covered the subsequent 31 days of the trip.

Beat-to-beat Zt and ECG data were acquired remotely on a daily basis while the athlete was seated and in a relaxed state for 3 minutes. Using the LabChart reader (ADInstruments, Oxford, UK) [16], a trained operator at the RSMC identified 10 consecutive heartbeats beginning 1.5 minutes into each recording. From each beat, the operator extracted LVPLI (TFI in Ω^{-1}), LVMCI (EVI in $\Omega\ s^{-1}$), ventricular ejection time (VET in s), and heart rate (HR in *beats* min^{-1}) from the R–R intervals.

At each selected heartbeat, the operator at the RSMC calculated the stroke volume (SV) by applying Equation (1), and subsequently derived the CO, expressed in $l\ min^{-1}$ as follows:

$$CO = SV * HR \qquad (2)$$

Furthermore, the mean ± standard deviation (M ± SD) of the ten measurements obtained for each variable (TFI, EVI, VET, SV, and CO), were computed. During the same experimental session, to avoid any emotional interference related to the temporal overlap with the subsequent impedance data collection, the athlete self-recorded SABP DABP at the wrist at the beginning of the 3-minute impedance data acquisition period. After the 3 minutes of relaxation, the athlete proceeded with the remaining instrumental assessments, as described in Figure 5, and concluded with the SO_2%, SUG, and BT measurements. These manually recorded readings were transmitted to the RSRC via WhatsApp application, along with a self-reported rating of perceived exertion (RPE) for the same day, expressed on a 6–20 scale according to Borg's method [17]. From the data acquired on the same day at the RSMC, the mean arterial blood pressure (MABP) was calculated in *Torr* using the following equation:

$$MABP = [(SABP + 2*DABP) : 3] \tag{3}$$

The left ventricular afterload index (LVALI), also referred to as the peripheral heterometric modulator of SV, was estimated in terms of total peripheral vascular resistance (TPVR), calculated as:

$$TPVR = [MABP : CO] \tag{4}$$

and expressed in $Torr\ l^{-1}$ min, considering that the CO value used corresponds to the average of ten cardiac beats. Further, rate–pressure product (RPP), an index of cardiac oxidative energy expenditure [18], was determined as:

$$TPVR = [MABP : CO] \tag{5}$$

and expressed in $Torr\ beats\ min^{-1}$.
The heart mechanical work index (HMW) [8] was computed as:

$$HMW = [SV * MABP] \tag{6}$$

expressed in *ml Torr*.
Finally, the heart mechanical efficiency index (HME) [8] was obtained as:

$$HME = [HMW : RPP] \tag{7}$$

and expressed in $ml\ min\ beats^{-1}$.
Both descriptive and predictive statistics were used, including linear and quadratic regression analyses. The model with the highest significance was selected. A P-value < 0.05 was considered as statistically significant.

2 RESULTS

Firstly, it should be noted that, in the x-axis of the following graphs, the time data refer to a 16-day period, with measurements taken every two days during the athlete's 31-day journey, as described in the Methods section. Table I reports the mean ± standard deviation (SD) of all cardiovascular variables derived from the beat-to-beat analysis of bioimpedance and ECG recordings obtained using the e-Physio Tool worn by the kayaker on 14 of the 16 days considered in this study. Data from two days were excluded due to electrical interference that prevented reliable impedance measurements. As indicated in the table, each reported value represents the average of 140 beats, corresponding to 10 consecutive beats selected within the 3-minute resting bioimpedance recording period. These recordings were acquired at the end of his daily physical activity before going to sleep.

Table I – Average values of beat-to-beat assessed cardiovascular variables

N (140)	TFI Ω	EVI $\Omega\ s^{-1}$	VET ms	HR $b\ min^{-1}$	SV ml	CO $l\ min^{-1}$
Mean	32.5	1.89	373	64.4	62.9	4.19
±SD	3.2	0.5	31.8	8.9	14.6	1.43
VI%	9.8	26.4	8.5	13.8	23.2	34.1

TFI: bioimpedance index of thoracic fluids; EVI: left ventricle index of the blood ejection velocity peak; VET: left ventricle ejection time; HR: heart rate in beats (b) per minute; SV: left ventricle stroke volume; CO: cardiac output per minute; VI: variability index as SD percentage on Mean. N: number of considered beats to calculate average values (Mean) and its standard deviation (±SD).

Figure 7 shows the geometric representation of the linear regression of stroke volume (SV) across the selected days during which the tested athlete was engaged in the circumnavigation of Sardinia by kayak. The regression equation was that following:

$$SV\ (ml) = 55.97 + 1.22\ (days) \tag{8}$$

Equation (8) predicts that, over the course of the kayaking days, the athlete's resting SV increased by approximately 1.22 ml every two days. However, Equation (8) yielded a "P" value of 0.06, which was not statistically significant,

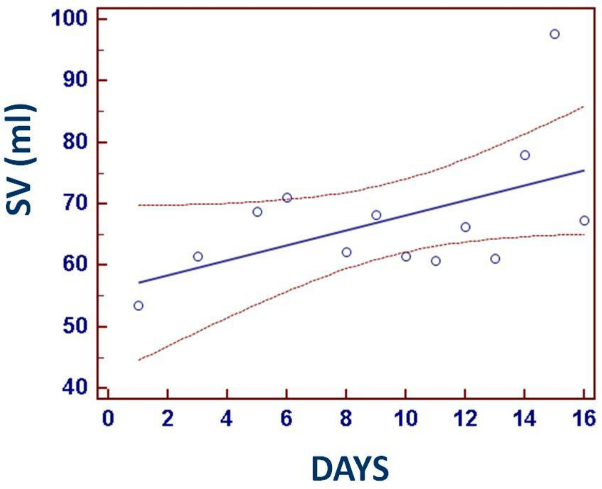

Figure 7 The linear regression of stroke volume (SV) values against the corresponding days of assessment, represented by a straight line fitted to 13 valid data points (open circles). One data point was excluded from the analysis as an outlier. The two orange dashed lines indicate the 95% confidence interval.

although it was close to the threshold of $P < 0.05$ adopted in this study as the criterion for significance. The following regression equations best describe the relationships between the preload index TFI, i.e. 1/Zt, (8) and the contractility index EVI (10) of the left ventricle over the tested days of cruising, as graphically illustrated in Figures 8 and 9, respectively.

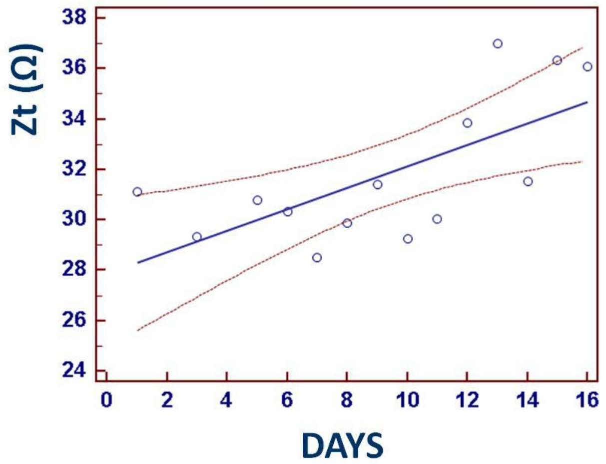

Figure 8 The linear regression of Zt values (the reciprocal of TFI, representing preload) plotted against the corresponding days of assessment. The regression is depicted as a straight line segment with 14 open circles indicating the accepted measurements. The two orange dashed lines represent the 95% confidence interval.

Each of these indices, as is well established, contributes to the central (cardiac) regulation of SV through heterometric and homeometric mechanisms, respectively.

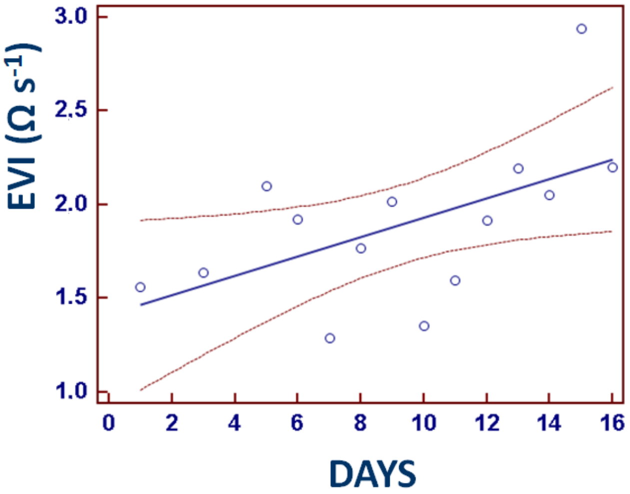

Figure 9 shows the linear regression of EVI values (contractility index) plotted against the corresponding days of assessment. The regression is depicted as a straight line segment with 13 open circles indicating the accepted measurements, as one data point was excluded due to being identified as an outlier. The two orange dashed lines represent the 95% confidence interval.

$$Zt\ (\Omega) = 27.89 + 0.42\ (days) \tag{9}$$

$$EVI\ (\Omega\ s^{-1}) = 1.416 + 0.052\ (days) \tag{10}$$

Both Equations (9) and (10) represent linear regressions that reached statistical significance ($P = 0.007$ and $P = 0.037$, respectively). In contrast, the linear ($P = 0.161$) and quadratic ($P = 0.209$) regression models describing the relationship between HR and the 14 days of paddling did not achieve statistical significance. Nevertheless, this relationship is illustrated graphically in Figure 10.

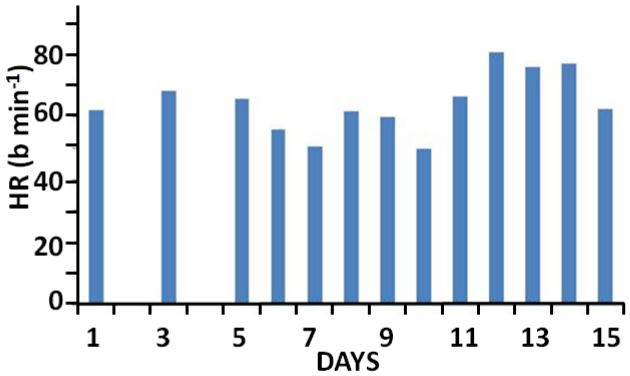

Figure 10 A column histogram showing the heart rate (HR, beats per minute) for each of the 13 selected days out of the 16 days of kayaking.

As previously described in the Methods section, data from days 2 and 4 were excluded from the analysis, while day 16 was identified as an outlier. E-Physio Tool. These measurements were recorded simultaneously with the impedance assessments and, in some cases, were mathematically integrated with the corresponding averaged impedance-derived values, as clearly described in the Methods section. Although the HR regressions shown were not statistically significant, the linear regression of CO over the 14 selected days (Figure 10) was:

$$CO\ (l\ min^{-1}) = 3.35 + 0.13\ (days) \tag{11}$$

Table II reports the mean ± SD values of cardiovascular variables obtained from different devices, in addition to the

Table II – Non-impedance deriving cardiovascular variables

N (13)	MABP Torr	TPVR Torr ml^{-1} min	RPP beats min^{-1} Torr	HMW ml Torr	HME beats^{-1} min ml
Mean	82.9	18.9	7574.5	5225.4	0.75
±SD	9.1	9.8	674.1	936.1	0.13
VI%	11.0	51.8	8.9	17.9	17.3

MABP: mean arterial blood pressure; TPVR: total peripheral vascular resistance; RPP: rate–pressure product; HMW: heart mechanical work; HME: heart mechanical efficiency; VI: variability index, expressed as the percentage of the standard deviation relative to the variable mean. N indicates the total number of measurements considered for calculating the mean value (Mean) and its corresponding standard deviation (±SD).

which yielded a "P" value of 0.017, thus reaching statistical significance. Figure 11 shows the linear relationship between MABP and the selected days.
The corresponding regression equation was:

$$MABP\ (Torr) = 91.28 - 1.19\ (days) \qquad (12)$$

Equation (12) yielded a "P" value of 0.009, indicating statistical significance. Figure 13 shows the linear inverse regression of TPVR over the selected days.

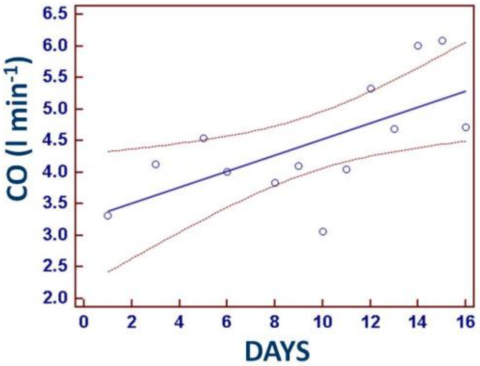

Figure 11 The linear regression of cardiac output (CO) values plotted against the corresponding days of assessment. The regression is depicted as a straight line segment with 13 open circles indicating the accepted measurements, as one data point was excluded after being identified as an outlier. The two orange dashed lines represent the 95% confidence interval.

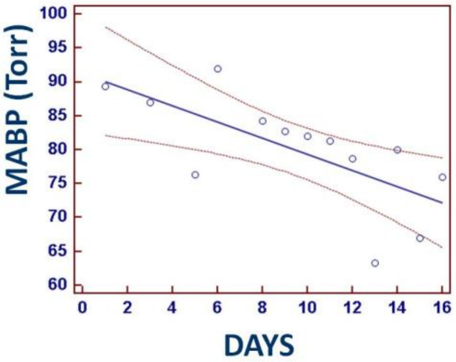

Figure 12 The linear inverse regression of mean arterial blood pressure (MABP) values plotted against the corresponding days of assessment. The regression is depicted as a straight line segment with 13 open circles indicating the accepted measurements, as one data point was excluded after being identified as an outlier. The two orange dashed lines represent the 95% confidence interval.

The corresponding regression equation was:

$$TPVR\ (Torr\ l^{-1}\ min) = 26.14 - 0.77\ (days) \qquad (13)$$

Equation (13) showed a P = 0.007, so reaching the statistical significance. Similarly to HR, the HMW did not show any statistically significant trend in both linear and quadratic HMW-versus-days regression analyses. Nevertheless, this relationship is illustrated in Figure 14 for completeness. Figure 15 shows the quadratic regression of the rate–pressure product (RPP) values plotted against the corresponding days. The RPP–days regression equation was as follows:

$$RPP\ (b\ min^{-1}\ Torr) = 7418.9 - 229.1(days) + 17.9(days)^2 \qquad (14)$$

Table III – Clinical-functional variables

N (16)	SO2 %	BT °C	PEF l min^{-1}	HAG kg
Mean	97.1	35.7	513.7	44.0
±SD	1.1	0.4	21.2	2.1
VI%	1.13	1.12	4.13	4.77

SO2: oxygen percentage in saturation of arterial blood; BT: body temperature measured at tympanic level; PEF: peak of the maximum expiratory flow; HAG: handgrip maximum effort. VI: variability index as SD percentage on Mean. N is the total number of considered measurements to calculate their average value (Mean) together with its standard deviation (±SD).

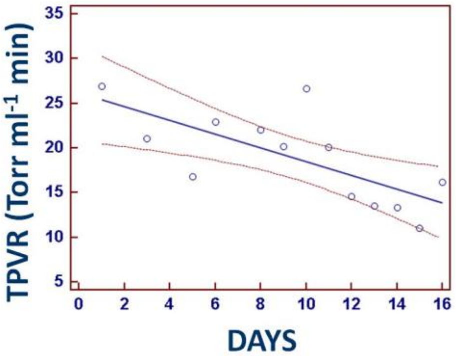

Figure 13 The linear regression of total peripheral vascular resistance (TPVR) values plotted against the corresponding days of assessment. The regression includes 13 open circles representing the accepted measurements, as one data point was excluded after being identified as an outlier. The two orange dashed lines represent the 95% confidence interval.

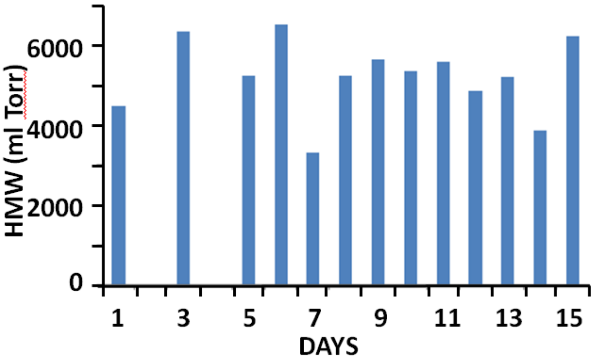

Figure 14 The column histogram represents the heart's mechanical work (HMW) for each of the 13 selected days of kayak paddling. As described in the Methods section, data from days 2 and 4 were excluded from the analysis, while day 16 was identified as an outlier.

Equation (14) showed a “P” value of 0.023, indicating statistical significance. The vertex of the parabola was negative and located at approximately 6.4 days on the x-axis, corresponding to between the 12th and 13th days from the start of the measurements. As shown in Figure 16, the relationship between heart mechanical efficiency (HME) and days was also modelled using a quadratic regression, expressed as:

$$HME\ (b^{-1}\ min\ ml)=0.586+0.068(days)-0.0045(days)^2 \quad (15)$$

Equation (15) yielded a “P” value of 0.071which almost reached statistical significance. However, the vertex of the parabola was positive and positioned at approximately 7.5 days on the x-axis, corresponding to between the 14th and 15th days from the beginning of the measurements.

Figure 17 illustrates the quadratic regression of SO2% values plotted against the corresponding measurement days. The SO2%–days regression equation was:

$$SO2\ (\%) = 96.43 + 0.39\ (days) - 0.03\ (days)^2 \quad (16)$$

Equation (16) showed a “P” value of 0.011, indicating statistical significance. The vertex of the parabola was positive and located at approximately 6.5 days on the x-axis, corresponding to between the 12th and 13th days from the start of data collection. Figure 17 shows the linear regression of BT values plotted against days. The corresponding regression equation was:

$$BT\ (°C) = 36.143 - 0.055\ (days) \quad (17)$$

Equation (17) yielded a “P” value of 0.0002, indicating a highly significant statistical relationship. Figure 18 shows the quadratic regression of HAG values plotted against days. The corresponding regression equation was:

$$HAG\ (kg) = 40.391 + 1.024\ (days) - 0.052\ (days)^2 \quad (18)$$

Equation (19) yielded a “P” value of 0.06, which—similar to the SV versus days relationship—did not reach the threshold for statistical significance, although it was very close to the 0.05 cut-off adopted in this study. The parabola had a positive vertex located at approximately 9.8 days on the x-axis, corresponding to between the 19th and 20th days from the start of measurements. Regarding the relationships of peak expiratory flow (PEF) as well as the other two assessed variables which were the urine specific gravity (USG) and rate of perceived exertion (RPE) variations across the selected days of kayak paddling, both the linear and quadratic regression analyses were far from reaching statistical significance. Therefore, these daily variations were represented graphically as histograms, shown in Figures 20, 21 and 22.

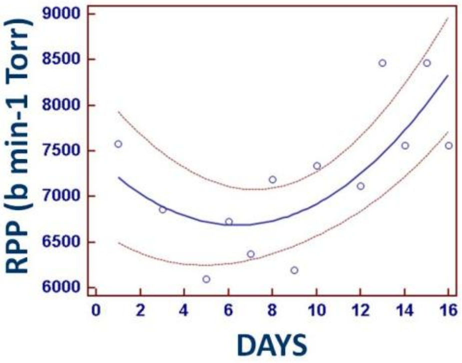

Figure 15 The quadratic regression of the rate–pressure product (RPP) values plotted against the corresponding assessment days, represented as a segment of a parabolic curve. Thirteen open circles indicate the accepted measurements, as one data point was excluded as an outlier. The orange dashed lines represent the 95% confidence interval.

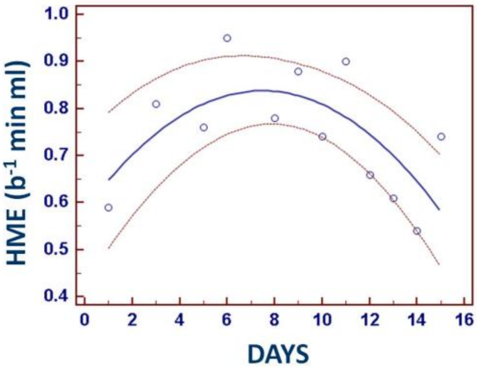

Figure 16 The quadratic regression of heart mechanical efficiency (HME) values plotted against the corresponding assessment days, represented as a segment of a parabolic curve. Twelve open circles indicate the accepted measurements, as two data points were excluded as outliers. The two orange dashed lines represent the 95% confidence interval.

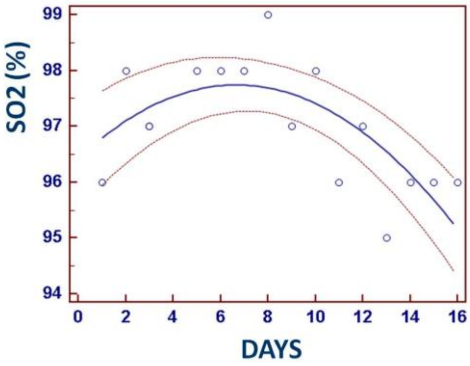

Figure 17 The quadratic regression of the arterial blood oxygen saturation in percentage values (SO2) versus corresponding days of their assessment represented as a segment of a parabolic curve with 15 empty circles concerning the 16 accepted measurements since one of those considered was excluded resulting as an outlier value. The two orange dashed lines represent 95% confidence interval.

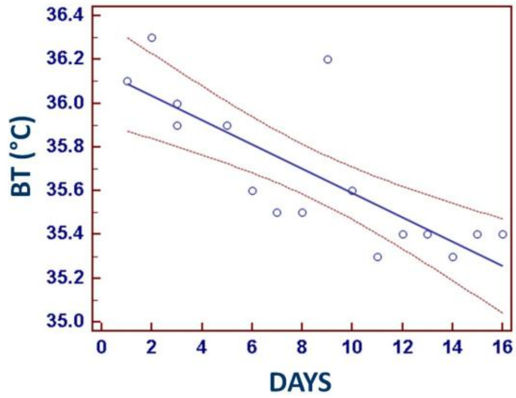

Figure 18 shows the linear regression of body temperature (BT) values plotted against the 16 corresponding assessment days. Sixteen open circles represent the accepted measurements, while the two orange dashed lines indicate the 95% confidence interval.

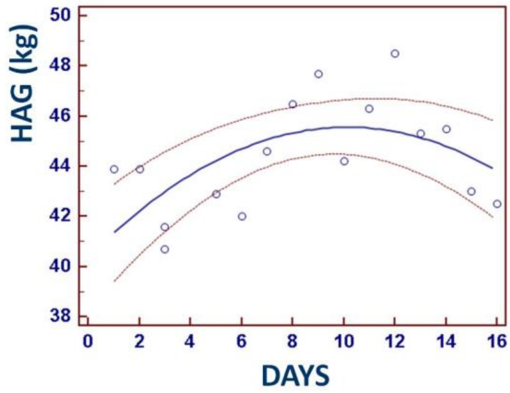

Figure 19 shows the quadratic regression of handgrip maximum effort (HAG) values plotted against the 16 corresponding assessment days, represented as a segment of a parabolic curve. Sixteen open circles indicate the accepted measurements, while the two orange dashed lines represent the 95% confidence interval.

3 DISCUSSION

To obtain daily resting values for blood flow variables—whose mean values are reported in the Tables I and II—a custom-built impedance cardiograph was employed in this study. This device had previously been validated by comparing its measurements with those obtained from commercially available ICG systems considered the gold standard for cardiovascular assessments [19]. To further enhance the reliability of the present results, Table IV shows the mean values of TFI, SV, CO, EVI, and TPVR—cardiovascular variables measured almost with the E-Physio tool—visually correlated with corresponding resting-state values obtained in two independent experiments that used two well-established commercial ICG instruments. As illustrated in the table, except for EVI, the four other variables assessed with the E-Physio tool fall within an intermediate range between the values obtained using the two commercial devices: the BioZ ICG Monitor

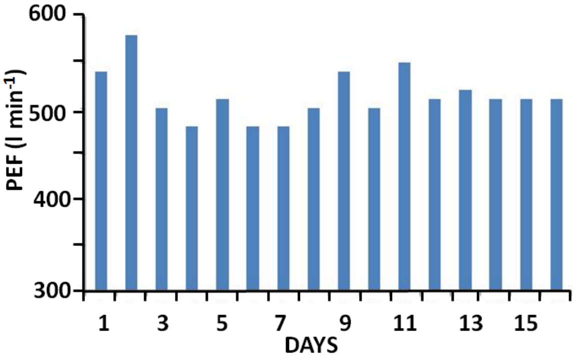

Figure 20 shows the column histogram representing the peak expiratory flow (PEF) values for each of the 16 selected days of the athlete's kayak paddling.

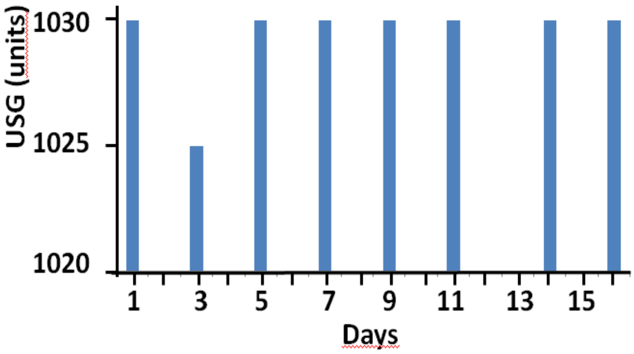

Figure 21 shows the column histogram representing the urine specific gravity (USG) values. Due to practical difficulties in recording this parameter nightly before bedtime, the athlete was instructed to perform the measurements every two days. However, the assessment planned for day 13 could not be completed and was postponed to day 14, with the final measurement taken on day 16.

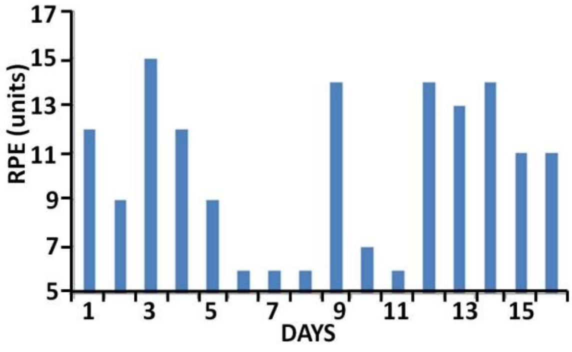

Figure 22 shows the column histogram representing the rate of perceived exertion (RPE) values for each of the 16 selected days of kayak paddling.

Table IV – Comparison from different ICG devices

Variables	BioZ ICG (2006)	E-Physio (actual)	Niccomo^{TM} (2025)
TFI(Ω)	33.1	32.5	29.1
SVI(ml/m^2)	33.0	37.0	50.2
COI(l/min/m^2)	2.3	3.2	3.3
EVI(Ω/s)	1.16	1.89	1.38
PVR(Torr/ml/min)	33.3	25.8	24.7

(CardioDynamics, San Diego, California, USA) [20] and the Niccomo™ (Medis Medizintechnik, Ilmenau, Germany) [21]. This finding supports the view that the variables measured with the E-Physio tool can be regarded as reasonably reliable, despite the higher LVMCI (EVI) value compared to the other two methods. This discrepancy may be attributed to quantitative and qualitative differences among the three groups of subjects included in the comparison. Of primary importance, however, is that—as shown in Equation (11)—these experimental results revealed several cardiovascular adaptations which, over the 30-day observation period, collectively led in this kayaker to a predicted linear increase in resting CO of approximately 65 $ml\ min^{-1}$ per day. As is well known, both SV and HR are the variables that determine CO through their mathematical product. It must therefore be considered that SV, in turn, depends on central (cardiac) determinants—namely, the thoracic fluid index (TFI) and ejection velocity index (EVI)—as well as on peripheral (vascular) determinants such as ventricular afterload, expressed as total peripheral vascular resistance (TPVR).

The experimental data predicted a linear increase in SV of about 0.61 $ml\ day^{-1}$, corresponding to a rate of increase of 1.09 % day^{-1}. However, this latter result requires further confirmation, as its current statistical significance was marginal ($P = 0.06$). However, the ICG-derived reciprocal indicator of LVPL, i.e. Zt, or the thoracic fluid index (TFI), showed a significant linear increase of approximately 0.21 $\Omega\ day^{-1}$. This finding indicates a corresponding reduction in LVPL, the heterometric (central) variable influencing SV. In contrast, this trend was opposed by the concurrent linear increase in the EVI, the ICG-derived indicator of LVMC—that is, the homeometric (central) factor determining SV—which increased by about 26 $m\Omega\ s^{-1}\ day^{-1}$.

When the daily rate of variation of LVPL and LVMC was expressed as a percentage of their respective intercept values on the ordinate axis (see Equations 9 and 10), the results indicated a change of –0.75% day^{-1} for LVPL and +1.83 % day^{-1} for LVMC. These findings suggest that, in our athlete, prolonged kayak paddling induced a progressive increase in resting SV, not primarily through an enhancement of ventricular preload, but rather through a predominant contribution from myocardial contractility. This pattern indicates a sympathetic dominance in the autonomic control of cardiac function, as the daily percentage rate of increase in SV more closely matched that of LVMC than that of LVPL. In previous work by Sheykhlouvand et al. [22], well-trained sprint kayakers underwent incremental cardiopulmonary tests on a kayak ergometer before and after eight weeks of high-intensity interval training performed on the same device. Following the training period, these authors reported that, in elite kayakers, the increase in LVMC did not coincide with a parallel rise in LVPL. Specifically, they found that resting SV increased significantly due to enhanced ventricular contractility, as evidenced by an elevated left ventricular ejection fraction (LVEF), while the increase in SV exceeded that observed for LVPL. Therefore, consistent with the findings of the present study, those authors concluded that in trained kayakers, an improvement in myocardial contractility can enhance SV even in the absence of an increase in LVPL, with this adaptation being primarily attributable to an increase in LVEF. In this context, it is noteworthy that in the previously reported post-trip echocardiographic evaluation at rest [1], our kayaker exhibited a 4% increase in LVEF compared with the pre-trip value. Furthermore, Bertozzi et al. [23] observed that high-intensity kayak sprints predominantly affect the kinematics of the shoulders, trunk, and hips during paddling, while exerting a much smaller influence on lower limb motion. This finding is consistent with a reduced contribution of the calf muscle pump to venous return during paddling, resulting in a comparatively lower preload stimulus. Consequently, a limited functional adaptation of LVPL, even when measured at rest, could reasonably be expected in our kayaker. Moreover, based on Equation (8), which describes the relationship between SV and days of observation, the predicted increase in resting SV after 30 days of navigation was +32.6%. This value closely matches the +31.2% increase previously measured at rest by echocardiography at the end of the kayak cruise [1]. With regard to the potential influence of the peripheral heterometric vascular factor—namely, total peripheral vascular resistance (TPVR)—on SV and, consequently, on CO, it is noteworthy that TPVR exhibited a negative and highly significant linear regression with respect to trip duration, as shown in Equation (13). Specifically, TPVR decreased by approximately 0.77 $Torr\ l^{-1}\ min\ day^{-1}$ (Figure 13). This finding resulted in a clear inverse CO–TPVR relationship, illustrated in Figure 23, which likely contributed to the observed time-dependent increase in cardiac output. Indeed, the daily self-recorded measurements of these two variables, collected each evening by the athlete after setting up camp, revealed a strong inverse dependence of CO on TPVR. As demonstrated by the linear regression depicted in Figure 23 and described by Equation (19), this relationship predicted an increase in CO of approximately 170 ml min^{-1} for each unit decrease in TPVR, with a very high level of statistical significance ($P < 0.0001$).

$$CO\ (l\ min^{-1}) = 7.64 - 0.17\ (Torr\ l^{-1}\ min) \tag{19}$$

It has been well established that regular aerobic exercise training—such as that performed by this kayaker—promotes skeletal muscle angiogenesis [24], leading to an increase in muscle capillarization [25]. From a purely hemodynamic perspective, an increase in muscle capillarization corresponds to an expansion of the hydraulic conduits within striated muscles, which are arranged in parallel, resulting in a consequent decrease in TPVR [26]. This is precisely what was observed in our kayaker at the end of the cruise. In a recent study involving healthy adults performing the 6-minute walk test (6MWT) [27], a submaximal-intensity exercise, a negative association was found between the distance covered and TPVR.

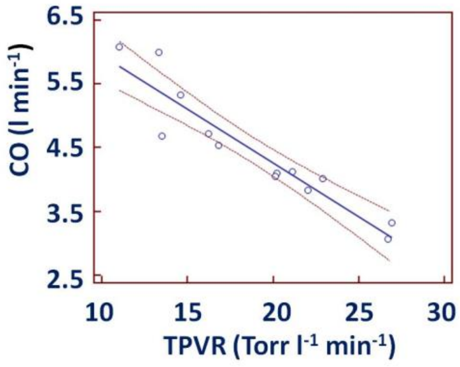

Figure 23 shows the inverse linear regression of cardiac output (CO) values against the corresponding total peripheral vascular resistance (TPVR) values. Thirteen open circles represent the 14 accepted measurements, since one data point was excluded as an outlier. The two orange dashed lines indicate the 95% confidence interval.

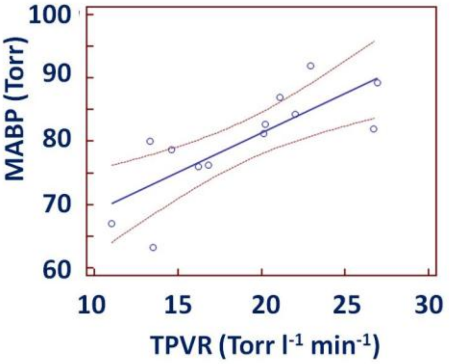

Figure 24 The linear regression of mean arterial blood pressure (MABP) against total peripheral vascular resistance (TPVR). Thirteen open circles represent the accepted measurements, while one data point was excluded as an outlier. The two orange dashed lines indicate the 95% confidence interval.

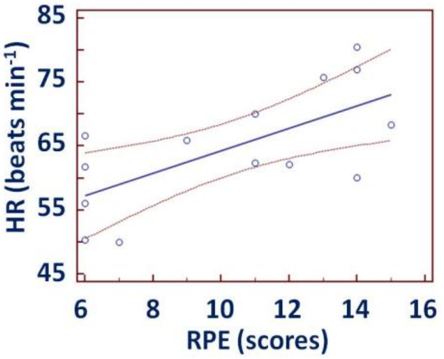

Figure 25 shows the linear regression of heart rate (HR) against the corresponding ratings of perceived exertion (RPE). Fourteen open circles represent the accepted measurements, while the two orange dashed lines indicate the 95% confidence interval

At the same time, a moderate-to-strong positive correlation emerged between 6MWT distance and oxygen consumption. Therefore, it can be hypothesized that the prolonged, submaximal exercise performed by our kayaker—since it produced a progressive and significant reduction in TPVR—may also have led to an improvement in aerobic capacity. This hypothesis is strongly supported by the previous observation [1] that this athlete's maximal oxygen consumption, measured during the cardiopulmonary exercise test conducted after the kayak expedition, was approximately 13% higher than the value recorded during the pre-expedition test. As expected [26], the Figure 24 illustrates the kayaker's daily decrease in TPVR, which was accompanied by a parallel reduction in MABP, quantified by Equation (20) as approximately -1.3 Torr for each unit decrease in TPVR (P = 0.001).

$$MABP\ (Torr) = 56.44 + 1.24\ (Torr\ l^{-1}\ min \qquad (20)$$

The effect described in Equation (20) was not chronotropically compensated by increases in HR, as the two here chosen kind of regressions for MABP on HR—namely linear and quadratic—here chosen, did not reach statistical significance.

Conversely, during the coastal trip, the kayaker's HR at rest was strongly and directly correlated with his RPE. The relationship between HR and RPE scores is illustrated in Figure 25 as a linear regression line, described by the following equation:

$$HR\ (b\ min^{-1}) = 46.77 + 1.75\ (RPE\ scores) \qquad (21)$$

Equation (21) indicates a predicted increase of nearly 2 beats per minute for each unit increase in RPE score (P = 0.0091). The absence of any statistically significant relationship between HR and MABP reasonably excludes modulatory influences from carotid and aortic baroreflex activity [28]. This finding supports the interpretation that the observed increases in HR are better explained by the classical Cannon–Bard physiological principle [29], whereby sympathetic chronotropic activation of the heart arises from persistent painful sensations associated with increased physical effort [30], as clearly shown in Figure 25 and Equation (21). Furthermore, from a strictly clinical perspective, the results of this experiment suggest that continuous sea kayaking may elicit an antihypertensive effect of non-pharmacological origin. In this experiment, it was also possible to collect data on the mechanical work and efficiency adaptations of the athlete's heart over the month of daily resting measurements, which he self-performed each evening. As shown in Table II, the mean HMW value reached a VI% approaching 20%, while the histogram in Figure 25 clearly shows a positively skewed distribution, with more than 50% of the HMW values ranging between 5000 and 6500 *Torr ml*. As shown in Figure 26, the higher HMW values are located in the right half of the graph, suggesting that these elevated values occurred during the second half of the kayak journey.

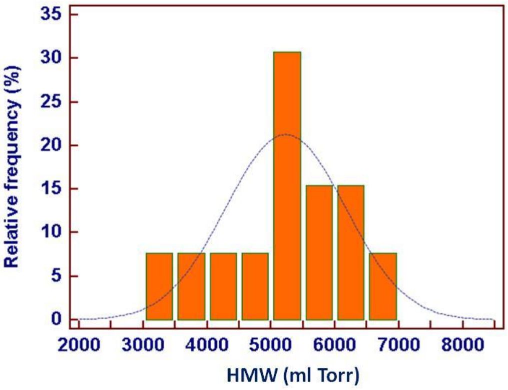

Figure 26 The columns in the histogram represent the relative frequency distribution of the athlete's heart mechanical work (HMW) values measured daily during the last 30 days of navigation. Although a positive skewness of the descriptive distribution is evident, the D'Agostino–Pearson test indicates that the data follow a normal (parametric) distribution (P = 0.544).

This observation indicates that during the final two weeks of paddling, the mechanical work performed by the heart was slightly greater than during the first two weeks. The asymmetrical distribution of HMW values therefore accounts for the relatively high VI% associated with their mean. An interesting finding emerges from the observation that, during the second half of the trip, the workload imposed on the athlete's heart resulted in a markedly high and progressively increasing oxidative energy cost. This is illustrated in Figure 15, which shows the squared regression of RPP versus days, as well as in the corresponding Equation (14) that generated the graph. As expected at this stage, the trend of HME over time was nearly the inverse of the previous one. Indeed, as shown in Figure 16 and described by Equation (15), the HME–days relationship is represented by a parabolic curve with its vertex directed upward, corresponding to an abscissa value around day 15—approximately two weeks after the start of measurements. This clearly indicates that, from the beginning of the third week until its end, the mechanical efficiency of the heart decreased in a quadratic manner, returning to values similar to those recorded at the start of the trip when the journey ended. Unfortunately, the parabolic regression equation (15) for HME versus days did not reach a full up statistical significance since a P-value of 0.071. To better contextualize the behaviour of the mechanical and energetic variables of our resting athlete's heart during the final days of his coastal cruise, Figure 27 (bottom panel) shows a graph in which the curve derived from the RPP–days relationship is superimposed with the corresponding temporally matched HME–days curve. The top panel of Figure 26 presents a graph adapted from the study by Evans and Matsuoka, published in "The Journal of Physiology" (London, 1915) [31]. In their experiment on an isolated heart from a small mammal (59 g), conducted under constant blood pressure and temperature but with varying cardiac output, they demonstrated that as the mechanical work of the heart (abscissa, expressed in *kg m^{-1} h^{-1}*) increased linearly, oxygen consumption (solid curve) rose exponentially. The geometry of this curve closely resembles that of the RPP curve for our athlete (bottom panel), particularly during the second half of the observation period. Correspondingly, the mechanical efficiency of the isolated heart (dotted curve in the top graph) followed a parabolic trend with a positive vertex, analogous to the HME behaviour observed in the kayaker's data. Notably, in both cases—approximately halfway through the maximum workload of the isolated heart in the first graph and at midway through the total duration of the athlete's monitoring period—the mechanical efficiency of each heart began to decline from its respective maximum value, corresponding to the vertex of the parabola. The data reported by Evans and Matsuoka [31] could undoubtedly be regarded as a milestone in understanding the bioenergetics underlying the mechanical activity of the mammalian heart [32]. In that study, the authors—consistent with the conclusions of Patterson et al. [33]—

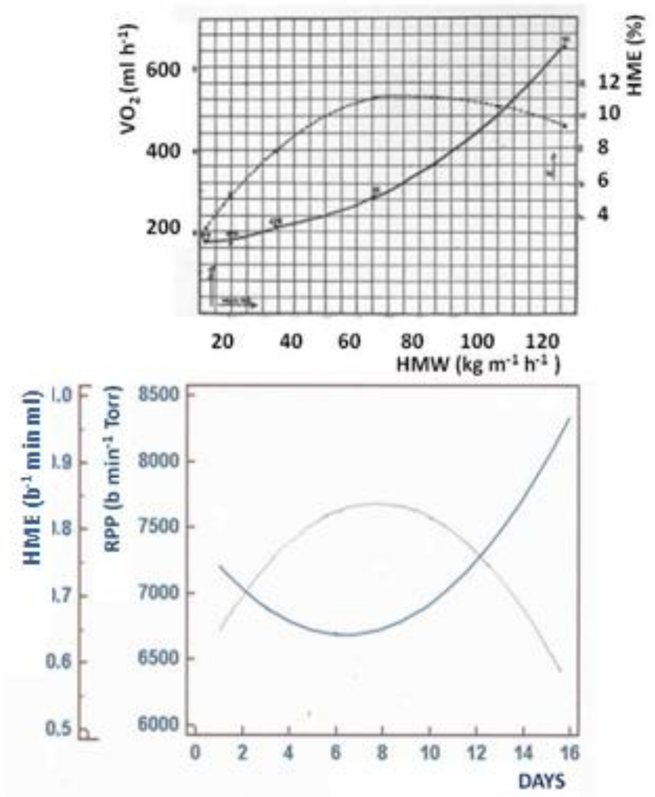

Figure 27 Top panel: Graphical representation of oxygen consumption (VO$_2$, solid curve) and mechanical efficiency (HME, dotted curve) as functions of the linearly increasing heart mechanical work (HMW) in an isolated small mammalian heart. Bottom panel: Graphical representation of the rate–pressure product (RPP, blue solid curve) as an index of myocardial oxygen consumption, and of the heart's mechanical efficiency (HME, black solid curve), both plotted as functions of the progressive days of the athlete's paddling activity.

demonstrated that under very high cardiac workloads, signs of myocardial fatigue emerge, manifested by an increased energy cost (i.e., higher VO_2 consumption) and a consequent reduction in mechanical efficiency. Translating these experimental findings from ex vivo animal preparations to the indirect measurements of cardiac mechanics obtained from this kayaker, it can be inferred that, during the final weeks of his circumnavigation of the island of Sardinia, the athlete may have developed a state of cardiac fatigue. Interestingly, the HAG/days curve shown in Figure 19 predicted that as the days of the cruise progressed, the maximum handgrip force—measured at rest—gradually increased during the early phase of the voyage, peaking around the tenth day of observation, and subsequently declined toward the end of the journey. This progressive reduction in HAG during the final part of the cruise seemsto temporally coincide with both the ascending limb of the quadratic RPP/days curve (representing the increasing energetic cost of cardiac work) and the descending limb of the HME/days quadratic curve (indicating reduced mechanical efficiency of cardiac performance). Taken together, these three concomitant trends suggest the development of a generalized fatigue condition in our kayaker during the latter stages of his daily paddling routine. This hypothesis is further supported by the persistently high values of urinary specific gravity, averaging 1.030 (as shown in Figure 21), which point to a state of pronounced dehydration. Indeed, in previous studies dehydration has been shown to impair both the mechanical efficiency of the cardiac cycle [34] and the force transmission capacity of striated muscles [35]. In addition, the quadratic relationship between SO2% and days ($P = 0.011$; see Figure 16 and Equation 16) revealed a clear and progressive decline beginning approximately in the second half of the monitoring period, further supporting the hypothesis of cumulative physiological fatigue during the final phase of the coastal cruise. Similarly, the progressive reduction in body temperature (BT/days) should not be overlooked, as shown in Figure 18 and described by the corresponding regression Equation (17). According to this equation, the rate of decrease in BT was approximately –0.027 *°C* per day. By 30th day of navigation, this corresponded to a total decline of about –0.82 *°C*, indicating that body temperature decreased from an initial value of 36.14 *°C* (the intercept of the regression line at the start of the experiment) to 35.32 °C at the end of the observation period—representing an overall reduction of roughly 1 *°C*. During the athlete's navigation, data recorded by the HOBO device indicated that the average minimum environmental temperatures ranged between 8 °C and 11 °C, with the lowest values occurring during nighttime hours when the kayaker was resting on the beach inside his tent and performing self-measurements. Relative humidity averaged 70–75%, with higher peaks at night and in the early morning. Therefore, the observed trend in BT can reasonably be interpreted as a physiological response consistent with the environmental conditions encountered during the expedition. It is noteworthy that, as previously reported, blood flow to the fingers decreases during cold exposure, and this phenomenon appears to result from cold-induced increases in blood viscosity rather than from vasoconstriction [36]. Consequently, it is possible that the progressive reduction in BT observed during the trip also lowered the temperature of the fingers, through which SO2% was measured. The resulting increase in blood viscosity could have contributed to a reduction in local SO2%, particularly during the latter part of the trip (as shown by the SO2%/days curve in Figure 17). This effect might, in turn, have been transmitted retrogradely to the vascular, muscular, and ligamentous structures responsible for hand contractile activity, thereby contributing to a decline in mechanical efficiency. Furthermore, it was previously reported [1] that, by the end of his kayaking expedition, this athlete had lost 3.5 kg of body weight, of which 1.9 kg corresponded to free fat mass (FFM). This reduction included a loss of total body water (TBW), which had decreased by 1.5 kg at the end of the trip. Considering that the other components of FFM—namely internal organs (approximately 25%), bones (approximately 15%), and mineral reserves (approximately 15%)—are unlikely to undergo substantial reductions in a healthy, physically active individual, the remaining 0.4 kg decrease in FFM can reasonably be attributed to a loss of skeletal muscle mass (MM). This reduction in MM likely contributed to the observed decrease in maximal force output during the HAG tests performed towards the end of the kayaking journey. It is therefore not surprising that, as shown in the bar graph in Figure 22, depicting the athlete's (RPE) every two days, the mean RPE value during the final eight measurements was approximately 20% higher than that recorded during the first eight. Finally, although the variability index (VI) of the mean daily self-assessed PEF measured by the kayaker was only 4% (as shown in Table III), the column histogram in Figure 20 suggests that, after the first three days of observation, this variable showed a slight but noticeable reduction—approximately −4%—over the remaining days of the trip. This may indicate the presence of a subclinical dysfunction of the upper airways that developed gradually during the athlete's prolonged performance at sea. Indeed, exercising in a challenging environment such as the marine setting—characterized by high humidity, fluctuating temperatures, and prolonged exposure to wind and salt—may disrupt the delicate water–salt balance of the bronchial mucosa, potentially leading to respiratory impairment [37]. Such an effect appears to have occurred in our long-distance kayaker, possibly exacerbated by a state of borderline dehydration. However, recent studies [38] have suggested that sea spray aerosols (SSAs) contain bioactive compounds derived from marine algae that can modulate cellular processes relevant to human health. Specifically, exposure of human bronchial epithelial cells to natural SSA samples has been shown to activate gene clusters associated with anti-inflammatory and anti-tumor responses. These findings therefore support the notion that our kayaker was exposed to potentially beneficial effects during his prolonged coastal journey [2].

4 STUDY LIMITATIONS

The main limitation of this study is that it was conducted on a single subject. However, implementing an experimental protocol involving several kayakers simultaneously undertaking the same course as our athlete is currently impractical for this research team. Another limitation is that the statistical regressions of some key variables—SV, HME, and HAG—yielded "P" values ranging from 0.055 to 0.071, thus not achieving full statistical significance. Considering the observed temporal trends of these variables, it is reasonable to assume that this outcome might have differed had data collection included the first 10 days of navigation. To verify this hypothesis, the authors plan to repeat the experiment on the same athlete under conditions involving a substantially longer navigation period.

5 CONCLUSION

The experimental results presented here can reasonably be regarded as the first comprehensive dataset describing the physiological adjustments and adaptations of multiple organs and body systems involved in a long-duration kayaking performance. In this context, the findings of the present study—together with those previously obtained from the same kayaker [1]—make a significant and original contribution to our understanding of the functional model of athletes engaged in prolonged paddling activities.

REFERENCES

[1] Tocco F., Massidda M., Ghiani G., Palmas M., Ruggiu M., Velluzzi F., Solinas R., Masala A., Fois A., Melis L., Manuello Bertetto A., Dell'Osa A.H., Cerina A., Cappagli C., Melis S., Loi V., Marcello R. and Concu A., Biomechanical and cardiometabolic changes in skilled kayaker after 41 days of cruising around the island of Sardinia: a case study (part 1). *International Journal of Mechanics and Control*, Vol. 25, No. 02, pp. 113-119, 2024.

[2] Tocco F., Mattana D.V., Solinas R., Velluzzi F., Usai P., Fois A., Melis L., Bianco P., Serra C., Manuello Bertetto A., Dell'Osa A.H., Pereira A.F., Cerina A., Loviselli L., Marcello R., Melis S. and Concu A., Cardiometabolic benefits from a coastal sailing in a radical cystectomy patient remotely controlled by an internet of thing mechatronic tool: a case study. *International Journal of Mechanics and Control*, Vol. 24, No. 02, pp. 39-61, 2023.

[3] Campagna M., Lecca L.I., Velluzzi F., Serra C., Bianco P., Manuello Bertetto A., Dell'Osa A.H., Fanni B., De Pau A., Fois A., Melis L., Kalb A., Marcello R., Melis S., Concu A. and Tocco F., A mechatronic simulator of an aircraft cockpit to study, by a virtual flight test, cardiovascular fitness in airline pilots banned to fly since covid-19 lockdown. *International Journal of Mechanics and Control*, Vol. 23, No. 02, pp. 85-99, 2022.

[4] Saito K., Hishiki Y. and Takahashi H., Validation of two automatic devices, Omron HEM-6232T and HEM-6181, for self-measurement of blood pressure at the wrist according to the ANSI/AAMI/ISO 81060-2:2013 protocol and the European Society of Hypertension International Protocol revision 2010. *Vasc Health Risk Manag*, Vol. 15, pp. 47-55, 2019.

[5] Buyse G.M., Rummey C., Meier T., Leinonen M., Voit T., McDonald C.M. and Mayer O.H.J., Home-Based Monitoring of Pulmonary Function in Patients with Duchenne Muscular Dystroph. *Neuromuscul Dis*, Vol. 5, No. 4, pp. 419-430, 2018.

[6] Daneshparvar A., Hemmatinafar M., Salesi M., Rezaei R., Imanian B. and Pirmohammadi S., The effect of acute beetroot juice consumption prior to climbing on lower-body isokinetic and isometric strength, aerobic power, and muscle soreness among mountain climbers. *J Int Soc Sports Nutr*, Vol. 22, No. 1, pp. 2502656, 2025.

[7] Leppänen T., Kainulainen S., Korkalainen H., Sillanmäki S., Kulkas A., Töyräs J. and Nikkonen S., Pulse Oximetry: The Working Principle, Signal Formation, and Applications. *Adv Exp Med Biol*, Vol. 1384, pp. 205-218, 2022.

[8] Nobel J.J., Infrared ear thermometry. *Pediatr Emerg Care*, Vol. 8, No. 1, pp. 54-58, 1992.

[9] Wu W.C., Concu A., Solinas R., Meloni L., Manuello-Bertetto A., Fois A., Loviselli A., Deledda A. and Velluzzi F., Metabolic power and energy cost of mechanical work carried out by a sailor engaged in a solo ocean race: a case study. *International Journal of Mechanics and Control*, Vol. 19, No. 02, pp. 19-32, 2018.

[10] Marongiu E., Crisafulli A., Ghiani G., Olla S., Roberto S., Pinna M., Pusceddu M., Palazzolo M., Sanna I., Concu A. and Tocco F., Cardiovascular Responses during free-diving in the sea. *Int J Sports Med*, Vol. 36, pp. 297-301, 2015.

[11] Tocco F., Solinas R., Velluzzi F., Massidda M., Mattana D.V., Fois A., Melis L., Manuello Bertetto A., Bonisoli E.†, Venturini S., Bianco P., Dell'Osa A.H., Pereira A.F., Melis S., Cerina A., Loviselli L., Marcello R. and Concu A., A mechatronic tool for revealing inverse relationships among heart's stroke volume and head's linear acceleration induced by moored boats rolling in elderly sailors with unchanged body sizes: a non-drug anti-hypertensive advantage?. *International Journal of Mechanics and Control*, Vol. 25, No. 01, pp.133-142, 2024.

[12] Dell'Osa A.H., Fois A., Cerina A., Pili F., Manuello Bertetto A., Bellomi G., Palmas M., Ruggiu M., Melis S., Tocco F. and Concu A., Impedance cardiography assessment during body immersion in a high concentrated water solution of magnesium chloride simulating space microgravity: a pilot study. *J Phys: Conf. Ser.* 3014, 012006, 2025.

[13] Manuello Bertetto A.,Tocco F., Bellomi G., Mulargia L., Ruggiu M., Palmas M., Massidda M., Ghiani G., Velluzzi F., Melis S., Fois A., Dell'Osa A.H., Cerina A., Bertelli U., Carta M.G., Bianco P.R. and Concu A., Cardiovascular and metabolic engagement after an endurance race in pilots driving motorboats electrically powered by green Energy. *International Journal of Mechanics and Control*, Vol. 26, No. 01, pp. 221-230, 2025.

[14] Bernstein D.P., A new stroke volume equation for thoracic electrical bioimpedance: theory and rationale. *Crit Care Med*, Vol. 14, No. 10, pp.904-909, 1986.

[15] Sramek B.B., Noninvasive technique for measurement of cardiac output by means of electrical impedance. *Proc. of the 5th International Conference on Electrical Bioimpedance*, Tokyo, Japan, pp. 39-42, 1981.

[16] Dash R.R., Samanta P., Das S., Jena A., Panda B., Parida B.B. and Mishra J., Heart Rate Variability in Unexplained Syncope Patients Versus Healthy Controls: A Comparative Study. *Cureus*, Vol. 15, No. 7, pp. e41370, 2023.

[17] Borg G. and Dahlstrom H., A case study of perceived exertion during a work test. *Acta Soc Med Ups*, Vol. 67, pp. 91-93, 1962.

[18] Keyser R.E., Andres F.F., Wojta D.M. and Gullett S.L., Variations in cardiovascular response accompanying differences in arm-cranking rate. *Arch Phys Med Rehabil*, Vol. 69, No. 11, pp. 941-945, 1988.

[19] Tocco F., Crisafulli A., Marongiu E., Milia R., Kalb A. and Concu A. (2012). A portable device to assess underwater changes of cardiodynamic variables by impedance cardiography. *J Phys: Conf. Ser.* 407, 012026, 2012.

[20] Packer M., Abraham W.T., Mehra M.R. *et al.*, Utility of impedance cardiography for the identification of short-term risk of clinical decompensation in stable patients with chronic heart failure. *J Am Coll Cardiol*, Vol. 47, No. 11, pp. 2245-2252, 2006.

[21] Domino B., Wlochacz A., Maciorowska M. *et al.*, Impaired cardiovascular hemodynamics in patients hospitalized with COVID-19 pneumonia. *J Clin Med*, Vol. 14, pp. 1806, 2025.

[22] Sheykhlouvand M., Arazi H., Astorino T.A. and Suzuki K., Effects of a new form of resistance-type high-intensity interval training on cardiac structure, hemodynamics, and physiological and performance adaptations in well-trained kayak sprint athletes. *Front Physiol*, Vol. 13, pp, 850768, 2022.

[23] Bertozzi F., Porcelli S., Marzorati M., Pilotto A.M., Galli M., Sforza C. and Zago M. Whole-body kinematics during a simulated sprint in flat-water kayakers. *Eur J Sport Sci*, Vol. 22, No. 6, pp. 817-825, 2022.

[24] Rodrigues L.F.,Rocha Avila Pelozin B., da Silva Junior N.D. *et al.*, Angiotensin II promotes skeletal muscle angiogenesis induced by volume-dependent aerobic exercise training: effects on miRNAs-27a/b and oxidant-antioxidant balance. *Antioxidants (Basel)*, Vol. 11, No. 4, pp. 651, 2022.

[25] Liu Y., Christensen P.M., Hellsten Y. and Gliemann L., Effects of exercise training intensity and duration on skeletal muscle capillarization in healthy subjects: a meta-analysis. *Med Sci Sports Exerc*, Vol. 54, No. 10, pp. 1714-1728, 2022.

[26] Berne R.M. and Levy M.N., *Cardiovascular Physiology*. 5th edition, McGraw-Hill, New York, USA, 1986.

[27] Singhasoot S.,Srijunto W.,Werasirirat P., Namsawang J.,Chaovalit S. and Muanjai P., Associations between 6-min walk distance and cardiopulmonary parameter in non-obese older adults: An observational study. *Respir Med*, Vol. 236, pp. 107912, 2025.

[28] Concu A., Cardiovascular adjustments during exercise: points and counterpoints. Eds. Crisafulli A. and Concu A., *New insight into cardiovascular apparatus during exercise. Physiological and physio-pathological aspects*. Research Signipost, Kerala, India, pp. 61-84, 2007.

[29] Cannon W.B., The James-Lange theory of emotions: a critical examination and an alternative theory. *Am J Psychol*, Vol. 39, pp. 106-124, 1927.

[30] Glenn E.W., and Goetz S.M.M., Applying Evolutionary Thinking to the Study of Emotion. *Behav Sci*, Vol. 3, pp. 388–407, 2013.

[31] Evans C.L. and Matsuoka Y., The effect of various mechanical conditions on the gaseous metabolism and efficiency of the mammalian heart. *J Physiol*, Vol. 49, No. 5, pp. 378-405, 1915.

[32] Margaria R. and De Caro L., *Fisiologia Umana*. Vol. 1, Ed. Vallardi, Milano, Italy, pp. 13, 1967.

[33] Patterson S.W., Piper H. and Starling E.H.J., The regulation of the heart beat. *J Physiol*, Vol. 48, No. 6, pp. 465-513, 1914.

[34] Lax D., Eicher M. and Goldberg S.J., Mild dehydration induces echocardiographic signs of mitral valve prolapse in healthy females with prior normal cardiac findings. *Am Heart J*, Vol. 124, No. 6, pp. 1533-40, 1992.

[35] De Moura R.C., De Moura Costa C., Ferreira C.P. *et al.*, Hydration assessment and physical performance of mountain bike cyclists in competition in a hot environment. *Sci Rep*, Vol. 15, No. 1, pp. 21183, 2025.

[36] Scotto G.,Miniaci M.C., Silipo F. and Scotto P., Reduction of cutaneous blood flow in cold fingers. *Boll Soc Ital Biol Sper*, Vol. 74, No. 3-4, pp. 35-41, 1998.

[37] Karamaoun C., Haut B., Blain G., Bernard A., Daussin F., Dekerle J., Bougault V. and Mauroy B.J., Is airway damage during physical exercise related to airway dehydration: Inputs from a computational model. *J Appl Physiol*, Vol. 132, No. 4, pp. 1031-1040, 2022.

[38] Liu Z., Van Acker E., De Rijcke M., Van Nieuwerburgh F., Janssen C. and Asselman J., Exploring seasonal dynamics of sea spray aerosol bioactivity: Insights into molecular effects on human bronchial epithelial cells, *Environ Int*, Vol. 195 pp. 109255, 2025.

ISSN 1590-8844
International Journal of Mechanics and Control, Vol. 25, No. 02, 2024
https://doi.org/10.69076/jomac.20XX.00YY

TEMPLATE FOR PREPARING PAPERS FOR PUBLISHING IN INTERNATIONAL JOURNAL OF MECHANICS AND CONTROL

Author1*   Author2**

* affiliation Author1
** affiliation Author2

ABSTRACT

This is a brief guide to prepare papers in a better style for publishing in International Journal of Mechanics and Control (JoMaC). It gives details of the preferred style in a template format to ease paper presentation. The abstract must be able to indicate the principal authors' contribution to the argument containing the chosen method and the obtained results. (max 200 words)

Keywords: keywords list (max 5 words)

1 TITLE OF SECTION (E.G. INTRODUCTION)

This sample article is to show you how to prepare papers in a standard style for publishing in International Journal of Mechanics and Control.
It offers you a template for paper layout, and describes points you should notice before you submit your papers.

2 PREPARATION OF PAPERS

2.1 SUBMISSION OF PAPERS

The papers should be submitted in the form of an electronic document, either in Microsoft Word format (Word'97 version or earlier).
In addition to the electronic version a hardcopy of the complete paper including diagrams with annotations must be supplied. The final format of the papers will be A4 page size with a two column layout. The text will be Times New Roman font size 10.

2.2 DETAILS OF PAPER LAYOUT

2.2.1 Style of Writing

The language is English and with UK/European spelling. The papers should be written in the third person. Related work conducted elsewhere may be criticised but not the individuals conducting the work. The paper should be comprehensible both to specialists in the appropriate field and to those with a general understanding of the subject.
Company names or advertising, direct or indirect, is not permitted and product names will only be included at the discretion of the editor. Abbreviations should be spelt out in full the first time they appear and their abbreviated form included in brackets immediately after. Words used in a special context should appear in inverted single quotation mark the first time they appear. Papers are accepted also on the basis that they may be edited for style and language.

2.2.2 Paper length

Paper length is free, but should normally not exceed 10000 words and twenty illustrations.

2.2.3 Diagrams and figures

Figures and Tables will either be entered in one column or two columns and should be 80 mm or 160 mm wide respectively. A minimum line width of 1 point is required at actual size. Captions and annotations should be in 10 point with the first letter only capitalised *at actual size* (see Figure 1, Figure 2, Table VII and Table VIII).

Contact author: author1[1], author2[2]

[1]Address of author1.
[2]Address of author2 if different from author1's address
E-mail: author1@univ1.com , author2@univ2.com

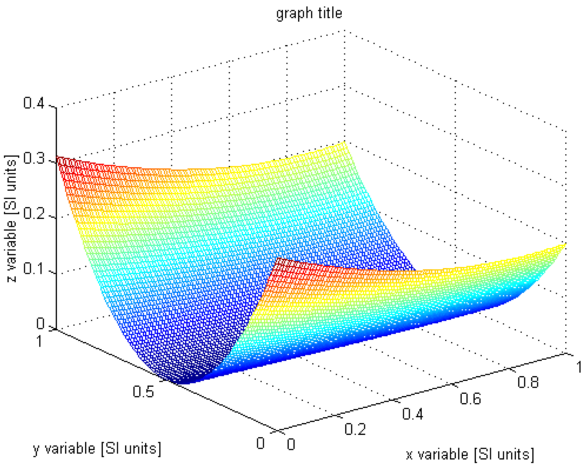

Figure 1 Simple chart.

Table VII - Experimental values

Robot Arm Velocity (rad/s)	Motor Torque (Nm)
0.123	10.123
1.456	20.234
2.789	30.345
3.012	40.456

2.2.4 Photographs and illustrations

Authors could wish to publish in full colour photographs and illustrations. Photographs and illustrations should be included in the electronic document and a copy of their original sent. Illustrations in full colour …

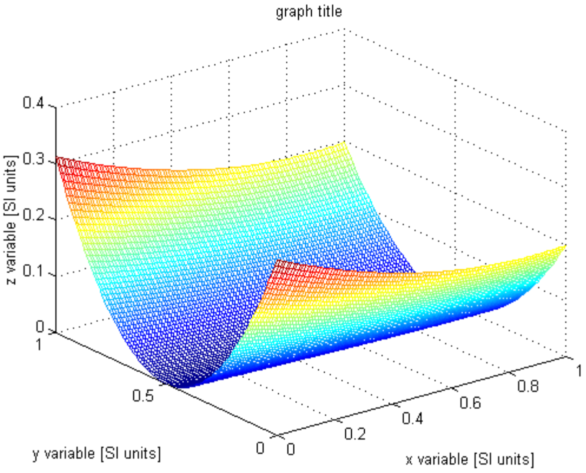

Figure 2 Simple chart.

2.2.5 Equations

Each equation should occur on a new line with uniform spacing from adjacent text as indicated in this template. The equations, where they are referred to in the text, should be numbered sequentially and their identifier enclosed in parenthesis, right justified. The symbols, where referred to in the text, should be italicised.

- point 1
- point 2
  - point 3

1. numbered point 1
   2. numbered point 2
      3. numbered point 3

$$W(d) = G(A_0, \sigma, d) = \frac{1}{T}\int_0^{+\infty} A_0 \cdot e^{-\frac{d^2}{2\sigma^2}}\, dt \qquad (1)$$

3 COPYRIGHT

Authors will be asked to sign a copyright transfer form prior to JoMaC publishing of their paper. Reproduction of any part of the publication is not allowed elsewhere without permission from JoMaC whose prior publication must be cited. The understanding is that they have been neither previously published nor submitted concurrently to any other publisher.

4 PEER REVIEW

Papers for publication in JoMaC will first undergo review by anonymous, impartial specialists in the appropriate field. Based on the comments of the referees the Editor will decide on acceptance, revision or rejection. The authors will be provided with copies of the reviewers' remarks to aid in revision and improvement where appropriate.

5 REFERENCES (DESCRIPTION)

The papers in the reference list must be cited in the text. In the text the citation should appear in square brackets [ ], as in, for example, "the red fox has been shown to jump the black cat [3] but not when...". In the Reference list the font should be Times New Roman with 10 point size. Author's first names should be terminated by a 'full stop'. The reference number should be enclosed in brackets.

The book titles should be in *italics*, followed by a 'full stop'. Proceedings or journal titles should be in *italics*. For instance:

Table VIII - Experimental values

Robot Arm Velocity (rad/s)	Motor Torque (Nm)	Motor Torque (Nm)	Motor Torque (Nm)
0.123	10.123	10.123	10.123
1.456	20.234	20.234	20.234
2.789	30.345	30.345	30.345
3.012	40.456	40.456	40.456

REFERENCES (EXAMPLE)

[1] Smith J., Jones A.B. and Brown J., *The title of the book*. 1st edition, Publisher, 2001.

[2] Smith J., Jones A.B. and Brown J., The title of the paper. *Proc. of* C*onference Name*, where it took place, Vol. 1, paper number, pp. 1-11, 2001.

[3] Smith J., Jones A.B. and Brown J., The title of the paper. *Journal Name*, Vol. 1, No. 1, pp. 1-11, 2001.

[4] Smith J., Jones A.B. and Brown J., *Patent title*, U.S. Patent number, 2001.

International Journal of Mechanics and Control – JoMaC
Published by ASTRA M B S.R.L.

TRANSFER OF COPYRIGHT AGREEMENT

NOTE:
Authors/copyright holders are asked to complete this form signing section A, B or C and mail it to the editor office with the manuscript or as soon afterwards as possible.

Editorial Secretary address:
Andrea Manuello Bertetto
Matteo D. L. Dalla Vedova, Simone Venturini, Alessandro Aimasso
Dept. of Mechanical and Aerospace Engineering
Politecnico di Torino
C.so Duca degli Abruzzi, 24 – 10129 Torino – Italy
e_mail: jomac@polito.it
fax n.: +39.011.090.6999

The article title:

By:____

To be Published in ***International Journal of Mechanics and Control JoMaC***
Official legal Turin court registration Number 5320 (5 May 2000) - reg. Tribunale di Torino N. 5390 del 5 maggio 2000

A Copyright to the above article is hereby transferred to the JoMaC, effective upon acceptance for publication. However the following rights are reserved by the author(s)/copyright holder(s):

1. All proprietary rights other than copyright, such as patent rights;
2. The right to use, free or charge, all or part of this article in future works of their own, such as books and lectures;
3. The right to reproduce the article for their own purposes provided the copies are not offered for sale.

To be signed below by all authors or, if signed by only one author on behalf of all co-authors, the statement A2 below must be signed.

A1. All authors:

SIGNATURE______________________________________DATE_______________ SIGNATURE______________________________________DATE_______________

PRINTED NAME____ PRINTED NAME____

SIGNATURE______________________________________DATE_______________ SIGNATURE______________________________________DATE_______________

PRINTED NAME____ PRINTED NAME____

A2. One author on behalf of all co-authors:
"I represent and warrant that I am authorised to execute this transfer of copyright on behalf of all the authors of the article referred to above"

PRINTED NAME____

SIGNATURE____ TITLE____ DATE______________________

B. The above article was written as part of duties as an employee or otherwise as a work made for hire. As an authorised representative of the employer or other proprietor. I hereby transfer copyright to the above article to *International Journal of Mechanics and Control* effective upon publication. However, the following rights are reserved:

1. All proprietary rights other than copyright, such as patent rights;
2. The right to use, free or charge, all or part of this article in future works of their own, such as books and lectures;
3. The right to reproduce the article for their own purposes provided the copies are not offered for sale.

PRINTED NAME____

SIGNATURE____ TITLE____ DATE______________________

C. I certify that the above article has been written in the course of employment by the United States Government so that no copyright exists, or by the United Kingdom Government (Crown Copyright), thus there is no transfer of copyright.

PRINTED NAME____

SIGNATURE____ TITLE____ DATE______________________

CONTENTS – Regular Issue

NEWS FROM THE JOMAC EDITORIAL BOARD:

Starting from the June 2024 issue, JoMaC provides an Open Access service to our authors.
You are invited to visit the JoMaC website (http://www.jomac.it) for further details.